UNIVERSIDAD NACIONAL AUTÓNOMA DE MÉXICO

POSGRADO EN CIENCIAS DE LA TIERRA

INSTITUTO DE GEOFÍSICA

GEOLOGY, GEOCHEMISTRY AND MINERALOGY OF THE "MONTAÑA DE MANGANESO" MANGANESE DEPOSIT: IMPLICATIONS FOR GENESIS.

TESIS

QUE PARA OPTAR POR EL GRADO DE:

DOCTOR EN CIENCIAS DE LA TIERRA

PRESENTA:

JOSEPH MADONDO

DIRECTOR DE TESIS

DR. CARLES CANET MIQUEL

INSTITUTO DE GEOFÍSICA

CIUDAD UNIVERSITARIA, CD. MX. MARZO 2022

This thesis is dedicated

to my mother,

Rezinath Chinyerere

Acknowledgements

I wish to express my sincere gratitude to all those persons and institutions that have lent their help and support during the completion of this doctoral thesis.

I thank first and foremost my thesis director Dr. Carles Canet Miquel for his steadfast support, assistance, patience, understanding and guidance during the development of this investigation. Dr. Canet encouraged me to work independently and productively to materialize my own ideas and models for the study area whilst at the same time creating an environment for collaborating with other research teams. I also thank my committee members Dr. Eduardo González Partida and Dr Ofelia Morton Bermea for advice, help, invaluable insight, and continued support throughout this thesis provided.

I thank Dr. Fernando Nuñez Useche and Dr. Augusto Rodriguez Diaz for their precious support during fieldwork, analyses, and interpretation of results. I especially thank Dr. Teresa Pi Puig for helping with the X ray diffraction analyses of clay and manganese ore samples at the Laboratorio de Difracción de Rayos X, UNAM and for the many life lessons taught during our time in the laboratory. I also thank and acknowledge the technical and finacila support provided by the following collaborators:

Dr. Pura Alfonso Abella, of the Universidad Politécnica de Cataluña, for the measurement of sulfur isotopes. M.Sc. Edith Cienfuegos Alvarado, for the measurement of C and O isotopes in carbonates (Laboratorio de Isótopos Estables). Msc. Edith Fuentes for cathodoluminescence analyses (Laboratorio de Catodoluminiscencia e Inclusiones Fluidas). Eng. Carlos Linares for the electronic microprobe data (Laboratorio Universitario de Petrologia, Instituto de Geofísica, UNAM). Dra. Margarita Reyes and Quim. Sonia Angeles for SEM analyses at the Laboratorio Nacional de Geoquímica y Mineralogía (LANGEM), Instituto de Geologia. Msc. Ulises Loredo Jasso for ATR-FTIR measurements (Laboratorio de Geoquímica Ambiental Molecular) and Dra Augusto Antonio Rodriguez-Diaz for complimentary SEM analyses (Laboratorio de Petrografía y Microtermometría). Dr. Vanessa Colas Guines for financial support with ICP MS analyses.

I thank CONACYT, for the scholarship (# 706156) that made it possible for me to study in Mexico.

I thank the following people for their comments, reviews and criticisms that enriched the present work: Dr. Abdorrahman Rajabi, Msc. Miguel Angel Cruz Perez, Msc. Cesar Aguilar Ramirez,

Last but not least, I would like to thank my family, particularly my wife Nidia Carolina Cerda Aleman for invaluable support throughout the duration of this thesis.

Resumen

La Montaña de Manganeso es un depósito tipo veta de manganeso asociado espacialmente con depósitos de posarco perteneciente al Terreno Guerrero. La mineralización de manganeso consiste en minerales de óxido que forman contactos bruscos con las rocas volcánicas encajonantes en forma de vetas y masas irregulares, y localmente como brechas mineralizadas. Los análisis petrográficos indican que la mineralización es multiepisódica, con predominio de texturas coloformes y crustiformes. La difracción de rayos X y la microscopía electrónica muestran que los óxidos de manganeso (todorokita, birnessita, pirolusita, romanechita, hollandita, coronadita y criptomelano) son los principales minerales, mientras que los óxidos y sulfuros de hierro (goethita, magnetita, hematita y pirita) son accesorios. Los minerales de ganga más comunes son la calcita y el cuarzo, con cantidades subordinadas de barita. El estudio de las características geoquímicas de los elementos principales y traza del depósito proporciona información sobre los controles de los procesos de formación de minerales dentro del área. El depósito se caracteriza por una baja abundancia de Co, Cu y Ni, y altos contenidos de Ba (>10,000 ppm) y relaciones Mn/ Fe <500, típicas de los depósitos hidrotermales de Mn. Además, las abundancias bajas de ∑REE (19 a 103 ppm), las anomalías negativas de Ce (0,2 a 0,6), las anomalías positivas de Y (1,00 a 2,34) y las anomalías de Eu (0,6 a 4,4) también sugieren una fuente hidrotermal para el depósito. Las gráficas de discriminación de ∑REE y Zr vs. (Cu+Ni+Co) y Ce/Ce* versus Nd e Y/Ho indican, además, una fuente hidrotermal en un ambiente de depósito oxidante. Los diagramas Mn-Fe- (Ni+Cu+Co), MnO2-MgO-Fe2O3, (Cu/Zn)/Fe2O3 vs. (Zn/Ni)/MnO2 y Na/Mg muestran firmas intermedias entre los ambientes marino y terrestre. De acuerdo con la microtermometría de inclusiones fluidas, la mineralización está asociada a soluciones acuosas de salinidad intermedia (8–16% en peso equivalente de NaCl) y temperaturas entre 101 y 140 °C. El análisis de isótopos estables de calcita (δ13CPDB: -7.76 a -6.32 ‰; δ18OPDB: -8.01 a -4.71 ‰) y barita (δ34S: 7.9-13.6 ‰) muestra una contribución de volátiles magmáticos a fluidos hidrotermales dominados por agua meteórica (δ18Ofluid calculada : 6,58–13,14 ‰, relativo a SMOW). La alteración argílica es la alteración hidrotermal más extendida en Montaña de Manganeso e indica una temperatura del fluido por debajo de ~ 150 °C y un pH casi neutro. Una alteración argílica mucho más local y

avanzada, revelada por la aparición de caolinita, se interpreta como resultado de calentamiento por vapor, lo que a su vez sugiere un proceso de ebullición que debe haber ocurrido a mayores profundidades. Los resultados de este estudio sugieren la formación del depósito durante dos etapas metalogénicas: (I) la etapa más temprana involucró la formación de óxidos de Mn por procesos hidrotermales en una cuenca de posarco (Arperos) durante el Cretácico; y (II) la última etapa tuvo lugar posterior a la acreción del Terreno Guerrero en el continente e implicó la removilización de los óxidos de Mn submarinos del Cretácico (y elementos traza asociados) y la posterior redeposición por la actividad hidrotermal continental Terciaria. En esta segunda etapa, los minerales de Mn se formaron en la parte somera de un sistema epitermal a través de un proceso de mezcla de: (*a*) fluidos hidrotermales ebullidas, con (*b*) aguas meteóricas diluidas y frías, lo cual apoya un modelo tipo *hot-spring* para esta etapa.

Abstract

The Montana de Manganeso is a manganese vein-type deposit spatially associated with back-arc basin remnants of the Guerrero tectonostratigraphic terrane. Manganese mineralization consists of oxide ores that form sharp contacts with volcanic host rocks in the form of veins and irregular masses, and locally as mineralized breccias. Petrographic analyses indicate that the mineralization is multi-episodic, with colloform and crustiform textures predominating. The X-ray diffraction and electron microscopy show that manganese oxides (todorokite, birnessite, pyrolusite, romanechite, hollandite, coronadite and cryptomelane) are the main ore minerals, while iron oxides (goethite, magnetite, and hematite) are accessory. The most common gangue minerals are calcite and quartz with subordinate amounts of barite.

The study of major- and trace-element geochemical characteristics of the deposit provides insight into the controls on ore-forming processes within the area. The deposit is characterized by low Co, Cu and Ni abundances, and high Ba (>10,000 ppm) contents and Mn/Fe ratios (<500), typical of hydrothermal Mn deposits. In addition, the low ∑REE abundances (18.7 to 103 ppm), negative Ce anomalies (0.2 to 0.6), and positive Y (1.00 to 2.34) and Eu anomalies (0.6 to 4.4) also suggest a hydrothermal source for the deposit. Discrimination plots involving ∑REE and Zr vs. (Cu + Ni + Co) and Ce/Ce* vs. Nd and Y/Ho further indicate a hydrothermal source in an oxidizing depositional environment. The Mn-Fe-(Ni + Cu + Co), MnO2-MgO-Fe2O3, (Cu/Zn)/Fe2O3 vs. (Zn/Ni)/MnO2 and Na/Mg diagrams display intermediate signatures between marine and terrestrial environments.

According to fluid inclusion microthermometry, the mineralization is associated with aqueous solutions of intermediate salinity (8–16 wt% NaCl equivalent) and temperatures between 101 and 140 °C. Stable isotope analysis of calcite ($\delta^{13}C_{PDB}$: -7.76 to -6.32‰; $\delta^{18}O_{PDB}$: -8.01 to -4.71‰) and barite (δ34S: 7.9–13.6‰) shows a contribution of magmatic volatiles to hydrothermal fluids dominated by meteoric water (calculated δ^{18}Ofluid: 6.58–13.14‰, relative to SMOW). Argillic alteration is the most widespread hydrothermal alteration at Montaña de Manganeso and indicates fluid temperature below ~150 °C and near neutral pH. Much more local, advanced argillic alteration, revealed by the occurrence of

kaolinite, is interpreted as a steam-heated overprint, which in turn suggests a boiling process that must have happened at greater depths.

The results of this study suggest formation of the deposit during two metallogenic stages: (I) the earliest stage involved the formation of Mn oxides by hydrothermal/ diagenetic processes in the Arperos back-arc basin during the Cretaceous; and (II) the latest stage took place subsequent to the accretion of the Guerrero tectonostratigraphic terrane onto the continent and involved the remobilization of the Cretaceous submarine Mn oxides (and associated trace elements) and subsequent redeposition by Tertiary continental hydrothermal activity. In this second stage Mn ores formed in the shallowest portion of an epithermal system through a process of mixing of: (*a*) boiled-off hydrothermal fluids, with (*b*) cold, diluted meteoric waters supporting a hot-spring deposit model for this stage.

Table of Contents

CHAPTER 1

INTRODUCTION

1.Introduction

1.1 General introduction

Manganese is the tenth most abundant element in the Earth's crust constituting approximately 0.1% (by weight) of the Earth´s crust (Kuleshov and Maynard, 2017; Maynard, 2014). Chemically manganese is similar to Fe (Maynard, 2014). Under reducing conditions, it exists as Mn^{2+} forming minerals such as rhodochrosite and under oxidizing conditions it exists as Mn^{4+} mainly as an oxide (eg pyrolusite).

Historically, manganese has mainly been used in steel production. The rest has traditionally been used in battery production, fertilizers, water treatment etc. However, with a global shift toward environmentally friendly energy production manganese oxides have become an important energy metal due to their low-cost applicability in the production of next generation battery and power storage applications such as rechargeable batteries, supercapacitors and catalysts (Barbato, 2001; Birkner and Navrotsky, 2017; Fan et al., 2018; Post, 1999; Tompsett and Islam, 2013). Consequently, this has increased demand and interest in finding and diversifying new supplies of manganese. Nevertheless, the extraction of Mn oxides requires a complete and multidisciplinary understanding of the genesis of the deposits that contain them.

1.2 Objectives

The main objective of this investigation is thus to investigate the principal geologic and geochemical characteristics of the Montaña de Manganeso Mn deposit and review the current understanding of the genesis of the deposit. Emphasis will be placed on some of the recent developments in the geochemistry of manganese deposits that may shed new light on the processes involved in the formation of this deposit. It is hoped the findings of this study can be applied for exploration of the vein-type manganese deposits that are widespread in the Central Plateau and similar deposits worldwide.

1.2.1 Specific Objectives

- To describe the geologic setting and lithological associations of the Montaña de Manganeso deposit.
- To describe in detail the mineralogical and geochemical characteristics of the Montaña de Manganeso vein-type manganese deposit.
- To describe the ore paragenesis.
- To determine the source of the ore-forming fluids and processes experienced by them.
- To estimate physicochemical conditions of the mineralizing fluids and deposition mechanism(s) through fluid inclusion systematics.
- To constrain the age of the deposit through U-Pb geochronology
- To infer a depositional environment and to develop a genetic model.

1.3 Thesis Outline

The author was privileged in that he undertook the first preliminary study on the petrography and mineralogy of parts of the Montaña de Manganeso deposit in 2015 as an MSc project at the National Autonomous University of Mexico (UNAM). This study is essentially the continuation of that early work on a much broader scale.

The thesis consists of five manuscripts, three published and two under preparation, which deal individually with different aspects of the deposit, but together provide complete picture of the processes involved in deposit formation. The first manuscript is a review of the relationship between Mn and the precious metals Ag and Au. These metals are closely associated, generally forming deposits in the epithermal environment that are spatially and possibly genetically related (Hewett, 1964; Roy, 1981). The study region is host to both Mn and Ag ± Au epithermal deposits that present a common association with jasperoid bodies (Albinson, 1988; Camprubí and Albinson, 2007; Labarthe Hernández et al., 1992; Nieto-Samaniego et al., 2007; Ponce and Clark, 1988).

The second manuscript, consequently, deals with the silicification and formation of jasperoid bodies that are the morphological expression of the Montaña de Manganeso deposit and form the most noticeable characteristic of the deposit. The paper focuses on the

conditions required for massive silica formation and uses the mineralogy and geochemistry of the non-silica component to determine the conditions of formation of the Montaña de Manganeso jasperoids (Adachi et al., 1986; Dasgupta et al., 1999). The third manuscript focuses on hydrothermal alteration associated with the Montaña de Manganeso deposit with emphasis on the processes that controlled the alteration observed in the host rocks. The mineralogy and chemistry of the hydrothermal clays is also studied in order to determine the nature of the fluids responsible for the alteration (Fulignati, 2020; Reyes, 1990; Thompson and Thompson, 1996).

The fourth manuscript deals with the petrography, mineralogy, and geochemistry of the manganese ore with particular emphasis placed on the physicochemical conditions pertaining to the deposition of the Montaña de Manganeso. The petrographic characteristics are described to provide a framework for the evaluation of the geochemical data. The major, minor, trace and REE composition of the Montaña de Manganeso are presented and employed as redox and paleonvironmental proxies (Bau et al., 2014; Conly et al., 2011; Josso et al., 2017; Nicholson, 1992; Roy, 1992). Comparisons with selected major Mn deposit types is provided, facilitating a better understanding of the origin of the Montaña de Manganeso deposit.

The fifth manuscript provide an integrated view of the deposit and provides a significant amount of new data on the petrography and mineralogy of the Montaña de Manganeso deposit that allowed determination of the mineral paragenesis. Stable isotope systematics (C, O and S) and fluid inclusions microthermometry allowed determination of the source of the ore-forming fluids and estimation of the physicochemical conditions of the mineralizing fluids and depositional mechanism(s). U-Pb geochronology provided additional constraints on the age and genesis of the deposit.

The final discussion provides an overall account on the genesis of the Montaña de Manganeso deposit and comprises a detailed discussion based on the five manuscripts. In addition, implications regarding mineral exploration of the vein-type manganese deposits that are widespread in the Central Plateau (Mesa Central), are briefly discussed.

1.4 Background

1.4.1 History of production

Manganese is found in 20 of the 31 states of Mexico with the majority of deposits located in Hidalgo, Chihuahua, Zacatecas, Baja California, Durango, Sonora, Sinaloa, Jalisco and San Luis Potosí (Trask and Cabo, 1948; Wilson and Rocha, 1948). Although manganese in Mexico has a long history that goes back to colonial times, commercial interest in manganese had its peak between the First and Second World Wars (Ayub, 1960). During the World War 1 and in the years prior to the World War 2 the loci of production was in Chihuahua (Talamantes deposits), San Luis Potosi (Montaña de Manganeso deposits), Zacatecas (Negra deposits), Sonora (Antillas deposits) and Baja California (Gavilan deposits). Production peaks occurred during the period 1918-1920 estimated at 2000 tones and during the mid-1920s at around 3000 tons per year (Bancomext, 1976). During the rest of the pre-WWII period production averaged 1000 tons per year (Bancomext, 1976).

With the beginning of the World War II the production of manganese ore increased sharply, and the loci of production changed. The total recorded production of manganese ore in Mexico prior to 1942 amounted to about 54,000 tons (Trask and Cabo, 1948). During the period 1942-1945 an estimated annual average of 20 500 tones were produced (Bancomext, 1976). Trask and Cabo (1948) estimated that 80,671 tons were produced in 1944 alone. Most of the production came from deposits in Baja California (Lucifer deposits) and Zacatecas (Abundancia deposits) which are said to have produced up to 2,500 tons and 1000 tons a month respectively, during the WWII (Trask and Cabo, 1948). The plummeting prices of manganese on international markets due to the end of the WWII depressed production in the late 1940s and the beginning of the 1950s. However, the Korean War in the 1950s and the suspension of exports to the USA by the Soviet Union due to the Cold War again drove Mexican production high, which surpassed 83 000 tons in 1954 (Bancomext, 1976; Torres-Montufar, 2017). Although production varied greatly these levels of production were maintained in the 50s and 60s (Ayub, 1960; Bancomext, 1976). Much of this production came from the newly discovered San Francisco deposits of (Jalisco) owned by the Autlan mining company.

The discovery of the Molango deposits in Hidalgo in 1960s by the same company was a game changer. By 1975 a total of 150 000 tons were produced in Mexico, 90 % of which was produced from the Molango deposits (Bancomext, 1976). Sustained increase in production throughout the years has seen production reaching around 233 000 tons in 2019 (SGM, 2020). For a more detailed analysis of manganese production in Mexico, the reader is referred to the report by Bancomext (1976) and the review by Torres-Montufar, (2017).

1.4.2 Mn metallogenesis in Mexico

Globally, the most important manganese deposits are sedimentary or sedimentary-exhalative (Laznicka, 1992; Roy, 1997). The giant sedimentary Upper Jurassic Molango deposits in the State of Hidalgo are considered as the largest and most important Mn deposits in North America (Okita et al., 1988; Okita and Shanks, 1992). These deposits were formed through a bacterially mediated reduction of Mn oxides in a restricted marine environment (Okita, 1992). The primary source of Mn is not known although hydrothermalism associated with the opening of the Gulf of Mexico and fluvial runoff have been proposed (Okita et al., 1988). Biostratigraphic correlation indicate that the deposits formed during the Kimmeridgian (Okita et al., 1988).

Mexico also has a substantial number of Mn deposits of epigenetic hydrothermal origin. These deposits are widely scattered in various mining districts throughout Mexico, with at least 335 deposits and occurrences reported in 20 states (Trask and Cabo, 1948). They are generally small to medium-sized deposits hosted within mostly volcanic rocks. They mainly occur as veins, breccias, stockworks or as strata-bound lenticular and concordant bodies (Hewett, 1964; Laznicka, 1992; Mapes-Vazquez, 1956; Roy, 1997, 1992; Zantop, 1978). Most of these deposits formed in an epithermal environment and are believed to be fossil analogues of active land based hot springs (Hewett, 1964; Zantop, 1978). Well-known Mn hydrothermal deposits are those of the Talamantes (Chihuahua, northwestern Mexico) and the San Francisco districts (Jalisco, central Mexico) (Wilson and Rocha, 1948; Zantop, 1978).

A variety of these deposits were formed through shallow sedimentary exhalative processes within extensional settings. Such is the case of the deposits of the Baja California peninsula such as the Lucifer, El Gavilán and Guadalupe deposits in Bahía Concepción (Camprubí et al., 2008; Rodríguez-Díaz et al., 2010). There are also Mn manifestations currently being generated in shallow water active thermal springs in the Bahía Concepción area (Camprubí et al., 2008; Canet et al., 2005; Rodríguez-Díaz et al., 2019). These deposits show intermediate characteristics between deep sea submarine systems and continental hydrothermal systems (Canet et al., 2005). The fluid geochemistry and mineralogy of these deposits has been extensively studied (Canet et al., 2005; Prol-Ledesma et al., 2004; Villanueva-Estrada et al., 2013, 2012) due to their affinity and genetic relationship with epithermal deposits and geothermal systems (Canet et al., 2005; Prol-Ledesma et al., 2004; Rodríguez-Díaz et al., 2019; Villanueva-Estrada et al., 2012).

1.4.3 History of Mn studies in Mexico

Manganese deposits in Mexico were first discussed in detail by Trask and Cabo (1948) who carried out a comprehensive description of the Mn deposits of Mexico known at the time. Because their work was directed towards reserve estimation and production only descriptive work on the geology of the manganese deposits was carried out. The greatest part of their work was the classification of Manganese deposits of Mexico based on lithological characteristics of the host rocks and their relation to mineralization. This work was also published in a symposium of the XX International Geological Congress volume III (edited by Gonzalez-Reyna, 1956b). The deposits of Chihuahua, Sonora, Durango, Zacatecas and San Luis Potosi where revisited by Ayub (1960) who provided a more detailed description of these deposits. Similar to the work of Trask and Cabo (1948), this work was also directed towards reserve estimation.

In light of the new knowledge on the chemistry of Mn deposits brought by the discovery and study of the Mn nodules and crusts by the Deep Sea Drilling Project (DSDP) exploration, Zantop (1981) first applied trace element analysis to interpret the genesis of the Mn deposits in Mexico. He interpreted trace element concentration in the San Francisco deposit as

supporting evidence for volcanic contributions to deposit formation. The decade of the 1980s also saw an agreement between Mexico and Spain for the exploration of manganese deposits in central Mexico (Reyes-Reyes et al., 1988). A Mn reserve (*Reserva Minera Nacional Villa de Cos*) was declared in 1979 in the region covering northcentral Zacatecas and northwest San Luis Potosi and geophysical and geochemical regional studies were carried for the purpose of prospection and reserve estimation.

With the discovery of the Molango deposits in the decade of the 1960s came the interest to study the sediment hosted deposits of the district. A series of publications were made in the late 1980s and early 1990s mostly by researchers from the University of Cincinnati (USA). Okita et al., (1988), Maynard et al., (1990) and Okita and Shanks, (1992) investigated the formation of the primary Mn mineralization hosted at the basal sections of the Chipoco formation. The mineralization consists of Mn carbonates (rhodochrosite, kutnohorite and Mn-calcite) of diagenetic origin and a suite of supergene oxides principally nsutite, todorokite, birnessite and pyrolusite. Carbon and sulfur isotope studies coupled with sedimentological and geochemical studies were used to infer a diagenetic origin of the Mn carbonates in a suboxic/anoxic environment. The ultimate source of Mn is not known but it is believed to be hydrothermalism associated with the opening Gulf of Mexico. This model implies a distal sedimentary-exhalative model for the Molango deposits.

At the turn of the century interest in manganese turned mainly to the processes leading to Mn accumulation on the modern seafloor (Canet et al., 2008) and in shallow marine environment (Canet et al., 2005; Rodríguez-Díaz et al., 2019, 2010) as well as studies on continental hydrothermal deposits (Conly et al., 2011; Del Rio-Salas et al., 2013; Del Rio Salas et al., 2008) mostly located along the peninsula of Baja California. These studies contributed immensely to the understanding of formation of manganese deposits in general. Studies by Canet et al., (2005), Conly et al., (2011) and Del Rio-Salas et al., (2008; 2013) have become reference material for understanding genetic processes in the shallow marine environment.

1.3.2 Previous works on the Montaña de Manganeso deposit

The Montaña de Manganeso mine is one of the oldest manganese mines in Mexico (Ayub, 1960). The discovery of Mn on the Montaña de Manganeso dates back to the beginning of the last century. Mining operations were started sometime around 1914 under the Adeleon, S.A. de CV company. Records of production are not complete but historically production peaks were recorded during the period 1939 to 1951, when the mine produced about 109,200 tons with an average grade of 40% manganese oxides making it the third largest producer of manganese ore in Mexico after the Lucifer (Baja California) and Talamantes (Chihuahua) deposits. Most of that production was exported to the U.S.A. and to the smelter at Monterrey, Nuevo Leon, operated by the Fundidora de Fierro y Acero de Monterrey company. The Adeleon, S.A. de CV company changed its name to Montaña de Manganeso in 1954 and production has been on and off since then. Publicly available data indicate that exploration was carried out in the 1980′s as part of a Mexico-Spain project on manganese whose objective was to evaluate the potential of the manganese deposits and the presence of any anomalous values of Au and Ag (Coremi, 1980; Reyes-Reyes et al., 1988). Electric, magnetic and gravimetric techniques were employed at Montaña de Manganeso to study the potential of more manganese at depth (Reyes-Reyes et al., 1988). Results of these studies were mostly unfavorable. The mine is now operated by the Huajicari, S.A. de C.V company and current production is about 4000 metric tons per day (SGM), 2011).

Very few publications are available on the Montaña de Manganeso deposit. Early research on Montaña de Manganeso focused on particular aspects of the geology, mineralogy and structure of this deposit, with a few studies having been published (Trask and Cabo, 1948; Wilson and Rocha, 1948). The mineralogy of the Montana de Manganeso deposit was first studied by Wilson and Rocha (1948), who identified the Mn ore as primarily comprising pyrolusite with subordinated manganite and braunite. The same minerals were reported by Ayub (1960). Cryptomelane, nsutite, bementite and Mn diopside were identified by Alexandri, (1976). Psilomelane (romanechite and hollandite) was identified during studies under the Mexico-Spain project on manganese (Reyes-Reyes et al., 1988). The occurrence of some of these minerals were confirmed in recent reports of the Mexican Geological Survey (Coremi, 2001).

These early studies also addressed the geology and structure of the deposit, however scarce outcrops due to recent sedimentary cover means most studies were limited to outcrops on the Montaña de Manganeso mine itself. Pervasive hydrothermal alteration of the deposit further limited proper description of the original lithologies of the host rocks. They have thus variably been described as tuffs (Trask and Cabo, 1948) or phyllites and lutites (Alexandri, 1976). Other investigations on the deposit have described these rocks as a mélange of shales, metasandstones and andesites belonging to the Guerrero terrane (Coremi, 2001). In most of these studies, proper identification based on detailed petrography and geochemistry is lacking. The predominant occurrence of hydrothermal alteration in the form of clays and jasperoids was obviously recognized in these early works given the extent and degree of alteration (Alexandri, 1976). However, no further studies to characterize this alteration were carried out. The structure of the deposit as occurring principally in the form of mineralized veins, stockworks and breccias was well described in almost all these previous studies. Despite the limited information available from these previous works, they did set the geologic framework of the deposit (Coremi, 2001).

References

Adachi, M., Yamamoto, K., Sugisaki, R., 1986. Hydrothermal chert and associated siliceous rocks from the northern Pacific their geological significance as indication od ocean ridge activity. Sedimentary Geology 47, 125–148. https://doi.org/10.1016/0037-0738(86)90075-8

Albinson, T.F., 1988. Geologic reconstruction of paleosurfaces in the Sombrerete, Colorado, and Fresnillo districts, Zacatecas State, Mexico. Economic Geology 83, 1647–1667. https://doi.org/10.2113/gsecongeo.83.8.1647

Alexandri, R.R., 1976. Estudio Geológico del Yacimiento Montaña de Manganeso.

Ayub, A.R., 1960. Minerales de Manganeso en los Estados de Sonora, Durango, Zacatecas y San Luis Potosí. Distrito Federal.

Bancomext, 1976. Manganeso y sus aleaciones [WWW Document]. URL

http://revistas.bancomext.gob.mx/rce/magazines/374/12/RCE11.pdf (accessed 8.30.21).

Barbato, S., 2001. Hollandite cathodes for lithium ion batteries. 2. Thermodynamic and kinetics studies of lithium insertion into BaMMn7O16 (M=Mg, Mn, Fe, Ni). Electrochimica Acta 46, 2767–2776. https://doi.org/10.1016/S0013-4686(01)00506-0

Bau, M., Schmidt, K., Koschinsky, A., Hein, J., Kuhn, T., Usui, A., 2014. Discriminating between different genetic types of marine ferro-manganese crusts and nodules based on rare earth elements and yttrium. Chemical Geology 381, 1–9. https://doi.org/10.1016/j.chemgeo.2014.05.004

Birkner, N., Navrotsky, A., 2017. Thermodynamics of manganese oxides: Sodium, potassium, and calcium birnessite and cryptomelane. Proceedings of the National Academy of Sciences of the United States of America 114, E1046–E1053. https://doi.org/10.1073/pnas.1620427114

Camprubí, A., Albinson, T., 2007. Epithermal deposits in México—Update of current knowledge, and an empirical reclassification, in: Special Paper 422: Geology of México: Celebrating the Centenary of the Geological Society of México. Geological Society of America, pp. 377–415. https://doi.org/10.1130/2007.2422(14)

Camprubí, A., Canet, C., Rodríguez-Díaz, A.A., Prol-Ledesma, R.M., Blanco-Florido, D., Villanueva, R.E., López-Sánchez, A., 2008. Geology, ore deposits and hydrothermal venting in Bahía Concepción, Baja California Sur, Mexico. Island Arc 17, 6–25. https://doi.org/10.1111/j.1440-1738.2007.00586.x

Canet, C., Prol-Ledesma, R.M., Bandy, W.L., Schaaf, P., Linares, C., Camprubí, A., Tauler, E., Mortera-Gutiérrez, C., 2008. Mineralogical and geochemical constraints on the origin of ferromanganese crusts from the Rivera Plate (western margin of Mexico). Marine Geology 251, 47–59. https://doi.org/10.1016/j.margeo.2008.01.012

Canet, C., Prol-Ledesma, R.M., Proenza, J.A., Rubio-Ramos, M.A., Forrest, M.J., Torres-Vera, M.A., Rodríguez-Díaz, A.A., 2005. Mn-Ba-Hg mineralization at shallow submarine hydrothermal vents in Bahía Concepción, Baja California Sur, Mexico.

Chemical Geology 224, 96–112. https://doi.org/10.1016/j.chemgeo.2005.07.023

Conly, A.G., Scott, S.D., Bellon, H., 2011. Metalliferous manganese oxide mineralization associated with the Boléo Cu-Co-Zn district, Mexico. Economic Geology 106, 1173–1196. https://doi.org/10.2113/econgeo.106.7.1173

Consejo de Recursos Minerales (COREMI), 2001. Informe final de la carta geologico-minera Villa de Santo Domingo F14-A-31. Pachuca, Hgo, Hgo.

Dasgupta, H.C., Sambasiva Rao, V. V., Krishna, C., 1999. Chemical environments of deposition of ancient iron- and manganese-rich sediments and cherts. Sedimentary Geology 125, 83–98. https://doi.org/10.1016/S0037-0738(98)00148-1

Del Rio-Salas, R., Ochoa-Landín, L., Eastoe, C.J., Ruiz, J., Meza-Figueroa, D., Valencia-Moreno, M., Zúñiga-Hernández, H., Zúñiga-Hernández, L., Moreno-Rodríguez, V., Mendívil-Quijada, H., 2013. Genesis of manganese oxide mineralization in the boleo region and concepción peninsula, baja california sur: Constraints from Pb-Sr isotopes and REE geochemistry. Revista Mexicana de Ciencias Geologicas 30, 482–499.

Del Rio Salas, R., Ruiz, J., Ochoa-Landín, L., Noriega, O., Barra, F., Meza-Figueroa, D., Paz-Moreno, F., 2008. Geology, Geochemistry and Re-Os systematics of manganese deposits from the Santa Rosalía Basin and adjacent areas in Baja California Sur, México. Mineralium Deposita 43, 467–482. https://doi.org/10.1007/s00126-008-0177-3

Fan, C., Xu, L., Zhao, W., 2018. Transformation of birnessite into hollandite under the influence of silver cations in aqueous medium. Journal of Solid State Chemistry 268, 136–148. https://doi.org/10.1016/j.jssc.2018.08.039

Fulignati, P., 2020. Clay minerals in hydrothermal systems. Minerals 10, 1–17. https://doi.org/10.3390/min10100919

Hewett, D.F., 1964. Veins of hypogene manganese oxide minerals in the southwestern United States. Economic Geology 59, 1429–1472. https://doi.org/10.2113/gsecongeo.59.8.1429

Josso, P., Pelleter, E., Pourret, O., Fouquet, Y., Etoubleau, J., Cheron, S., Bollinger, C., 2017.

A new discrimination scheme for oceanic ferromanganese deposits using high field strength and rare earth elements. Ore Geology Reviews 87, 3–15. https://doi.org/10.1016/j.oregeorev.2016.09.003

Kuleshov, V., Maynard, J.B., 2017. Isotope Geochemistry: The Origin and Formation of Manganese Rocks and Ores, Elsevier. Elsevier Inc.

Labarthe Hernández, G., Jiménez López, L., Motilla Moreno, J., 1992. Jasperoide--guía posible en la exploración minera, Mesa Central, México. Revista mexicana de ciencias geológicas 10, 137–142.

Laznicka, P., 1992. Manganese deposits in the global lithogenetic system: Quantitative approach. Ore Geology Reviews 7, 279–356. https://doi.org/10.1016/0169-1368(92)90013-B

Mapes-Vazquez, E., 1956. El manganeso en México, in: González-Reyna, J. (Ed.), Symposium Sobre Yacimientos de Manganeso. Congreso Geológico Internacional, pp. 35–78.

Maynard, J.B., 2014. Manganiferous Sediments, Rocks, and Ores, in: Holland, H.D., Turekian, K.K. (Eds.), Treatise on Geochemistry. Elsevier, Oxford, pp. 327–349.

Maynard, J.B., Okita, P.M., May, E.D., Martinez-Vera, A., 1990. Palaeogeographic Setting of Late Jurassic Manganese Mineralization in the Molango District, Mexico, in: Parnel, J., Ye, L.., Chen, C.M. (Eds.), Sediment-Hosted Mineral Deposits. Blackwell Publishing Ltd., New York, pp. 17–29. https://doi.org/10.1002/9781444303872.ch2

Nicholson, K., 1992. Contrasting mineralogical-geochemical signatures of manganese oxides: guides to metallogenesis. Economic Geology 87, 1253–1264. https://doi.org/10.2113/gsecongeo.87.5.1253

Nieto-Samaniego, Á.F., Alaniz-Álvarez, S.A., Camprubí, A., 2007. Mesa Central of México: Stratigraphy, structure, and Cenozoic tectonic evolution, in: Special Paper 422: Geology of México: Celebrating the Centenary of the Geological Society of México. Geological Society of America, pp. 41–70. https://doi.org/10.1130/2007.2422(02)

Okita, P.M., 1992. Manganese carbonate mineralization in the Molango district, Mexico. Economic Geology 87, 1345–1366. https://doi.org/10.2113/gsecongeo.87.5.1345

Okita, P.M., Maynard, J.B., Spiker, E.C., Force, E.R., 1988. Isotopic evidence for organic matter oxidation by manganese reduction in the formation of stratiform manganese carbonate ore. Geochimica et Cosmochimica Acta 52, 2679–2685. https://doi.org/10.1016/0016-7037(88)90036-1

Okita, P.M., Shanks, W.C., 1992a. Origin of stratiform sediment-hosted manganese carbonate ore deposits: Examples from Molango, Mexico, and TaoJiang, China. Chemical Geology 99, 139–163. https://doi.org/10.1016/0009-2541(92)90036-5

Okita, P.M., Shanks, W.C., 1992b. Origin of stratiform sediment hosted manganese carbonate ore deposites: Examples from Molango, Mexico, and TaoJiang, China. Chemical Geology 99, 139–164.

Ponce, S.F., Clark, B., 1988. The Zacatecas mining district: a tertiary caldera complex associated with precious and base metal mineralization. Economic Geology 83, 1668–1682. https://doi.org/10.2113/gsecongeo.83.8.1668

Post, J.E., 1999. Manganese oxide minerals: Crystal structures and economic and environmental significance. Proceedings of the National Academy of Sciences of the United States of America 96, 3447–3454. https://doi.org/10.1073/pnas.96.7.3447

Prol-Ledesma, R.M., Canet, C., Torres-Vera, M.A., Forrest, M.J., Armienta, M.A., 2004. Vent fluid chemistry in Bahía Concepción coastal submarine hydrothermal system, Baja California Sur, Mexico. Journal of Volcanology and Geothermal Research 137, 311–328. https://doi.org/10.1016/j.jvolgeores.2004.06.003

Reyes-Reyes, N.A., Valdez-Monsivais, A., Gastro-Garcia, S., 1988. Estudio Geologico Minero Regional de la Reserva Minera Nacional Villa de Cos Estados de San Luis Potosi y zacatecas. San Luis Potosi.

Reyes, A.G., 1990. Petrology of Philippine geothermal systems and the application of alteration mineralogy to their assessment. Journal of Volcanology and Geothermal

Research 43, 279–309.

Rodríguez-Díaz, A.A., 2018. Los depósitos de manganeso de la Península de Baja California: Génesis, evolución del proceso hidrotermal e implicaciones metalogenéticas.

Rodríguez-Díaz, A.A., Blanco-Florido, D., Canet, C., Gervilla-Linares, F., González-Partida, E., Prol-Ledesma, R.M., Morales-Ruano, S., García-Vallès, M., 2010. Metalogenia del depósito de manganeso Santa Rosa, baja California sur, México. Boletin de la Sociedad Geologica Mexicana 62, 141–159. https://doi.org/10.18268/BSGM2010v62n1a8

Rodríguez-Díaz, A.A., Canet, C., Villanueva-Estrada, R.E., Chacón, E., Gervilla, F., Velasco-Tapia, F., Cruz-Gámez, E.M., González-Partida, E., Casas-García, R., Linares-López, C., Pérez-Zárate, D., 2019. Recent Mn-Ag deposits in coastal hydrothermal springs in the Baja California Peninsula, Mexico. Mineralium Deposita 54, 849–866. https://doi.org/10.1007/s00126-018-0846-9

Roy, S., 1997. Genetic diversity of manganese deposition in the terrestrial geological record. Geological Society Special Publication 119, 5–27. https://doi.org/10.1144/GSL.SP.1997.119.01.02

Roy, S., 1992. Environments and processes of manganese deposition. Economic Geology 87, 1218–1236. https://doi.org/10.2113/gsecongeo.87.5.1218

Roy, S., 1981. Manganese deposits. Academic Press.

Servicio Geológico Mexicano (SGM), 2020. Panorama minero del Estado de San Luis Potosi.

Servicio Geológico Mexicano (SGM), 2011. Panorama Minero del estado de San Luis Potosí, Servicio Geológico Mexicano. Pachuca.

Thompson, A., Thompson, J., 1996. Atlas of Alteration: A field and petrographic guide to hydrothermal alteration minerals, Mineral Deposits Division, Geological Association of Canada.

Tompsett, D.A., Islam, M.S., 2013. Electrochemistry of Hollandite α-MnO2 : Li-Ion and Na-

Ion Insertion and Li 2 O Incorporation. Chemistry of Materials 25, 2515–2526. https://doi.org/10.1021/cm400864n

Torres-Montufar, O.M., 2017. La mineria de manganeso en Mexico durante la Segunda Guerra Mundial. Cuadernos Americanos: Nueva Epoca 4, 109–136.

Trask, P.D., Cabo, J.R.J., 1948. Manganese Deposits of Mexico. Geologic Investigations in the American Republics, 1946; pp. 209-316.

Villanueva-Estrada, R.E., Prol-Ledesma, R.M., Rodríguez-Díaz, A.A., Canet, C., Armienta, M.A., 2013. Arsenic in hot springs of Bahía Concepción, Baja California Peninsula, México. Chemical Geology 348, 27–36. https://doi.org/10.1016/j.chemgeo.2012.09.008

Villanueva-Estrada, R.E., Prol-Ledesma, R.M.M., Rodríguez-Díaz, A.A., Canet, C., Torres-Alvarado, I.S., González-Partida, E., Rodrguez-Daz, A.A., Canet, C., Torres-Alvarado, I.S., González-Partida, E., 2012. Geochemical processes in an active shallow submarine hydrothermal system, Bahía Concepción, México: mixing or boiling? International Geology Review 54, 907–919. https://doi.org/10.1080/00206814.2011.588496

Wilson, I.F., Rocha, V.S., 1948. Manganese deposits of the Montaña de Manganeso mine, San Luis Potosí, Mexico.

Zantop, H., 1978. Geologic setting and genesis of iron oxides and manganese oxides in the San Francisco manganese deposit, Jalisco, Mexico. Economic Geology 73, 1137–1149. https://doi.org/10.2113/gsecongeo.73.6.1137

CHAPTER 2

MANGANESE IN THE EPITHERMAL ENVIRONMENT

MANGANESE IN EPITHERMAL DEPOSITS: A REVIEW

Manuscript in preparation

Joseph Madondo*

Posgrado en Ciencias de la Tierra, Universidad Nacional Autónoma de México,

Ciudad Universitaria, 04510 CdMx, México

* joseph.madondo85@gmail.com

Abstract

Manganese halos and dispersion patterns commonly occur in magmatic-hydrothermal and hydrothermal type deposits such as porphyry Cu, Sedex Zn-Pb-Cu base metal deposits and epithermal precious metal deposits. In epithermal precious metal deposits such halos often contain anomalous manganese concentrations. These manganese minerals are often visible as Mn oxides in the weathered and oxidized caps of some of these deposits. The common primary manganese minerals are often the Mn silicate rhodonite and Mn carbonate rhodochrosite. Rhodonite and rhodochrosite are in fact characteristic gangue minerals of intermediate sulfidation epithermal deposits. Kutnohorite and Mn-Ca silicates such as johannsenite, bustamite, pyroxmangite, tephroite, and penwithite are rare. The distribution and zonation of Mn minerals in epithermal deposits indicate that rhodochrosite and rhodonite are often associated with the ore zone while the Mn oxides are associated with the supergene zone of these deposits. Presence of Mn minerals has been used in exploration of epithermal deposits as an exploration guide. This work aims to give a general review of the current knowledge concerning the occurrence of Mn minerals in epithermal type deposits, their significance, and the information that can be deduced by their presence, with some examples from epithermal deposits around the world.

Keywords : Manganese, gold, silver, epithermal, intermediate sulfidation.

1. Introduction

The spatial relationship between manganese and the precious metals gold and silver is well documented throughout the world (Roy, 1981). Notable examples of this spatial relationship include the Early Proterozoic Birimian gold and manganese deposits of West Africa (Leube et al., 1990; Milési et al., 1991; Ntiamoah-Agyakwa, 1979; Nyame, 2008) and the Mn and Ag + base metal deposits of the USA (Dorr, 1977). Expectedly then, significant precious metal contents are commonly found in fossil manganese deposits (Hewett, 1964; Hewett et al., 1963). Silver, for instance, was recovered in several Mn deposits of hypogene origin in the southwest USA (Hewett and Radtke, 1967). Conversely some Ag mines were reopened as Mn mines after exhaustion of the Ag (Dorr, 1977). This association of Mn and the precious metals occurs even at atomic level. Manganese oxide minerals in fossil Mn deposits, for example, often accommodate a substantial content of Ag in their lattice structure. The association of precious metals with Mn is, however, rare in modern ferromanganese crusts and nodules developing at the bottom of the world´s oceans (Bolton et al., 1986; Hein et al., 2005). Only in PGE-Au enriched ferromanganese nodules have anomalous concentration of gold been detected (Balaram et al., 2006; Banakar et al., 2007; Berezhnaya and Dubinin, 2017).

The association of Mn and the precious metals Au and Ag extends to several types of ore deposits. Anomalous manganese concentrations and manganese containing dispersion patterns commonly occur within or on the peripheries of porphyry Cu-Au deposits (Jones, 1992; Megaw et al., 1988; Sillitoe, 2010, 2000), Ag-rich base metal deposits (Emsbo, 2000;

Jones, 1992; Large et al., 2000; Large and McGoldrick, 1998; McLemore et al., 1999)and in some intrusion-related carbonate-hosted gold deposits (Pareja, 1995).

Manganiferous minerals are also commonly associated throughout the world with precious and base-metal epithermal deposits (Filimonova et al., 2010; Leroy et al., 2000). Spatial and possibly genetic association is documented in several epithermal Au-Ag and Ag-Au + base metal deposits of the world (Roy, 1981). Rhodonite and rhodochrosite are in fact characteristic gangue minerals of intermediate sulfidation epithermal deposits (Hedenquist et al., 2000, 2017; Wang et al., 2019) although they have also been reported, in lesser abundances, in some purportedly low sulfidation Au-Ag epithermal deposits (Corbett, 2002; Hewett, 1968, 1964).

Manganese oxide caps derived from supergene alteration of rhodonite and rhodochrosite occur in the oxidation zones of these deposits where they are regarded as prospecting guides for silver–base metal deposits (Filimonova et al., 2010) and as an indicator of the transitions to the low sulfidation gold deposits in telescoped intermediate sulfidation/low sulfidation deposits (Cooke and Bloom, 1990; Corbett, 2002). The Mn oxide caps are also known to scavenge anomalous gold concentrations (Corbett, 2002; Nicholson, 1992; Roslyakov et al., 2005). In the epithermal Au-Ag Dukat ore field (Russia) manganese oxides (bixbyite; pyrolusite, cryptomelane, hollandite, coronadite and manganite) and Mn rich aluminosilicates (spessartine, bustamite, tephroite, rhodonite, and pyroxmangite) accompany ore minerals made up of native silver, acanthite, pyrargyrite, eustelite, electrum, and rarely, native gold (Filimonova et al., 2014, 2010; Filimonova and Chugaev, 2006).

Although a few investigators have studied the relationship between gold and silver accumulation and the manganese mineral abundance (Corbett, 2013, 2002; Corbett and Leach, 1998; Leach and Corbett, 1994; Roy, 1981), manganese distribution in epithermal precious metal deposits, its controlling factors and role in precious metal mineralization, remain unclear. The present review aims to discuss the occurrence and significance of manganese minerals in epithermal gold and silver deposits.

2. Au and Ag occurrence in Mn deposits

Fossil manganese deposits are commonly associated with significant precious metal contents (Hewett, 1964; Hewett et al., 1963). The association with Ag is more common and a genetic association is often recognized, particularly in hot spring type Mn deposits (Hein et al., 2005; Hewett, 1968, 1964; Hewett and Radtke, 1967; Nicholson, 1992; Rodríguez-Díaz et al., 2019; Roy, 1981). Studies on active shallow marine vents and continental hot springs have demonstrated the primary enrichment of Ag within Mn mineralization from ascending fluids (Canet et al., 2005a, 2005b; Prol-Ledesma et al., 2004; Rodríguez-Díaz et al., 2019). The enrichment in Ag often occurs within the lattice of Mn oxides, in some cases leading to the formation of specific minerals such as aurorite (Roy, 1981). At Bahia Concepcion (Mexico) Mn oxides, mainly todorokite and romanechite occur together with acanthite and native silver (Rodriguez-Diaz et al., 2019). A similar relationship occurs at Milos (Greece) where the formation of the epithermal Mn oxides represents the final stage of the hydrothermal activity responsible for the epithermal Ag + base metals deposits (Liakopoulos et al., 2001; Papavassiliou et al., 2017; Roy, 1981). Ag-rich Mn oxides also occur along faults in numerous small Mn deposits of hypogene origin scattered in the west

and southwest of USA (Dorr, 1977; Hein et al., 2005; Hewett, 1964; Hewett et al., 1963, 1960).

3. Mn occurrence in epithermal deposits

Mn bearing minerals are common in epithermal deposits (Filimonova et al., 2010; Hedenquist et al., 2000; Leroy et al., 2000; Shikazono, 1985; Sillitoe, 2015; Sillitoe and Hedenquist, 2005). Manganese oxides commonly occur as products of supergene origin, derived from weathering of primary Mn carbonates. In some cases, the manganese oxides are primary (Filimonova et al., 2010).

Intermediate sulfidation deposits developed in magmatic arc environments commonly contain appreciable Mn carbonate at the expense of quartz (Corbett and Leach, 1998; Hedenquist et al., 2017; Sillitoe, 2010) and often develop halos enriched in Mn (± Ag) (Corbett and Leach, 1998; Sillitoe, 2010). Manganese carbonates and silicates are in fact characteristic gangue minerals of intermediate sulfidation epithermal deposits (Hedenquist et al., 2000; Sillitoe, 2015; Sillitoe and Hedenquist, 2005) and are used as a diagnostic feature to discern intermediate sulfidation from low-sulfidation deposits when present (Corbett, 2013; Simmons et al., 2005; Wang et al., 2019).

The Mn carbonate rhodochrosite is the most common Mn mineral in intermediate sulfidation deposits and rarely in Au-Ag low sulfidation deposits (Sillitoe and Hedenquist, 2005). Rhodochrosite is well documented in the Dukat (Russia; Filimonova et al., 2014, 2010; Filimonova and Chugaev, 2006), Orcopampa (Peru) and Cavnic (Romania) (LeRoy et al., 2000), North Amethyst (Creede District, USA; Barton et al., 2000; Foley, 1990; Foley et al., 1993; Guzman and Monecke, 2014, 2016) Au-Ag epithermal deposits.

Kutnohorite is relatively rare in epithermal deposits but has been reported in the Pongkor (Milesi et al., 1999), La Guitara (Mexico; Camprubí et al., 2006) and the North Amethyst (Foley, 1990; Foley et al., 1993) Au-Ag epithermal deposits. The Mn silicate rhodonite is also common in Ag-Au + base metal deposits accompanying rhodochrosite (LeRoy et al., 2000). Another Mn silicate inesite is reportedly common in Au-Ag deposits of the Izu peninsula (Shikazono, 1985) associated with high-grade Au-Ag ores. The occurrence of Mn-Ca silicates such as johannsenite, bustamite, pyroxmangite, tephroite, penwithite, alleghanyite and friedelite has been reported in the epithermal deposits of Japan (Shikazono, 1985) and the USA (Hewett et al., 1960), but are generally not common in epithermal deposits (Roy, 1981). The Mn sulfide alabandite coexists with rhodonite and rhodochrosite in the deposits of the San Juan Mountains, (Colorado, USA) accompanying silver sulphosalts and native gold but is quite rare in these deposits (Roy, 1981).

The occurrence of Mn minerals is notorious in the Au rich and quartz poor intermediate sulfidation subtype deposits of the SW Pacific rim such as the Victoria (Phillipines; (Hedenquist et al., 2000), Acupan (Cooke et al., 1996; Cooke and Bloom, 1990); Pongkor and Ciawitali (Western Java, Indonesia (Marcoux et al., 1993; Marcoux and Milési, 1994; Milesi et al., 1994; Milési et al., 1999), Cirotan (Indonesia, LeRoy et al., 2000), Porgera, (Papua New Guinea, (Corbett, 2013; Corbett and Leach, 1998; Leach and Corbett, 1994) and Wau (Papua New Guinea; (Webster and Mann, 1984).

In the Pongkor and Cirotan epithermal deposits the relationship between Mn mineralization and the Au mineralization has been well studied (Leroy et al., 2000; Milési et al., 1999). At Pongkor the ore stage Mn mineralization consists predominantly of

alternating quartz–rhodonite and quartz–rhodochrosite bands. Cross cutting veinlets are composed of mainly rhodochrosite and rare quartz-adularia-rhodonite-rhodochrosite bands (Koichiro et al., 2005; Milési et al., 1999; Warmada et al., 2003). Gold and silver grades are low in the manganese carbonate – quartz facies, increasing gradually in the quartz dominated facies (Milesi et al., 1999). At Cirotan Mn mineralization is pre ore stage and is associated with polymetallic sulfides (LeRoy et al., 2000). Mn bearing minerals were deposited in cockade breccias as early rhodonite accompanied by Mn rich silicates of the clinochlore–pennantite solid solution (LeRoy et al., 2000). Rhodochrosite formed as an alteration product of rhodonite (LeRoy et al., 2000).

Manganese bearing minerals are not so common in the epithermal deposits of Latin America (Corbett, 2013). The intermediate sulfidation deposits of Latin America tend to be quartz rich and Mn carbonate poor (Corbett, 2013). However, Mn carbonates are reported in some deposits such as Fresnillo; La Colorada; Real de Angeles; Tayoltita, La Guitara and Pachuca-Real de Monte deposits in Mexico (Camprubí et al., 2006; Camprubí and Albinson, 2007; Clarke and Titley, 1988; Enríquez et al., 2018; Smith et al., 1982; Wang et al., 2019). At Pachuca-Real de Monte Mn-bearing minerals, rhodonite and bustamite, are present in trace amounts in many veins but occur in significant abundance in the Ag rich zones (Simmons et al., 2005). A few Mn carbonate rich epithermal deposits were also recognized in the El Indio district, Chile (Corbett, 2002) and at Purisima, Peru (Cook and Bloom, 1990). Manganese minerals are even rarer in the low sulfidation epithermal deposits of Latin America where carbonates generally occur as calcite (Camprubí and Albinson, 2007; Corbett, 2002; Hedenquist et al., 2000, 2017). However, rhodochrosite and

kutnohorite have been reported in the purportedly low sulfidation epithermal deposit of El Peñon, Chile (Bissig et al., 2007).

4. Weathering and supergene processes

Mn oxide caps also commonly form over epithermal Au and Ag mineralization by dissolution and remobilization of mostly rhodochrosite and rhodonite by supergene oxidation (Hedenquist et al., 2000; Hewett and Radtke, 1967; Nicholson, 1992). In regions of arid and semi-arid climate they may form Ag-Mn ores (Corbett, 2002; Fan et al., 2015; Gómez-Caballero et al., 2010; Milési et al., 1999; Webster and Mann, 1984).

Several supergene Ag-Mn ores formed from weathering of Ag-rich polymetallic deposits are documented in the United States, Mexico, South America and China (Du et al., 2020; Fan and Yang, 1999; Hewett and Radtke, 1967; Jiang et al., 2003; Ravikumar and Fuerstenau, 2011; Rutten et al., 1997; Wu et al., 1993; Zhang et al., 2006). Examples in the USA are the Lucky Cuss mine (Tombstone district; Arizona); Aurora mine (Hamilton, Nevada) and Silver Cliff mine (Colorado) (Hewett, 1964; Radtke et al., 1967). In China examples are the Sanbao Mn-Ag deposit; Xiangguang Mn–Ag deposit, Changtuxili Mn–Ag–Pb–Zn deposit (Du et al., 2020; Fan et al., 2015; Zhang et al., 2020). In some of these Chinese deposits, both Mn and Ag have been recovered (Jiang et al., 2003**)**. In Arizona (USA) several mines exploited for Ag were reopened as Mn mines after the Ag had been exhausted (Dorr, 1977). Likewise, silver was recovered from some manganese mines in the Tombstone district (New Mexico, USA) (Hewett and Radtke, 1967) and San Miguel Tenango and Tetela de Ocampo districts (Puebla, Mexico) (Gomez-Caballero and Villaseñor-Cabral, 2010).

In these deposits silver is either disseminated in manganese oxides in mineral form (Calderon-Rodarte et al., 2017; Gasparrini, 1993) or present in the crystal lattice of manganese oxides (Hewett, 1968; Jiang et al., 2003) replacing potassium and barium in minerals such as cryptomelane, hollandite, romanechite and todorokite (Calderon-Rodarte et al., 2017; Ravikumar and Fuerstenau, 2011). The replacement leads to formation of argentian manganese oxides such as Ag-cryptomelane, Ag-todorokite, Ag-hollandite and minerals such as Aurorite (Fan et al., 2015; Hildebrand and Mosier, 1974; Radtke et al., 1967).

The manganese oxides caps can also be associated with gold. Examples of gold rich epithermal deposits where supergene manganese oxides have been well documented are the Cikidang (Basuki et al., 1999; Rosana and Matsueda, 2002), Ciawitali (Soeria-Atmadja et al., 1998), Pongkor, (Milesi et al., 1999), Upper Ridges mine (Papua New Guinea) (Webster and Mann, 1984) and some deposits of western United States (Hewett and Radtke, 1967; Radtke et al., 1967). In the Upper Ridges mine (Papua New Guinea) manganese oxides are enriched in gold and silver in the form of electrum (Webster and Mann, 1984). Similarly, the Ciguha, Ciurug and Gudang Handak veins of the Pongkor deposit (Indonesia) variably contain rhodochrosite ± rhodonite ± kutnohorite partially weathered to Mn oxides alternating with gold and silver (electrum) rich quartz bands (Bahna and Chovan, 2001; Milési et al., 1999; Warmada et al., 2003).

5. Paragenetic zonation.

The formation of manganese bearing minerals in primarily intermediate sulfidation epithermal deposits follow a paragenetic zonation whereby manganese oxides formed near the paleosurface by supergene processes are succeeded at depth by primary Mn carbonates and silicates coexisting with Ag-Au+(Pb+Zn+Cu) (Roy, 1981). Most manganese oxides in intermediate sulfidation deposits are of supergene origin, derived from weathering of primary Mn carbonates. In some rare cases, the manganese oxides are primary (Filimonova et al., 2010).

The timing of the Mn carbonate minerals is variable. They could be pre ore (Bulldog and North Amethyst mines, Creede District, Colorado, (Barton et al., 2000); Pongkor and Cirotan deposits, western Java, Indonesia; (Marcoux et al., 1993; Milesi et al., 1994; Milési et al., 1999); contemporaneous (Acupan, Baguio District, Philippines; Cooke et al., 1996) and/or post ore (Acupan, Baguio District, Philippines; Cook and Bloom 1990). These minerals are, in some deposits, also zoned. Mn carbonate zonation was described at the El Peñon deposit, Chile (Bissig et al., 2007). Paragenetically early Mn rich carbonates comprised of rhodochrosite and kutnohorite ± ankerite ± calcite ± dolomite are associated with gold mineralization, whereas the late-stage carbonates comprised of mainly Mn poor calcite are barren (Bissig et al., 2007). Similar situation to El Peñon also occurs at Kelian (Indonesia), Porguera (Papa New Guinea), and Umuna (Papua New Guinea) deposits (Corbett, 2002). Carbonates exhibit a spatial zonation with increasing depth or proximity to an intrusion source, from the Fe-rich (siderite) and Mn-rich (rhodochrosite) zone to the Mg-rich (dolomite) and Ca-rich (calcite) zone (Corbett, 2002; Corbett and Leach, 1998). The

multi-element Mn-Mg-Fe-Ca carbonate species (ankerite and kutnahorite) occur intermediate between the Fe/Mn and Ca/Mg carbonate end members. Bulk low-grade gold mineralization is usually encountered in the mixed carbonate, kutnahorite/ankerite zones. High grade gold mineralization preferentially occurs with Mn/Mg zone (Corbet and Leach, 1998). That is Au grades are partially related to the type of carbonate in such a way that most high-grade deposits contain rhodochrosite (Corbett, 2013).

The carbonate zonation and the co-existence of manganese carbonates with silver and gold can be explained by the carbonate-base metal Au deposit model of Leach and Corbett (2008). In this model the progressive mixing of cool descending CO_2 rich bicarbonate waters with hot ascending metal-bearing fluids results in the destabilization of bisulfide complexes carrying Au and to the precipitation of gold + base metals + Mn carbonates (Corbett, 2002; Corbett and Leach, 1998; Leach and Corbett, 1995, 1994).

Highly acidic waters are more effective in the destabilization of bisulfide complexes leading to precipitation of Au with Fe sulfide (pyrite) and carbonate (siderite). However, the bicarbonate waters envisaged in the model of Leach and Corbett (2008) are generally not this acidic and typically serve to dissolve manganese cations from the wall rocks, leading to the deposition of manganese carbonates (rhodochrosite) in association with Au mineralization. Progressive neutralization of the bicarbonate waters by wall rock interaction, is reflected in declining Au grades as the carbonate chemistry moves from manganese to magnesian, and then to Ca dominant mixed carbonates (progressively kutnahorite, ankerite, dolomite, Mg calcite and calcite) (Corbett and Leach, 1998). Minor

amount of Au is associated with calcite as it is deposited from near neutral waters (Leach and Corbett, 2008).

6. Role and significance of Mn bearing minerals in epithermal Au-Ag deposits

Manganese oxides are commonly used as prospecting guides for silver–base metal deposits (Filimonova et al., 2010) and as an indicator in telescoped low sulfidation deposits/intermediate sulfidation, of the transitions to the intermediate sulfidation gold deposits (Cooke and Bloom, 1990; Corbett, 2002). Mn carbonates coexisting with precious metals can also provide constraints on the depositional environment within epithermal districts. For instance, rhodochrosite constrains the physico-chemical conditions of formation due to its restricted circumneutral pH precipitation range (6.6–7.4). Stable isotope analysis of carbon and oxygen compositions of Mn carbonates are frequently used to determine the nature of the ore forming fluids in some precious metal epithermal deposits, particularly the Ag-rich base metal deposits (e.g Zhang et al., 2020).

The role of the manganese carbonates in intermediate sulfidation mineralization, however, is still not fully understood. A role as an efficient fluid pH buffer is possible (Leach and Corbett, 2008; Simmons and Browne, 1990; Wang et al., 2019). The buffering of pH by carbonates is thought to indirectly affect gold solubility by changing solution acidity (Webster ad Mann, 1984). At epithermal conditions (≤300 ºC), such buffering, may be favorable for Au transport as $Au(HS)_2$ (Pokrovski et al., 2014). The role of Mn oxides, if any, in the epithermal ore fluids is even less understood. (Likhoidov et al., 2000) suggested that for saline highly oxidized fluids where Mn is present, buffering by Mn_2O_3-Mn_3O_4 and Mn_2O_3-MnO_2 assemblages enhances transport of gold. Although our

knowledge on the role of Mn in the epithermal fluid is limited a discussion on what is known on the behavior of Mn in the epithermal fluid is summarized below.

Gammons and Seward, (1996) extensively discussed the solubility of Mn bearing minerals in hydrothermal fluids, which is briefly discussed here. Rhodonite (MnSiO3) and rhodochrosite (MnCO3) are the most common Mn minerals formed in reduced hydrothermal systems (Gammons and Seward, 1996). These minerals are highly soluble in mildly acidic solutions and therefore most hydrothermal solutions are undersaturated with respect to rhodonite or rhodochrosite. Rhodochrosite is generally less soluble than rhodonite at low temperature (<200°C) and is thus expected to dominate in epithermal deposits (Gammons and Seward, 1996).

Depending on salinity, rhodochrosite exhibits either prograde or retrograde solubility with respect to temperature, (Gammons and Seward, 1996). For dilute fluids, rhodochrosite solubility is retrograde, similar to other carbonate minerals (Gammons and Seward, 1996). In contrast, in saline brines at epithermal temperatures, rhodochrosite solubility is prograde (Gammons and Seward, 1996). Thus, precipitation of rhodochrosite in epithermal deposits, unlike rhodonite, could in theory occur in response to cooling. However, since cooling is not an important mechanism for gold precipitation, the precipitation of rhodochrosite by cooling has no bearing on the presence or transport of gold in the epithermal fluid.

The solubility of rhodonite, unlike rhodochrosite, is markedly retrograde and tend to dissolve in solutions undergoing cooling hence only drastic changes in pH (through boiling) or concentration of the transporting chloride complex (through dilution) can effectively deposit rhodonite (Gammons and Seward, 1996). Boiling as an effective

mechanism is supported by the common occurrence of rhodonite in epithermal veins that also present evidence of boiling (Gammons and Seward, 1996). However, since solubility of rhodonite is high at low temperature, it is likely to dissolve and reprecipitate as Mn-oxides and/or Mn carbonate in the near-surface environment, as is observed in several epithermal deposits (Gammons and Seward, 1996).

Fluid mixing is also an important mechanism of precipitation for rhodochrosite and rhodonite (Gammons and Seward 1996), and to a lesser extent for gold (Leach and Corbett, 2008; Wang et al., 2019). In the carbonate-base metal Au deposit model of Leach and Corbett, (2008), the mixing of rising Au-Ag bearing fluids with descending weakly acidic bicarbonate waters can destabilize the bisulfide complexes carrying Au and so deposit Au in association with base metal sulphides and carbonates (Corbett, 2013, 2002; Leach and Corbett, 2008, 1995, 1994). The bicarbonate waters also serve to dissolve manganese cations from the wall rocks leading to the simultaneous formation of rhodochrosite (Leach and Corbett, 2008; Wang et al., 2019).

8. The mechanism of Mn enrichment

The close relationship between Ag and Mn in hydrothermal deposits is a result of their close association during transport and deposition (Cook and Bloom, 1990). The association thus mainly depends on the nature of the transporting complexes. In the epithermal environment, under reduced, circumneutral pH conditions chloride complexes are the chief carrier of Ag and other base metals (Fe, Zn, Pb) (e.g., Pokrovski et al., 2005; Seward et al., 2014; Seward and Barnes, 1997). The generally large amount of Ag and base metals in intermediate sulfidation deposits is therefore consistent with their high fluid salinity (cf.,

(Albinson et al., 2001; Sillitoe and Hedenquist, 2005). Because Mn is also transported primarily as a chloride complex in hydrothermal fluids it is expected that veins rich in Ag^{+} base metals will also be richer in Mn bearing minerals (Gammons and Seward, 1996). Boiling and dilution of the intermediate sulfidation fluid with meteoric water can cause co-precipitation of Ag, Pb, Zn and Mn, giving rise to localized vein concentrations (Hemley and Hunt, 1992; Sillitoe, 2010)**.** This partly explains the abundance of rhodochrosite and rhodonite in intermediate sulfidation deposits. Au does not form strong chloride complexes at temperatures corresponding to epithermal fluids (Gammons and Seward, 1996; Gammons and Williams-Jones, 1997, 1995), but rather form strong bisulfide complexes (Cooke and Simmons, 2000; Hedenquist and Henley, 1985; Seward and Barnes, 1997). Hence, deposits rich in Au would be expected to have a relatively lower Mn concentrations (Gammons and Seaward, 1996) as evidenced by the scarcity of Mn bearing minerals in Au rich low salinity low sulfidation epithermal deposits (Gammons and Seward, 1996; Hedenquist and Henley, 1985; Leroy et al., 2000).

Chloride complexes can contribute to Au transport in high temperature, acidic, high salinity, and strongly oxidizing solutions (Pokrovski et al., 2015; Wang et al., 2019). However, in such systems (e.g Cu + Au porphyry systems), Au and Ag preferentially partition into the vapor phase during phase separation whereas Fe, Zn, Pb and Mn partition into the hypersaline liquid (Heinrich, 2005; Heinrich et al., 1999; Pokrovski et al., 2008, 2005; Sillitoe, 2010; Williams-Jones and Heinrich, 2005). Cooling of the hypersaline liquid, interaction with wall rocks and dilution with meteoric waters leads to the formation of Zn, Pb, Ag, and Mn containing dispersion patterns and halos on the peripheries of the porphyry system (Hemley and Hunt, 1992; Sillitoe, 2010, 2000).

The co-existence of Mn and Ag is, however, mostly a consequence of supergene enrichment. Experimental studies have demonstrated that Mn^{2+} + and Ag^{+} are able to coexist in acidic solution (Fig. 1). In weathering zones of intermediate sulfidation epithermal deposits, Mn and Ag are leached through supergene processes from the Mn carbonates (mainly rhodochrosite, kutnohorite and Mn calcite) and the silver rich base metal sulfides, respectively (e.g Du et al., 2020). Reprecipitation under oxidizing conditions leads to formation of manganese oxides whose texture and elevated adsorption capacity enables the isomorphic replacement of K (in cryptomelane) and Ba (in romanechite and hollandite) by Ag (Du et al., 2020; Fan et al., 2015; Gac, 2006; Pasero, 2005; Zhang et al., 2006), leading to the formation of new minerals (aurorite) and silver rich manganese oxides (eg Ag- todorokite, Ag-cryptomelane and Ag-calchophanite) (Hewett and Radtke, 1967; Simmons and Browne, 1990; Webster and Mann, 1984).

Significant supergene enrichment of gold also occurs within the manganese oxide rich zones of epithermal deposits (e.g (Simmons and Browne, 1990; Webster, 1986). The mobilization and transport of gold in the supergene environment is facilitated by formation of gold complexes such as hydroxides, chlorides, hydrogen sulfide, thiosulphate and organic matter (Pokrovski et al., 2014; Roslyakov et al., 2005). Under acidic conditions gold is believed to be mainly transported as chloride complexes $[AuCl_4]^-$ (Cloke and Kelly, 1964; Gammons and Williams-Jones, 1997; Krauskopf, 1951) whereas in alkaline fluids thiosulfate complexes $[Au(S2O3)_2]^{3-}$ have been proposed as the main transporting complexes (Webster, 1986; Webster and Mann, 1984). The role of Mn oxides in the mobilization and redeposition of gold in the supergene environment is not yet completely understood but the presence of a strong oxidizing agent such as Mn oxides is believed to

enhance the solubility of gold (Cloke and Kelly, 1964; Emmons, 1911; Krauskopf, 1951; Ran et al., 1999; Roslyakov et al., 2005; Ta et al., 2015; Webster, 1986; Webster and Mann, 1984; Yamashita et al., 2008). The mechanism widely proposed involves oxidation of Au^0 to Au^+ and possibly Au^{3+} by Mn oxides under acid solutions and in the presence of chloride ions to form the $AuCl4^-$ complex (Boyle, 1979; Emmons, 1911; Krauskopf, 1951; Ta et al., 2015) according to the following equations:

$2Au\ (s) + 8Cl^- \leftrightarrow 2AuCl_4 + 6e\ (E_0 = -1.00\ V)$

$3Mn^{2+} + 6H_2O \leftrightarrow 3MnO2\ (s) + 6\ e\ (E0 = -1.28V)$

The few experimental studies that have been carried out on the mobilization of Au by Mn have demonstrated that Mn^{2+} and Mn oxides can coexist with gold complexes and that the oxidation and mobilization of Au by Mn oxides in acidic aqueous solutions can occur (Cloke and Kelly, 1964; Ta et al., 2015) (e.g Fig. 2). Acid conditions are necessary as the [AuCl4]- ion is only stable in strong acid solutions (Fig.2) (Ta et al., 2015; Yamashita et al., 2008). Apparently, at circum-neutral and alkaline conditions Mn oxides cannot easily oxidize gold but can adsorb Au-complexes and spontaneously reduce them (Ohashi et al., 2005; Ta et al., 2015; Yamashita et al., 2008). Proposed mechanisms are those of Brokaw, (2015) and Webster and Mann, (1984).

$2AuCl4 + 3Mn^{2+} + 12OH^- \leftrightarrow 2Au\ (s) + 3MnO2\ (s) + 8Cl^- + 6\ H2O$

$2Au\ (S2O3)_2^{3-} + MnO2 + 4H^+ = 2Au0 + 2S_4O_6^{2-} + Mn^{2+} + 2H2O$

These studies reveal that depending on the physiochemical conditions, interactions between Mn and Au in the supergene environment can lead to Au mobilization or immobilization.

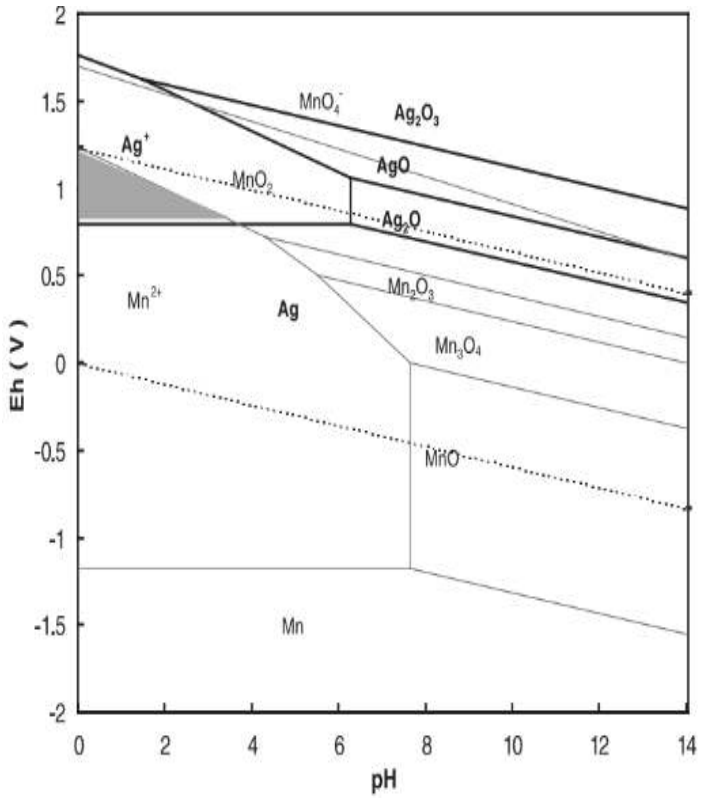

Figure 1. Eh–pH diagram show that Mn^{2+} + and Ag^{+} are able to coexist in acidic solution and that the coexistence area is extended with the decrease in Mn^{2+} and Ag^{+} concentration in the solution. The maximum pH for Mn^{2+} and Ag+ coexistence is 3.64 at standard conditions. Diagram after Jiang et al., (2003).

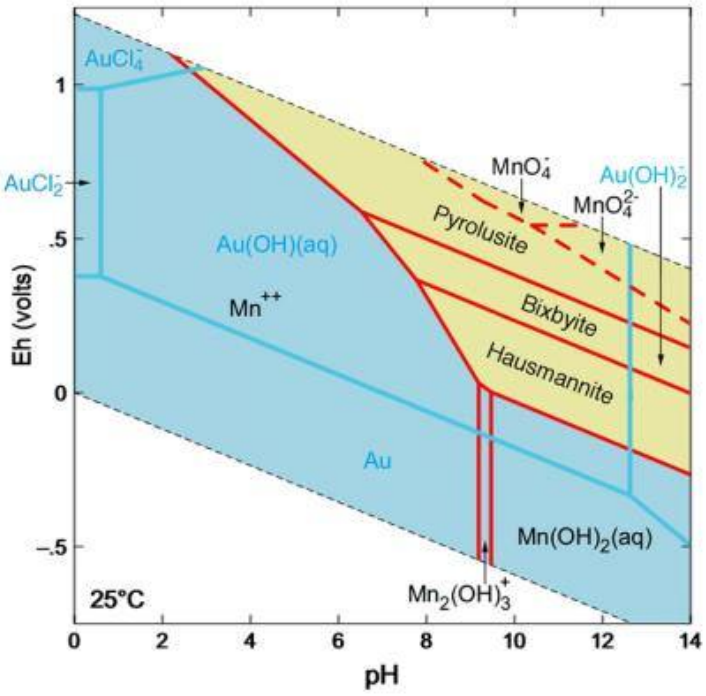

Figure 2. Eh–pH diagram indicate that Mn^{2+} can co-exist with Au species (hydroxide and chloride complexes of Au) in acidic solution and Mn oxides are able to co-exist with the hydroxyl complex under alkaline conditions. Diagram after Ta et al., (2015).

Conclusions

Manganese minerals commonly occur in epithermal Au ± Ag and Ag + base metal deposits. These manganese minerals are often visible as Mn oxides in the weathered and oxidized caps of these deposits as a result of dissolution and remobilization of primary Mn carbonates and silicates. The manganese oxides caps are often enriched in Au and more commonly, in Ag. The common primary manganese minerals are the Mn silicate rhodonite and Mn carbonate rhodochrosite, minerals that are characteristic gangue minerals of

intermediate sulfidation epithermal deposits. Kutnohorite and other Mn-Ca silicates are rare.

The co-occurrence of Au ad Ag with Mn carbonates and silicates is due to the progressive mixing of cool descending CO_2 rich bicarbonate waters with hot ascending metal-bearing fluids which results in the destabilization of bisulfide complexes and to the precipitation of gold + base metals + Mn carbonates (Corbett, 2002; Corbett and Leach, 1998; Leach and Corbett, 1995, 1994). The role of the manganese carbonates in intermediate sulfidation mineralization, however, is still not fully understood although a role as an efficient fluid pH buffer has been proposed (Leach and Corbett, 2008; Simmons and Browne, 1990; Wang et al., 2019). Because Mn and Ag are both transported primarily as a chloride complexes in hydrothermal fluids, Ag + base metals intermediate sulfidation epithermal veins are more enriched in Mn bearing minerals than in Au ± Ag low sulfidation epithermal veins (Gammons and Seward 1996). Gold rather form strong bisulfide complexes (Cooke and Simmons, 2000; Hedenquist and Henley, 1985; Seward and Barnes, 1997).

References

Albinson, T., Norman, D.I.D.I., Cole, D., Chomiak, B., 2001. Controls on Formation of Low-Sulfidation Epithermal Deposits in Mexico: Constraints from Fluid Inclusion and Stable Isotope Data. New Mines and Discoveries in Mexico and Central America 8, 0. https://doi.org/10.5382/SP.08.01

Bahna, B., Chovan, M., 2001. Low-Sulfidation Type of Epithermal Au-Ag Mineralization Near Pukanec (Central Slovakia Neogene Volcanic Fields). Geolines 13, 11–17.

Balaram, V., Mathur, R., Banakar, V.K., Hein, J.R., Rao, C.R.M., Gnaneswara Rao, T., Dasaram, B., 2006. Determination of the platinum - Group elements (PGE) and gold (Au) in manganese nodule reference samples by nickel sulfide fire-assay and Te coprecipitation with ICP-MS. Indian Journal of Marine Sciences 35, 7–16.

Banakar, V.K., Hein, J.R., Rajani, R.P., Chodankar, A.R., 2007. Platinum group elements and gold in ferromanganese crusts from Afanasiy-Nikitin seamount, equatorial Indian Ocean: Sources and fractionation. Journal of Earth System Science 116, 3–13. https://doi.org/10.1007/s12040-007-0002-x

Barton, P.B., Rye, R.O., Bethke, P.M., 2000. Evolution of the Creede caldera and its relation to mineralization in the Creede mining district, Colorado. Special Paper of the Geological Society of America 346, 301–326. https://doi.org/10.1130/0-8137-2346-9.301

Basuki, A., Suparka, E., Sunarya, Y., 1999. Gold deposit in the Cikidang area, West Java, Indonesia. Bulletin of the Geological Society of Malaysia 43, 251–259. https://doi.org/10.7186/bgsm43199925

Berezhnaya, E.D., Dubinin, A. V., 2017. Determination of the platinum-group elements and gold in ferromanganese nodule reference material NOD-A-1. Geochemistry International 55, 218–224. https://doi.org/10.1134/S0016702917010037

Bissig, T., Donoso, D., Guerra, N.C., Dipple, G.M., 2007. Vein carbonates in the low sulfidation epithermal Au-Ag District of El Peñón, II Región, Chile: environment of formation and exploration implications. Revista geológica de Chile 34, 291–303. https://doi.org/10.4067/S0716-02082007000200007

Bolton, B.R., Ostwald, J., Monzier, M., 1986. Precious metals in ferromanganese crusts from the south-west Pacific. Nature 1986 320:6062 320, 518–520. https://doi.org/10.1038/320518a0

Boyle, R.W., 1979. The geochemistry of gold and its deposits (together with a chapter on geochemical prospecting for the element). https://doi.org/10.4095/105577

Brokaw, A.D., 2015. The Secondary Precipitation of Gold in Ore Bodies. https://doi.org/10.1086/622056 21, 251–267. https://doi.org/10.1086/622056

Calderon-Rodarte, J., Lopez-Valdivieso, A., Aragon-Pina, A., Reyes-Bahena, J.L., Gallegos-Garcia, M.I.L., Zapata-Velazquez, A., Robledo-Cabrera, A., 2017. Mineralogy and silver distribution in argentiferous manganese ores from la encantada mines in Mexico. Physicochemical Problems of Mineral Processing 53, 591–600. https://doi.org/10.5277/PPMP170146

Camprubí, A., Albinson, T., 2007. Epithermal deposits in México—Update of current knowledge, and an empirical reclassification, in: Special Paper 422: Geology of México: Celebrating the Centenary of the Geological Society of México. Geological Society of America, pp. 377–415. https://doi.org/10.1130/2007.2422(14)

Camprubí, A., Chomiak, B.A., Villanueva-Estrada, R.E., Canals, À., Norman, D.I., Cardellach, E., Stute, M., 2006. Fluid sources for the La Guitarra epithermal deposit (Temascaltepec district, Mexico): Volatile and helium isotope analyses in fluid inclusions. Chemical Geology 231, 252–284. https://doi.org/10.1016/j.chemgeo.2006.02.002

Canet, C., Prol-Ledesma, R.M., Proenza, J.A., Rubio-Ramos, M.A., Forrest, M.J., Torres-Vera, M.A., Rodríguez-Díaz, A.A., 2005a. Mn-Ba-Hg mineralization at shallow submarine hydrothermal vents in Bahía Concepción, Baja California Sur, Mexico. Chemical Geology 224, 96–112. https://doi.org/10.1016/j.chemgeo.2005.07.023

Canet, C., Prol-Ledesma, R.M., Torres-Alvarado, I., Gilg, H.A., Villanueva, R.E., Cruz, R.L.-S., 2005b. Silica-carbonate stromatolites related to coastal hydrothermal venting in Bahía Concepción, Baja California Sur, Mexico. Sedimentary Geology 174, 97–113.

https://doi.org/10.1016/j.sedgeo.2004.12.001

Clarke, M., Titley, S.R., 1988. Hydrothermal evolution in the formation of silver-gold veins in the Tayoltita mine, San Dimas district, Mexico. Economic Geology 83, 1830–1840. https://doi.org/10.2113/gsecongeo.83.8.1830

Cloke, P.L., Kelly, W.C., 1964. Solubility of gold under inorganic supergene conditions. Economic Geology 59, 259–270. https://doi.org/10.2113/GSECONGEO.59.2.259

Cooke, D.R., Bloom, M.S., 1990. Epithermal and subjacent porphyry mineralization, Acupan, Baguio District, Philippines: a fluid-inclusion and paragenetic study. Journal of Geochemical Exploration 35, 297–340. https://doi.org/10.1016/0375-6742(90)90042-9

Cooke, D.R., McPhail, D.C., Bloom, M.S., 1996. Epithermal gold mineralization, Acupan, Baguio District, Philippines; geology, mineralization, alteration, and the thermochemical environment of ore deposition. Economic Geology 91, 243–272. https://doi.org/10.2113/GSECONGEO.91.2.243

Cooke, D.R., Simmons, S.F., 2000. Characteristics and Genesis of Epithermal Gold Deposits. Gold in 2000 221–244. https://doi.org/10.5382/REV.13.06

Corbett, G., 2013. Pacific rim epithermal Au-Ag. World Gold Conference.

Corbett, G., 2002. Epithermal gold for explorationists. AIG Journal, Applied Geoscientific Practice and Research in Australia 26 p.-26 p.

Corbett, G., Leach, T.M., 1998. Southwest Pacific rim gold–copper systems: structure, alteration and mineralization. Society of Economic Geologists, Special Publication, 6. Society of Economic Geologists 236.

Dorr, J., 1977. Manganese, uses, sources, and price. New Mexico Bureau of Mines and Mineral Resources Bulletin 87, 183–195.

Du, S., Wen, H., Liu, S., Qin, C., Yan, Y., Yang, G., Feng, P., 2020. Mineralogy and Metallogenesis of the

Sanbao Mn–Ag (Zn-Pb) Deposit in the Laojunshan Ore District, SE Yunnan Province, China. Minerals 2020, Vol. 10, Page 650 10, 650. https://doi.org/10.3390/MIN10080650

Emmons, W.H., 1911. The Agency of Manganese in the Superficial Alteration and Secondary Enrichment of Gold Deposits. The Journal of Geology 19, 15–46. https://doi.org/10.1086/621805

Emsbo, P., 2000. Gold in sedex deposits. Reviews in Economic Geology 13, 427–437.

Enríquez, E., Iriondo, A., Camprubí, A., 2018. Geochronology of Mexican mineral deposits. VI: The Tayoltita lowsulfidation epithermal Ag-Au district, Durango and Sinaloa. Boletin de la Sociedad Geologica Mexicana 70, 531–547. https://doi.org/10.18268/BSGM2018v70n2a13

Fan, C., Wang, L., Fan, X., Zhang, Y., Zhao, L., 2015. The mineralogical characterization of argentian cryptomelane from Xiangguang Mn–Ag deposit, North China. Journal of Mineralogical and Petrological Sciences 110, 214–223. https://doi.org/10.2465/jmps.150119

Fan, D., Yang, P., 1999. Introduction to and classification of manganese deposits of China. Ore Geology Reviews 15, 1–13. https://doi.org/10.1016/S0169-1368(99)00011-6

Filimonova, L.G., Chugaev, A. V., 2006. Chronology of hydrothermal and magmatic activity in the Dukat gold-silver ore field. Geology of Ore Deposits 48, 489–498. https://doi.org/10.1134/S1075701506060043

Filimonova, L.G., Sivtsov, A. V., Trubkin, N. V., 2010. Manganese oxides and associated minerals as constituents of dispersed mineralization of metasomatic rocks in the Dukat ore field. Geology of Ore Deposits 52, 322–333. https://doi.org/10.1134/S1075701510040069

Filimonova, L.G., Trubkin, N. V., Chugaev, A. V., 2014. Mineral types of hydrothermal alteration zones in the Dukat ore field and their relationships to leucogranite and epithermal gold-silver ore, northeastern Russia. Geology of Ore Deposits 56, 169–199. https://doi.org/10.1134/S1075701514030015

Foley, N.K., 1990. Petrology and geochemistry of precious and base metal mineralization, North Amethyst vein system, Mineral County, Colorado. Viginia Polytechnic Institute.

Foley, N.K., Caddey, S.W., Byington, C.B., Vardiman, D.M., 1993. Mineralogy, mineral chemistry, and paragenesis of gold, silver, and base-metal ores of the north Amethyst vein system, San Juan Mountains, Mineral County, Colorado. US Geological Survey Professional Paper 1537. https://doi.org/10.3133/pp1537

Gac, W., 2006. FT-IR/PAS studies of the silver modified manganese oxides. Journal De Physique. IV : JP 137, 283–286. https://doi.org/10.1051/JP4:2006137055

Gammons, C.H., Seward, T.M., 1996. Stability of manganese (II) chloride complexes from 25 to 300°C. Geochimica et Cosmochimica Acta 60, 4295–4311. https://doi.org/10.1016/S0016-7037(96)00275-X

Gammons, C.H., Williams-Jones, A.E., 1997. Chemical mobility of gold in the porphyry-epithermal environment. Economic Geology 92, 45–59. https://doi.org/10.2113/gsecongeo.92.1.45

Gammons, C.H., Williams-Jones, A.E., 1995. The solubility of Au□Ag alloy + AgCl in HCl/NaCl solutions at 300°C: New data on the stability of Au (1) chloride complexes in hydrothermal fluids. Geochimica et Cosmochimica Acta 59, 3453–3468. https://doi.org/10.1016/0016-7037(95)00234-Q

Gasparrini, C., 1993. Gold and Other Precious Metals. Gold and Other Precious Metals. https://doi.org/10.1007/978-3-642-77184-2

Gómez-Caballero, A.J., Villaseñor-Cabral, M., Santiago-Jacinto, P., Ponce-Abad, F., Arturo Gómez-Caballero, J., Guadalupe Villaseñor-Cabral, M., Santiago-Jacinto, P., Ponce-Abad, F., 2010. Hypogene Ba-rich todorokite and associated nanometric native silver in the San Miguel Tenango mining area, Zacatlán, Puebla, Mexico. Canadian Mineralogist 48, 1237–1253. https://doi.org/10.3749/canmin.48.5.1237

Guzman, M., Monecke, T., 2014. Geology of the North Amethyst Au-Ag epithermal deposit, Creede District, Colorado, in: Society of Economic Geologists 2014 Conference.

Guzman, M.A., Monecke, A., 2016. Vein Petrography and Geochemistry of the North Amethyst Au-Ag epithermal Deposit, Creede, Colorado USA, in: Goldschmidt 2016 Conference.

Hedenquist, J., Arribas, A., Gonzalez-Urien, E.G., Hagemann, S.G., Brown, P.E., 2000. Exploration for Epithermal Gold Deposits. SEG Reviews 13, 245–277. https://doi.org/10.5382/rev.13.07

Hedenquist, J.W., Arribas R., A., Aoki, M., 2017. Zonation of Sulfate and Sulfide Minerals and Isotopic Composition in the Far Southeast Porphyry and Lepanto Epithermal Cu–Au Deposits, Philippines. Resource Geology 67, 174–196. https://doi.org/10.1111/rge.12127

Hedenquist, J.W., Henley, R.W., 1985. Hydrothermal eruptions in the Waiotapu geothermal system, New Zealand; their origin, associated breccias, and relation to precious metal mineralization. Economic Geology 80, 1640–1668. https://doi.org/10.2113/gsecongeo.80.6.1640

Hein, J.R., Koschinsky, A., McIntyre, B.R., 2005. Mercury- and silver-rich ferromanganese oxides, southern California Borderland: Deposit model and environmental implications. Economic Geology 100, 1151–1168. https://doi.org/10.2113/gsecongeo.100.6.1151

Heinrich, C.A., 2005. The physical and chemical evolution of low-salinity magmatic fluids at the porphyry to epithermal transition: a thermodynamic study. Mineralium Deposita 2005 39:8 39, 864–889. https://doi.org/10.1007/S00126-004-0461-9

Heinrich, C.A., Günther, D., Audétat, A., Ulrich, T., Frischknecht, R., 1999. Metal fractionation between magmatic brine and vapor, determined by microanalysis of fluid inclusions. Geology 27, 755. https://doi.org/10.1130/0091-7613(1999)027<0755:MFBMBA>2.3.CO;2

Hemley, J.J., Hunt, J.P., 1992. Hydrothermal ore-forming processes in the light of studies in rock- buffered systems: II. Some general geologic applications. Economic Geology 87, 23–43. https://doi.org/10.2113/gsecongeo.87.1.23

Hewett, D.F., 1968. Silver in Veins of Hypogene Manganese Oxides, geological survey circular.

Hewett, D.F., 1964. Veins of hypogene manganese oxide minerals in the southwestern United States. Economic Geology 59, 1429–1472. https://doi.org/10.2113/gsecongeo.59.8.1429

Hewett, D.F., Fleischer, M., Conklin, N., 1963. Deposits of the manganese oxides; supplement. Economic

Geology 58, 1–51. https://doi.org/10.2113/GSECONGEO.58.1.1

Hewett, D.F., Fleischer, M., Conklin, N., 1960. Deposits of the manganese oxides. Economic Geology 55, 1–55. https://doi.org/10.2113/gsecongeo.55.1.1

Hewett, D.F., Radtke, A.S., 1967. Silver-bearing black calcite in western mining districts. Economic Geology 62, 1–21. https://doi.org/10.2113/gsecongeo.62.1.1

Hildebrand, F.A., Mosier, E.L., 1974. Argentian cryptomelane and bromargyrite in volcanic rocks near Silver Cliff, Colorado. Bulletin. https://doi.org/10.3133/B1382C

Jiang, T., Yang, Y., Huang, Z., Qiu, G., 2003. Simultaneous leaching of manganese and silver from manganese–silver ores at room temperature. Hydrometallurgy 69, 177–186. https://doi.org/10.1016/S0304-386X(03)00033-1

Jones, B.K., 1992. Application of metal zoning to gold exploration in porphyry copper systems. Journal of Geochemical Exploration 43, 127–155. https://doi.org/10.1016/0375-6742(92)90003-Q

Koichiro, S., Watanabe, Y., Imai, A., Motomura, Y., 2005. Alteration and gold mineralization of the Ciurug vein, Pongkor Au-Ag deposit, Indonesia. Mineral Deposit Research: Meeting the Global Challenge 995–998. https://doi.org/10.1007/3-540-27946-6_254

Krauskopf, K.B., 1951. The solubility of gold. Economic Geology 46, 858–870. https://doi.org/10.2113/GSECONGEO.46.8.858

Large, R.R., Bull, S.W., McGoldrick, P.J., 2000. Lithogeochemical halos and geochemical vectors to stratiform sediment hosted Zn-Pb-Ag deposits Part 2. HYC deposit, McArthur river, North Territory. Journal of Geochemical Exploration 68, 105–126. https://doi.org/10.1016/S0375-6742(99)00084-9

Large, R.R., McGoldrick, P.J., 1998. Lithogeochemical halos and geochemical vectors to stratiform sediment hosted Zn-Pb-Ag deposits, 1. Lady Loretta deposit, Queensland. Journal of Geochemical Exploration. https://doi.org/10.1016/S0375-6742(98)00013-2

Leach, T., Corbett, G., 2008. Fluid mixing as a mechanism for bonanza grade epithermal gold formation. Terry Leach Symposium 2008.

Leach, T.M., Corbett, G., 1995. Characteristics of low sulfidation gold-copper systems in the southwest Pacific, in: Pacific Rim Congress 95. The Australasian Institute of Mining and Metallurgy, Auckland, New Zealand, pp. 327–332.

Leach, T.M., Corbett, G., 1994. Porphyry-related carbonate base metal gold systems, in: Rogerson, R. (Ed.), Geology, Exploration and Mining Conference. The Australasian Institute of Mining and Metallurgy, Lae, Papua New Guinea, pp. 84–91.

Leroy, J.L., Hubé, D., Marcoux, E., Hube, D., Marcoux, E., Hubé, D., Marcoux, E., 2000. Episodic deposition of Mn Minerals in cockade breccia structures in three low-sulfidation epithermal deposits: A mineral stratigraphy and fluid-inclusion approach. Canadian Mineralogist 38, 1125–1136. https://doi.org/10.2113/gscanmin.38.5.1125

Leube, A., Hirdes, W., Mauer, R., Kesse, G.O., 1990. The early Proterozoic Birimian Supergroup of Ghana and some aspects of its associated gold mineralization. Precambrian Research 46, 139–165. https://doi.org/10.1016/0301-9268(90)90070-7

Liakopoulos, A., Glasby, G.P., Papavassiliou, C.T., Boulegue, J., 2001. Nature and origin of the Vani manganese deposit, Milos, Greece: An overview. Ore Geology Reviews 18, 181–209. https://doi.org/10.1016/S0169-1368(01)00029-4

Likhoidov, G.G., Plyusnina, L.P., Scheka, J.A., Aphanas'eva, T.B., 2000. Experimental study of gold and platinum solubility in a complex fluid under hydrothermal conditions. Resource Geology 50, 83–92. https://doi.org/10.1111/j.1751-3928.2000.tb00058.x

Marcoux, E., Milesi, J.-P., Sohearto, S., Rinawan, R., 1993. Noteworthy mineralogy of the Au-Ag-Sn-W(Bi) epithermal ore deposit of Cirotan, west Java, Indonesia. Canadian Mineralogist 31, 727–744.

Marcoux, E., Milési, J.P., 1994. Epithermal gold deposits in West Java, Indonesia: geology, age and crustal

source. Journal of Geochemical Exploration 50, 393–408. https://doi.org/10.1016/0375-6742(94)90033-7

McLemore, V.T., Munroe, E.A., Heizler, M.T., McKee, C., 1999. Geochemistry of the Copper Flat porphyry and associated deposits in the Hillsboro mining district, Sierra County, New Mexico, USA, in: Journal of Geochemical Exploration. https://doi.org/10.1016/S0375-6742(99)00072-2

Megaw, P.K.M., Ruiz, J., Titley, S.R., 1988. High-temperature, carbonate-hosted Ag-Pb-Zn(Cu) deposits of northern Mexico. Economic Geology 83, 1856–1885. https://doi.org/10.2113/GSECONGEO.83.8.1856

Milési, J.P., Ledru, P., Ankrah, P., Johan, V., Marcoux, E., Vinchon, C., 1991. The metallogenic relationship between Birimian and Tarkwaian gold deposits in Ghana. Mineralium Deposita 26, 228–238. https://doi.org/10.1007/BF00209263

Milesi, J.P., Marcoux, E., Nehlig, P., Sunarya, Y., Sukandar, A., Felenc, J., 1994. Cirotan, west Java, Indonesia: a 1.7 Ma hybrid epithermal Au-Ag-Sn-W deposit. Economic Geology 89, 227–245. https://doi.org/10.2113/gsecongeo.89.2.227

Milési, J.P., Marcoux, E., Sitorus, T., Simandjuntak, M., Leroy, J., Bailly, L., 1999. Pongkor (west Java, Indonesia): A Pliocene supergene-enriched epithermal Au-Ag-(Mn) deposit. Mineralium Deposita 34, 131–149. https://doi.org/10.1007/s001260050191

Nicholson, K., 1992. Contrasting Signatures of Manganese Oxides ' Guides to Metallogenesis. Economic Geology 1253–1264.

Ntiamoah-Agyakwa, Y., 1979. Relationship between gold and manganese mineralizations in the Birimian of Ghana, West Africa. Geological Magazine 116, 345–352. https://doi.org/10.1017/S0016756800043983

Nyame, F.K., 2008. Petrography and geochemistry of intraclastic manganese-carbonates from the ~2.2 Ga Nsuta deposit of Ghana: Significance for manganese sedimentation in the Palaeoproterozoic of West Africa. Journal of African Earth Sciences 50, 133–147. https://doi.org/10.1016/j.jafrearsci.2007.09.007

Ohashi, H., Ezoe, H., Okaue, Y., Kobayashi, Y., Matsuo, S., Kurisaki, T., Miyazaki, A., Wakita, H.,

Yokoyama, T., 2005. The effect of UV irradiation on the reduction of Au(III) ions adsorbed on manganese dioxide. Analytical Sciences 21, 789–793. https://doi.org/10.2116/analsci.21.789

Papavassiliou, K., Voudouris, P., Kanellopoulos, C., Glasby, G., Alfieris, D., Mitsis, I., 2017. New geochemical and mineralogical constraints on the genesis of the Vani hydrothermal manganese deposit at NW Milos island, Greece: Comparison with the Aspro Gialoudi deposit and implications for the formation of the Milos manganese mineralization. Ore Geology Reviews 80, 594–611. https://doi.org/10.1016/j.oregeorev.2016.07.023

Pareja, G.A., 1995. Dolostone-Hosted Gold-Rich Jasperoids and their Relationship to Copper Replacement Mantos, LS &A and Queen Creek Mines, Superior District, Arizona, in: Geological Society of Nevada Symposium on Geology and Ore Deposits of the American Cordillera. Reno, pp. 1–2.

Pasero, M., 2005. A Short Outline of the Tunnel Oxides. Reviews in Mineralogy and Geochemistry 57, 291–305. https://doi.org/10.2138/RMG.2005.57.9

Pokrovski, G.S., Akinfiev, N.N., Borisova, A.Y., Zotov, A. V., Kouzmanov, K., 2014. Gold speciation and transport in geological fluids: Insights from experiments and physical-chemical modelling. Geological Society Special Publication 402, 9–70. https://doi.org/10.1144/SP402.4

Pokrovski, G.S., Borisova, A.Y., Harrichoury, J.C., 2008. The effect of sulfur on vapor-liquid fractionation of metals in hydrothermal systems. Earth and Planetary Science Letters 266, 345–362. https://doi.org/10.1016/j.epsl.2007.11.023

Pokrovski, G.S., Kokh, M.A., Guillaume, D., Borisova, A.Y., Gisquet, P., Hazemann, J.L., Lahera, E., Del Net, W., Proux, O., Testemale, D., Haigis, V., Jonchière, R., Seitsonen, A.P., Ferlat, G., Vuilleumier, R., Saitta, A.M., Boiron, M.C., Dubessy, J., 2015. Sulfur radical species form gold deposits on Earth. Proceedings of the National Academy of Sciences of the United States of America 112, 13484–13489. https://doi.org/10.1073/pnas.1506378112

Pokrovski, G.S., Roux, J., Harrichoury, J.-C., 2005. Fluid density control on vapor-liquid partitioning of metals in hydrothermal systems. Geology 33, 657–660. https://doi.org/10.1130/G21475AR.1

Prol-Ledesma, R.M., Canet, C., Torres-Vera, M.A., Forrest, M.J., Armienta, M.A., 2004. Vent fluid chemistry in Bahía Concepción coastal submarine hydrothermal system, Baja California Sur, Mexico. Journal of Volcanology and Geothermal Research 137, 311–328. https://doi.org/10.1016/j.jvolgeores.2004.06.003

Radtke, A.S., Taylor, C.M., Hewett, D.F., 1967. Aurorite, argentian todorokite, and hydrous silver-bearing lead manganese oxide. Economic Geology 62, 186–206. https://doi.org/10.2113/GSECONGEO.62.2.186

Ran, Y., Fu, J., Lu, J., Rate, A.W., Gilkes, R.J., 1999. Sorption of Au (I , III) complexes on Fe, Mn oxides and humic Acid. Chinese Science Bulletin 44, 193–195. https://doi.org/10.1360/sb1999-44-S2-193

Ravikumar, R., Fuerstenau, D.W., 2011. Silver Sorption by Manganese Oxide. MRS Online Proceedings Library 1996 432:1 432, 243–248. https://doi.org/10.1557/PROC-432-243

Rodríguez-Díaz, A.A., Canet, C., Villanueva-Estrada, R.E., Chacón, E., Gervilla, F., Velasco-Tapia, F., Cruz-Gámez, E.M., González-Partida, E., Casas-García, R., Linares-López, C., Pérez-Zárate, D., 2019. Recent Mn-Ag deposits in coastal hydrothermal springs in the Baja California Peninsula, Mexico. Mineralium Deposita 54, 849–866. https://doi.org/10.1007/s00126-018-0846-9

Rosana, M.F., Matsueda, H., 2002. Cikidang Hydrothermal Gold Deposit in Western Java, Indonesia. Resource Geology 52, 341–352. https://doi.org/10.1111/j.1751-3928.2002.tb00144.x

Roslyakov, N.A., Belevantsev, V.I., Kalinin, Y.A., 2005. Supergene gold in manganese-bearing weathered rocks. Geokhimiya 43, 1015–1018.

Roy, S., 1981. Manganese deposits. Academic Press.

Rutten, O.W.J.S., Van Sandwijk, A., Van Weert, G., 1997. Electrolytic Processing of Manganiferous-Silver Ores in Acidic Nitrate Medium.

Seward, T.M., Barnes, H.L., 1997. Metal transport by hydrothermal ore fluids, in: Foster, R.P. (Ed.), Geochemistry of Hydrothermal Ore Deposits. John Wiley, New York, pp. 435–486.

Seward, T.M., Williams-Jones, A.E., Migdisov, A.A., 2014. The Chemistry of Metal Transport and Deposition by Ore-Forming Hydrothermal Fluids, in: Treatise on Geochemistry: Second Edition. https://doi.org/10.1016/B978-0-08-095975-7.01102-5

Shikazono, N., 1985. A comparison of temperatures estimated from the electrum- sphalerite-pyrite-argentite assemblage and filling temperatures of fluid inclusions from epithermal Au-Ag vein-type deposits in Japan. Economic Geology 80, 1415–1424. https://doi.org/10.2113/gsecongeo.80.5.1415

Sillitoe, R.H., 2015. Epithermal paleosurfaces. Mineralium Deposita 50, 767–793. https://doi.org/10.1007/s00126-015-0614-z

Sillitoe, R.H., 2010. Porphyry copper systems. Economic Geology 105, 3–41. https://doi.org/10.2113/gsecongeo.105.1.3

Sillitoe, R.H., 2000. Gold-Rich Porphyry Deposits: Descriptive and Genetic Models and Their Role in Exploration and Discovery. Gold in 2000 315–345. https://doi.org/10.5382/REV.13.09

Sillitoe, R.H., Hedenquist, J.W., 2005. Linkages between Volcanotectonic Settings, Ore-Fluid Compositions, and Epithermal Precious Metal Deposits. Volcanic, Geothermal, and Ore-Forming Fluids 315–343. https://doi.org/10.5382/SP.10.16

Simmons, S.F., Browne, P.R.L., 1990. Mineralogic, alteration and fluid-inclusion studies of epithermal gold-bearing veins at the Mt. Muro Prospect, Central Kalimantan (Borneo), Indonesia. Journal of Geochemical Exploration 35, 63–103. https://doi.org/10.1016/0375-6742(90)90036-A

Simmons, S.F., White, N.C., John, D.A., 2005. Geological Characteristics of Epithermal Precious and Base Metal Deposits. One Hundredth Anniversary Volume. https://doi.org/10.5382/AV100.16

Smith, D.M., Albinson, T., Sawkins, F.J., 1982. Geologic and fluid inclusion studies of the Tayoltita silver-gold vein deposit, Durango, Mexico. Economic Geology 77, 1120–1145. https://doi.org/10.2113/gsecongeo.77.5.1120

Soeria-Atmadja, R., Sunarya, Y., Sutanto, S., Hendaryono, H., 1998. Epithermal gold-copper mineralization

associated with Late Neogene-magmatism and crustal extension in the Sunda-Banda Arc. Bulletin of the Geological Society of Malaysia 42, 257–268. https://doi.org/10.7186/bgsm42199821

Ta, C., Brugger, J., Pring, A., Hocking, R.K., Lenehan, C.E., Reith, F., 2015. Effect of manganese oxide minerals and complexes on gold mobilization and speciation. Chemical Geology 407–408, 10–20. https://doi.org/10.1016/j.chemgeo.2015.04.016

Wang, L., Qin, K.-Z., Song, G.-X., Li, G.-M., 2019. A review of intermediate sulfidation epithermal deposits and subclassification. Ore Geology Reviews 107, 434–456. https://doi.org/10.1016/j.oregeorev.2019.02.023

Warmada, I.W., Lehmann, B., Simandjuntak, M., 2003. Polymetallic sulfides and sulfosalts of the Pongkor epithermal gold-silver deposit, West Java, Indonesia. Canadian Mineralogist 41, 185–200. https://doi.org/10.2113/gscanmin.41.1.185

Webster, J.G., 1986. The solubility of gold and silver in the system Au-Ag-SO2-H2O at 25°C and 1 atm. Geochimica et Cosmochimica Acta 50, 1837–1845. https://doi.org/10.1016/0016-7037(86)90242-5

Webster, J.G., Mann, A.W., 1984. The influence of climate, geomorphology and primary geology on the supergene migration of gold and silver. Journal of Geochemical Exploration 22, 21–42. https://doi.org/10.1016/0375-6742(84)90004-9

Williams-Jones, A.E., Heinrich, C.A., 2005. Vapor transport of metals and the formation of magmatic-hydrothermal ore deposits. Economic Geology 100, 1287–1312. https://doi.org/10.2113/gsecongeo.100.7.1287

Wu, C.Y., Bai, G., Xu, L.M., 1993. Types and distribution of silver ore deposits in China. Mineralium Deposita 1993 28:4 28, 223–239. https://doi.org/10.1007/BF02421573

Yamashita, M., Ohashi, H., Kobayashi, Y., Okaue, Y., Kurisaki, T., Wakita, H., Yokoyama, T., 2008. Coprecipitation of gold(III) complex ions with manganese(II) hydroxide and their stoichiometric reduction to atomic gold (Au(0)): Analysis by Mössbauer spectroscopy and XPS. Journal of Colloid and

Interface Science 319, 25–29. https://doi.org/10.1016/j.jcis.2007.10.034

Zhang, K., Jin, R.S., Sun, F.Y., Li, B. Le, He, P., Zhang, Y.L., Guo, S., Zhang, T.F., 2020. Metallogenesis and ore-forming time of the Changtuxili Mn–Ag–Pb–Zn deposit in Inner Mongolia: Evidence from C–O–S isotopes and U–Pb geochronology. Geoscience Frontiers 11, 1369–1380. https://doi.org/10.1016/j.gsf.2019.11.013

Zhang, X.Y., Tian, X. Da, Zhang, D.F., 2006. Separation of silver from silver-manganese ore with cellulose as reductant. Transactions of Nonferrous Metals Society of China 16, 705–708. https://doi.org/10.1016/S1003-6326(06)60125-8

CHAPTER 3

RELATIONSHIP BETWEEN JASPEROID AND MN ORE

Geology and geochemistry of jasperoids from the 'Montaña de Manganeso' district, San Luis Potosí, north-central Mexico

Joseph Madondo[1], Carles Canet[2,3,*], Fernando Nuñez-Useche[4], and Eduardo Gonzalez-Partida[5]

[1] *Posgrado en Ciencias de la Tierra, Universidad Nacional Autónoma de México, Ciudad Universitaria, 04510, Mexico City, Mexico.*
[2] *Instituto de Ciencias de la Atmósfera y Cambio Climático, Universidad Nacional Autónoma de México, Ciudad Universitaria, 04510, Mexico City, Mexico.*
[3] *Instituto de Geofísica, Universidad Nacional Autónoma de México, Ciudad Universitaria, 04510, Mexico City, Mexico.*
[4] *Instituto de Geología, Universidad Nacional Autónoma de México, Ciudad Universitaria, 04510, Mexico City, Mexico.*
[5] *Centro de Geociencias, Universidad Nacional Autónoma de México, Juriquilla, Querétaro, 76230, Mexico.*
* *ccanet@atmosfera.unam.mx*

ABSTRACT

Large outcrops of jasperoids occur in the 'Montaña de Manganeso' mining district in north-central Mexico. They range from massive manganiferous jasperoids to highly brecciated, hematitic jasperoid. The jasperoids of 'Montaña de Manganeso' occur mainly as replacements of limestone, sandstone and shale, commonly nearby high-angle fault systems. The mineralogy of the jasperoids consist of quartz and its polymorphs (chalcedony, tridymite and cristobalite), Fe-Mn oxyhydroxides, calcite and minor barite. Many outcrops show evidence of several periods of brecciation and silicification. The geochemical signature of the jasperoids suggests that silicification was product of hydrothermal activity. The jasperoids display enrichment in elements of hydrothermal provenance such as Ba, Sr, As, Cr, Mo, Sb, Ni, Zn and Cu, whereas are strongly depleted in the elements indicative of clastic sources such as Ti, K, Th and Zr. Element ratios such as (Fe+Mn)/Ti, Al/(Al+Fe+Mn), Fe/Mn and U /Th, along with the Al-Fe-Mn and Fe-Mn-(Ni+Co+Cu)×10 ternary diagrams confirm a hydrothermal origin. Low ∑REE, an enrichment of LREE over HREE, negative Ce anomalies and positive Y anomalies (Y_{PASS}/Ho_{PAAS}) also support the hydrothermal processes. The geological evidence, in the form of a feeder zone and extensive hydrothermal alteration, show that the silica forming the rocks originated from ascending hot fluids.

Key words: jasperoid; hydrothermal; silicification; Fe-Mn oxides; San Luis Potosí.

RESUMEN

En el distrito minero de la Montaña de Manganeso en el centro-norte de México se encuentran grandes afloramientos de jasperoides que van desde jasperoides manganíferos masivos hasta jasperoides hematíticos muy brechados. Los jasperoides de la Montaña de Manganeso ocurren principalmente como reemplazamientos de calizas, areniscas y pizarras, comúnmente cerca de sistemas de fallas de alto ángulo. La mineralogía de los jasperoides consiste en cuarzo y sus polimorfos (calcedonia, tridimita y cristobalita), oxihidróxidos de Fe-Mn, calcita y en menor grado barita. Muchos afloramientos muestran evidencia de varios episodios de brechamiento y silicificación. La firma geoquímica de los jasperoides sugiere que la silicificación fue producto de la actividad hidrotermal. Los jasperoides muestran enriquecimiento en elementos de procedencia hidrotermal como Ba, Sr, As, Cr, Mo, Sb, Ni, Zn y Cu, mientras que están fuertemente empobrecidos en los elementos indicativos de fuentes clásticas como Ti, K, Th y Zr. Relaciones de elementos como (Fe+Mn)/Ti, Al/(Al+Fe+Mn), Fe/Mn y U/Th, junto con los diagramas ternarios Al-Fe-Mn y Fe-Mn- (Ni+Co+Cu)×10 confirman un origen hidrotermal. Un bajo ∑REE, un enriquecimiento de LREE sobre HREE, anomalías negativas de Ce y positivas de Y (Y_{PASS}/Ho_{PAAS}) también apoyan un origen hidrotermal. La evidencia geológica, en forma de una 'zona de alimentación' y alteración hidrotermal extensa, muestra que la sílice que forma las rocas se originó a partir de fluidos calientes ascendentes.

Palabras clave: jasperoide; hidrotermal; silicificación; óxidos de Fe-Mn; San Luis Potosí.

INTRODUCTION

Jasperoid is a rock composed mainly of quartz and/or other silica polymorphs, formed by epigenetic hydrothermal replacement of a previously lithified rock (Lovering, 1962, 1972; Fournier, 1985; Theodore and Jones, 1992; Hofstra and Cline, 2000; Yigit *et al.*, 2006). They are documented in several countries including the United States, Mexico, Peru, Australia and China, where they form topographically prominent outcrops because of their resistance to weathering (Bailey, 1974; Murphy, 1995; Arehart, 1996). Lovering (1972) investigated several jasperoid provinces and districts in the USA and Mexico recognizing a genetic and spatial association between jasperoid and ore deposits.

Madondo, J., Canet, C., Nuñez-Useche, F., Gonzalez-Partida, E., 2021, Geology and geochemistry of jasperoids from the 'Montaña de Manganeso' district, San Luis Potosí, north-central Mexico: Revista Mexicana de Ciencias Geológicas, v. 38, núm. 3, p. 193-209.

DOI: http://dx.doi.org/10.22201/cgeo.20072902e.2021.3.1651

Jasperoid formation is commonly attributed to hydrothermal activity because of a general spatial relationship between jasperoids and igneous rocks (Lovering, 1972; O'Neil and Bailey, 1979; Wilson *et al.*, 1987; Nelson, 1990; Theodore and Jones, 1992; Murphy, 1995; Johnston *et al.*, 2008; Kirwin and Royle, 2019; Huff *et al.*, 2020). Consequently, most jasperoids are localized along faults, fractures, and shear zones that could serve as channel ways for ascending silica-rich hydrothermal fluids (McKay and Finlow-Bates, 1977; Wilson *et al.*, 1987; Kuehn and Rose, 1992; Yigit *et al.*, 2006). Some jasperoids, however, form lenticular and layered bodies that may resemble bedded chert (Lovering, 1972). Such jasperoids may be difficult to distinguish from bedded cherts, unless the feeder channels can be identified (Lovering, 1972; Wilson *et al.*, 1987; Nelson, 1990).

Jasperoid deposits, as hydrothermal products, can be expected to exhibit the geochemical signature of the fluids from which they precipitated (Renault *et al.*, 1995). Moreover, as jasperoids generally contain substantial amounts of Fe and Mn oxides with strong adsorption capacity for cations, they even more strongly acquire the geochemical signatures of the mineralizing fluid (Bau *et al.*, 1996; Conly *et al.*, 2011; Sinisi *et al.*, 2012; Papavassiliou *et al.*, 2017). Also, as they are very resistant to chemical weathering and are barely affected by diagenetic changes, their chemistry is suitable for interpreting depositional processes and environment of formation of associated ore deposits (Murray, 1994; Dasgupta *et al.*, 1999). For this reason, jasperoids and their geochemistry have long been applied to mineral exploration, in particular, gold exploration (Lovering and Heyl, 1974; O'Neil and Bailey, 1979; Holland *et al.*, 1988; Nelson, 1990; Graney *et al.*, 1991; Theodore and Jones, 1992; Kirwin and Royle, 2019; Huff *et al.*, 2020).

Massive siliceous bodies crop out prominently in the Central Plateau region of Mexico (Labarthe-Hernandez *et al.*, 1992). These bodies occur as fault-controlled veins and irregular bodies that cut rocks of known continental origin, making it unlikely that they are submarine exhalative Fe-Mn cherts (Crerar *et al.*, 1982; Adachi *et al.*, 1986). Hence, in agreement with previous studies involving these bodies (Albinson, 1988; Labarthe-Hernández *et al.*, 1992), the term *jasperoid* is preferred here for the Central Plateau siliceous bodies to avoid connotation of diagenetic or exhalative origin usually associated with the term *chert* (Adachi *et al.*, 1986; Murray, 1994; Murphy, 1995; Binns, 2007).

The common association of jasperoids with precious and base-metal enrichment has focused attention on these metals and not on their generally sub-economic iron and manganese content (Hesse, 1990). This investigation instead takes advantage of the high abundances of manganese and iron oxides in the jasperoids of the Central Plateau region to characterize and understand jasperoid formation through the Fe-Mn oxide geochemistry. The problem of differentiating hydrothermal silica from other types such as biogenic and sedimentary silica is dealt with by demonstrating through field and geochemical characteristics of the jasperoids, the hydrothermal origin of both the silica and the Fe-Mn oxides. The results of this research provide a new approach to understand the metallogenesis of the Central Plateau.

REGIONAL GEOLOGY

The study area is located in central Mexico on an elevated plateau (average altitude: ~2000 m a.s.l.) known as the *Mesa Central* or Central Plateau (Figure 1) (Nieto-Samaniego *et al.*, 2005, 2019). The geology of the study region is characterized by the accretion of the Guerrero terrane over continental Mexico represented by the Sierra Madre terrane (Centeno-García and Silva-Romo, 1997; Centeno-García *et al.*, 2003; Martini *et al.*, 2013). Jurassic ocean floor and island arc volcano-sedimentary rocks geologically circumscribed to the Guerrero terrane accreted over the Sierra Madre terrane marine carbonate successions during the Late Cretaceous Laramide orogenesis (Centeno-García and Silva-Romo, 1997; Centeno-García *et al.*, 2003; Martini *et al.*, 2013). In the region, isolated outcrops of intraoceanic arc andesitic and pillow lavas, cherty pelagic limestones and radiolarite-chert blocks

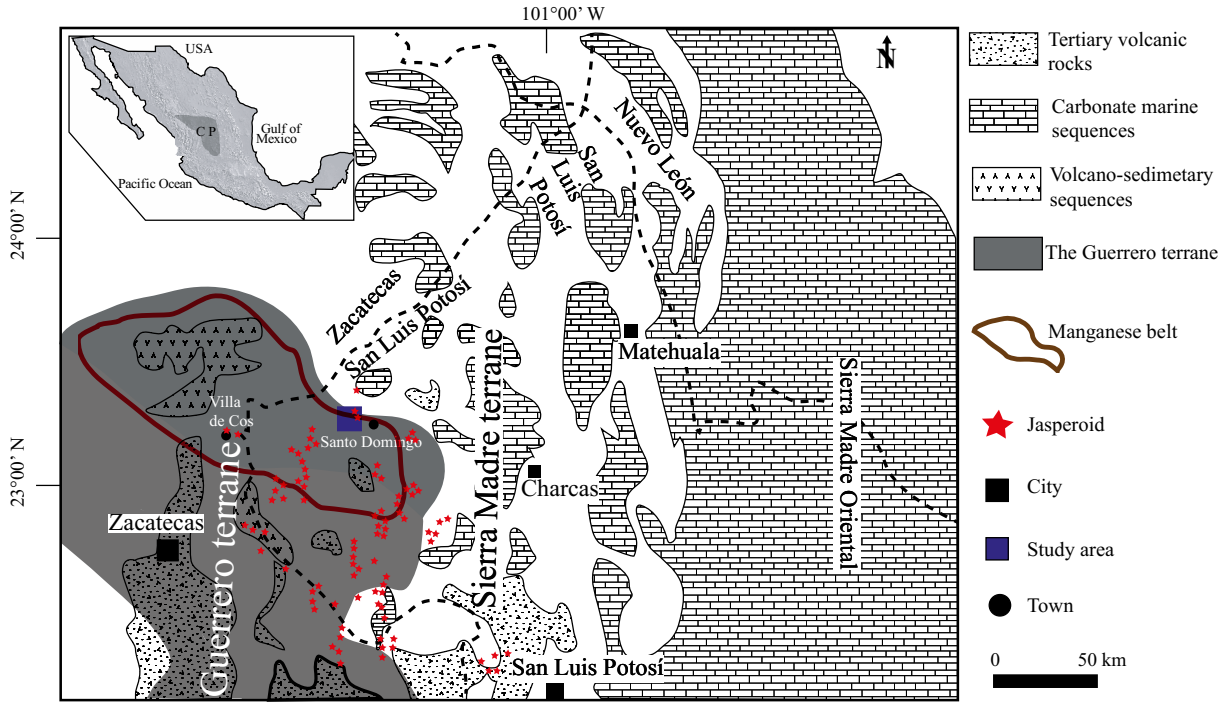

Figure 1. Geologic map of the region (modified after Hope *et al.*, 2002) showing the distribution of some jasperoid bodies (after Sanchez-Rojas, 2013). The boundary of the Guerrero terrane reflects the limit recommended by SGM (2016, 2018).

characterize the Guerrero terrane (Centeno-García and Silva-Romo, 1997) (Figure 2).

Marine Mesozoic successions of late Triassic to late Cretaceous age constitute the Sierra Madre terrane (Carrillo-Bravo, 1982; Juárez-Arriaga *et al.*, 2019). The basement rocks, which correspond to Upper Triassic-middle Jurassic turbidites (Centeno-García and Silva-Romo, 1997; Barboza-Gudiño *et al.*, 1998, 2010), are overlain by Lower to Middle Jurassic continental arc deposits (Barboza-Gudiño *et al.*, 1999, 2008). Upper Jurassic to Late Cretaceous shallow marine carbonate sequences and clastic sediments cover the continental arc deposits (Carrillo-Bravo, 1982).

The Guerrero terrane accretion to continental Mexico in the Late Cretaceous, caused by the subduction of the Farallon plate beneath the North American plate, produced regional thrust faults (Figure 2). These faults were partly reactivated as normal faults during the subsequent development of the Paleogene Basin and Range extensional tectonics (Tristán-González *et al.*, 2009b). The transition from compressional tectonics of the Guerrero terrane accretion to extensional tectonics of the Basin and Range was marked by the onset of the continental volcanism of the Sierra Madre Occidental (Ferrari *et al.*, 2002; Aguirre-Díaz *et al.*, 2008). During the Oligocene, the ignimbrite flare-up event resulted in the large-volume ignimbrites which make the Sierra Madre Occidental one of the largest silicic igneous province on earth (McDowell and Clabaugh, 1979; Ferrari *et al.*, 2002, 2007; Aguirre-Díaz *et al.*, 2008; Aguirre-Díaz and Labarthe-Hernández, 2003).

The partial overlap of this silicic magmatic event and the Basin and Range extension generated multiple and discrete episodes of fissural rhyolitic volcanism mostly controlled by major NW–SE trending fault systems (Tristán-González, 1986; Aguirre-Díaz and Labarthe-Hernández, 2003; Aguirre-Díaz *et al.*, 2008; Tristán-González *et al.*, 2008, 2009b; Aguillón-Robles *et al.*, 2012, 2014; Zamora-Vega *et al.*, 2018). The silicic nature of the volcanism also ensured the supply of vast amounts of silica, which generated extensive areas of jasperoid occurrences in the Central Plateau (Labarthe-Hernández *et al.*, 1992). The Sierra Madre Occidental magmatism triggered a period of intense hydrothermal activity in the Central Plateau that generated different types of mineral deposits (Aranda-Gómez and Mcdowell, 1998; Aranda-Gómez *et al.*, 2007; Nieto-Samaniego *et al.*, 2007; Tristán-González *et al.*, 2008, 2009b; Rodríguez-Ríos *et al.*, 2013). In the Zacatecas state, west of the study area, this hydrothermal activity is associated with precious metal and polymetallic epithermal deposits (Ponce and Clark, 1988; Henry and Aranda-Gomez, 1992; Nieto-Samaniego *et al.*, 1996, 2007; Aguirre-Díaz *et al.*, 2008; Aguillón-Robles *et al.*, 2009; Zamora-Vega *et al.*, 2018).

METHODOLOGY

Eleven highly silicified samples, collected from different outcrops, were analyzed for this study. Most of these are jasperoids, but three of the samples show contents of silica (<10.1 %) lower than those of jasperoids (Lovering, 1972) due to high contents of MnO_2, and in fact represent manganese ore. However, for convenience, the general term jasperoid is used here for all the samples analyzed.

Textural characterization of the Fe-Mn oxides was first carried out visually in hand specimens and in thin sections. For a more detailed textural and mineral identification, petrography and scanning electron microscopy (SEM) were carried out on six polished sections at the Central Analytical Facility of the Faculty of Science of the University of Johannesburg, South Africa. Energy dispersive spectrometry (EDS) was used for semi-quantitative determination of concentration of elements in certain minerals. Microscopic images were taken on carbon-coated polished sections using backscattered electrons (BSE) on a Vega 3 Tescan system equipped with an Oxford X-Max 50 mm^2 energy dispersive spectrometer (EDS). The software used was an Oxford Aztec software V. 2.2.

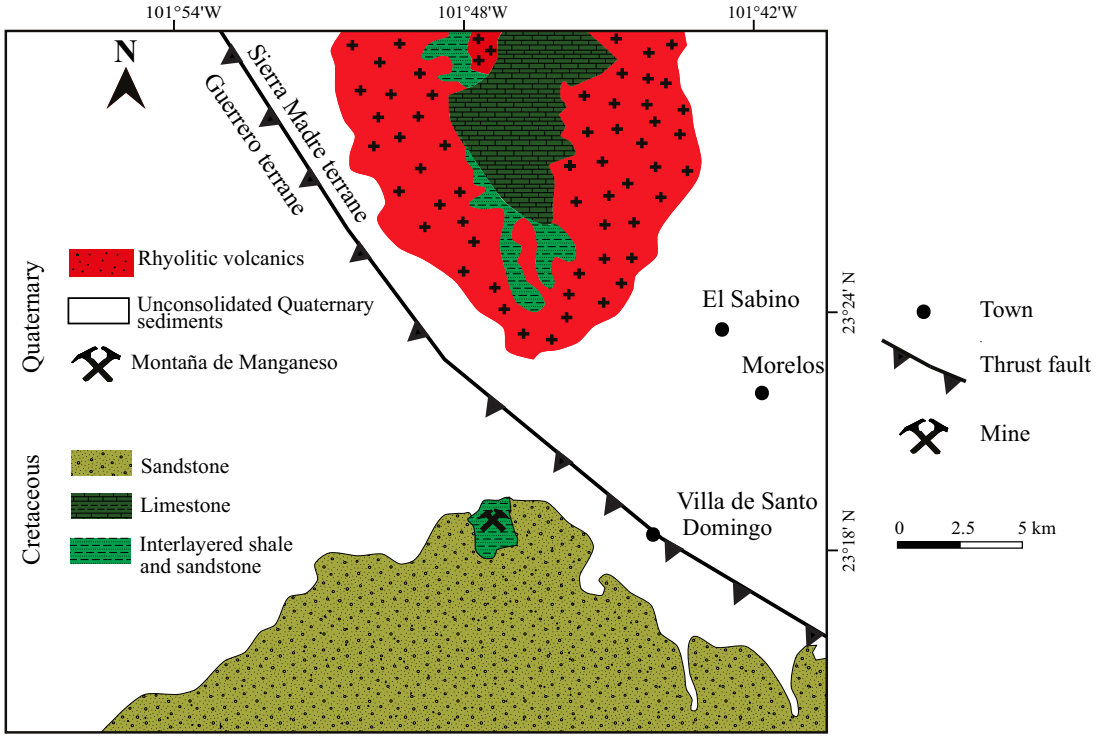

Figure 2. Generalized geologic map of the study area (modified after SGM, 2001).

Bulk mineralogy of 10 samples was determined by powder X-ray diffraction (XRD) using an Empyrean diffractometer equipped with Ni filter, a Cu tube of fine focus and a PIXcel^{3d} detector, at the Instituto de Geología, Universidad Nacional Autónoma de México (UNAM). Measurements were performed in the 2θ angular range from 5° to 70°, in step scanning with a step scan of 0.003° (2θ) and an integration time of 40 s per step. Rock samples were previously crushed and milled to 200 mesh and homogenized. Data were interpreted using HighScore Plus v4 software (PANalytical). Conventional search and match techniques were employed for qualitative analysis.

Major and trace elements (including REE) concentrations were determined for nine samples at Activation Laboratories (ActLabs, Canada) using the Lithogeochemistry analytical package '4Litho'. This method is a combination of lithium metaborate/tetraborate fusion ICP whole rock for major elements and ICP-MS for major elements and REE (for details see http://www.actlabs.com). Calibration was performed using prepared USGS- and CANMET-certified reference materials. A correlation matrix of elemental concentrations was prepared using the software Statistica version 13. Binary and ternary discrimination diagrams were processed with the GCDkit package for R version 3.6.0.

To evaluate the influence of hydrothermal activity, the Fe/Mn (Hein *et al.*, 1997), (Fe+Mn)/Ti (Jun *et al.*, 2010) and Al/(Al+Fe+Mn) ratios were calculated (Adachi *et al.*, 1986). To determine the source of Fe and Mn in the jasperoids Ce and Eu anomalies (Ce/Ce* and Eu/Eu*) were calculated using the equations proposed by Taylor and McLennan (1985):

$$Ce/Ce^{*}=(Ce)CN/\sqrt{\left[(La)CN\times(Pr)CN\right]}$$

$$Eu/Eu^{*}=(Eu)CN/\sqrt{\left[(Sm)CN\times(Gd)CN\right]}$$

wherein these expressions, Eu and Ce are the actual concentrations and Eu* and Ce* are the predicted concentrations based on interpolation of neighboring REE, using chondrite-normalized abundances (Boynton, 1984). The Y anomaly, also used to determine the source of Fe and Mn, was calculated using the equation (Y_{PAAS}/Ho_{PAAS}) (Bau *et al.*, 2014). The subscript "CN" and "PAAS" indicate chondrite-normalized (Boynton, 1984) and Post Archean Australian Shale normalized values, respectively. The heavy-REE (HREE), middle-REE (MREE) and light-REE (LREE) are defined as the elements from La to Nd, Sm to Tb and Dy to Lu, respectively.

GENERAL CHARACTERISTICS OF MEXICAN JASPEROIDS

Several protruding jasperoid outcrops (Figure 1) are documented in the Mexican Central Plateau (Labarthe-Hernández *et al.*, 1992). The jasperoids generally occur as flared-up, funnel shaped veins of widely variable dimensions. Tabular bodies with thicknesses ranging from 2 to 20 m (and rare bodies of up to 50 m) occur occasionally, extending up to 2 km in length (Labarthe-Hernández *et al.*, 1992). Most jasperoid bodies are black or red, although yellow, green, and brown colored jasperoids often occur. Outcrops range from hard, massive jasperoids to highly brecciated jasperoids re-cemented by younger quartz. Textures vary from aphanitic to coarse crystalline varieties. Late quartz, calcite and barite form crosscutting veinlets or fill vugs and open spaces (Labarthe-Hernández and Aguillón-Robles, 1986). Iron and manganese oxides dominate the non-silica components of the jasperoids.

Most jasperoid bodies trend NW-SE (with subordinate NE-SW and E-W directions) and are fracture controlled (Labarthe-Hernández *et al.*, 1992). The NW-SE trending direction fairly coincides with that of the regional San Luis-Tepehuanes-fault system, whose main activity occurred during the early Oligocene, with multiple reactivations in the late Oligocene and Miocene (Nieto-Samaniego *et al.*, 2007). This fault system controlled the distribution of several mineral deposits in the Central Plateau (Camprubí and Albinson, 2007; Nieto-Samaniego *et al.*, 2007). The manganiferous jasperoids are more widespread in the regions close to the boundary of the Guerrero terrane and the Sierra Madre terrane, where they constitute a metallogenetic belt (Labarthe-Hernández *et al.*, 1992; Sánchez-Rojas, 2013). Trask and Rodríguez-Cabo (1948) reported at least 20 manganiferous jasperoids in this region, with exploitation of the manganese content occurring at Montaña de Manganeso (MdM) and the La Abundancia districts (~60 km W of MdM). A similar close spatial relationship exists between jasperoids and base metal deposits at Real de Ángeles and Villa de Ramos (~55 and 100 km SSE of MdM, respectively) (Labarthe-Hernández *et al.*, 1992).

The jasperoids of the Central Plateau replace Cretaceous marine carbonate rocks of the Sierra Madre terrane, but occasionally replace volcano-sedimentary rocks of the Guerrero terrane and Oligocene continental igneous rocks (Labarthe-Hernández *et al.*, 1982, 1992). Silicification is typically pervasive, obliterating the original characteristics of the rocks. However, in some jasperoids the replacement is partial, preserving the original host rock textures. An argillic alteration often exists laterally to the jasperoids suggesting formation from near neutral pH, low temperature hydrothermal solutions (cf. Reyes, 1990; Sánchez-Córdova *et al.*, 2019; Fulignati, 2020). According to Labarthe-Hernández and Aguillón-Robles (1986), the jasperoids formed from replacement of host rocks by multiple silica generations injected from ascending hot fluids during the waning stage of hydrothermal activity associated with mostly unidentified intrusions.

The age of the Central Plateau jasperoids is not well constrained. The available ages, based on stratigraphic correlation of replaced rocks and the age of the associated intrusives, are not consistent, varying from <30 Ma to >32.7 Ma (K/Ar) (Labarthe-Hernández *et al.*, 1992). Based on intimate spatial association to intrusive rocks of Tertiary age, Labarthe-Hernández *et al.* (1992) assumed the majority of jasperoids to be Oligocene. This age is consistent with the 30 to 35 Ma (K/Ar) range estimated for the La Colorada, Fresnillo and Sombrerete jasperoids (Albinson, 1988).

The Montaña de Manganeso jasperoids

Jasperoids from the MdM occur primarily as fault-controlled blocky bodies of variable size (Figure 3a, 3b), mostly confined to NE-trending faults within strongly folded and fractured volcaniclastic rocks (Trask and Rodríguez-Cabo, 1948; Wilson and Rocha, 1948; Alexandri, 1976). The epigenetic nature of the jasperoids is unambiguous, exhibiting a cross-cutting relationship with their host rocks. The jasperoids generally strike N 25° E with a dip of 70° to 80° NW (Wilson and Rocha, 1948). Occasionally they present transitional contacts that grade into partly silicified limestone, sandstone and shale. They are closely associated with manganese ores, and occasionally present mutual cutting relationships and gradational contacts.

In MdM red and black jasperoids usually occur spatially separated (Figure 3a, 3b). However, occasionally the hematitic (red) jasperoids gradually change into the manganiferous (black) jasperoids, which in turn transition into Mn ore with an associated increase in Mn content (Figure 4).

The differences in color reflect varying proportions of non-silica minerals, particularly the iron and manganese oxide content (Figure 3c, 3e, 3f). The red jasperoids are rich in iron oxides, mainly hematite, which imparts them a distinctive intense red tint (Figure 5a–5d). Minor yellowish brown (goethitic) and rare green (pyritiferous) varieties also occur among the Fe rich jasperoids (Figure 5e–5g). Some jasperoids are mineralogically heterogeneous, with cm to mm scale variations in color visible at outcrop and thin section scale (Figure 3d). Bleaching of

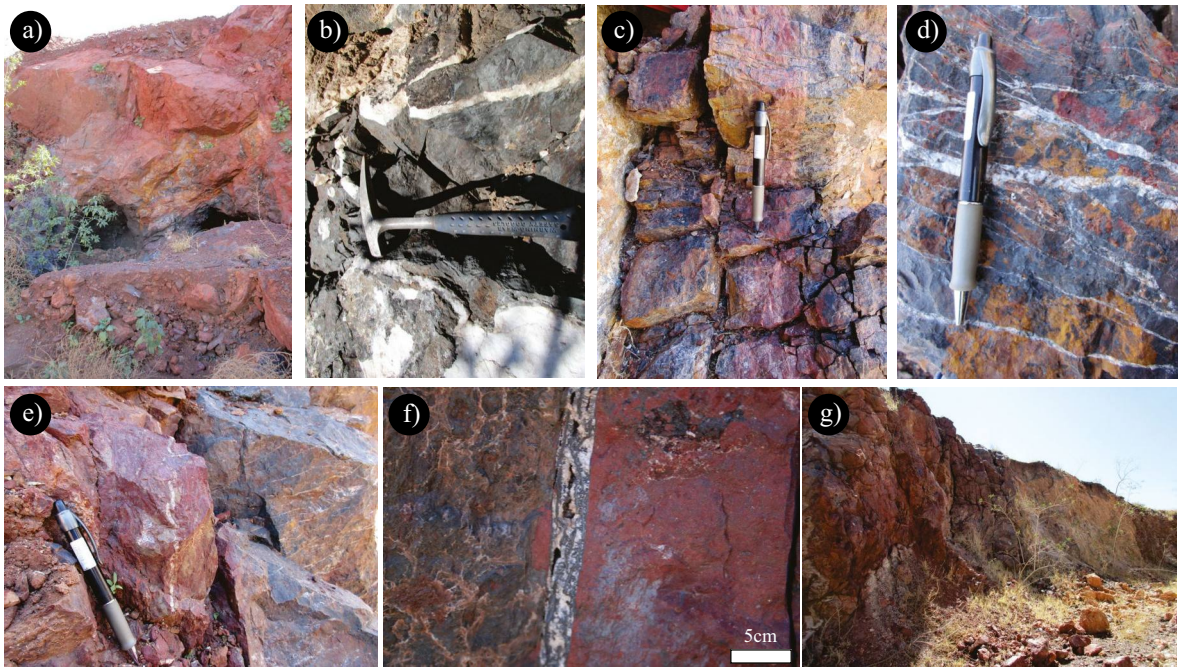

Figure 3. Representative outcrop photos of jasperoids from the Montaña de Manganeso: (a) Blocky hematitic jasperoids. (b) Manganiferous jasperoids with calcite veins. (c-f) Veined and mineralogically heterogeneous jasperoids, with mm to cm scale variations in color visible at outcrop scale; a complete separation of Mn and Fe in the jasperoids is commonly observed. (g) Exposed part of the feeder zone with silicified Fe-Mn oxides lining the fractures.

the hematitic jasperoids produced a characteristic pseudo-brecciated texture characterized by hematite-rich zones surrounded by a white microcrystalline matrix (Figure 5h). The manganiferous jasperoids are less heterogenous, exhibiting various shades of gray (Figure 5i–5l) depending on the Mn oxide concentrations.

The MdM jasperoids display a variety of macroscopic textures such as massive (Figures 3a,3b, 5e), brecciated (Figure 5a–5c) and laminated (Figure 6a, 6b). These textures are a result of multiple episodes of replacement, brecciation, and veining through episodic injection of silica by the hydrothermal system. Massive jasperoids are relatively common and have a dense aphanitic texture that reflects uniform distribution of either manganese oxides (Figure 7c) or hematite grains (Figure 7d, 7h) within the silica matrix. The laminated jasperoids consist of fine grained visually distinctive hematite-rich laminae variably modified or obliterated by veining and brecciation (Figures 6c-6f, 7a, 7b). Veining is manifested as a network of quartz veinlets that replace older generations of quartz and Fe-Mn oxides (Figure 8f, 8g). Brecciation is characteristic of samples from the feeder zone (Figure 3g).

The jasperoids also exhibit several ductile (Figure 6a, 6b) and brittle (Figure 6d, 6f) deformation structures. Diagenetic dehydration (Figure 6c, 6e) produced fractures expressed as a pseudobreccia texture in some jasperoids. These structures are easily identifiable in the red iron-rich jasperoids but are less visible in the black manganese-rich jasperoids because the darker color of the latter has obscured them (Figure 6i-6l).

RESULTS

Petrography

Quartz, the main component of the jasperoids at MdM, occurs mainly as anhedral crystals ranging in size from cryptocrystalline to microcrystalline and coarse crystalline (<2 mm) (Figure 8a–8c). A greater part of the quartz appears to have recrystallized from chalcedony (Figure 5k), as in most samples a transition from chalcedony to coarse quartz is observed (Figure 8d, 8e). Rare euhedral quartz grains (Figure 8h, 8i), probably representing quartz precipitated directly from the hydrothermal fluid, also occur. Late stage quartz appears as mostly anhedral coarse crystalline grains that fill fractures whose walls are lined by a thin layer of microcrystalline quartz (Figures 5j, 8f, 8g).

Manganese and iron oxides are ubiquitous in the jasperoids. They mostly occur as Fe-oxide rich and Mn-oxide rich bands (Figure 7a, 7b). The intense black, red or brown colored jasperoids suggestive of high Fe-Mn oxide contents can actually result from silica sparsely stained with disseminated and fine-grained manganese oxides (Figure 7c),

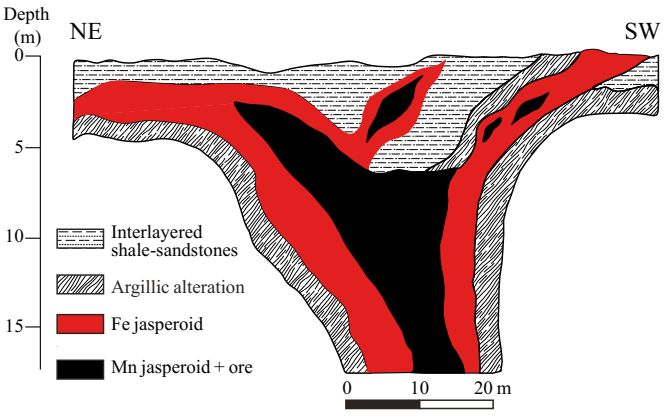

Figure 4. Schematic cross-section of an ore related jasperoid body at Montaña de Manganeso showing major alteration and mineralization features. The ore occur as massive black lenses of manganiferous jasperoid within hematitic jasperoids. The jasperoids have associated zones of argillic alteration that are suggestive of a hydrothermal origin.

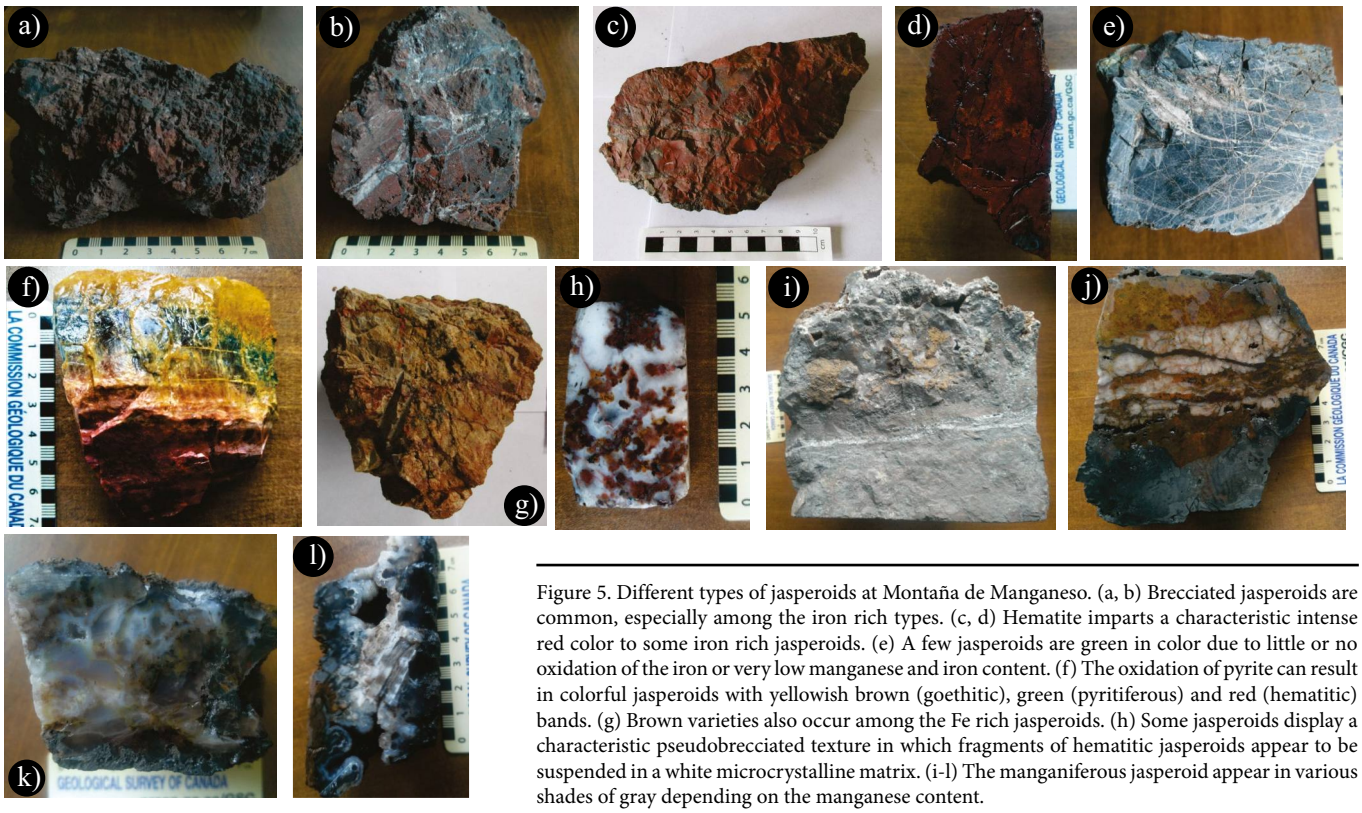

Figure 5. Different types of jasperoids at Montaña de Manganeso. (a, b) Brecciated jasperoids are common, especially among the iron rich types. (c, d) Hematite imparts a characteristic intense red color to some iron rich jasperoids. (e) A few jasperoids are green in color due to little or no oxidation of the iron or very low manganese and iron content. (f) The oxidation of pyrite can result in colorful jasperoids with yellowish brown (goethitic), green (pyritiferous) and red (hematitic) bands. (g) Brown varieties also occur among the Fe rich jasperoids. (h) Some jasperoids display a characteristic pseudobrecciated texture in which fragments of hematitic jasperoids appear to be suspended in a white microcrystalline matrix. (i-l) The manganiferous jasperoid appear in various shades of gray depending on the manganese content.

hematite (Figure 7d) and goethite (Figure 7e), respectively. Hematite also occurs as globular aggregates of smaller microspheroids (<1μm) (Figure 7f, 7g). In samples where hydrothermal replacement has been incomplete radiolarians locally accompany iron and manganese oxides (Figure 7h, 7i).

Mineralogy

Quartz and its polymorphs cristobalite and tridymite make up the major component of the jasperoids (71–98 %). Besides quartz, the samples contain barite, calcite, pyrite, goethite, hematite, magnetite, hollandite, pyrolusite, todorokite and birnessite in varying proportions (Table 1). Except for the abundance of manganese oxides, the mineralogy of the MdM jasperoids is similar to that of other jasperoids (*e.g.* Lovering, 1972; Wilson *et al.*, 1987; Nelson, 1990; Theodore and Jones, 1992; Yigit *et al.*, 2006).

Iron and Mn oxyhydroxide minerals make the major accessory minerals, a characteristic that has been used to group the samples into Fe-rich (mostly hematitic) and Mn-rich (manganiferous) jasperoids (Table 1). Although the proportions vary, the mineralogy of the hematitic jasperoids is quite simple, with most samples having 80–95 % quartz, 2–16 % hematite and minor amounts of goethite. Hematite and goethite are recognizable in hand specimens (Figure 5). The manganiferous jasperoids are more heterogeneous in terms of their accessory mineral contents. X-ray diffraction identified todorokite, pyrolusite, hollandite and birnessite. Finely disseminated pyrite coexists with hematite, goethite and magnetite in the manganiferous jasperoids.

Whole-rock geochemistry

Major elements

Jasperoids from the MdM deposit are composed predominantly of Si, Fe, Mn and volatile components (LOI) (Table 2). SiO_2 concentrations in the jasperoids vary from 65.53 to 91.96 wt.% in the non-ore jasperoid proper. The high values of SiO_2 reflect the abundance of quartz and its polymorphs tridymite, cristobalite and chalcedony, as the dominant minerals in the jasperoids.

The MnO(tot) varies from 0.08 to 12.44 wt.% in the jasperoids proper, and from 57.68 to 59.69 wt.% in the two ore samples analyzed here. High Mn concentrations are related to the occurrence of Mn oxides (birnessite, todorokite and hollandite; Table 1). Fe_2O_3(tot) content in the jasperoids varies from 1.31 to 32.09 wt.%, related with the presence of hematite and subordinate goethite, magnetite and pyrite. In the two ore samples Fe_2O_3(tot) concentrations are low, ranging from 1.31 to 2.77 wt.%. The Al/(Al+Fe+Mn) ratio for the MdM jasperoids varies from 0.01 to 0.05, with one anomalous value of 0.45. The ratios (Fe+Mn)/Ti and Fe/Mn vary widely, from 76 to 94803 and from 0.02 to 152.95, respectively.

The remaining major elements (Ti, Al, Mg, Ca, Na, K, and P) are less than 3 wt.%. CaO (<1.46 wt.%) concentrations can be accounted for by the presence of calcite and/or the Ca content in the lattice structure of some manganese oxides such as todorokite and birnessite. The low concentrations of K_2O (<0.64 wt.%) reflect the absence of cryptomelane in the studied samples and possibly also the leaching of K to form illite, which is widespread as hydrothermal alteration at MdM (Madondo *et al.*, 2020). Na_2O (<0.2 wt.%) concentrations are very low, reflecting the presence of minor amounts of Na bearing minerals like birnessite and/or smectites (Table 1; Madondo *et al.*, 2020).

Low TiO_2 (<0.035 wt.%) concentrations indicate limited lithogenic components whereas the moderate Al_2O_3 (<1.9 wt.%) concentrations may be reflecting presence of hydrothermal kaolinite that is abundant at MdM (Madondo *et al.*, 2020). The Al_2O_3 concentrations in the MdM jasperoids may also be representing the detrital aluminosilicate fraction from the replaced host rock, as reflected by the positive correlation between Al_2O_3 *vs.* TiO_2, MgO, CaO and K_2O (*r*: 0.66, 0.94, 0.81 and 0.72, respectively; Table 3) (Hein *et al.*, 2000).

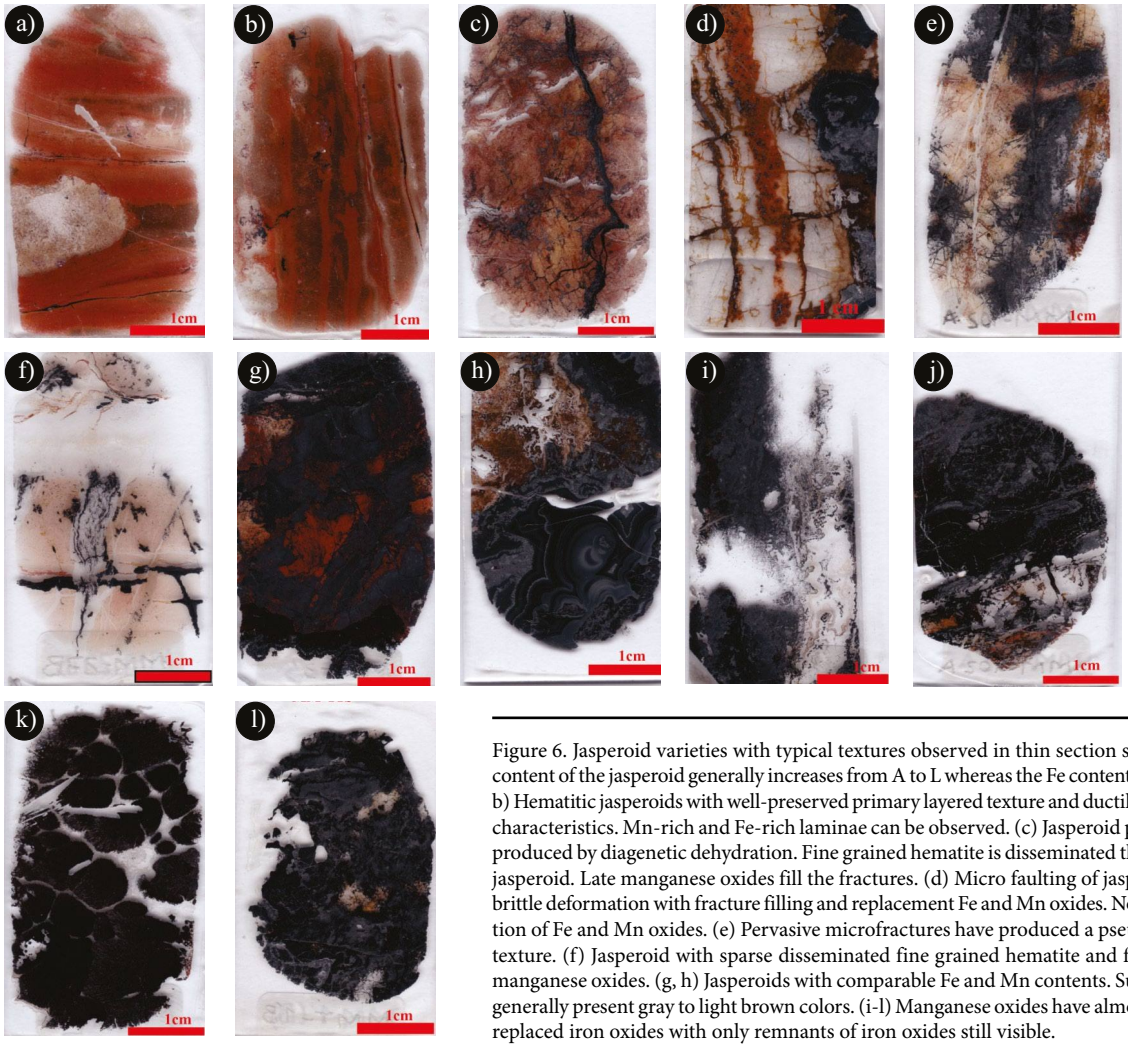

Figure 6. Jasperoid varieties with typical textures observed in thin section scans. The Mn content of the jasperoid generally increases from A to L whereas the Fe content decreases. (a, b) Hematitic jasperoids with well-preserved primary layered texture and ductile deformation characteristics. Mn-rich and Fe-rich laminae can be observed. (c) Jasperoid pseudobreccia produced by diagenetic dehydration. Fine grained hematite is disseminated throughout the jasperoid. Late manganese oxides fill the fractures. (d) Micro faulting of jasperoids due to brittle deformation with fracture filling and replacement Fe and Mn oxides. Note the separation of Fe and Mn oxides. (e) Pervasive microfractures have produced a pseudobrecciated texture. (f) Jasperoid with sparse disseminated fine grained hematite and fracture filling manganese oxides. (g, h) Jasperoids with comparable Fe and Mn contents. Such jasperoids generally present gray to light brown colors. (i-l) Manganese oxides have almost completely replaced iron oxides with only remnants of iron oxides still visible.

The Loss on Ignition (LOI) varies from 0.55 to 13.45 % (Table 2); representing mostly the water content of the jasperoids. However, this water is associated with the content of the Mn oxides in the jasperoids and not with chalcedony, as might be expected. Manganese oxides, particularly birnessite and todorokite frequently contain water in their crystal lattice (*e.g.* Post, 1999). A near perfect positive correlation exists between MnO and LOI (r = 0.98; Table 3). On the contrary, a marked negative correlation occurs between SiO_2 and LOI (r = -0.96; Table 3). A possible cause for the negative correlation could be the fact that SiO_2 mainly exists as quartz rather than the often water-bearing chalcedony. Furthermore, MnO and SiO_2 show a high negative correlation (r = -0.98), which reflects their co-occurrence as the dominant constituents of the jasperoids. K_2O show negative correlations with SiO_2 and Fe_2O_3(tot) (r: -0.40 and -0.70, respectively). These correlations probably reflect the jasperoid replacement of K feldspar in the host rocks. Fe_2O_3(tot) shows a weak negative correlation CaO (r = -0.48) with, reflecting the replacement of carbonate during jasperoid formation. Mn and Fe_2O_3(tot) are negatively correlated (r = -0.52) reflecting the geochemical fractionation of Fe and Mn in the hydrothermal precipitates.

The weak positive correlation between SiO_2 and Fe_2O_3 contrasts with the strong negative correlation between SiO_2 and MnO. The weak correlation between SiO_2 and Fe_2O_3 is due to the co-precipitation of Si and Fe during jasperoid formation. This correlation can also due to the weak adsorption of SiO_2 on iron oxides (Anderson and Benjamin, 1985; Taylor, 1995; Pokrovski *et al.*, 2003).

Trace elements

Trace element contents of MdM jasperoids are highly variable (Table 4). In comparison to the upper continental crust, samples exhibit a general enrichment in elements such as Ba (<96620 ppm), Sr (<1999 ppm), As (103 ppm), Cr (<640 ppm), Mo (>100 ppm), Sb (<10.4 ppm), Ge (<26 ppm), Ni (<110 ppm), Zn (<140 ppm), and Cu (<200 ppm), and are depleted in elements such as Pb (<12 ppm), Sn (<1 ppm), Ta (<0.1 ppm), Th (<0.6 ppm) and Rb (<29 ppm) (Figure 9). Co (15 ppm), W (<4 ppm) and V (<128 ppm) have average values close to those of the upper continental crust.

Most trace elements (Ba, Ni, Co, Zn, Cu, Ga, U, Mo and As) in the MdM jasperoids are particularly enriched in the manganiferous jasperoids. In fact, the most trace element-rich samples (MM-105A; MM-101; MMT-1) are those with the highest Mn content (Table 2). Sample MM-108, the most hematite-rich sample (Table 1), is depleted in trace elements compared with the Mn-rich samples, which suggests a control of the trace elements content by Mn oxides. Among the trace metals, only Cr shows preference for the hematitic jasperoids. The enrichment of Cr in the hematitic jasperoids is consistent with the one reported in Fe-rich hydrothermal precipitates

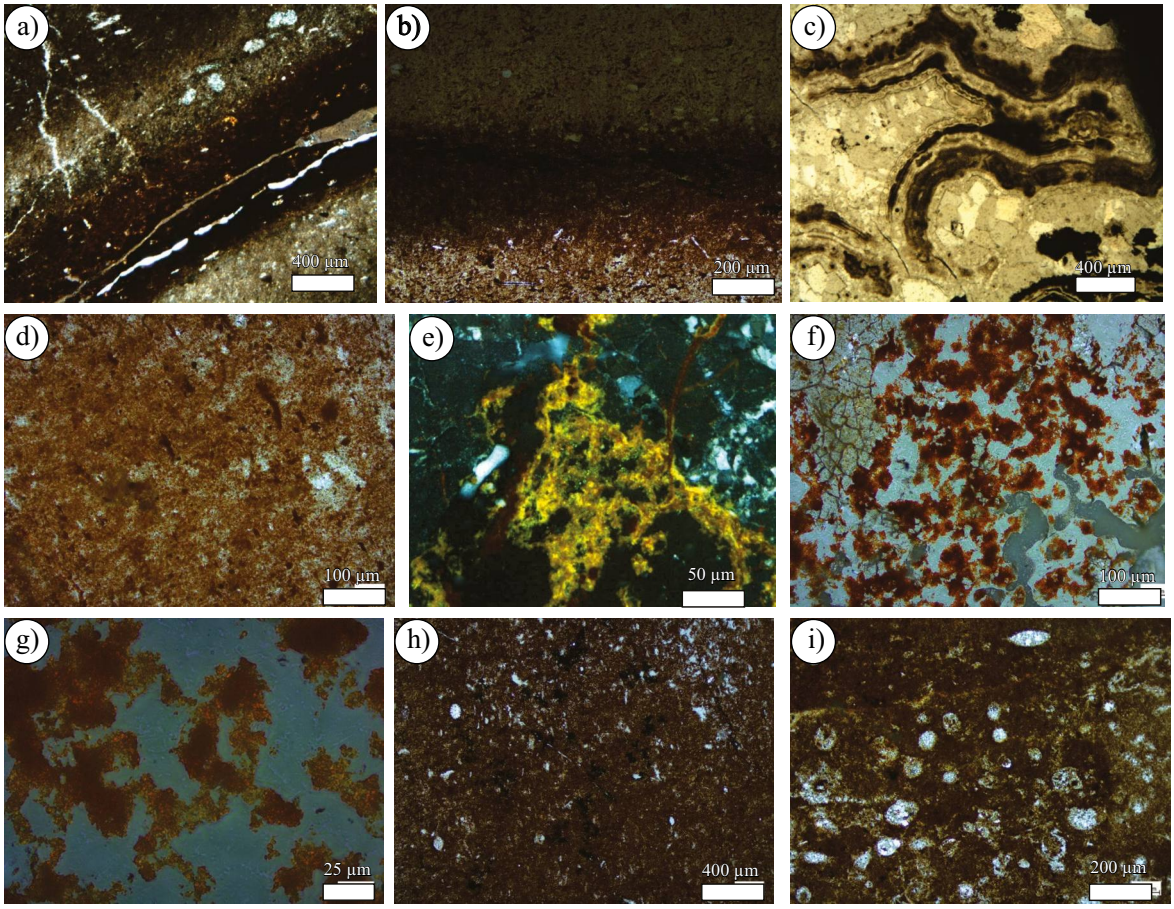

Figure 7. Photomicrographs showing the mineralogical and textural characteristics of jasperoids from the Montaña de Manganeso deposit. (a, b) Fe-rich and Fe-poor bands of a partially silicified limestone. The jasperoid still preserves some textures of the original host rock. (c) Colloform Mn oxides co-precipitated with chalcedony. (d) Disseminated and uniformly distributed fine-grained hematite. (e) Goethite and minor hematite in a quartz matrix. (f, g) Globular aggregates of hematite. (h) Deformed spherical recrystallized skeletons of radiolarians co existing with Fe-Mn oxides. (i) Close up of (h) showing radiolarians and other fossil remains.

(hydrothermal ironstones) of the Pacific seamounts (Hein *et al.*, 1997).

Elevated Ba and Sr concentrations of the MdM jasperoids reflect the occurrence of barite in veinlets. Barium is also a dominant tunnel cation in manganese oxide minerals such as hollandite (Miura *et al.*, 1987). High Ni and moderate Zn concentrations in samples MM 101 and MM 105A are consistent with enrichment of these elements in hydrothermal manganese rich deposits (Hein *et al.*, 1997). Zinc concentrations are similar to those reported in other jasperoids of the Central Plateau (Labarthe-Hernandez *et al.*, 1992). Low Pb and Cu concentrations indicate lack of sulfides in the deposit or significant sulfide precipitation at greater depths (*e.g.* Hein *et al.*, 2000).

Co and Ni show a good correlation with Zn (r = 0.91 and 0.64, respectively; Table 5), as has been reported for other Mn-rich deposits (Hein *et al.*, 2000). Similarly, Mo and V are correlated with Ba (r = 0.92 and 0.99, respectively; Table 5), which suggests that these metals probably occur in minerals that co-precipitated (*e.g.* McLemore *et al.*, 1999). The lack of correlation between Cu and Pb with Zn (r = 0.02 and 0.33, respectively; Table 5) is further evidence of absence of sulfides (chalcopyrite, galena, sphalerite) or at least lack of co-precipitation (*e.g.* Hein *et al.*, 2000).

REE geochemistry

Total REE (ΣREE) contents are low, ranging from 7.7 to 55.2 ppm, with an average of 26.9 ppm (Table 6). Samples are enriched in LREE compared with MREE (La_{CN}/Sm_{CN} ratio =2.47 to 6.47) and HREE (La_{CN}/Yb_{CN} = 1.71 to 10.33). MREE are just slightly enriched over HREE (Gd_{CN}/Yb_{CN} = 0.43 to 3.00); however, samples MM-108 and MM-13 show a marked enrichment in HREE. Ce anomalies are negative, ranging from 0.2 to 0.8, whereas Y anomalies (Y_{PASS}/Ho_{PAAS}) range from 0.37 to 1.47. Eu anomalies are variable, ranging from 0.6 to 1.7.

DISCUSSION

Silica-rich precipitates such as jaspers, bedded cherts, hydrothermal cherts and syngenetic cherts are often difficult to differentiate macroscopically (Baltuck, 1982). Most silica-rich precipitates, however, frequently contain non-silica phases whose mineralogy and geochemical signature can be used to determine the origin of the precipitates and thus differentiate them (Jones and Murchey, 1986; Murray, 1994). The mineralogy, chemical composition and element associations of the MdM jasperoids are therefore investigated to shed new light on their conditions of formation and origin.

Geochemical signatures

The major- and trace-elements chemistry of the MdM jasperoids is characterized by high Si, Fe and Mn contents and low trace element concentrations. The latter reflects the low compatibility of quartz

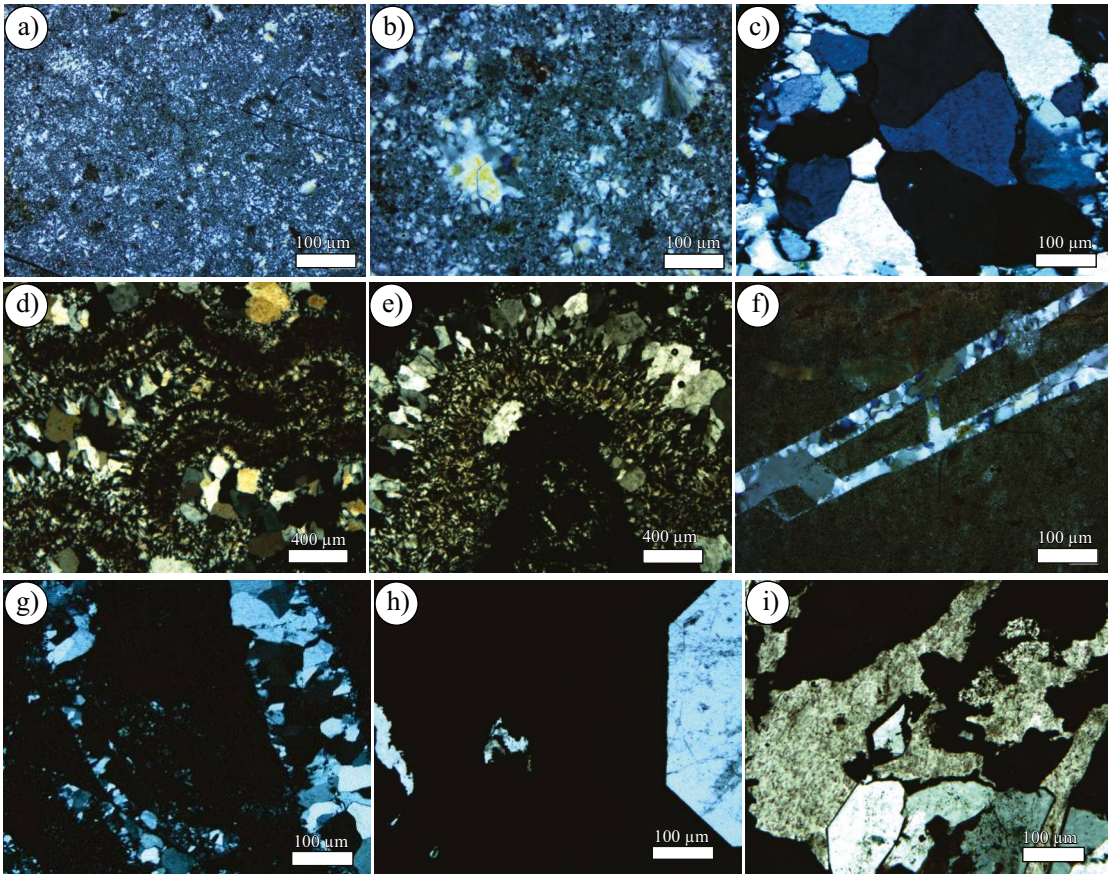

Figure 8. Photomicrographs showing the different quartz textures in the jasperoids of the Montaña de Manganeso deposit: (a) Cryptocrystalline quartz. (b) Microcrystalline quartz. (c) Coarse crystalline quartz. (d, e) Chalcedony transitioning to anhedral crystalline quartz, forming concentric colloform banding. (f, g) Quartz veins crosscut a jasperoid sample. The fractures are filled by a thin layer of first generation of microcrystalline quartz followed by coarse crystalline quartz. (h) Rare euhedral quartz grains. (i) Coarse crystalline quartz, consisting of crystals with planar and curved contacts. The dark dots are pores within the quartz crystals. Fe-Mn oxides particles replace different generations of quartz and fill spaces between quartz grain boundaries.

to incorporation of impurities (Heaney, 1994; Renault *et al.*, 1995; McLemore *et al.*, 1999). Unlike jasperoids from the southwest USA that are commonly associated with Carlin-type deposits (Nelson, 1990; Theodore and Jones, 1992; Arehart, 1996), the analyzed jasperoids from the MdM have high concentrations of manganese oxides and a depleted base metal content. Nonetheless, they have lower overall abundances of Sb, As, and Au than the Carlin type deposits (Theodore and Jones, 1992; Arehart, 1996; Stenger *et al.*, 1998). Due to their enrichment in As, Sb, Zn, Mo, Ni, and Cr, the jasperoids from the MdM have a geochemical signature more similar to that of submarine hydrothermal manganese deposits (Hein *et al.*, 1997, 2000).

A striking geochemical characteristic of the MdM jasperoids is the

Table 1. Results of powder X-ray diffraction (XRD) analysis showing major mineralogical compositions and their abundance (weight percent, semiquantitative).

	Manganese ore		Black jasperoids				Red jasperoids				
Mineral	MM 105A	MM 103	MM 25C	MM T2	MM 106A	MM 101	MM 13	MM 202	MM 203	MM 108	MM 23
Hematite			9		2	2	5	6	2	16	2
Magnetite		15									
Goethite	11		3								
Quartz		21	71	98	78	71	92	77	94	84	90
Cristobalite						5					
Tridymite						12					
Pyrite		25						17	4		
Barite					5		3				
Hollandite		39			11						
Pyrolusite	78		17		4	10					
Todorokite				2							
Birnessite	11										

Table 2. Summary of major element concentrations. For the chemical ratios calculations, atomic contents were recalculated from element concentrations (wt%).

	SiO_2	Al_2O_3	$Fe_2O_3^T$	MnO	MgO	CaO	Na_2O	K_2O	TiO_2	P_2O_5	LOI	Total	Fe/Mn	(Fe+Mn)/ Ti	Al/ (Al+Mn+Fe)	Si/Al
MM-106A	75.92	0.50	7.72	12.44	0.08	0.1	< 0.01	0.04	0.002	0.03	3.07	99.84	0.56	12539.26	0.02	134.12
MM-101	4.12	1.69	2.77	59.69	0.33	0.56	0.11	0.40	0.025	0.18	13.45	83.33	0.04	3213.81	0.02	2.15
MM-13	84.32	0.24	13.21	0.08	0.02	0.03	< 0.01	0.02	0.012	0.02	0.55	98.42	152.95	1292.79	0.01	310.32
MM-202	71.86	0.24	15.64	7.26	0.07	0.24	0.03	0.05	0.001	0.10	2.08	97.57	1.95	27628.42	0.01	264.47
MM-203	83.98	0.82	9.22	3.53	0.10	0.18	0.10	0.08	0.035	0.15	1.73	99.92	2.36	437.69	0.05	90.46
MM-108	65.53	0.45	32.09	1.44	0.03	0.17	< 0.01	0.02	0.020	0.14	0.75	100.6	20.13	1965.06	0.01	128.62
MM-23	91.96	1.90	1.57	0.17	0.51	1.46	0.05	0.64	0.027	0.01	2.21	100.50	8.39	75.93	0.45	42.75
MM-105A	1.52	0.40	1.31	72.20	0.04	0.34	0.15	0.36	0.001	0.27	12.35	88.93	0.02	94803.55	0.00	3.36
MMT-I	10.07	0.47	4.30	57.68	0.16	0.50	0.20	0.42	0.002	0.18	12.05	86.04	0.07	39766.88	0.01	18.92

preferential enrichment of most trace elements (Ba, Ni, Co, Zn, Cu, Ga, U, Mo and As) in the manganiferous jasperoids. At near neutral pH Mn oxides have a stronger adsorption capacity for cations than Fe oxides, as cationic species are attracted to the negatively charged surface of Mn oxides (McKenzie, 1980; Hein *et al.*, 1997; Suda and Makino, 2016). This implies that the cationic signature of the MdM jasperoids is strongly dependent on the concentration of Mn oxides in these jasperoids. Iron oxides, on the other hand, will preferentially adsorb neutral and negatively charged species, due to the slightly positive charge of the hydrated Fe oxide surfaces (Koschinsky and Halbach, 1995; Hein *et al.*, 1997, 2005). Trace elements that commonly form anions or oxyanions such as Cr, As, V and P therefore generally characterize Fe-rich hydrothermal precipitates (ironstones) (Hein *et al.*, 1997).

Adsorption of oppositely charged species by Fe-Mn oxyhydroxides alone cannot account for the preferential enrichment in the manganiferous jasperoids of MdM of some trace elements such as Mo and As. These elements commonly form negatively charged species such as the molybdate and arsenate (or arsenite) oxyanions, respectively and as such are expected to be enriched in the hematitic jasperoids. The depletion of trace elements in the hematitic jasperoids can additionally be explained by adsorption of silica on the surfaces of the Fe oxyhydroxides, decreasing significantly the number of available sorption sites, and thus reducing the incorporation of other anions and cations (Anderson and Benjamin, 1985; Taylor, 1995; Pokrovski *et al.*, 2003). Further, depletion of trace elements in the hematitic jasperoids might be an indication that Fe was initially precipitated mainly as pyrite (Lovering, 1972). As Mn oxides have higher adsorption capacity of trace elements than pyrite, the hematite rich samples do not present the same trace element enrichment equal to that of manganese oxides rich samples. For As in particular, the preferential enrichment in the manganiferous jasperoids, despite higher affinity of As for iron oxides (Manning *et al.*, 2002; Ouvrard *et al.*, 2005; Ying *et al.*, 2012; Zhang *et al.*, 2014; Bai *et al.*, 2016), can be explained by inhibition of As adsorption on hematite by carbonate species during replacement of the host rocks (*e.g.* Brechbühl *et al.*, 2012).

Source of silica and Fe-Mn oxides

Determination of the sources or origin of SiO_2, Fe and Mn is fundamental to understanding the genesis of the MdM jasperoids. Major potential sources of silica include biogenic, diagenetic, detrital and hydrothermal (Sugisaki *et al.*, 1982; Adachi *et al.*, 1986; Yamamoto, 1986), whereas for manganese and iron oxides they can be hydrothermal, hydrogenetic and diagenetic in origin (Roy, 1981, 1997). At MdM, field, petrographic and geochemical evidence indicate that hot hydrothermal solutions ascending from depths along faults and fractures supplied at least part of the silica and Fe-Mn for jasperoid formation.

Steep dipping faults and fractures lined with silicified Fe and Mn oxides characterize the MdM (Figure 3g). The rocks around the faults and fractures present different degrees of silicification. Those nearest to the fractures are completely silicified and those furthest are only partially silicified and still preserve textures of the original host rock (Figure 7a). Some of the jasperoids have associated zones of argillic alteration and stockwork that can be interpreted as feeder channel ways for upwelling hydrothermal fluids. These structural and alteration features suggest flow of ascending Fe-Mn bearing, silica-rich hydrothermal fluids through the host rock.

The MdM jasperoids also exhibit textural features indicating their formation from hot hydrothermal solutions. Textural evidence such as dehydration cracks and growth patterns suggest crystallization from amorphous silica (Figures 7, 8), with poorly crystalline cristobalite and tridymite as intermediate phases (McKay and Finlow-Bates, 1977; Fournier, 1985; Heaney, 1994). Silica appears to have crystallized episodically within open spaces initially, with replacement and silicification of host rocks becoming more pervasive in the later stages. Episodic deposition of silica and Fe-Mn oxides led to the formation of highly brecciated jasperoids. Although some jasperoids are roughly laminated and locally contain radiolarians, a biogenic origin of the jasperoids is unlikely. The lamination probably resulted from deposition as gel and variations in the physico-chemical conditions of the hydrothermal fluid during precipitation (Chi Fru *et al.*, 2018).

The geochemical signature of the jasperoids also suggest that silicification was the result of hydrothermal activity. They display enrichment in the concentrations of the typically hydrothermal elements such as Ba, Sr, As, Cr, Mo, Sb, Ni, Zn, and Cu, and are strongly depleted in the elements indicative of clastic input such as Ti, K, Th and

Table 3. Correlation coefficient (r) matrix of various major elements of the Montaña de Manganeso jasperoids.

	SiO_2	Al_2O_3	Fe_2O_3(tot)	MnO	MgO	CaO	K_2O	TiO_2	P_2O_5
SiO_2	1.00								
Al_2O_3	-0.02	1.00							
Fe_2O_3(tot)	0.38	-0.46	1.00						
MnO	-0.98	0.06	-0.55	1.00					
MgO	0.00	0.94	-0.52	0.05	1.00				
CaO	0.01	0.81	-0.48	0.05	0.93	1.00			
K_2O	-0.41	0.72	-0.70	0.49	0.83	0.89	1.00		
TiO_2	0.33	0.66	0.05	-0.35	0.48	0.34	0.16	1.00	
P_2O_5	-0.83	-0.14	-0.14	0.79	-0.24	-0.18	0.18	-0.12	1.00

Table 4. Trace element composition of the jasperoids from the Montaña de Manganeso deposit.

	Sc	V	Ba	Sr	Y	Zr	Cr	Co	Ni	Cu	Zn	Tl	Ge	As	Rb	Nb	Mo	Ag	Sn	Sb	Cs	Hf	W	Pb	Th	U
	ppm																									
MM-106A	< 1	22	4017	70	4	3	280	3	20	200	30	<0.1	5	29	< 2	< 1	13	< 0.5	< 1	0.8	< 0.5	< 0.2	< 1	< 5	< 0.1	0.6
MM-101	2	126	96620	1768	15	12	< 20	15	110	60	140	0.1	26	81	2	< 1	95	< 0.5	< 1	9	< 0.5	0.3	2	< 5	0.3	6.2
MM-13	< 1	40	17310	180	< 1	5	640	1	< 20	< 10	< 30	<0.1	6	8	< 2	< 1	24	< 0.5	< 1	2.4	< 0.5	< 0.2	1	< 5	0.2	0.2
MM-202	< 1	58	7246	145	3	< 2	330	3	50	40	90	<0.1	6	74	< 2	< 1	13	< 0.5	< 1	4	< 0.5	< 0.2	3	5	< 0.1	1
MM-203	1	54	3741	105	9	12	330	3	30	20	40	<0.1	5	28	2	< 1	6	< 0.5	< 1	1.7	0.9	0.2	< 1	< 5	0.3	0.4
MM-108	< 1	128	2079	59	4	7	340	2	< 20	< 10	< 30	<0.1	6	20	< 2	< 1	27	< 0.5	< 1	5	< 0.5	< 0.2	4	5	0.1	0.4
MM-23	1	12	554	63	4	16	480	2	< 20	40	< 30	<0.1	1	< 5	29	< 1	4	< 0.5	< 1	< 0.5	1.1	0.3	< 1	11	0.6	0.2
MM-105A	2	102	43710	1999	14	4	< 20	11	70	50	140	0.1	7	103	< 2	< 1	> 100	< 0.5	< 1	10.4	< 0.5	< 0.2	2	12	< 0.1	3.9
MMT-I	< 1	102	24480	1519	19	3	< 20	8	80	80	120	<0.1	7	78	2	< 1	39	< 0.5	1	2.1	< 0.5	< 0.2	< 1	5	< 0.1	5.2

Zr (Brusnitsyn and Zhukov, 2012, 2018) (Figure 9). The abundance of Fe-Mn oxides and the depletion of Al and Ti oxides suggest a role for hydrothermal activity (Adachi *et al.*, 1986; Yongzhang *et al.*, 1994; Jun *et al.*, 2010).

The Fe/Mn ratios for the MdM jasperoids vary widely from 0.02 to 152.95, typical of hydrothermal precipitates which vary from about 24000 for hydrothermal seamount ironstones to about 0.001 for hydrothermal stratabound manganese oxides from active volcanic arcs (Hein *et al.*, 1997). In contrast, hydrogenetic precipitates vary within a restricted range close to unity: from 0.7 for open-ocean seamount crusts to 1.2 for continental margin seamount crusts (Hein *et al.*, 1997). The (Fe+Mn)/Ti ratio (<94803) is also remarkably high, indicating a hydrothermal formation for the jasperoids (Boström *et al.*, 1973; Cronan, 1980; Brusnitsyn and Zhukov, 2012, 2018). These values can be contrasted with metalliferous sediments deposited distal to hydrothermal vents and composed of mostly clastic and biogenic material with (Fe+Mn)/Ti ratio between 68 to 770 (Brusnitsyn and Zhukov, 2012). The extremely high values of the (Fe+Mn)/Ti ratio for the MdM samples partly reflect transition of some manganiferous jasperoids to Mn ore. The low Al/(Al+Fe+Mn) ratio for the MdM jasperoids (0.01–0.05 with one anomalous value of 0.45) likewise suggests predominant hydrothermal source. The Al/(Al+Fe+Mn) ratio of siliceous rocks ranges from as low as 0.01 for pure hydrothermal precipitates to as high as 0.60 for pure pelagic biological precipitates (Adachi *et al.*, 1986; Yamamoto, 1986).

The element ratios discussed so far are commonly coupled with discrimination diagrams to differentiate between hydrothermal, hydrogenous and diagenetic silica rich deposits (Adachi *et al.*, 1986; Yamamoto, 1986; Yongzhang *et al.*, 1994). For the Fe-Mn rich type additional discrimination diagrams have also been proposed (Bonatti *et al.*, 1972; Toth, 1980; Choi and Hariya, 1992; Nicholson, 1992; Conly *et al.*, 2011; Bau *et al.*, 2014). These diagrams are adapted here to determine the sources of silica and Fe-Mn oxides for the MdM jasperoids (Figure 10). Uranium and Th concentrations of the MdM jasperoids are comparable to those of cherts of hydrothermal origin (Crerar *et al.*, 1982; Hein *et al.*, 1987; Flohr and Huebner, 1992), and effectively plot within or close to the hydrothermal field of Bonatti *et al.* (1976) on the U-Th binary diagram (Figure 10a). On the Fe-Mn-Al, Ni-Co-Zn and Fe-Mn-(Co+Ni+Cu) ternary diagrams all samples also fall within the hydrothermal field (Figure 10b-10d).

The chondrite-normalized REE patterns (REE_{CN}) (Figure 11) of the jasperoid samples are characterized by a general decrease in normalized concentrations from LREE to HREE and have well-defined negative Ce anomalies typical of hydrothermal Fe-Mn oxide deposits precipitated under oxidizing conditions (Crerar *et al.*, 1982; Wright *et al.*, 1987; Öztürk and Hein, 1997; Usui and Someya, 1997; Sinisi *et al.*, 2012; Öksüz

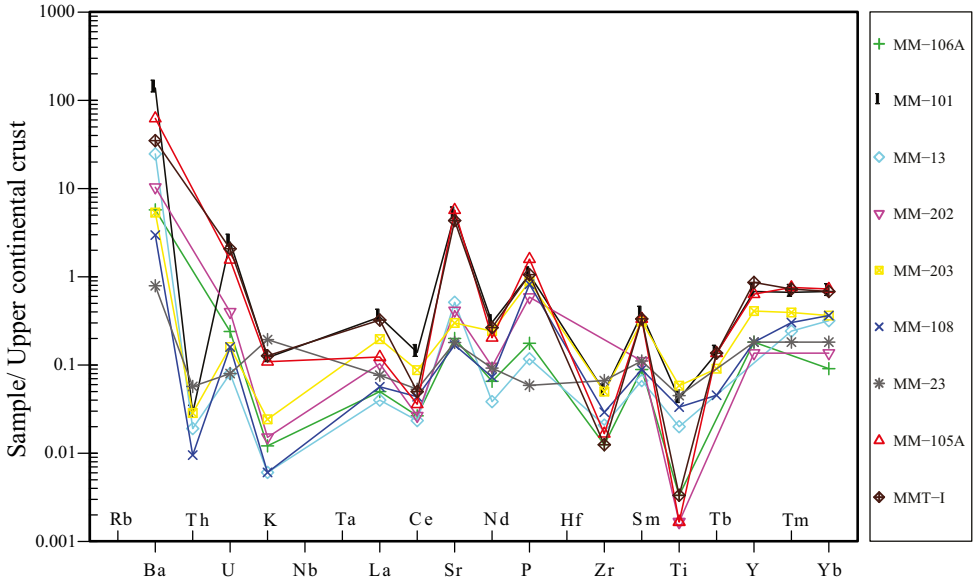

Figure 9. The Upper Continental Crust (Taylor and McLennan, 1985) normalized elemental distribution pattern of the Montaña de Manganeso jasperoids.

Table 5. Correlation coefficient (*r*) matrix of various trace elements of the Montaña de Manganeso jasperoids.

	V	Ba	Sr	Zr	Cr	Co	Ni	Cu	Zn	As	Mo	Pb	Th	U
V	1.00													
Ba	0.99	1.00												
Sr	0.31	0.34	1.00											
Zr	0.38	0.31	-0.07	1.00										
Cr	0.67	0.68	0.74	0.22	1.00									
Co	0.06	0.08	0.93	-0.13	0.68	1.00								
Ni	0.58	0.62	0.57	0.02	0.47	0.40	1.00							
Cu	-0.42	-0.37	0.05	-0.44	-0.41	0.11	-0.08	1.00						
Zn	0.25	0.27	0.93	0.10	0.71	0.91	0.64	0.02	1.00					
As	0.23	0.25	0.84	0.17	0.56	0.81	0.70	0.11	0.96	1.00				
Mo	0.92	0.92	0.51	0.17	0.68	0.25	0.56	-0.26	0.33	0.28	1.00			
Pb	0.57	0.52	0.44	0.55	0.45	0.29	0.27	-0.09	0.33	0.33	0.67	1.00		
Th	0.46	0.45	-0.18	0.49	0.03	-0.35	-0.08	0.20	-0.18	-0.11	0.35	0.41	1.00	
U	0.85	0.87	0.36	0.19	0.56	0.12	0.80	-0.44	0.36	0.40	0.77	0.27	0.13	1.00

and Okuyucu, 2014; Maghfouri *et al.*, 2017). Positive Ce anomalies in Fe-Mn deposits are regarded as typical of hydrogenetic precipitation (Choi and Hariya, 1992; Canet *et al.*, 2008; Josso *et al.*, 2017).

Yttrium anomalies (Y_{PASS}/Ho_{PASS}) of the MdM jasperoid samples are mostly positive, with the exception of two samples (Table 6). Positive Y anomalies (Y_{PASS}/Ho_{PASS} >1) are typical of hydrothermal Fe-Mn deposits whereas hydrogenetic and diagenetic Mn deposits form negative anomalies (Y_{PASS}/Ho_{PASS} <1) (Bau *et al.*, 2014).

Genesis of the Montaña de Manganeso jasperoids

The great amounts of quartz, cristobalite and tridymite which form the MdM jasperoids suggest that cooling of ascending hot hydrothermal fluids was the primary mechanism for the formation of the jasperoids (Fournier, 1985; Heaney, 1994; Hedenquist *et al.*, 2000). In the near surface environment, cooling of silica-rich hydrothermal fluids is known to precipitate amorphous silica which then transitions to quartz through intermediate, metastable polymorphs such as opal-CT, cristobalite and tridymite (Fournier, 1985; Canet *et al.*, 2005).

It is known that the replacement of limestone by silica, generally necessary for jasperoid formation (Lovering, 1972), can be achieved during cooling of a solution with a circumneutral pH in the near surface environment (Fournier, 1985). The retrograde solubility of calcite and the prograde solubility of quartz below 300 °C enables the replacement. Boiling is not an ideal mechanism for jasperoid formation, as it is more likely to lead to deposition of calcite, which is counterproductive to the replacement of calcite by silica (Lovering, 1972; Theodore and Jones, 1992). However, as calcite is abundant at MdM and the host rocks are predominantly sandstones and shale with only remnant carbonate rocks present, it is possible that boiling played a role in jasperoid formation.

Field and petrological observations suggest that iron mineralization preceded manganese mineralization. The replacement of iron oxides by manganese oxides observable throughout the deposit suggests an early deposition of Fe minerals and the inflow of a later Mn rich fluid. Manganese oxide bearing veins frequently cut the hematitic jasperoids, but the reverse is not common. The hematitic jasperoids originally deposited under reducing conditions and the manganiferous jasperoids were deposited later, under oxidizing conditions. The occurrence of pyrite, a common early mineral in jasperoids (Lovering, 1972), suggests that the oxidized iron minerals (hematite, goethite and magnetite) resulted from oxidation of pyrite (Schwertmann and Murad, 1983; Chi Fru *et al.*, 2018). The existence of only manganese oxides with no Mn^{2+} bearing minerals indicates formation at a later stage, under oxidizing conditions.

A cooling intrusive at depth possibly served as the driving force for deep circulating hydrothermal fluids that deposited silica and Fe-Mn oxides. Labarthe-Hernández *et al.* (1992) considered the felsic El Socorro intrusive, exposed about 55 km to the SW of the MdM, as the cause of the formation of the main known jasperoids of the region. The Cenozoic volcanism linked in certain parts of the Central Plateau to the volcanism of the Sierra Madre Occidental (Aranda-Gómez and Mcdowell, 1998; Aranda-Gómez *et al.*, 2007; Tristán-González *et al.*, 2008, 2009a; Aguillón-Robles *et al.*, 2009; Rodríguez-Ríos *et al.*, 2013) could have supplied the vast amounts of silica required for the formation of the jasperoid of the Central Plateau, including those of the MdM.

Table 6. Rare Eearth elements plus Ytrium (REY) compositions of the Montaña de Manganeso jasperoids. Eu, Ce and Y anomalies are also shown in Table 6.

	La	Ce	Pr	Nd	Sm	Eu	Gd	Tb	Dy	Ho	Er	Tm	Yb	Lu	Y	Y_{PASS}/Ho_{PAAS}	ΣREE	Eu/Eu*	Ce/Ce*
MM-106A	1.5	1.7	0.37	1.7	0.4	0.16	0.6	0.1	0.5	0.1	0.3	0.05	0.2	0.03	4	1.47	11.7	1.0	0.5
MM-101	10.5	8.9	1.72	7.9	1.7	1.11	2.4	0.3	1.9	0.4	1.4	0.22	1.5	0.22	15	1.38	55.2	1.7	0.5
MM-13	1.2	1.5	0.25	1.0	0.3	0.21	0.3	0.1	0.4	0.1	0.4	0.08	0.7	0.12	1	0.37	7.7	2.1	0.7
MM-202	3.1	1.7	0.65	2.5	0.5	0.21	0.5	0.1	0.5	0.1	0.3	0.05	0.3	0.05	3	1.10	13.6	1.3	0.3
MM-203	5.9	5.6	1.45	6.3	1.4	0.38	1.5	0.2	1.4	0.3	0.8	0.13	0.8	0.14	9	1.10	35.3	0.8	0.5
MM-108	1.7	2.8	0.47	1.9	0.4	0.09	0.5	0.1	0.7	0.2	0.5	0.1	0.8	0.13	4	0.73	14.4	0.6	0.8
MM-23	2.3	3.4	0.61	2.4	0.5	0.09	0.5	0.1	0.6	0.1	0.4	0.06	0.4	0.06	4	1.47	15.5	0.6	0.7
MM-105A	3.7	2.3	1.09	5.3	1.5	0.7	2.1	0.3	2.3	0.5	1.5	0.25	1.6	0.28	14	1.03	37.4	1.2	0.3
MMT-I	9.7	3.2	1.49	6.9	1.5	0.62	2.1	0.3	2.2	0.5	1.6	0.24	1.5	0.25	19	1.39	51.1	1.1	0.2

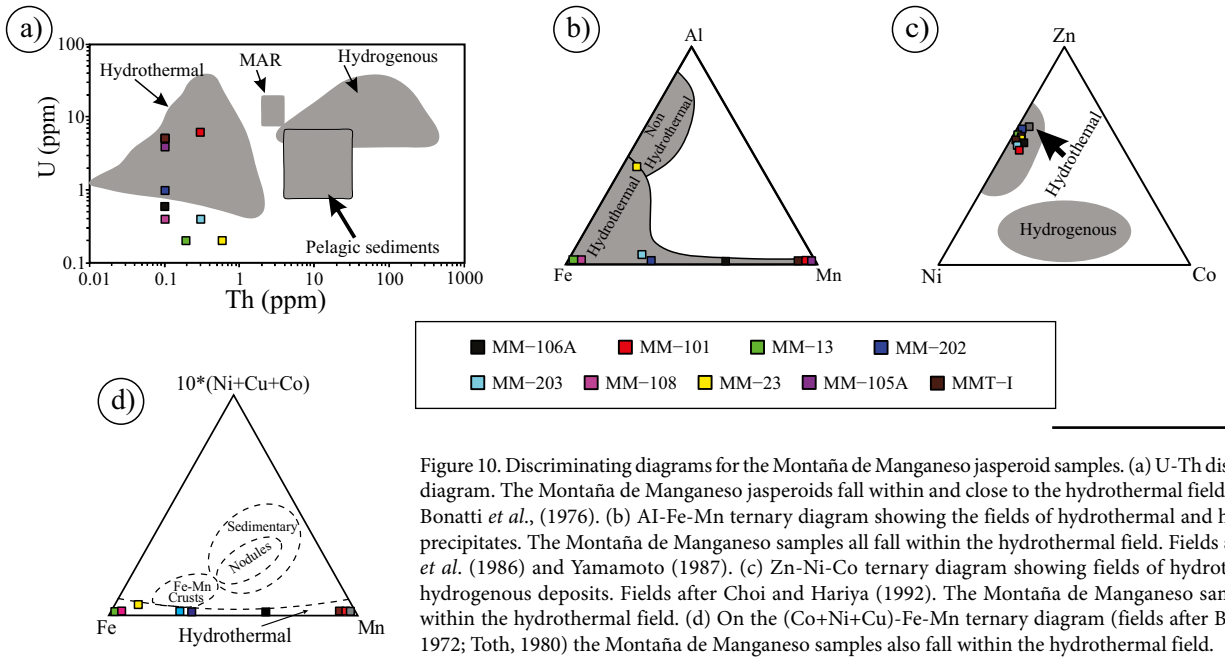

Figure 10. Discriminating diagrams for the Montaña de Manganeso jasperoid samples. (a) U-Th discrimination diagram. The Montaña de Manganeso jasperoids fall within and close to the hydrothermal field. Fields after Bonatti *et al.*, (1976). (b) AI-Fe-Mn ternary diagram showing the fields of hydrothermal and hydrogenous precipitates. The Montaña de Manganeso samples all fall within the hydrothermal field. Fields after Adachi *et al.* (1986) and Yamamoto (1987). (c) Zn-Ni-Co ternary diagram showing fields of hydrothermal and hydrogenous deposits. Fields after Choi and Hariya (1992). The Montaña de Manganeso samples all fall within the hydrothermal field. (d) On the (Co+Ni+Cu)-Fe-Mn ternary diagram (fields after Bonatti *et al.*, 1972; Toth, 1980) the Montaña de Manganeso samples also fall within the hydrothermal field.

CONCLUSIONS

The MdM jasperoids occur as primarily fault-controlled blocky and lenticular bodies of diverse sizes confined to NE-trending faults within strongly folded and fractured sedimentary and volcaniclastic rocks. There is field, petrographic and geochemical evidence that hot hydrothermal solutions ascending from depths along faults and fractures supplied silica and at least part of the manganese and iron oxides for jasperoid formation. The presence of a feeder fault system, well-manifested differentiation of Mn from Fe and Si, banded and brecciated jasperoids, with associated zones of argillic alteration strongly suggest formation by hydrothermal processes close to the paleosurface. Textural evidence indicates multiple episodes of replacement, brecciation, and veining by episodic injection of silica-rich hydrothermal fluids. The geochemical signature of the jasperoids also suggest that silicification was product of hydrothermal activity. Silica and Fe-Mn oxyhydroxides were likely precipitated from cooling ascending silica-rich hydrothermal fluids that evolved from reduced to oxidized. The hydrothermal fluids filled faults and fractures, and penetrated permeable horizons and replaced favorable units forming massive jasperoid bodies. The ascending hot hydrothermal solutions leached trace metals from the host rocks, part of which were scavenged by Fe and Mn oxides. An intrusive at depth probably served as a driving force for deep circulating hydrothermal fluids that deposited silica and Fe-Mn oxides.

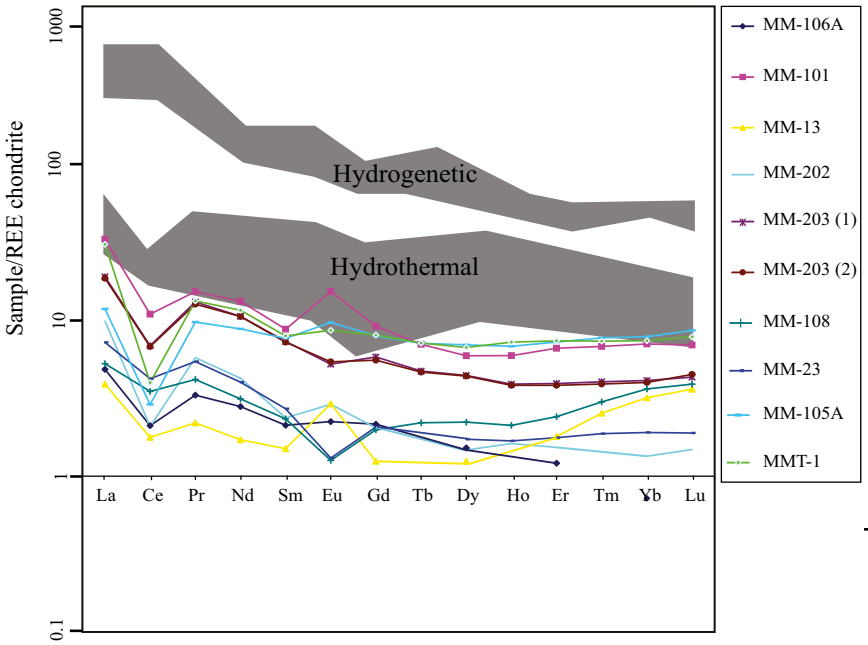

Figure 11. Chondrite normalized REE patterns displaying fields of hydrothermal and hydrogenetic deposits. The Montaña de Manganeso samples mostly fall below the hydrothermal field.

ACKNOWLEDGMENTS

This paper is part of J. M´s PhD thesis. J.M. acknowledges the support of CONACyT through a PhD scholarship. Funding for this work was provided by UNAM through research grant PAPIIT IG100116 to Eduardo González Partida. We would like to thank Teresa Pi Puig for the X ray diffraction analysis. Augusto Rodríguez Díaz is greatly thanked for help during fieldwork and for discussions on jasperoid formation. This manuscript was greatly improved thanks to the review by Jose Rafael Barboza-Gudiño and another anonymous reviewer. We also extend our appreciation to Dr. Ángel Nieto-Samaniego and Dr. Luca Ferrari for the editorial handling of this manuscript.

REFERENCES

Adachi, M., Yamamoto, K., Sugisaki, R., 1986, Hydrothermal chert and associated siliceous rocks from the northern Pacific. Their geological significance as indication of ocean ridge activity: Sedimentary Geology, 47, 125-148, https://doi.org/10.1016/0037-0738(86)90075-8

Aguillón-Robles, A., Tristán-González, M., Aguirre-Díaz, G.J., Bellon, H., 2009, Syn-extensional intra-plate trachydacite-rhyolitic dome volcanism of the Mesa Central, southern Sierra Madre Occidental volcanic province, Mexico: Journal of Volcanology and Geothermal Research 187, 33-52, https://doi.org/10.1016/j.jvolgeores.2009.08.021

Aguillón-Robles, A., Tristán-González, M., López-Doncel, R.A., García-Arreola, M.E., Almaguer-Rodríguez, J. de L., Maury, R.C., 2012, Trace elements geochemistry and origin of volcanic units from the San Luis Potosí and Río Santa María volcanic fields, Mexico: The bearing of ICP-QMS data: Geofísica Internacional, 51, 293-308.

Aguillón-Robles, A., Tristán-González, M., De Jesús Aguirre-Díaz, G., López-Doncel, R.A., Bellon, H., Martínez-Esparza, G., 2014, Eocene to Quaternary mafic-intermediate volcanism in San Luis Potosí, central Mexico: The transition from Farallon plate subduction to intra-plate continental magmatism: Journal of Volcanology and Geothermal Research, 276, 152-172, https://doi.org/10.1016/j.jvolgeores.2014.02.019

Aguirre-Díaz, G.J., Labarthe-Hernández, G., 2003, Fissure ignimbrites: Fissure-source origin for voluminous ignimbrites of the Sierra Madre Occidental and its relationship with Basin and Range faulting: Geology, 31, 773, https://doi.org/10.1130/G19665.1

Aguirre-Díaz, G.J., Labarthe-Hernández, G., Tristán-González, M., Nieto-Obregón, J., Gutiérrez-Palomares, I., 2008, The Ignimbrite Flare-Up and Graben Calderas of the Sierra Madre Occidental, Mexico, in: Developments in Volcanology: Elsevier, 143-180, https://doi.org/10.1016/S1871-644X(07)00004-6

Albinson F., T., 1988, Geologic reconstruction of paleosurfaces in the Sombrerete, Colorado, and Fresnillo districts, Zacatecas State, Mexico: Economic Geology, 83, 1647-1667, https://doi.org/10.2113/gsecongeo.83.8.1647

Alexandri, R.R., 1976, Estudio Geológico del Yacimiento Montaña de Manganeso: San Luis Potosí, Universidad Autónoma de San Luis Potosí, Bsc Thesis, 94 pp.

Anderson, P.R., Benjamin, M.M., 1985, Effects of Silicon on the Crystallization and Adsorption Properties of Ferric Oxides: Environmental Science and Technology, 19, 1048-1053, https://doi.org/10.1021/es00141a004

Aranda-Gómez, J.J., Mcdowell, F.W., 1998, Paleogene Extension in the Southern Basin and Range Province of Mexico: Syndepositional Tilting of Eocene Red Beds and Oligocene Volcanic Rocks in the Guanajuato Mining District: International Geology Review, 40, 116-134, https://doi.org/10.1080/00206819809465201

Aranda-Gómez, J.J., Molina-Garza, R., McDowell, F.W., Vassallo-Morales, L.F., Ortega-Rivera, M.A., Solorio-Munguía, J.G., Aguillón-Robles, A., 2007, The relationships between volcanism and extension in the Mesa Central: The case of Pinos, Zacatecas, Mexico: Revista Mexicana de Ciencias Geológicas, 24, 216-233.

Arehart, G.B., 1996, Characteristics and origin of sediment-hosted disseminated gold deposits: A review: Ore Geology Reviews, 11, 383-403, https://doi.org/10.1016/S0169-1368(96)00010-8

Bai, Y., Yang, T., Liang, J., Qu, J., 2016, The role of biogenic Fe-Mn oxides formed in situ for arsenic oxidation and adsorption in aquatic ecosystems: Water Research, 98, 119-127, https://doi.org/10.1016/j.watres.2016.03.068

Bailey, G.B., 1974, The Occurrence, Origin, and Economic Significance of Gold-Bearing Jasperoids in the Central Drum Mountains, Utah: Palo Alto, CAL, USA, Stanford University, Ph.D thesis, 300 pp.

Baltuck, M., 1982, Provenance and distribution of tethyan pelagic and hemipelagic siliceous sediments, pindos mountains, Greece: Sedimentary Geology 31, 63-88, https://doi.org/10.1016/0037-0738(82)90008-2

Barboza-Gudiño, J.R., Tristán-González, M., Torres-Hernández, J.R., 1998, The late Triassic-early Jurassic active continental margin of western north America in northeastern Mexico: Geofisica Internacional, 37, 283-292.

Barboza-Gudiño, J.R., Tristán-González, M., Torres-Hernández, J.R., 1999, Tectonic setting of pre-Oxfordian units from central and northeastern Mexico: A review, *in* Mesozoic Sedimentary and Tectonic History of North-Central Mexico: Geological Society of America, Special Paper 340, 197-210, https://doi.org/10.1130/0-8137-2340-x.197

Barboza-Gudiño, J.R., Orozco-Esquivel, M.T., Gómez-Anguiano, M., Zavala-Monsiváis, A., 2008, The Early Mesozoic volcanic arc of western North America in northeastern Mexico: Journal of South American Earth Sciences 25, 49-63, https://doi.org/10.1016/j.jsames.2007.08.003

Barboza-Gudiño, J. R., Zavala-Monsivais, A., Venegas-Rodriguez, G., Barajas-Nigoche, L. D., 2010, Late Triassic stratigraphy and facies from northeastern Mexico: Tectonic setting and provenance: Geosphere, 6(5), 621-640

Bau, M., Koschinsky, A., Dulski, P., Hein, J.R., 1996, Comparison of the partitioning behaviours of yttrium, rare earth elements, and titanium between hydrogenetic marine ferromanganese crusts and seawater: Geochimica et Cosmochimica Acta, 60, 1709-1725, https://doi.org/10.1016/0016-7037(96)00063-4

Bau, M., Schmidt, K., Koschinsky, A., Hein, J., Kuhn, T., Usui, A., 2014, Discriminating between different genetic types of marine ferro-manganese crusts and nodules based on rare earth elements and yttrium: Chemical Geology, 381, 1-9, https://doi.org/10.1016/j.chemgeo.2014.05.004

Binns, R.A., 2007, Data report: Petrography and geochemistry of jasperoids from site 1189, ocean drilling program Leg 193: Proceedings of the Ocean Drilling Program: Scientific Results 193, https://doi.org/10.2973/odp.proc.sr.193.211.2006

Bonatti, E., Fisher, D.E., Joensuu, O., Rydell, H.S., Beyth, M., 1972,. Iron-Manganese-Barium Deposit from the Northern Afar Rift (Ethiopia): Economic Geology, 67, 717-730, https://doi.org/10.2113/gsecongeo.67.6.717

Bonatti, E., Zerbi, M., Kay, R., Rydell, H., 1976, Metalliferous deposits from the Apennine ophiolites: Mesozoic equivalents of modern deposits from oceanic spreading centers: Bulletin of the Geological Society of America, 87, 83-94, https://doi.org/10.1130/0016-7606(1976)87<83:MDFTAO>2.0.CO;2

Boström, K., Peterson, M.N.A., 1969, The origin of aluminum-poor ferromanganoan sediments in areas of high heat flow on the East Pacific Rise: Marine Geology, 7, 427-447, https://doi.org/10.1016/0025-3227(69)90016-4

Boström, K., Kraemer, T., Gartner, S., 1973, Provenance and accumulation rates of opaline silica, Al, Ti, Fe, Mn, Cu, Ni and Co in Pacific pelagic sediments: Chemical Geology, 11, 123-148, https://doi.org/10.1016/0009-2541(73)90049-1

Boynton, W.V., 1984, Cosmochemistry of the Rare Earth Elements: Meteorite Studies: Developments in Geochemistry, 2, 63-114, https://doi.org/10.1016/B978-0-444-42148-7.50008-3

Brechbühl, Y., Christl, I., Elzinga, E.J., Kretzschmar, R., 2012, Competitive sorption of carbonate and arsenic to hematite: Combined ATR-FTIR and batch experiments: Journal of Colloid and Interface Science, 377, https://doi.org/10.1016/j.jcis.2012.03.025

Brusnitsyn, A.I., Zhukov, I.G., 2012, Manganese deposits of the Devonian Magnitogorsk palaeovolcanic belt (Southern Urals, Russia): Ore Geology Reviews, 47, 42-58. https://doi.org/10.1016/j.oregeorev.2012.01.003

Brusnitsyn, A.I., Zhukov, I.G., 2018, Geochemistry and formation model of manganiferous rocks in jaspers of the South Urals: Lithology and Mineral Resources, 53, 14-35, https://doi.org/10.1134/S0024490218010030

Camprubí, A., Albinson, T., 2007, Epithermal deposits in México—update of current knowledge, and an empirical reclassification, *in* Geology of México: Celebrating the Centenary of the Geological Society of México: Geological society of America, Special Paper 422, 377-415, https://doi.

org/10.1130/2007.2422(14)

Canet, C., Prol-Ledesma, R.M., Torres-Alvarado, I., Gilg, H.A., Villanueva, R.E., Lozano-Santa Cruz, R., 2005, Silica-carbonate stromatolites related to coastal hydrothermal venting in Bahía Concepción, Baja California Sur, Mexico: Sedimentary Geology, 174, 97-113.

Canet, C., Prol-Ledesma, R.M., Bandy, W.L., Schaaf, P., Linares, C., Camprubí, A., Tauler, E., Mortera-Gutiérrez, C., 2008, Mineralogical and geochemical constraints on the origin of ferromanganese crusts from the Rivera Plate (western margin of Mexico): Marine Geology, 251, 47-59, https://doi.org/10.1016/j.margeo.2008.01.012

Carrillo-Bravo, J., 1982, Exploración Petrolera de la Cuenca Mesozoica del Centro de México: Boletín de la Asociación Mexicana de Geólogos Petroleros, 34, 21-46.

Centeno-García, E., Silva-Romo, G., 1997, Petrogenesis and tectonic evolution of Central Mexico during Triassic-Jurassic time: Revista Mexicana de Ciencias Geológicas, 14, 244-260.

Centeno-García, E., Corona-Chávez, P., Talavera-Mendoza, O., Iriondo, A., 2003, Geology and tectonic evolution of the western Guerrero terrane—A transect from Puerto Vallarta to Zihuatanejo, Mexico, *in* Geologic Transects across Cordilleran Mexico: Guidebook for the Field Trips of the 99th Geological Society of America Cordilleran Section Annual Meeting: Puerto Vallarta, Jal., Mexico, Geological Society of America, 201-228.

Centeno-García, E., Guerrero-Suastegui, M., Talavera-Mendoza, O., 2008, The Guerrero Composite Terrane of western Mexico: Collision and subsequent rifting in a supra-subduction zone, *in* Special Paper 436: Formation and Applications of the Sedimentary Record in Arc Collision Zones: Geological Society of America, 279-308, https://doi.org/10.1130/2008.2436(13)

Chi Fru, E., Kilias, S., Ivarsson, M., Rattray, J.E., Gkika, K., McDonald, I., He, Q., Broman, C., 2018, Sedimentary mechanisms of a modern banded iron formation on Milos Island, Greece: Solid Earth, 9, 573-598, https://doi.org/10.5194/se-9-573-2018

Choi, J.H., Hariya, Y., 1992, Geochemistry and depositional environment of Mn oxide deposits in the Tokoro Belt, northeastern Hokkaido, Japan: Economic Geology, 87, 1265-1274, https://doi.org/10.2113/gsecongeo.87.5.1265

Conly, A.G., Scott, S.D., Bellon, H., 2011, Metalliferous manganese oxide mineralization associated with the Boléo Cu-Co-Zn district, Mexico: Economic Geology, 106, 1173-1196, https://doi.org/10.2113/econgeo.106.7.1173

Crerar, D.A., Namson, J., Chyi, M.S., Williams, L., Feigenson, M.D., 1982, Manganiferous cherts of the Franciscan assemblage; I, General geology, ancient and modern analogues, and implications for hydrothermal convection at oceanic spreading centers: Economic Geology, 77, 519-540, https://doi.org/10.2113/gsecongeo.77.3.519

Cronan, D.S., 1980. Metallogenesis at Oceanic Spreading Centers: Journal of the Geological Society, 137, 369-371, https://doi.org/10.1146/annurev.ea.03.050175.002153

Dasgupta, H.C., Sambasiva Rao, V. V., Krishna, C., 1999, Chemical environments of deposition of ancient iron- and manganese-rich sediments and cherts: Sedimentary Geology, 125, 83-98, https://doi.org/10.1016/S0037-0738(98)00148-1

Ferrari, L., López-Martínez, M., Rosas-Elguera, J., 2002, Ignimbrite flare-up and deformation in the southern Sierra Madre Occidental, western Mexico: Implications for the late subduction history of the Farallon plate: Tectonics, 21, 17-24, https://doi.org/10.1029/2001tc001302

Ferrari, L., Valencia-Moreno, M., Bryan, S., 2007, Magmatism and tectonics of the Sierra Madre Occidental and its relation with the evolution of the western margin of North America, *in* Geology of México: Celebrating the Centenary of the Geological Society of México: Geological Society of America, Special Paper 422, 1-39, https://doi.org/10.1130/2007.2422(01)

Flohr, M.J.K., Huebner, J.S., 1992, Mineralogy and geochemistry of two metamorphosed sedimentary manganese deposits, Sierra Nevada, California, USA: Lithos 29, 57-85, https://doi.org/10.1016/0024-4937(92)90034-V

Fournier, R.O., 1985, The Behavior of Silica in Hydrothermal Solutions, *in* Berger, B.R., Bethke, P.M. (eds.), Geology and Geochemistry of Epithermal Systems: Reviews in Economic Geology, 2, 45-72, https://doi.org/10.5382/Rev.02.03

Fulignati, P., 2020, Clay minerals in hydrothermal systems: Minerals, 10, 1-17, https://doi.org/10.3390/min10100919

Graney, J.R., Kesler, S.E., Jones, H.D., 1991, Application of gas analysis of jasperoid inclusion fluids to exploration for micron gold deposits: Journal of Geochemical Exploration, 42, 91-106, https://doi.org/10.1016/0375-6742(91)90061-X

Heaney, P.J., 1994, Structure and chemistry of the low-pressure silica polymorphs, *in* Heaney,P.J., Prewitt, C.T., Gibbs, G.V. (eds) Silica. Physical Behavior, Geochemistry and Materials Applications: Mineralogical Society of America, Reviews in Mineralogy & Geochemistry, 29, 1-40.

Hedenquist, J., Arribas, A., Gonzalez-Urien, E.G., 2000, Exploration for Epithermal Gold Deposits: Society of Economic Geologists Reviews, 13, 245-277.

Hein, J.R., Koski, R.A., Yeh, H.-W., 1987. Chert-hosted manganese deposits in sedimentary sequences of the Franciscan Complex, Diablo Range, California, *in* Hein, J.R. (ed.), Siliceous Sedimentary Rocks-Hosted Ores and Petroleum: New York, Hutchinson Ross Publication, 206-230 pp.

Hein, J.R., Koschinsky, A., Halbach, P., Manheim, F.T., Bau, M., Kang, J.-K., Lubick, N., 1997, Iron and manganese oxide mineralization in the Pacific, *in* Nicholson, K., Hein, J. R., Bfihn, B., Dasgupta, S. (eds.), Manganese Mineralization: Geochemistry and Mineralogy of Terrestrial and Marine Deposits: Geological Society Special Publication, 123-138, https://doi.org/10.1144/GSL.SP.1997.119.01.09

Hein, J.R., Stamatakis, M.G., Dowling, J.S., 2000. Trace metal-rich Quaternary hydrothermal manganese oxide and barite deposit, Milos Island, Greece. Transactions of the Institutions of Mining and Metallurgy: Applied Earth Science, 109, 67-76, https://doi.org/10.1179/aes.2000.109.2.67

Hein, J.R., Koschinsky, A., McIntyre, B.R., 2005, Mercury- and silver-rich ferromanganese oxides, southern California Borderland: Deposit model and environmental implications: Economic Geology, 100, 1151-1168, https://doi.org/10.2113/gsecongeo.100.6.1151

Henry, C.D., Aranda-Gomez, J.J., 1992, The real southern Basin and Range: Mid- to late Cenozoic extension in Mexico: Geology 20, 701-704, https://doi.org/10.1130/0091-7613(1992)020<0701:TRSBAR>2.3.CO;2

Hesse, R., 1990, Silica diagenesis: origin of inorganic and replacement cherts: Earth Science Reviews, 26, 253-276.

Hofstra, A.H., Cline, J.S., 2000, Characteristics and Models for Carlin-Type Gold Deposits, *in* Hagemann, S.G., Brown, P.E. (eds.), Gold in 2000: Society of Economic Geologists Reviews, 163-220, https://doi.org/10.5382/Rev.13.05

Holland, P.T., Beaty, D.W., Snow, G.G., 1988, Comparative Elemental and Oxygen Isotope Geochemistry of Jasperoid in the Northern Great Basin: Evidence for Distinctive Fluid Evolution in Gold-Producing Hydrothermal Systems: Economic Geology, 83, 1401-1423.

Hoppe, M., Barboza-Gudiño, J.R., Schulz, H.M., 2002, Late Triassic submarine fan deposits in northwestern San Luis Potosí, Mexico - Lithology, facies and diagénesis: Neues Jahrbuch Fur Geologie Und Palaontologie - Monatshefte, 12, 705-724.

Huff, Dante E., Holley, E., Guenthner, W.R., Kaempfer, J.M., 2020, Fe-oxides in jasperoids from two gold districts in Nevada: characterization, geochemistry, and (U-Th)/He dating: Geochimica et Cosmochimica Acta, 286, 72-102 https://doi.org/10.1016/j.gca.2020.07.014

Johnston, M.K., Thompson, T.B., Emmons, D.L., Jones, K., 2008, Geology of the cove mine, Lander County, Nevada, and a genetic model for the McCoy-Cove hydrothermal system: Economic Geology, 103, 759-782, https://doi.org/10.2113/gsecongeo.103.4.759

Jones, D.L., Murchey, B., 1986, Geologic significance of Paleozoic and Mesozoic radiolarian chert: Annual review of Earth and planetary sciences, 14, 455-492, https://doi.org/10.1146/annurev.ea.14.050186.002323

Josso, P., Pelleter, E., Pourret, O., Fouquet, Y., Etoubleau, J., Cheron, S., Bollinger, C., 2017, A new discrimination scheme for oceanic ferromanganese deposits using high field strength and rare earth elements: Ore Geology Reviews, 87, 3-15, https://doi.org/10.1016/j.oregeorev.2016.09.003

Juárez-Arriaga, E., Lawton, T.F., Ocampo-Díaz, Y.Z.E., Stockli, D.F., Solari, L., 2019, Sediment provenance, sediment-dispersal systems, and major arc-magmatic events recorded in the Mexican foreland basin, North-Central and Northeastern Mexico: International Geology Review, 61, 2118-2142, https://doi.org/10.1080/00206814.2019.1581848

Jun, P., Haisheng, Y., Wenjie, X., 2010, Geochemical Indication of Sinian Bedded Siliceous Rocks in the Hunan-Guizhou-Guangxi Area and Their Environmental Significance: Acta Geologica Sinica, 74, 46-53, https://doi.org/10.1111/j.1755-6724.2000.tb00430.x

Kirwin, D.J., Royle, D.Z., 2019, Sediment-Hosted Gold Deposits in Southeast

Asia: Resource Geology, 69, 125-147, https://doi.org/10.1111/rge.12189
Koschinsky, A., Halbach, P., 1995, Sequential leaching of marine ferromanganese precipitates: Genetic implications: Geochimica et Cosmochimica Acta, 59, 5113-5132, https://doi.org/10.1016/0016-7037(95)00358-4
Kuehn, C.A., Rose, A.W., 1992, Geology and Geochemistry of Wall-Rock Alteration at the Carlin Gold Deposit, Nevada: Economic Geology, 87, 1697-1721.
Labarthe-Hernández, G., Aguillón-Robles, A., 1986, Cartografía geológica 1:50,000 hojas: Salinas y Villa de Ramos Edos. de San Luis Potosí y Zacatecas: San Luis Potosí: San Luis Potosí, SLP, Mexico, Universidad Autónoma de San Luis Potosi, Technical Report, 56 pp, https://doi.org/10.13140/rg.2.1.3596.0563
Labarthe-Hernández, G., Tristán-González, M., Aranda-Gómez, J.J., 1982, Revisión estratigráfica del Cenozoico de la parte central del Estado de San Luis Potosí: San Luis Potosí, Mexico, Universidad Autónoma de San Luis Potosí, Technical Report, 80 pp.
Labarthe-Hernández, G., Jimenez-López, L.S., Motilla-Moreno, J.L., 1992, Jasperoide guía posible en la exploración minera Mesa Central, México: Universidad Nacional Autónoma de México, Instituto de Geología, Revista, 10(2), 137-142.
Lovering, T.G., 1962, The origin of jasperoid in limestone: Economic Geology, 57, 861-889, https://doi.org/10.2113/gsecongeo.57.6.861
Lovering, T.G., 1972, Jasperoid in the United States - Its Characteristics, Origin, and Economic Significance: Washington, USA, US Geological Survey, Technical Report, 176 pp.
Lovering, T.G., Heyl, A.V, 1974, Jasperoid as a guide to mineralization in the Taylor Mining District and Vicinity near Ely, Nevada: Economic Geology, 69(1), 46-58, https://doi.org/10.2113/gsecongeo.69.1.46
Madondo, J., Canet, C., González-Partida, E., Rodríguez-Díaz, A.A., Núñez-Useche, F., Alfonso, P., Rajabi, A., Pi, T., Blignaut, L., Vafeas, N., 2020, Geochemical constraints on the genesis of the 'Montaña de Manganeso' vein-type Mn deposit, Mexican Plateau: Ore Geology Reviews, 125, 103680 https://doi.org/10.1016/j.oregeorev.2020.103680
Maghfouri, S., Rastad, E., Mousivand, F., Choulet, F., Ye, L., 2017, Geological and geochemical constraints on the Cheshmeh-Frezi volcanogenic stratiform manganese deposit, southwest Sabzevar basin, Iran: Ore Geology Reviews, 89, 96-113. https://doi.org/10.1016/j.oregeorev.2017.06.015
Manning, B.A., Fendorf, S.E., Bostick, B., Suarez, D.L., 2002, Arsenic(III) oxidation and arsenic(V) adsorption reactions on synthetic birnessite: Environmental Science and Technology, 36, 976-981, https://doi.org/10.1021/es0110170
Martini, M., Solari, L., Camprubí, A., 2013, Kinematics of the Guerrero terrane accretion in the Sierra de Guanajuato, central Mexico: New insights for the structural evolution of arc-continent collisional zones: International Geology Review, 55, 574-589, https://doi.org/10.1080/00206814.2012.729361
McDowell, F.W., Clabaugh, S.E., 1979, Ignimbrites of the Sierra Madre Occidental and their relation to the tectonic history of western Mexico: Geological Society Special Publication, 180, 113-124, https://doi.org/10.1130/SPE180-p113
McKay, W.J., Finlow-Bates, T., 1977, Tridymitic jasperoid deposits in N. W. Queensland: Mineralium Deposita, 12, 96-104, https://doi.org/10.1007/BF00204508
McKenzie, R.M., 1980, The adsorption of lead and other heavy metals on oxides of manganese and iron: Australian Journal of Soil Research, 18, https://doi.org/10.1071/SR9800061
McLemore, V.T., Munroe, E.A., Heizler, M.T., McKee, C., 1999, Geochemistry of the Copper Flat porphyry and associated deposits in the Hillsboro mining district, Sierra County, New Mexico, USA: Journal of Geochemical Exploration, 67, 167-189, https://doi.org/10.1016/S0375-6742(99)00072-2
Miura, H., Banerjee, H., Hariya, Y., Dasgupta, S., Roy, S., 1987, Hollandite and cryptomelane in the manganese oxide deposits of the Sausar Group, India: Mineralogical Journal, 13, 424-433, https://doi.org/10.2465/minerj.13.424
Murphy, R.J., 1995, Mapping of jasperoid in the Cedar Mountains, Utah, U.S.A., using imaging spectrometer data: International Journal of Remote Sensing, 16, 1021-1041. https://doi.org/10.1080/01431169508954461
Murray, R.W., 1994, Chemical criteria to identify the depositional environment of chert: general principles and applications: Sedimentary Geology, 90, 213-232, https://doi.org/10.1016/0037-0738(94)90039-6
Nelson, C.E., 1990, Comparative geochemistry of jasperoids from Carlin-type gold deposits of the western United States: Journal of Geochemical Exploration, 36, 171-195, https://doi.org/10.1016/0375-6742(90)90055-F
Nicholson, K., 1992, Contrasting mineralogical-geochemical signatures of manganese oxides: guides to metallogenesis: Economic Geology, 87, 1253-1264, https://doi.org/10.2113/gsecongeo.87.5.1253
Nieto-Samaniego, Á.F., Macías-Romo, C., Alaniz-Álvarez, S.A., 1996, Nuevas edades isotópicas de la cubierta volcánica cenozoica de la parte meridional de la Mesa Central, México: Revista Mexicana de Ciencias Geológicas, 13, 117-122.
Nieto-Samaniego, Á.F., Alaniz-Álvarez, S.A., Camprubí, A., 2005, La Mesa Central de México: estratigrafía, estructura y evolución tectónica cenozoica: Boletín de la Sociedad Geológica Mexicana, 57, 285-318, https://doi.org/10.18268/bsgm2005v57n3a3
Nieto-Samaniego, Á.F., Alaniz-Álvarez, S.A., Camprubí, A., 2007, Mesa Central of México: Stratigraphy, structure, and Cenozoic tectonic evolution, in: Special Paper 422: Geology of México: Celebrating the Centenary of the Geological Society of México. Geological Society of America, 41-70, https://doi.org/10.1130/2007.2422(02)
Nieto-Samaniego, A.F., Olmos-Moya, M. de J.P., Levresse, G., Alaniz-Alvarez, S.A., Abdullin, F., del Pilar-Martínez, A., Xu, S., 2019, Thermochronology and exhumation rates of granitic intrusions at Mesa Central, Mexico: International Geology Review, 62, 1-8, https://doi.org/10.1080/00206814.2019.1602789
O'Neil, J.R., Bailey, G.B., 1979, Stable isotope investigation of gold-bearing jasperoid in the central Drum Mountains, Utah: Economic Geology, 74, 852-859, https://doi.org/10.2113/gsecongeo.74.4.852
Öksüz, N., Okuyucu, N., 2014, Mineralogy, geochemistry, and origin of Buyukmahal manganese mineralization in the Artova ophiolitic complex, Yozgat, Turkey: Journal of Chemistry, 2014, 1-11. https://doi.org/10.1155/2014/837972
Ouvrard, S., de Donato, P., Simonnot, M.O., Begin, S., Ghanbaja, J., Alnot, M., Duval, Y.B., Lhote, F., Barres, O., Sardin, M., 2005, Natural manganese oxide: Combined analytical approach for solid characterization and arsenic retention: Geochimica et Cosmochimica Acta, 69, 2715-2724, https://doi.org/10.1016/j.gca.2004.12.023
Öztürk, H., Hein, J.R., 1997, Mineralogy and stable isotopes of black shale-hosted manganese ores, Southwestern Taurides, Turkey: Economic Geology, 92, 733-744, https://doi.org/10.2113/gsecongeo.92.6.733
Papavassiliou, K., Voudouris, P., Kanellopoulos, C., Glasby, G., Alfieris, D., Mitsis, I., 2017, New geochemical and mineralogical constraints on the genesis of the Vani hydrothermal manganese deposit at NW Milos island, Greece: Comparison with the Aspro Gialoudi deposit and implications for the formation of the Milos manganese mineralization: Ore Geology Reviews, 80, 594-611, https://doi.org/10.1016/j.oregeorev.2016.07.023
Pokrovski, G.S., Schott, J., Farges, F., Hazemann, J.L., 2003, Iron (III)-silica interactions in aqueous solution: Insights from X-ray absorption fine structure spectroscopy: Geochimica et Cosmochimica Acta, 67, 3559-3573, https://doi.org/10.1016/S0016-7037(03)00160-1
Ponce S., B.F., Clark, K.F., 1988, The Zacatecas mining district: a tertiary caldera complex associated with precious and base metal mineralization: Economic Geology, 83, 1668-1682. https://doi.org/10.2113/gsecongeo.83.8.1668
Post, J.E., 1999, Manganese oxide minerals: crystal structures and economic and environmental significance, *in* Proceedings of the 96th National Academy of Sciences Colloquium: Irvine, USA, National Academy of Sciences, 3447-3454, https://doi.org/10.1073/pnas.96.7.3447
Renault, J., Armstrong, A.K., Repetski, J.E., Oscarson, R.L., 1995, Geology, mineralogy, geochemistry, and geothermometry of Kelly Limestone jasperoids , Magdalena mining district , New Mexico: Socorro, New Mexico Bureau of Mines & Mineral Resources, Technical Report, 51 pp.
Reyes, A.G., 1990, Petrology of Philippine geothermal systems and the application of alteration mineralogy to their assessment: Journal of Volcanology and Geothermal Research, 43, 279-309.
Robertson, A., Degnan, P., 1998, Significance of modern and ancient oceanic Mn-rich hydrothermal sediments exemplified by Jurassic Mn-cherts from Southern Greece: Geological Society Special Publication, 148, 217-240, https://doi.org/10.1144/GSL.SP.1998.148.01.12
Rodríguez-Díaz, A.A., Canet, C., Villanueva-Estrada, R.E., Chacón, E., Gervilla, F., Velasco-Tapia, F., Cruz-Gámez, E.M., González-Partida, E., Casas-

García, R., Linares-López, C., Pérez-Zárate, C., 2019, Recent Mn-Ag deposits in coastal hydrothermal springs in the Baja California Peninsula, Mexico: Mineralium Deposita, 54, 849-866.

Rodríguez-Ríos, R, Tristán-González, M., Aguillón-Robles, A., 2013, Estructura y geoquímica de un grupo de domos dacíticos del norponiente del campo volcánico de San Luis Potosí, México: Boletín de la Sociedad Geológica Mexicana, 65, 109-122, https://doi.org/10.18268/bsgm2013v65n1a9

Roy, S., 1981, Manganese deposits: London, Academic Press, 451 pp.

Roy, S., 1997, Genetic diversity of manganese deposition in the terrestrial geological record: Geological Society Special Publication, 119, 5-27, https://doi.org/10.1144/GSL.SP.1997.119.01.02

Sánchez-Córdova, M. M., Canet, C., Rodríguez-Díaz, A., González-Partida, E., Linares-López, C., 2020, Water-rock interactions in the Acoculco geothermal system, eastern Mexico: Insights from paragenesis and elemental mass-balance: Chemie Der Erde, 80, 1, https://doi.org/10.1016/j.chemer.2019.06.003

Sánchez-Rojas, L.E., 2013, Jasperoides en el límite de los terrenos Guerrero y Sierra Madre Oriental, *in* AIMMGM, XXX Convención Internacional de Minería: Acapulco, Gro. Mexico, Asociación de Ingenieros de Minas, Metalurgistas y Geólogos de México, 312-319.

Schwertmann, U., Murad, E., 1983, Effect of pH on the formation of goethite and hematite from ferrihydrite: Clays & Clay Minerals, 31, 277-284 https://doi.org/10.1346/CCMN.1983.0310405

Sinisi, R., Mameli, P., Mongelli, G., Oggiano, G., 2012, Different Mn-ores in a continental arc setting: Geochemical and mineralogical evidences from Tertiary deposits of Sardinia (Italy): Ore Geology Reviews, 47, 110-125, https://doi.org/10.1016/j.oregeorev.2012.03.006

Stenger, D.P., Kesler, S.E., Peltonen, D.R., Tapper, C.J., 1998, Deposition of gold in carlin-type deposits: The role of sulfidation and decarbonation at twin creeks, Nevada: Economic Geology, 93, 201-215, https://doi.org/10.2113/gsecongeo.93.2.201

Suda, A., Makino, T., 2016, Functional effects of manganese and iron oxides on the dynamics of trace elements in soils with a special focus on arsenic and cadmium: A review: Geoderma, 270, 68-75 https://doi.org/10.1016/j.geoderma.2015.12.017

Sugisaki, R., Yamamoto, K., Adachi, M., 1982, Triassic bedded cherts in central Japan are not pelagic: Nature, 298, 644-647, https://doi.org/10.1038/298644a0

Taylor, P., 1995, Interactions of Silica with Iron Oxides: Effects on Iron oxide Transformation and Sorption Properties: Manitoba, Atomic Energy of Canada, Technical Report, 20 pp.

Taylor, S.R., McLennan, S.M., 1985, The Continental Crust: its Composition and Evolution. An Examination of the Geochemical Record Preserved in Sedimentary Rocks: Oxford, Blackwell Scientific Publications, 312 pp.

Theodore, T.G, Jones, G.M., 1992, Geochemistry and geology of gold in jasperoid, Elephant Head area, Lander County: Nevada, US Geological Survey Bulletin, 62 pp, https://doi.org/10.3133/b2009

Toth, J.R., 1980, Deposition of submarine crusts rich in manganese and iron: Geological Society of America Bulletin, 91, 44-54, https://doi.org/10.1130/0016-7606(1980)91<44:DOSCRI>2.0.CO

Trask, P.D., Rodríguez-Cabo, J.R., 1948, Manganese Deposits of Mexico, *in* Geologic Investigations in the American Republics, 1946: Washington, USA, United States Geological Survey, Bulletin 954, 209-316, https://doi.org/10.3133/b954F

Tristán-González, M., 1986, Estratigrafía y tectónica del graben de Villa de Reyes, en los Estados de San Luis Potosí y Guanajuato, México: San Luis Potosí, SLP, Mexico, Universidad Autónoma de San Luis Potosí, Technical Report, 107, 91 pp.

Tristán-González, M., Labarthe-Hernández, G., Aguirre-Díaz, G.J., Aguillón-Robles, A., 2008, Tectono-volcanic control of fissure type vents for the 28 Ma Panalillo ignimbrite in the Villa de Reyes Graben, San Luis Potosí, México: IOP Conference Series Earth and Environmental Science, 3, 012026. https://doi.org/10.1088/1755-1307/3/1/012026

Tristán-González, M., Aguillón-Robles, A., Barboza-Gudiño, J.R., Torres-Hernández, J.R., Bellon, H., López-Doncel, R., Rodríguez-Ríos, R., Labarthe-Hernández, G., 2009a, Geocronología y distribución espacial del vulcanismo en el Campo Volcánico de San Luis Potosí: Boletín de la Sociedad Geológica Mexicana, 61, 287-303, https://doi.org/10.18268/BSGM2009v61n3a1

Tristán-González, M., Aguirre-Díaz, G.J., Labarthe-Hernández, G., Torres-Hernández, J.R., Bellon, H., 2009b, Post-Laramide and pre-Basin and Range deformation and implications for Paleogene (55-25 Ma) volcanism in central Mexico: A geological basis for a volcano-tectonic stress model: Tectonophysics, 471, 136-152, https://doi.org/10.1016/j.tecto.2008.12.021

Usui, A., Someya, M., 1997, Distribution and composition of marine hydrogenetic and hydrothermal manganese deposits in the northwest Pacific: Geological Society Special Publications, 119, 177-198, https://doi.org/10.1144/gsl.sp.1997.119.01.12

Wilson, I.F., Rocha, V.S., 1948, Manganese deposits of the Montaña de Manganeso mine, San Luis Potosí, Mexico, *in* Trask, P.D., Rodríguez-Cabo, J.R. (eds.), Manganese Deposits of Mexico: United States Geological Survey, Bulletin,954-F, 267-271

Wilson, A.B., Soulliere, S.J., Skipp, B., Worl, R.G., Rhea, K.P., 1987, Geology and Geochemistry of Jasperoid Near Mackay, Idaho, *in* Link, P.K., Hackett, W.R., (eds), Guidebook to the Geology of Central and Southern Idaho: CITY, STATE, USA, Idaho Geological Survey Bulletin, 27, 183-192

Wright, J., Schrader, H., Holser, W.T., 1987, Paleoredox variations in ancient oceans recorded by rare earth elements in fossil apatite: Geochimica et Cosmochimica Acta, 51, 631-644, https://doi.org/10.1016/0016-7037(87)90075-5

Yamamoto, S., 1986, Correlation between iron and magnesium and its significance on the distribution of heavy metals in deep-sea cherts: Sedimentary Geology, 49, 261-280, https://doi.org/10.1016/0037-0738(86)90041-2

Yigit, O., Hofstra, A.H., Hitzman, M.W., Nelson, E.P., 2006, Geology and geochemistry of jasperoids from the Gold Bar district, Nevada: Mineralium Deposita, 41, 527-547, https://doi.org/10.1007/s00126-006-0080-8

Ying, S.C., Kocar, B.D., Fendorf, S., 2012, Oxidation and competitive retention of arsenic between iron- and manganese oxides: Geochimica et Cosmochimica Acta, 96, 294-303, https://doi.org/10.1016/j.gca.2012.07.013

Yongzhang, Z., Guangchi, T., Chown, E.H., Guha, J., Huanzhang, L., 1994, Petrologic and geochemical characteristics and origin of Gusui cherts, Guangdong Province, China: Chinese Journal of Geochemistry, 13, 118-131. https://doi.org/10.1007/BF02838512

Zamora-Vega, O., Richards, J.P., Spell, T., Dufrane, S.A., Williamson, J., 2018, Multiple mineralization events in the Zacatecas Ag-Pb-Zn-Cu-Au district, and their relationship to the tectonomagmatic evolution of the Mesa Central, Mexico: Ore Geology Reviews, 102, 519-561. https://doi.org/10.1016/j.oregeorev.2018.09.010

Zhang, G., Liu, F., Liu, H., Qu, J., Liu, R., 2014, Respective role of Fe and Mn oxide contents for arsenic sorption in iron and manganese binary oxide: An X-ray absorption spectroscopy investigation: Environmental Science and Technology, 48, 10316-10322, https://doi.org/10.1021/es501527c

Manuscript received: july 28, 2021
Corrected manuscript received: november 4, 2021
Manuscript accepted: november 6, 2021

CHAPTER 4

HYDROTHERMAL ALTERATION ASSOCIATED WITH MN MINERALIZATION

MINERALOGY OF THE HYDROTHERMAL ALTERATION SURROUNDING THE MONTAÑA DE MANGANESO DEPOSIT.

Manuscript in preparation

Joseph Madondo[a*], Teresa Pi[b], Jesus Sole[b], Carles Canet[c], Eduardo Gonzalez Partida[d]

[a]*Posgrado en Ciencias de la Tierra, Universidad Nacional Autonoma de Mexico, Ciudad Universitaria, 04510 CdMx, Mexico*

[b]*Instituto de Geología, Universidad Nacional Autonoma de Mexico, Ciudad Universitaria, 04510 CdMx, Mexico*

[c]*Instituto de Ciencias de la Atmosfera y Cambio Climatico, Universidad Nacional Autonoma de M´exico, Ciudad Universitaria, 04510 CdMx, Mexico*

[d]*Centro de Geociencias, Universidad Nacional Autonoma de Mexico, Juriquilla, 76230 Queretaro, Mexico*

[*] Joseph.madondo85@gmail.com

Abstract

Extensive fault and fracture controlled hydrothermal alteration surrounds the Montaña de Manganeso Mn deposit. Hydrothermal fluids percolated fractures and faults and deposited mainly manganese and iron oxides, quartz, calcite and minor barite. Mineral deposition was accompanied by intense hydrothermal alteration around the mineralized veins that is reflected in the strong silicification and clay alteration of the host rocks. Short wave infrared (SWIR) reflectance spectroscopy and X-ray diffraction (XRD) show that this quartz, calcite and clay minerals (illite, kaolinite, smectite and interstratified illite/smectite) are the dominant hydrothermal minerals in the altered rock samples. Fe and Mn oxides, alkali-feldspars (anorthoclase) and plagioclase (anorthite) are accessory minerals. Illite dominates proximal to the veins and extends into the host rocks grading into the interstratified illite-smectite and smectite at varying distances from the veins. Kaolinite locally predominates as a product of steam heated alteration with a typically accompanying silica cap. This mineral assemblage commonly occur in epithermal deposits and geothermal systems and constitutes an argillic alteration

Keywords: Hydrothermal, clay minerals, argillic, steam-heated,

1. Introduction

Hydrothermal ore deposits are commonly accompanied by hydrothermal alteration whose identification and characterization contribute to the understanding of the ore deposition process and the evolution of hydrothermal systems (Inoue, 1995; Thompson and Thompson, 1996). This alteration typically contain clays minerals whose study provide useful information that allows constraining the physico-chemical conditions, such as fluid acidity, solution chemistry and temperature, prevailing in the hydrothermal fluid that interacted with the host rock (Fulignati, 2020; Inoue, 1995; Inoue et al., 2005; Reyes, 1990; Yang et al., 2001). Additionally, the distribution of these clays help infer paleofluid flow pathways and thus serve as important exploration guides (Fulignati, 2020; Hedenquist et al., 2000; Herrmann et al., 2001; Inoue, 1995).

Short-wave infrared (SWIR) reflectance spectroscopy is commonly used during mineral exploration of hydrothermal deposits (Hedenquist et al., 2000; Herrmann et al., 2001; Thompson et al., 1999) and geothermal deposits (Canet et al., 2015a, 2010) to characterize alteration mineral assemblages. This is because it is a simple, low cost, non-destructive technique that enables rapid data acquisition with minimal sample preparation required (Herrmann et al., 2001; Thompson et al., 1999; Yang et al., 2005). This technique can identify infrared-active minerals, variations in their mineral composition, crystallinity, and relative abundance (Herrmann et al., 2001). SWIR radiation has high sensitivity to vibrations of the Al–OH, Mg–OH, Fe–OH, Si–OH, NH_4, molecular bonds present in the structure of various clay minerals (Clark et al., 1990; Thompson et al., 1999), and is thus ideal for analysis of clay minerals (da Cruz et al., 2015; Herrmann et al., 2001). The

mineralogy determined by SWIR is often complemented by XRD analyses, as not all alteration minerals can be detected by SWIR (Thompson et al., 1999).

In Mexico economically important hydrothermal clay deposits occur in the Sierra Madre Occidental of Mexico (De Pablo-Galan, 1979; Hanson et al., 1981) and the Trans-Mexican Volcanic belt (Canet et al., 2015b, 2010; De Pablo-Galan, 1979). To the east of the Sierra Madre Occidental, within the Mexican Central Plateau, hydrothermal clay deposits and occurrences, frequently associated with ore deposits, are reported from Zacatecas, San Luis Potosí and Guanajuato states (De Pablo-Galan, 1979; Hanson and Keller, 1966; Keller and Hanson, 1969, 1968; Vázquez et al., 2009). Examples include the Zaragosa mine in San Luis Potosi (Keller and Hanson, 1968), the San Jose de Ranchos deposit in Sombrerete, Zacatecas (Keller and Hanson, 1969), the Etzatlan mine, Jalisco (Keller, 1961), and the hotspring occurrence at Los Azufres, Michoacan (Hanson et al., 1981; Keller et al., 1971) and Acoculco, Hidalgo (Canet et al., 2015a, 2010).

The Montaña de Manganeso district, located within the Mexican Central Plateau is known for its manganese deposits (Madondo et al., 2020). The deposits are fault-controlled, silicified Fe-Mn oxides occurring as mineralized breccias, stockworks and veins hosted by thinly folded volcaniclastic host rocks. Accessory minerals are barite and calcite and rare pyrite. The Fe-Mn oxide mineralogy consists of pyrolusite, cryptomelane, hollandite, romanechite, todorokite, birnessite, hematite, magnetite and goethite (Madondo et al., 2020).

Previous studies in the Montaña de Manganeso area focused on the Mn ore with very little information available on the alteration zones surrounding the Mn deposits (Madondo

et al., 2020). This paper presents the mineralogy of the extensive hydrothermal alteration zones associated with the Montaña de Manganeso through interpretations of SWIR spectral analyses, complemented by XRD. This information will allow understanding the physico chemical conditions of the hydrothermal system active during the formation of the Montaña de Manganeso deposit and similar deposits in the region.

2. Geological setting

The study area is situated in the Mexican Central Plateau (CP) physiographic province, within the suture zone of the Guerrero terrane and the Sierra Madre tectonostratigraphic terranes (Fig. 1), (Centeno-García and Silva-Romo, 1997; Coremi, 2001; Freydier et al., 2000). The Guerrero terrane is a product of subduction related tectonics and terrane accretion (Centeno-Garcia et al., 1993; Centeno-García and Silva-Romo, 1997). In this region, the Guerrero terrane is characterized by isolated ophiolitic remnants of back-arc origin representing the eastern part of the Guerrero terrane (Centeno-García and Silva-Romo, 1997; De Cserna, 1976; Freydier, 2000; Martini et al 2011). The ophiolitic remnants comprises associations of cherty pelagic limestone, basaltic pillow lava, and radiolarite-chert blocks.

Underlying the Guerrero terrane in the study area are the Mesozoic Basin of Central Mexico succcesions belonging to the Sierra Madre terrane. The MBCM is constituted by a marine Mesozoic sedimentary sequence of late Triassic to late Cretaceous age (Carrillo-Bravo, 1982; Juárez-Arriaga et al., 2019). The basement rocks of the MBCM are Triassic low-grade metamorphic marine sedimentary rocks (Barboza-Gudino et al., 1998), which are overlain by Lower to Middle Jurassic continental arc deposits of the Nazas Formation

(Barboza-Gudiño et al., 1999; 2008; Zamora-Vega et al., 2018). The Upper Jurassic to Late Cretaceous shallow marine carbonate sequences and clastic sediments overlie the Lower to Middle Jurassic continental arc deposits in the MBCM (Carrillo-Bravo, 1982).

In the Central Plateau volcanism is represented mainly by rhyolitic-rhyodacitic lava flows that are product of Eocene-Oligocene bimodal andesitic-rhyolitic volcanic events of the Sierra Madre Occidental (Aguillón-Robles et al., 2014; Nieto-Samaniego et al., 1996). This volcanism occurred mostly as multiple discrete episodes of small rhyolitic volcanic fissures (Aguillón-Robles et al., 2014; Aguirre-Díaz et al., 2008; Tristán-González et al., 2009, 2008). Volcanic units consist of rhyolite, dacite, trachyte, trachyandesite, andesite, andesitic basalt, and pyroclastic rocks (Tristán-González et al., 2015, 2009, 2008). Volcanism was mostly controlled by major NW–SE trending fault systems of the region that also served as channels for economic mineralizations of the region (Nieto-Samaniego et al., 2007).

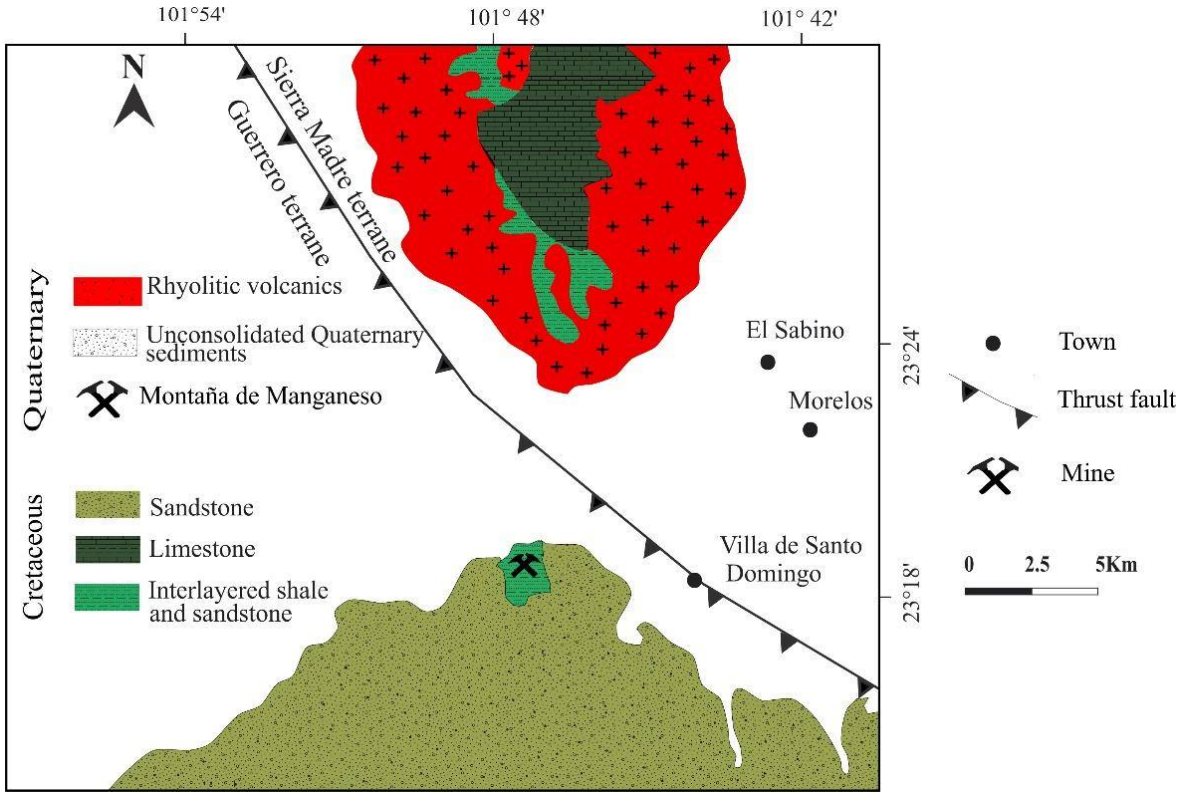

Fig.1. Geologic map of the study area.

2. 1 Alteration styles at Montaña de Manganeso

Silicification and argillization are the major types of hydrothermal alteration at Montaña de Manganeso. Hydrothermal minerals occur as vein fillings and as pervasive alteration of primary rock forming minerals of the host rocks to clays and silica polymorphs. Altered rocks generally form zoned halos around mineralized veins. Halos are occasionally narrow reflecting the fault-controlled mineralization and in other cases alteration is widespread due to the high permeability of the rocks in that particular area. The relative paragenetic position of the distinct alteration types and their relation to the Fe-Mn mineralization is complex and vary between bodies due to differences in the replaced rock lithology and the

multi-episodic nature of mineralization. However, the general sequence of alteration, with respect to the mineralized veins, proceeds from proximal silicification to distal argillization (Fig. 2C).

Silicification is the most widespread type of alteration affecting the surficial rocks. This alteration occurs mostly as a pervasive replacement of the host rocks and vein fillings. Silicification was contemporaneous with Fe-Mn mineralization, resulting in massive topographically elevated Fe-Mn rich jasperoids. Jasperoids at Montaña de Manganeso form massive bodies with heights of up to 20 m elongated in NE-SW direction subparallel to the orientation of major faults of the region (Madondo et al., 2020; Trask and Cabo, 1948). These silica bodies occasionally develop layers that range from a few centimeters to several meters in thickness (Madondo et al., 2020) and appear to have affected mostly the sandstone horizons (Fig. 2D) whilst the volcanic, shale and basaltic components are mostly argillized (Fig. 2E, F, G, H). The dominant presence jasperoids at Montaña de M clearly suggests an intense silicic alteration and a complete dissolution of the primary rock forming minerals.

Silicification gives way to intense argillization, conspicuous in the area due to the bleaching of the host rocks and formation of light-colored clay minerals. In most of the studied samples the protoliths to the altered rocks are not recognizable, although local preservation of original textures indicates that the protoliths were mainly thinly bedded tuffaceous sandstones and shales containing clasts of andesitic to basaltic volcanic rocks that are identifiable at the periphery of the deposit (Trask and Cabo, 1948; Wilson and Rocha, 1948).

The altered rocks are characterized by a whitish green and yellowish color (Fig. 4A, B, C) and are often accompanied by Fe oxyhydroxides that locally impart a brownish or yellowish–brown color (Fig. 2B, E and F, 4C). Halos of altered rocks are common around veins, breccia zones and steep stockworks of mineralized faults (Fig. 2B, C) that represent the feeder faults for ascending hydrothermal fluids. Alteration is intense close to or adjacent to these structures and is dominated by clay minerals whereas the least altered samples generally occur distal to ore bodies. The argillized zones are in turn cut by numerous mineralized veins and veinlets. This relationship indicate that there were several phases of alteration related to different mineralizing episodes. (Fig.4F)

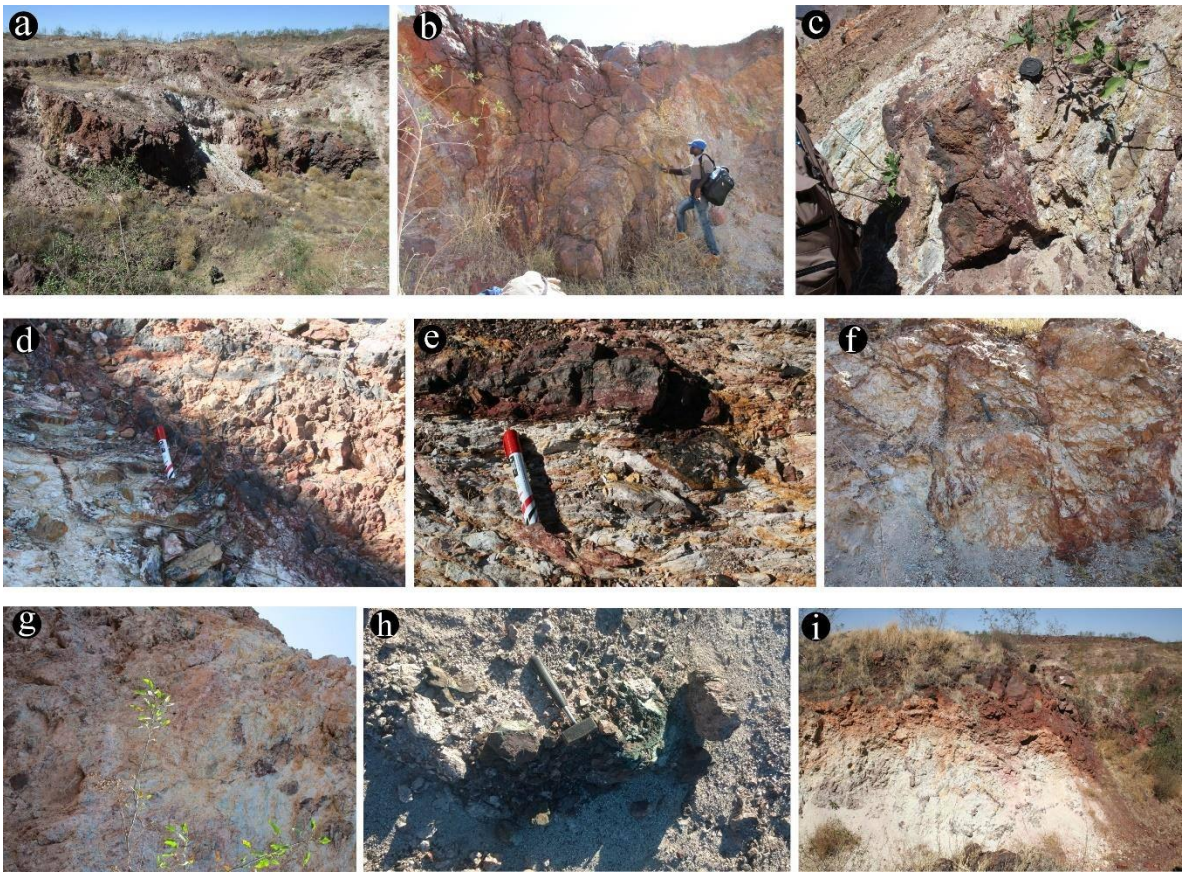

Fig. 2. Outcrop photographs of hydrothermally altered rocks A) Panoramic view of an outcrop of the Montaña de Manganeso deposit seen from the SW showing altered host rocks ± silicified Fe-Mn oxides ± quartz ± barite. B) Steep subvertical stockwork of silicified faults and breccia zones with accompanying Fe-Mn oxide bearing veins represent the feeder faults for the upwelling hydrothermal fluids C) A Fe-Mn oxide vein cuts through oxidized and hydrothermally altered host rocks D) Contact between sandstone and shale. The sandstone and the shale have been silicified and argillized respectively. E) A close up view of the argillized part of image in (D). Fe and Mn oxide veins cut across and stain the hydrothermal clays F) A stockwork zone with a dense network of Fe and Mn veins and veinlets. G) Pervasive and intense alteration has destroyed the original texture of the rocks reducing it to friable horizons rich in illite. H) Destruction and leaching of the andesitic and basaltic components of the Montaña de Manganeso host rocks has produced different degrees of alteration reflected as various shades of green I). A Fe oxide stained silica cap overlies a highly altered, leached and friable sandstone horizon.

To the southeast of the deposit away from the veins and distal to the ore bodies appears a a highly fractured and fragmented Fe-Mn oxides rich silica cap (Figs. 2I and Fig. 3). The massive silica cap is underlain by a completely leached and friable horizon. The top-down appearance of the exposed wall is similar to that produced from a steam heated alteration (Hedenquist et al., 2000). X-ray diffraction results of a sample from the outcrop indicate presence of mainly kaolinite and quartz.

Fig. 3. Close up of Fig. 2I showing an exposure that has undergone steam heated acid alteration. The silica cap probably deposited at the water table close the paleosurface (Hedenquist *et al*., 2000; Sillitoe, 2015). The contact between the fragmented silica cap and the altered rocks below indicates the level of the paleowater table. The underlying steam heated alteration would then be a result of a descending water table.

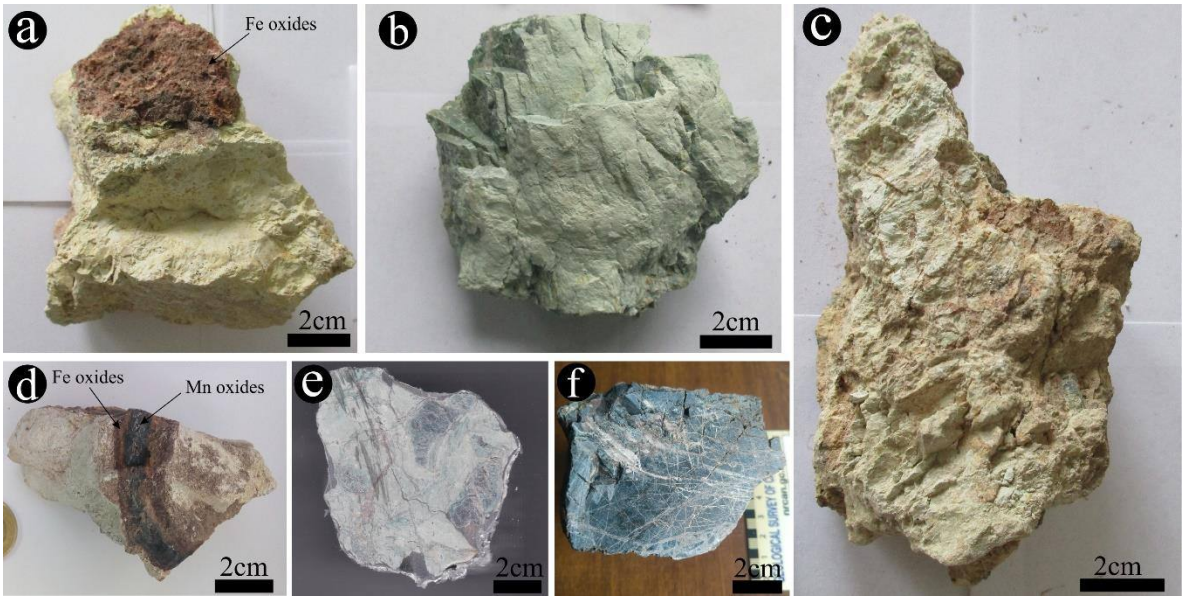

Fig. 4 Altered samples from the Montaña de Manganeso showing different degrees of alteration. Most of the samples are intensely and pervasively altered. A) A porous, leached yellowish hand-specimen of kaolin stained by Fe oxides (hematite and limonite) from Fig 2I B) A moderately altered basaltic andesite. The alteration mainly affected the sample surface C) An altered tuffaceous sandstone D) Fe-Mn veins cut through an altered rock sample E) Argillized basalt with remnant unaltered clasts. F) Silicified basalt fragment that still preserves much of its original texture.

3. Methodology

Field observations and sampling (n = 21) were carried out on outcrops and other surface exposures in order to identify the variation in the extent and intensity of the hydrothermal alteration around ore bodies. Samples representative of different alteration zones and degree of alteration (Fig. 4) were collected from the feeder zone shown in (Fig. 2B) every

0.5 m from the central vein. Additional samples representing various degrees of alteration, were collected from various locations (Fig. 2A, C–I).

Nineteen altered samples were analyzed by short-wave infrared (SWIR) reflectance spectroscopy using a portable LabSpec Pro Spectrophotometer (Analytical Spectral Devices, Inc.) at the Instituto de Geofísica, Universidad Nacional Autonoma de Mexico. Samples were spectrally measured in the laboratory, without any treatment prior to spectra collection. In total, 84 spectra were collected on 19 altered samples. Only the SWIR wavelength region (1300–2500 nm) was utilized, as it is particularly sensitive to OH, H_2O, NH_4, AlOH, FeOH, and MgOH molecular bonds that characterize many clay minerals (Thompson et al., 1999). Duplicate measurements were made for each spectral reading and white reference measurements were taken after every 5th sample. Identification of SWIR-active minerals was done manually by comparing the wavelength position of the absorption features and the general shape of the spectra with various spectral libraries and tables (Clark et al., 2007). The wavelength of the Al-OH spectral absorption feature was used to estimate the compositional variation of illite (Herrmann et al., 2001).

Bulk mineralogy of six altered samples was determined by X-ray diffraction (XRD) using an Empyrean diffractometer equipped with Ni filter, a Cu tube of fine focus and a PIXcel^{3d} detector, at the Instituto de Geología, Universidad Nacional Autonoma de Mexico. Rock samples were lightly crushed with an agate pestle and mortar to 200 mesh, homogenized and mounted in aluminum holders. Measurements were performed in the 2θ angular range from 5° to 70°, with a step scan of 0.003° (2θ) and an integration time of 40 s per step. Samples were analyzed as randomly oriented powder preparations.

The clay mineralogy of five of the samples was verified by powder XRD analyses of oriented aggregates following recommendations of (Moore and Reynolds, 1997). Samples were lightly crushed with an agate pestle and mortar and subsequently dispersed overnight in deionized water. The <2 μm clay fraction was separated in distilled water for 24 hours according to Stoke's law. Samples from the <2 μm clay fraction were spread on glass slides and allowed to dry under atmospheric conditions. Verification of the necessary thickness for measurement of the oriented aggregates (> 2.5mg / cm^2) was done by weighing. A portion of the <2 μm fraction of two samples was centrifuged using a speed of 6000 rpm/10 min in order to extract the coarse (2–0.5 μm), medium (0.5–0.05 μm) and fine (<0.05 μm) clay fractions. All fractions were analyzed by XRD in air-dried state, after ethylene glycolation at 70°C during 24 hours and after thermal treatment at 450 °C and 550 °C. Measurements were made over a 2θ range of 5–70 ° (air-dried) and 5–50 º (for glycolated and heated samples). Identification and semiquantitative relative abundances of the minerals were obtained using the software HIGHScore v4.5 and the ICDD (International Center for Diffraction DATA) and ICSD (Inorganic Crystal Structure Database) databases. For illite and mixed illite/smectite identification followed recommendations of Moore and Reynolds (1997).

Illite crystallinity was estimated for two samples using the XRD method (Kübler Index) and position of the AlOH trough (wAlOH) in illite (Harraden et al., 2013).The Kübler Index was determined from the <2 μm fraction using the full width at half maximum (FWHM) of the basal 10Å illite peak and is reported as degrees 2θ (Kubler, 1968, 1967; Kübler and Jaboyedoff, 2000). The position of the AlOH trough (wAlOH) in illite was also used as an approximation of relative illite crystallinity (Harraden et al., 2013). The ratio of

the depth of the AlOH feature (~2,200 nm) to the depth of the H_2O feature (~1,900 nm) was used to calculate the SWIR based illite crystallinity. Ratios less than 1 represent low crystallinity, whereas ratios greater than 1 represent high crystallinity (Harraden et al., 2013).

4. Results

4.1 Petrography

Samples studied by petrography are intensely and pervasively altered such that it is difficult to identify the protolith. The back-scattered electron (BSE) image of sample MM 5, (Fig. 4A) shows the principal textures observed by SEM. The image consists mostly of areas with light contrast with locally dark areas. Energy dispersive X-ray spectroscopy (EDS) analyses with the SEM shows that the light areas comprise mostly of clay minerals, characterized by elevated concentrations of Si and Al relative to the dark areas, and minor amounts of Ti and Fe bearing minerals.

The clay minerals in sample MM 5 comprise of illite, kaolinite and smectite (identified by XRD). Illite has significantly elevated K content (Fig. 4C) and very low Fe content. Smectite is reach in Ca and Na (Fig. 4D) suggesting that these are the dominant interlayer cations (Bishop et al., 2008; Tillick et al., 2001; Yildiz and Başaran, 2015). EDS spectra also shows very low Fe content for smectite (Fig. 4D). Kaolinite, characteristically, is dominated by Al and Si and only trace amounts of K and Ca (Fig. 4B) (Bishop et al., 2008; Kadir and Kart, 2009; Yildiz and Başaran, 2015).

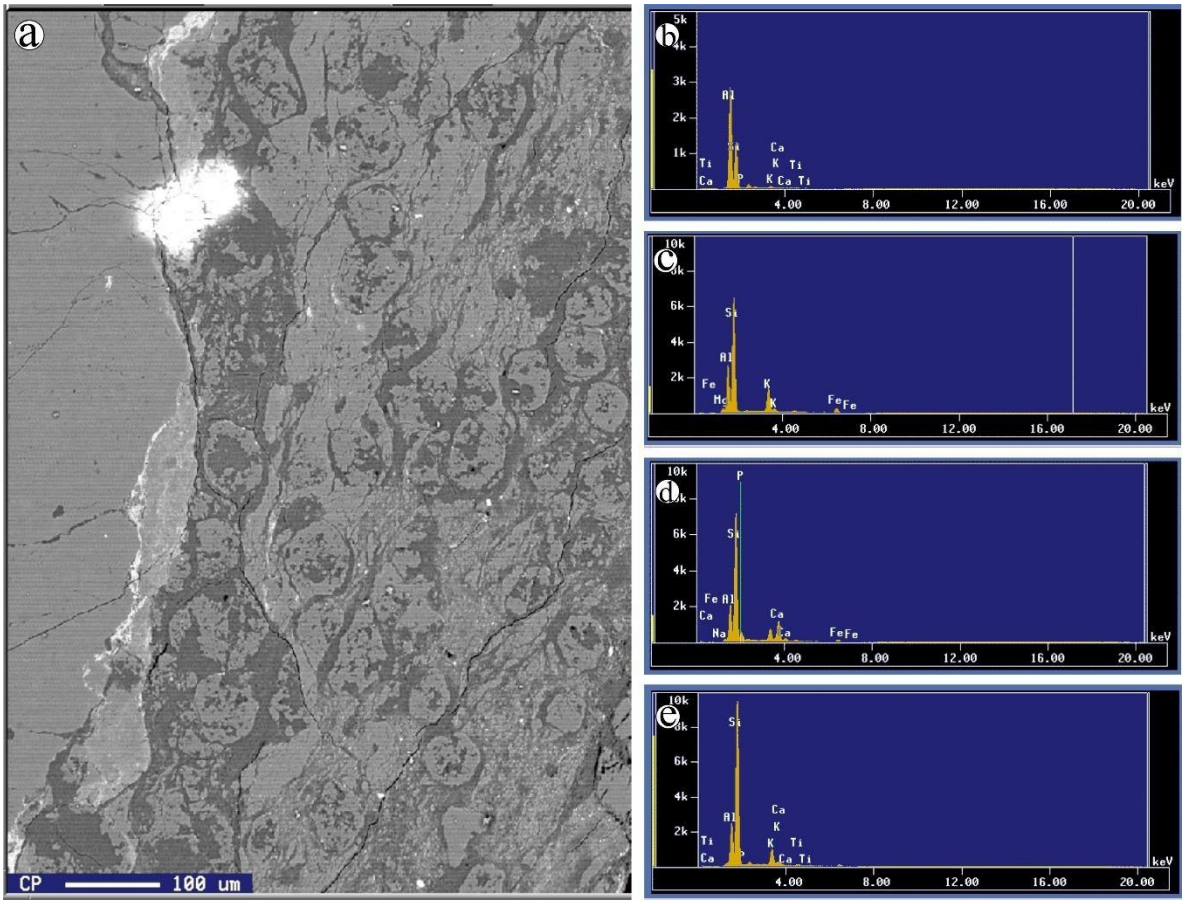

Fig. 4. Thin section SEM image (A) and EDS spectra showing the chemical composition of (B) Kaolinite (C) illite (D) smectite and (E) a possible illite-smectite composite.

4.2 Short wave infrared

The results of spectral measurements of the hydrothermally altered samples are summarized in Table 1. Representative reflectance spectra of the identified SWIR active minerals are shown in Fig. 5A, along with the reference spectra of kaolinite, montmorillonite, montmorillonite-illite and illite (Fig. 5B).

All the SWIR active minerals in this study show characteristic absorptions features associated with absorption of water at ~1400 nm (OH/H_2O) and at ~1900 nm (H_2O), indicating the presence of clay minerals (Pirajno, 2009). They also show features between 2200 and 2400 (Fig. 5A), corresponding to the Al–OH (~2200 nm), the Fe–OH (~2250 nm) and the Mg–OH (~2350 nm) bands characteristic of many sheet silicates (Clark et al., 1990).

Smectite was identified by its characteristic single absorption at 2200 nm which is asymmetric toward longer wavelengths (Fig. 5A) (Clark et al., 1990) and a small shoulder on the H_2O+OH absorption feature at ~1450 –1460 nm. Normally, variations in the content of Fe and Mg, the common cations in the octahedral layer of the smectite structure alter the SWIR spectrum between 2285 and 2292 nm (Fe–OH bond vibrations) and ~2310 nm (Mg–OH bond vibrations) (Bishop et al., 2008; McKeown et al., 2011). The spectrum of smectite from Montaña de Manganeso, however, does not show the Fe-OH feature typical of nontronite and the Mg-OH feature is barely developed, hence the smectite is likely to be montmorillonite. The spectrum also closely matches the reference spectrum of montmorillonite (Fig. 5B).

Kaolinite was identified in SWIR spectra by its diagnostic doublet absorption features (Bishop et al., 2008; Brindley and Brown, 1980). A characteristic reflectance spectrum of kaolinite from sample MM-5 is shown in Fig. 5A. One doublet has absorption at 2.155 and 2.202 nm and another, narrower doublet at 1390 and 1400 nm wavelengths. The 2.155/2.202 doublet corresponds to the Al-OH bond, whilst the 1.390/1.400 correspond to OH radicals and molecular H_2O vibrations. The well-defined Al–OH doublets suggest a fairly crystallized kaolinite, however the marked absorption at 1900 nm wavelength

corresponding to the presence of molecular water suggests the degree of crystallinity is not very high (da Cruz et al., 2015).

SWIR analyses suggests illite is the predominant clay mineral at Montaña de Manganeso. This study therefore provides a more detailed study of this mineral. The identification of illite by SWIR requires caution as its spectrum is similar to the reference SWIR spectrum of montmorillonite. The two minerals have identical absorption features of differing intensities at ~1410, ~1910 and ~2.210 nm (cita). Illite in the Montaña de Manganeso samples was identified by the characteristic small additional absorption features at 2350 and 2450 nm (Hocking et al., 2010). Illite in the Montaña de Manganeso samples can also be differentiated from montmorillonite by narrower hydroxyl features (at 1400 and 1900 nm) and deeper Al–OH absorption band (at 2.21 nm). The MgOH absorption feature at ~2.350 nm, though present in both smectite and illite, is also much more evident in the illite spectra.

The study of the composition illite, is particularly important as it can serve as a more reliable indicator of temperature, degree of alteration and relative reactivity of the hydrothermal fluid (Jin et al., 2002; Wang et al., 2021). SWIR reflectance spectroscopy is sensible to variations in mineral chemistry (Thompson et al., 1999) and can thus be used to determine compositional variations of illite. The wavelength of the AlOH feature (wAlOH) in illite is influenced by the proportion of octahedral Al in the structure of illite (Wang et al., 2021) which in turn is affected by compositional substitutions due to hydrothermal fluid composition and temperature among other factors (Wang et al., 2021). SWIR analysis is therefore able to distinguish between paragonitic (Al-OH at 2,180–2,195 nm), muscovitic (Al-OH at 2,200–2,210 nm) and phengitic (Al-OH at 2,210–2,228 nm) varieties of illite

(Herrmann et al., 2001; Yang et al., 2011) (Table A2) due to modifications in the Al–OH band caused mainly by Fe and Mg cation exchange (Clark et al., 1990; Herrmann et al., 2001). The wAlOH values of the Montaña de Manganeso illite (~ 2,220 nm), corresponds to a phengitic variety, and is generally higher than those reported from other epithermal systems (Wang et al., 2021; Yang et al., 2011).

Similar to illite, illite-smectite also has the same absorption features in the 2350 and 2450 nm region (Hocking et al., 2010) and these two cannot be easily differentiated by their SWIR spectra (Fig. 5). However, their spectral distinction can be broadly determined from the crystallinity index based on the H_2O/AlOH ratio. This ratio has been successfully used to differentiate illite–smectite from illite (Simpson, 2015). Simpson (2015) suggested a cut off value of 1.1, with values <1.1 representing illite–smectite and >1.1 representing illite. For the MM 25 sample, the calculated H_2O/AlOH ratio was 1.0 (0.97) indicating presence of illite-smectite. For the MM 5 sample the H_2O/AlOH ratio is 1.1 (1.09). This ratio is close to the cutoff value of 1.1 suggesting presence of illite or an extremely illite-rich interstratified illite–smectite.

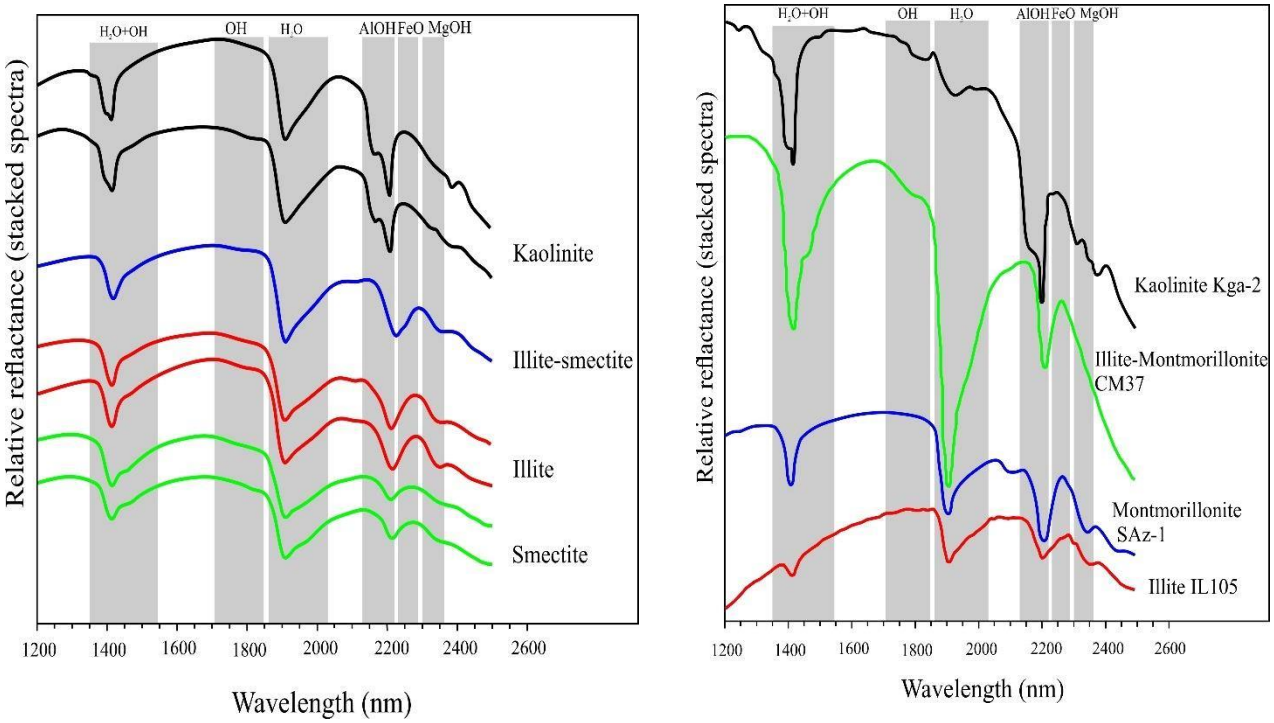

Fig. 5 A) Stacked SWIR reflectance spectra of the representative alteration clays of the Montaña de Manganeso deposit. The spectra have been offset for clarity. The absorption spectra are similar to those of illite, illite-smectite, kaolinite and smectite references. The "water" features in the SWIR spectra are shown for reference. B) SWIR reference spectra for montmorillonite, illite, illite-montmorillonite and kaolinite.

4.2 Diffraction

The results of the XRD analyses of the oriented aggregates are summarized in Table 1 and Fig. 6.

Bulk XRD analyses (Fig. A1) identified quartz and calcite as the dominant non-clay hydrothermal minerals in all the rock samples. Quartz is responsible for the sharp peaks between approximately 20 and 40° 2θ that characterizes X-ray diffraction spectra of most

of the samples (Fig. A1). Clay minerals are locally abundant ranging from from 9-59% of altered rocks (based on semi-quantitative XRD method) and are accompanied by alkali-feldspars (orthoclase), plagioclase feldspars (anorthite) and locally Mn oxides. Illite-mica is the major clay mineral in almost all the samples and subfractions. Other identified clay minerals are the kaolinite and smectite group clays. Illite-smectite was identified on oriented specimens (see below). Well-developed peaks suggests that the clays are well crystallized (Severmann et al., 2004). The relative percentages vary between 9-56% for illite-mica, between 3~39% for kaolinite and between 3~33% for smectite for all samples and subfractions.

The crystallinity index of illite was measured in two of the samples containing illite (MM-5, MM-25A). The results obtained are included in Table 1. Low Kubler Index values (<0.78), indicating high crystallinity, are recorded in those samples with Fe-Mn oxide veins and veinlets (Fig. 4D) whereas the higher (>1.18) were recorded in samples with no Fe-Mn oxide veining (Fig. 4B), suggesting that proximity to the mineralized fault zone and thus temperature influenced illite crystallinity (Merriman and Frey, 2009).

The identification of clay minerals was corroborated through XRD analyses of chemically and thermally treated oriented specimens. Illite was identified in sample MM-5 (Fig. 4B) by peaks at 10.02 Å and 4.93 Å, and additional minor peaks at 4.49 Å and 4.37 Å in untreated air-dried condition. Glycol solvation caused no change in the 10.3 Å illite peak but heat treatment caused a collapse of this peak to the 10 Å illite peak indicating trace illite-smectite. A smectite component in sample MM-5 was identified by the shift of the 14.4 Å peak to a d spacing of approximately 15.0 Å, following ethylene-glycol solvation.

Glycol solvation caused no change in the 7.1 Å X-ray peak, indicating presence of kaolinite (Fig. 5A). Heat treatment caused a collapse of the d_{001} smectite and kaolinite peaks.

Illite-smectite is the major clay mineral in sample MM 25. A sharp peak at 10.5 Å represent presence of the mixed-layer illite–smectite whose occurrence was suspected on the basis of SWIR analysis (Fig. 4D). The 10.5 Å peak expanded to a d spacing of 10.9 Å (Fig. 5C) following ethylene-glycol solvation, indicating the presence of an illite-smectite component. Heat treatment caused a collapse of this peak leaving only the illite 10 Å peak.

Pure smectite was identified in sample MM-125. Diffraction patterns of the untreated air-dried sample (Fig. 6C) show broad d00l peak at about 14.2 Å (Fig. 4C) diagnostic of smectite. The peak at 14.2 Å expanded to 16.0 Å following ethylene-glycol solvation and collapsed to 10 A˚ peak upon heating to 550ºC for 2 h (Figure 6).

Kaolinite was identified in sample MM 5 by diagnostic peaks at 7.2 and 3.6 Å and non-basal reflections at 1.34, 1.31, and 1.28A˚ (Brindley and Brown, 1980; Moore and Reynolds, 1989). The peak at 7.2 A˚ remained unchanged after treatment by ethylene-glycol but collapsed after heating to 550ºC.The sharp and well-defined peaks indicate well-ordered kaolinite (Kadir and Kart, 2009).

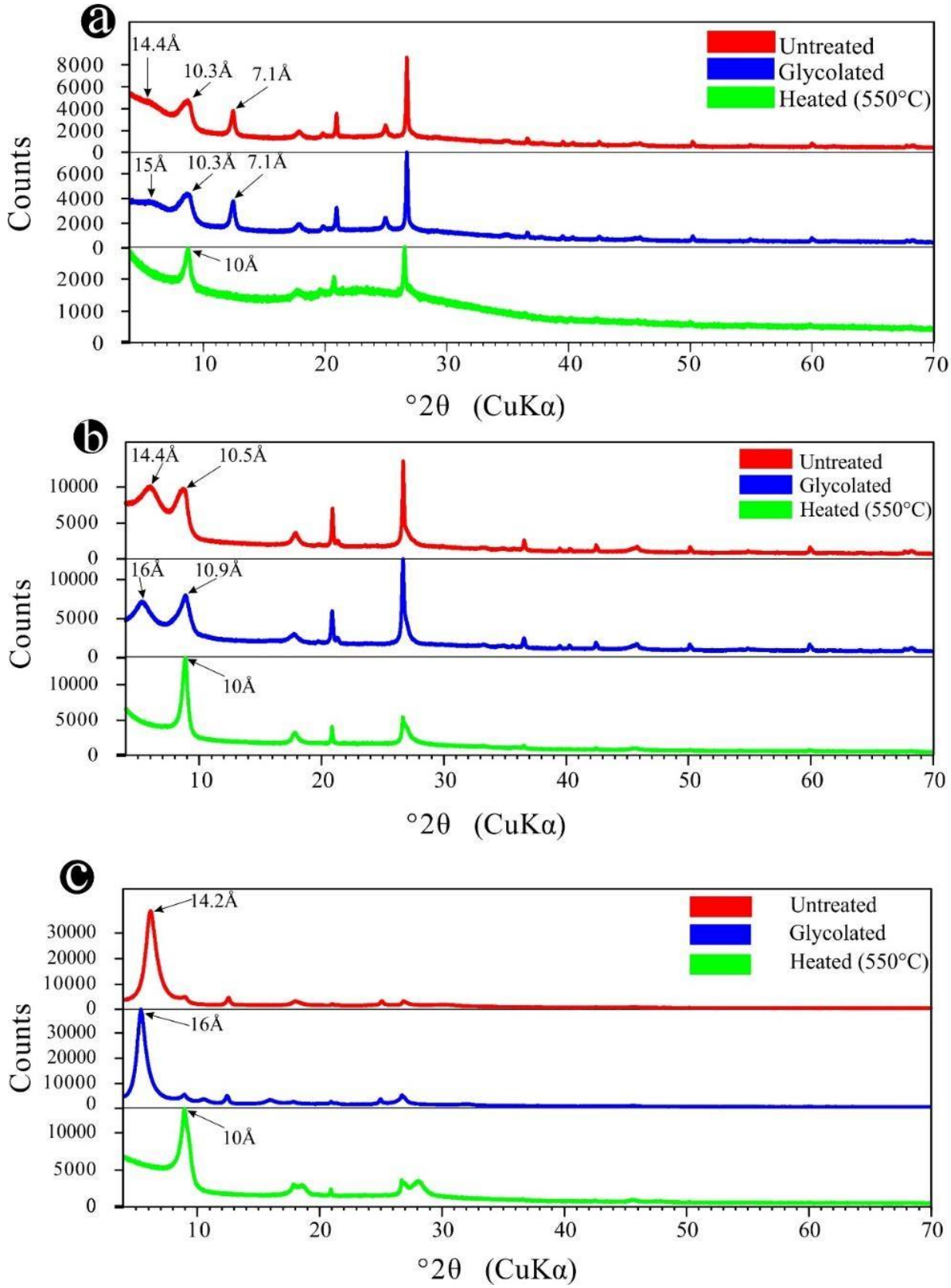
a
14.4Å
10.3Å
7.1Å
Untreated
Glycolated
Heated (550°C)
15Å
10Å
Counts
°2θ (CuKα)
b
14.4Å
10.5Å
16Å
10.9Å
10Å
c
14.2Å
16Å
10Å

Fig. 6 XRD patterns (oriented mounts) of representative alteration assemblages prepared from whole-rock powders of samples from the Montaña de Manganeso. A) Illite-rich sample with minor smectite and trace kaolinite (MM-5) with basal reflections at ~10.3 Å (untreated), ~10.3 Å (ethylene glycol solvated), and ~10 Å (heated to 550 °C). B) Interstratified Illite-smectite in sample (MM-25) with basal reflections at 10.5 Å (untreated), 10.9 Å (ethylene glycol solvated), and 10 Å (heated to 550 °C). Expansion of the 10.5 Å peak under glycol solvation indicates the presence of a mixed-layer clay. The sample also contain smectite with basal reflection at 14.4 that expands to 16 Å under glycol solvation C) Smectite (MM-125) with basal reflections at 14.2 Å (untreated), 16 Å (ethylene glycol solvated), and 10 Å (heated to 550 °C). All analyses were on oriented specimens. Unlabeled peaks with good definition in the XRD scans (Fig. 6) correspond to quartz.

Table 1.

Clay minerals identified by oriented X-ray diffraction and SWIR spectroscopic analysis of Montaña de Manganeso samples.

Sample	SWIR	Air-dried	Ethylene Glycolated	Heated (550 C)	XRD Identified Phases	Crystallinity Index
MM 5	Smectite	14.4Å	15Å	10Å	Traces of smectite	1.18
	Illite	10.3Å	10.3Å	10Å	Illite + illite-smectite	
	Kaolinite	7.1Å	7.1Å	X	Kaolinite	
MM 25	Smectite	14.4Å	16Å	10Å	Smectite	>1.5
	Illite	10.5Å	10.9Å	10Å	Illite-smectite	
MM 125	Smectite	14.2Å	16Å	10Å	Smectite	

5. Discussion

5.1 Geology

The most visible geologic evidence of hydrothermal activity at Montaña de Manganeso are the massive, silicified bodies that form topographically prominent outcrops at Montaña de Manganeso. These silica bodies are widespread in the Central Plateau and are associated with precious and base metal mineralizations (Albinson, 1988; Labarthe Hernández et al., 1992). At Montaña de Manganeso the jasperoids are associated with Fe-Mn mineralization (Madondo et al., 2020). The predominance of silicification and silica deposition at Montaña de Manganeso indicates involvement of cooling neutral-pH hydrothermal fluids (e.g Hedenquist et al., 2000).

Silicification at Montaña de Manganeso is associated with zones of intense argillic alteration (Figs. 2, 7). Porous and permeable host rocks enabled the movement of fluid and the development of widespread argillic alteration (Fig. 2A). Establishing the zonal distribution at the deposit level is difficult due to the irregular distribution of the ore bodies and the intense fracturing and faulting which provided several pathways for the percolating fluids. Alteration assemblages are characterized by different proportions and associations of clay minerals and silica polymorphs between ore bodies or veins. Other factors such as variations in the influx rate, temperature and composition of the hydrothermal fluids probably contributed to the complex relative paragenetic position of these minerals and their relation to the Fe-Mn mineralization. However, when individual mineralized veins or ore bodies are considered a zonal distribution of clay minerals consistent with temperature as a controlling factor (e.g Yang et al., 2001) becomes evident. For the samples taken around the feeder zone (Fig. 2B), those adjacent the Fe and Mn veins predominantly

contained illite (Sample MM 5) and illite-smectite (sample MM 25) whereas those distal to mineralization predominantly contained smectite (MM 125). This mineralogical zonation pattern from proximal illite rich zone to a distal smectite rich zone through interlayered illite-smectite, is similar to that observed in epithermal and geothermal systems (Yang et al., 2001) where the pattern is due to a lateral decrease in temperature due to a cooling hydrothermal fluid (Tillick et al., 2001). Other aspects of the alteration at Montaña de Manganeso, such as the presence of a leached porous alteration zone topped by a silica body (Fig. 3) is characteristic of low sulfidation epithermal deposits (Sillitoe, 2015, 1993). Such an alteration profile commonly develops when steam-heated waters collect below the water table and creates sub-horizontal zones of massive silicification (Sillitoe, 2015, 1993).

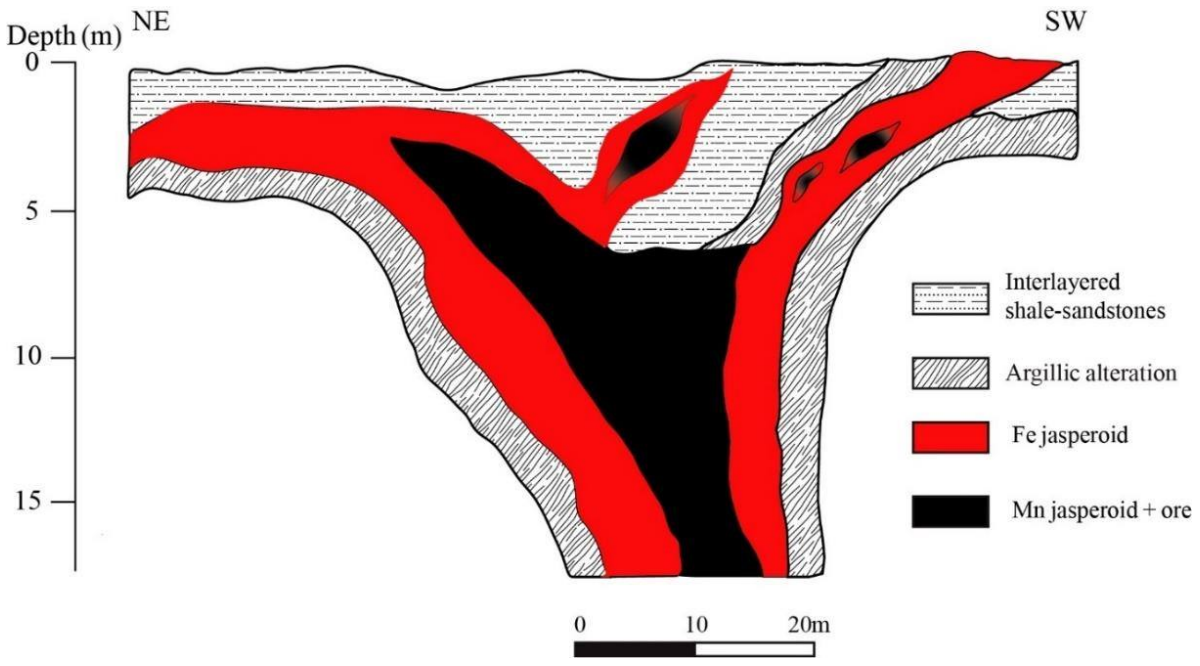

Fig. 7 A model of alteration at one of the major ore body at Montaña de Manganeso. A Manganese rich silicified ore body transitions in color from black at the center to red at the margins. The change in color is

probably due to different solubility and mobility of manganese and iron. The silicification extends into the volcaniclastic host rocks as the discharge of SiO_2-rich and metal-rich fluids was not restricted to fractures and veins. The clays formed at adjacent to the veins and present high quartz contents of up to 54% in bulk samples.

5.2 Depositional environment and fluid compositions

Clay formation generally occurs through weathering, diagenesis, and hydrothermal alteration (Inoue, 1995). During hydrothermal alteration, clay minerals form by alteration of primary rock forming minerals due to physical and chemical changes induced by circulating hot hydrothermal fluids (Inoue, 1995; Inoue et al., 2005; Maza et al., 2018; Pirajno, 2009). They are therefore useful for placing constraints on key characteristics of the hydrothermal fluid, such as composition, temperature and acidity of the fluid prevailing during the hydrothermal alteration process (Canet et al., 2015b; Fulignati, 2020; Hedenquist et al., 2000; Inoue, 1995; Pirajno, 2009; Reyes, 1990; Simmons and Browne, 2000; Yang et al., 2001).

The predominance of illite at Montaña de Manganeso gives insight into the nature of the hydrothermal fluids. Since illite formation is a K-fixation process (Inoue, 1983; Srodon et al., 1986) a higher abundance of illite at Montaña de Manganeso indicates that considerable quantities of K were available in solution for illite formation (Jin et al., 2002). As illite at Montaña de Manganeso is of the phengitic type, substantial concentration of Fe and Mg were also likely present in solution (Wang et al., 2021). High Fe and K concentrations are

corroborated by the occurrence of abundant Fe mineralization and K rich manganese oxide (cryptomelane) at Montaña de Manganeso (Madondo et al., 2020).

The above discussion supposes precipitation of illite and other clay minerals directly from the hydrothermal fluid (e.g Tillick et al., 2020). The common occurrence of clays in fractures and well-crystallized peaks on the X-ray diffractograms of clays from Montaña de Manganeso suggest that at least part of the illite, illite-smectite and smectite assemblage formed by direct crystallization from the hydrothermal fluid without undergoing the progressive transformations typical of smectite illitization (Inoue et al., 2005; Pandarinath et al., 2006; Severmann et al., 2004; Tillick et al., 2001; Yan et al., 2001). The presence of the interlayered illite-smectite, however, is often accepted as evidence of formation of illite through a primarily temperature dependent, stepwise illitization of smectite reaction similar to that which occur during burial metamorphism in sedimentary basins (Aja, 2019; Inoue, 1995; Inoue et al., 2005, 1978; Inoue and Utada, 1983; Simmons and Browne, 2000; Vázquez et al., 2016, 2014; Yan et al., 2001; Yang et al., 2001).

Illite, illite-smectite and smectite are temperature sensitive minerals and are useful for estimating the temperature of the hydrothermal fluid (Fulignati, 2020; Pandarinath et al., 2006; Reyes, 1990; Yang et al., 2001). Kaolinite, for example, generally occurs at temperatures <200°C in epithermal systems; at temperature above 200 °C, high crystallinity dickite is formed (Simmons and Browne, 2000). Smectite is typically stable below 160°C (Hedenquist, 1990; Reyes, 1990; Simmons and Browne, 2000) and the transition from smectite to illite (illite-smectite formation) takes place at temperatures generally between 130-220°C (Browne, 1978; Jin et al., 2002; Maza et al., 2018; Reyes, 1990; Thompson et al., 1994; Vázquez et al., 2016, 2014). Illite is typically stable between 220 and 300°C;

above 300°C it transforms to muscovite (sericite) (Browne, 1984; Hedenquist, 1990; Reyes, 1990). The widespread and predominant occurrence of illite at the Montaña de Manganeso seemingly suggest temperatures above 220°C, however the absence of other high temperature alteration minerals such as dickite, chlorite or epidote and the association with interlayered illite-smectite and smectite suggests a temperature range of <150-220°C (Fulignati, 2020). This temperature range is slightly higher than the temperature indicated by fluid inclusions in quartz at the time of mineralization (during ore stage) (101-140°C) (Madondo et al., 2020). Lower temperatures for the ore stage hydrothermal fluids compared to those responsible for hydrothermal alteration suggest that ore formation occurred from late stage influx of fluids that had a significant input of cooler meteoric waters (Madondo et al., 2020).

The presence of illite, as that of smectite and illite-smectite, indicate formation from near-neutral pH hydrothermal fluid (Çelik et al., 1999; Inoue, 1995; Inoue et al., 2005; Simmons et al., 2005; Wang et al., 2021). On the contrary, kaolinite generally form under acidic conditions (Bishop et al., 2008; Hedenquist et al., 2000; Reyes, 1990). Acidic fluids responsible for kaolinite formation may be generated in a number of environments including the near-surface parts of geothermal and epithermal systems and deep portions of some intermediate and high sulfidation epithermal deposits (Camprubí and Albinson, 2007). In the near surface epithermal environment, they are generated from gas rich near neutral systems by boiling which leads to loss of CO_2 and H_2S to the vapor (Hedenquist et al., 2000; Simmons et al., 2005). Partial condensation of the vapor below the water table forms steam-heated, mildly acid (pH 4–5) CO_2 rich waters (Hedenquist et al., 2000; Sillitoe, 2015, 1993; Simmons et al., 2000; Simmons and Browne, 2000). Since the gases

(CO2 and H2S) generally rise to the surface along a path distinct from the residual liquid, steam-heated waters commonly occur on the margins of geothermal and epithermal systems (Hedenquist et al., 2000; Hedenquist, 1990; Hedenquist and Browne, 1989; Simmons et al., 2005, 2000; Simmons and Browne, 2000; Yan et al., 2001). The leached, porous alteration zone topped by a silica body and occurring away from the main feeder zone (Fig. 3) is probably a result of steam heated alteration. Its occurrence below the silica top suggests that the silica forming hydrothermal activity was accompanied by descent of the water table, a phenomenon common during the wanning of the hydrothermal system (Hedenquist et al., 2000; Sillitoe, 2015; Simmons et al., 2005; Thompson et al., 1999, 1994; Tritlla et al., 2004).

Evidence for presence of CO_2 and H_2S in the fluid is indicated by occurrence of calcite and barite at Montaña de Manganeso (Madondo et al., 2020). Fluid inclusion microthermometry in quartz, coupled with stable isotope analysis in barite and calcite ($\delta^{34}S$, $\delta^{13}C$, $\delta^{18}O$), indicate that C and S in the aqueous fluids from Montaña de Manganeso were derived from magmatic sources (Madondo et al., 2020). It is inferred that mixing of hydrothermal fluids with meteoric water and reaction with the host rocks could have caused simultaneous cooling and neutralization of the fluid, resulting in the formation of the argillic type alteration (Madondo et al., 2020).

Acid sulfate steam-heated waters that generally condenses above the water table and characterized by the formation of an advanced argillic alteration assemblage (Hedenquist et al., 2000; Inoue, 1995; Simmons and Browne, 2000), were probably not formed at Montaña de Manganeso. The absence of alunite and other minerals indicative of an acid sulfate steam heated alteration, such as alunite, or native sulfur (Simmons and Browne, 2000), and

the abundance of calcite suggest that the main steam heated fluids at Montaña de Manganeso were relatively enriched in CO_2 than H_2S (Hedenquist and Browne, 1989; Simmons et al., 2005; Simmons and Browne, 2000).

Conclusions

Clay minerals define the hydrothermal alteration at Montaña de Manganeso. The extent of hydrothermal alteration was controlled by faults, fractures and high permeability which enabled ascent of Fe-Mn bearing, silica-rich hydrothermal fluids through the host rock. The mineral assemblage of illite, smectite, interlayered illite-smectite, calcite and quartz that characterized the alteration at Montaña de Manganeso is similar to that reported in low-sulfidation epithermal deposits (Hedenquist et al., 2000; Thompson et al., 1999). Alteration resulted from low temperature, near neutral pH fluids (Hedenquist et al., 2000) dominated by bicarbonate waters with a minor acid sulphate component that produced an argillic alteration assemblage. These waters were probably produced by partial condensation of gases released from boiling fluids at depths. The distribution of clay minerals around individual mineralized veins is consistent with temperature as a controlling variable. The main alteration products are illite, smectite, illite-smectite and kaolinite. Whilst a supergene origin for some of the smectite and kaolinite cannot be ruled out, the restriction of the clays studied here to the hydrothermally altered and brecciated zones characterized by Fe (oxyhydr)oxide veins, the clear presence of a steam heated alteration zone and a mineralogical zonation similar to that of clays in geothermal and epithermal systems

(Hedenquist et al., 2000; Simmons et al., 2005; Thompson et al., 1999) argue against formation by superficial weathering.

References

Aguillón-Robles, A., Tristán-González, M., De Jesús Aguirre-Díaz, G., López-Doncel, R.A., Bellon, H., Martínez-Esparza, G., 2014. Eocene to Quaternary mafic-intermediate volcanism in San Luis Potosí, central Mexico: The transition from Farallon plate subduction to intra-plate continental magmatism. Journal of Volcanology and Geothermal Research 276, 152–172. https://doi.org/10.1016/j.jvolgeores.2014.02.019

Aguirre-Díaz, G.J., Labarthe-Hernández, G., Tristán-González, M., Nieto-Obregón, J., Gutiérrez-Palomares, I., 2008. The Ignimbrite Flare-Up and Graben Calderas of the Sierra Madre Occidental, Mexico, in: Developments in Volcanology. Elsevier, pp. 143–180. https://doi.org/10.1016/S1871-644X(07)00004-6

Aja, S.U., 2019. on the Thermodynamic Stability of Illite and I-S Minerals. Clays and Clay Minerals 67, 518–536. https://doi.org/10.1007/s42860-019-00044-x

Albinson, T., 1988. Geologic reconstruction of paleosurfaces in the Sombrerete, Colorado, and Fresnillo districts, Zacatecas State, Mexico. Economic Geology 83, 1647–1667. https://doi.org/10.2113/gsecongeo.83.8.1647

Barboza-Gudiño, J.R., Orozco-Esquivel, M.T., Gómez-Anguiano, M., Zavala-Monsiváis, A., 2008. The Early Mesozoic volcanic arc of western North America in northeastern Mexico. Journal of South American Earth Sciences 25, 49–63. https://doi.org/10.1016/j.jsames.2007.08.003

Barboza-Gudino, J.R., Tristán-González, M., Torres-Hernández, J.R., 1999. Tectonic setting of pre-Oxfordian units from central and northeastern Mexico: A review, in: Special Paper 340: Mesozoic Sedimentary and Tectonic History of North-Central Mexico. Geological Society of America, pp. 197–210. https://doi.org/10.1130/0-8137-2340-x.197

Barboza-Gudino, J.R., Tristán-González, M., Torres-Hernández, J.R., 1998. The late Triassic-early Jurassic active continental margin of western north America in northeastern Mexico. Geofisica Internacional 37, 283–292.

Bishop, J.L., Lane, M.D., Dyar, M.D., Brown, A.J., 2008. Reflectance and emission spectroscopy study of four groups of phyllosilicates: smectites, kaolinite-serpentines, chlorites and micas. Clay Minerals 43, 35–54. https://doi.org/10.1180/claymin.2008.043.1.03

Brindley, G.W., Brown, G., 1980. Crystal Structures of Clay Minerals and their X-Ray Identification. Mineralogical Society of Great Britain and Ireland, Colchester and London. https://doi.org/10.1180/mono-5

Browne, P.R.L., 1984. Lectures on geothermal geology and Petrology. Iceland.

Browne, P.R.L., 1978. Hydrothermal Alteration in Active Geothermal Fields. Annual Review of Earth and Planetary Sciences 6, 229–248. https://doi.org/10.1146/annurev.ea.06.050178.001305

Camprubí, A., Albinson, T., 2007. Epithermal deposits in México - Update of current knowledge and an empirical reclassification. Special Paper of the Geological Society of America 422, 377–415. https://doi.org/10.1130/2007.2422(14)

Canet, C., Arana, L., González-Partida, E., Pi, T., Prol-Ledesma, R.M., Franco, S.I., Villanueva-Estrada, R.E., Camprubí, A., Ramírez-Silva, G., López-Hernández, A., 2010. A statistics-based method for the short-wave infrared spectral analysis of altered rocks: An example from the Acoculco Caldera, Eastern Trans-Mexican Volcanic Belt. Journal of Geochemical Exploration 105, 1–10. https://doi.org/10.1016/j.gexplo.2010.01.010

Canet, C., Hernández-Cruz, B., Jiménez-Franco, A., Pi, T., Peláez, B., Villanueva-Estrada, R.E., Alfonso, P., González-Partida, E., Salinas, S., 2015a. Combining ammonium mapping and short-wave infrared (SWIR) reflectance spectroscopy to constrain a model of hydrothermal alteration for the Acoculco geothermal zone, Eastern Mexico. Geothermics. https://doi.org/10.1016/j.geothermics.2014.05.012

Canet, C., Hernández-Cruz, B., Jiménez-Franco, A., Pi, T., Peláez, B., Villanueva-Estrada, R.E., Alfonso, P.,

González-Partida, E., Salinas, S., 2015b. Combining ammonium mapping and short-wave infrared (SWIR) reflectance spectroscopy to constrain a model of hydrothermal alteration for the Acoculco geothermal zone, Eastern Mexico. Geothermics 53, 154–165. https://doi.org/10.1016/j.geothermics.2014.05.012

Carrillo-Bravo, J., 1982. Exploración Petrolera de la Cuenca Mesozoica del Centro de México. Boletín de la Asociación Mexicana de Geólogos Petroleros 34, 21–46.

Çelik, M., Karakaya, N., Temel, A., 1999. Clay minerals in hydrothermally altered volcanic rocks, eastern Pontides, Turkey. Clays and Clay Minerals 47, 708–717. https://doi.org/10.1346/CCMN.1999.0470604

Centeno-Garcia, E., Ruis, J., Coney, P.J., Patchett, P.J., Ortega- Gutierrez, F., 1993. Guerrero terrane of Mexico: its role in the southern Cordillera from new geochemical data. Geology 21, 419–422. https://doi.org/10.1130/0091-7613(1993)021<0419:GTOMIR>2.3.CO;2

Centeno-García, E., Silva-Romo, G., 1997. Petrogenesis and tectonic evolution of Central Mexico during Triassic-Jurassic time. Revista Mexicana de Ciencias Geologicas 14, 244–260.

Clark, R.N., King, T.V.V., Klejwa, M., Swayze, G.A., Vergo, N., 1990. High spectral resolution reflectance spectroscopy of minerals. Journal of Geophysical Research 95. https://doi.org/10.1029/jb095ib08p12653

Clark, R.N., Swayze, G.A., Wise, R.A., Livo, K.E., Hoefen, T.M., Kokaly, R.F., Sutley, S.J., 2007. USGS Digital Spectral Library splib06a [WWW Document]. USGS Digital Data Series. URL http://speclab.cr.usgs.gov

Consejo de Recursos Minerales (COREMI), 2001. Informe final de la carta geologico-minera Villa de Santo Domingo F14-A-31. Pachuca, Hgo, Hgo.

da Cruz, R.S., Fernandes, C.M.D., Villas, R.N.N., Juliani, C., Monteiro, L.V.S., de Almeida, T.I.R., Lagler, B., de Carvalho Carneiro, C., Misas, C.M.E., 2015. A study of the hydrothermal alteration in Paleoproterozoic volcanic centers, São Félix do Xingu region, Amazonian Craton, Brazil, using short-wave infrared spectroscopy. Journal of Volcanology and Geothermal Research 304, 324–335.

https://doi.org/10.1016/j.jvolgeores.2015.09.005

De Cserna, Z., 1976. Geology of the Fresnillo area, Zacatecas, Mexico. Geological Society of America Bulletin 87, 1191. https://doi.org/10.1130/0016-7606(1976)87<1191:GOTFAZ>2.0.CO;2

De Pablo-Galan, L., 1979. The clay deposits of Mexico. Developments in Sedimentology 27, 475–486. https://doi.org/10.1016/S0070-4571(08)70745-3

Freydier, C., Lapierre, H., Ruiz, J., Tardy, M., Martinez-R, J., Coulon, C., 2000. The Early Cretaceous Arperos basin: An oceanic domain dividing the Guerrero arc from nuclear Mexico evidenced by the geochemistry of the lavas and sediments. Journal of South American Earth Sciences 13, 325–336. https://doi.org/10.1016/S0895-9811(00)00027-4

Fulignati, P., 2020. Clay minerals in hydrothermal systems. Minerals 10, 1–17. https://doi.org/10.3390/min10100919

Hanson, R.F., Keller, W.D., 1966. Genesis of Refractory Clay Near Guanajuato, Mexico. Clays and Clay Minerals 14, 259–267. https://doi.org/10.1346/ccmn.1966.0140123

Hanson, R.F., Zamora, R.A., Keller, W.D., 1981. Nacrite, Dickite, and Kaolinite in one Deposit in Nayarit, Mexico. Clays & Clay Minerals 29, 451–453.

Harraden, C.L., McNulty, B.A., Gregory, M.J., Lang, J.R., 2013. Shortwave infrared spectral analysis of hydrothermal alteration associated with the Pebble porphyry copper-gold-molybdenum deposit, Iliamna, Alaska. Economic Geology 108, 483–494. https://doi.org/10.2113/econgeo.108.3.483

Hedenquist, J., Arribas, A., Gonzalez-Urien, E.G., 2000. Exploration for Epithermal Gold Deposits. SEG Reviews 13, 245–277.

Hedenquist, J.W., 1990. The thermal and geochemical structure of the broadlands-ohaaki geothermal system, new zealand. Geothermics 19, 151–185. https://doi.org/10.1016/0375-6505(90)90014-3

Hedenquist, J.W., Browne, P.R.L., 1989. The evolution of the Waiotapu geothermal system, New Zealand, based on the chemical and isotopic composition of its fluids, minerals and rocks. Geochimica et

Cosmochimica Acta 53, 2235–2257. https://doi.org/10.1016/0016-7037(89)90347-5

Herrmann, W., Blake, M., Doyle, M., Huston, D., Kamprad, J., Merry, N., Pontual, S., 2001. Short Wavelength Infrared (SWIR) spectral analysis of hydrothermal alteration zones associated with base metal sulfide deposits at Rosebery and Western Tharsis, Tasmania, and Highway-Reward, Queensland. Economic Geology 96, 939–955. https://doi.org/10.2113/gsecongeo.96.5.939

Hocking, M.W.A., Hannington, M.D., Percival, J.B., Stoffers, P., Schwarz-Schampera, U., de Ronde, C.E.J., 2010. Clay alteration of volcaniclastic material in a submarine geothermal system, Bay of Plenty, New Zealand. Journal of Volcanology and Geothermal Research 191, 180–192. https://doi.org/10.1016/j.jvolgeores.2010.01.018

Inoue, A., 1995. Formation of Clay Minerals in Hydrothermal Environments. Origin and Mineralogy of Clays 268–329. https://doi.org/10.1007/978-3-662-12648-6_7

Inoue, A., 1983. Potassium fixation by clay minerals during hydrothermal treatment. Clays & Clay Minerals 31, 81–91. https://doi.org/10.1346/CCMN.1983.0310201

Inoue, A., Lanson, B., Marques-Fernandes, M., Sakharov, B.A., Murakami, T., Meunier, A., Beaufort, D., 2005. Illite-smectite mixed-layer minerals in the hydrothermal alteration of volcanic rocks: I. One-dimensional XRD structure analysis and characterization of component layers. Clays and Clay Minerals 53, 423–439. https://doi.org/10.1346/CCMN.2005.0530501

Inoue, A., Minato, H., Utada, M., 1978. Mineralogical properties and occurrence of illite/montmorillonite mixed layer minerals formed from Miocene volcanic glass in Waga- Omono district. Clay Science 5. https://doi.org/10.11362/jcssjclayscience1960.5.123

Inoue, A., Utada, M., 1983. Further investigations of a conversion series of dioctahedral mica/ smectites in the Shinzan hydrothermal alteration area, northeast Japan. Clays & Clay Minerals 31. https://doi.org/10.1346/CCMN.1983.0310601

Jin, Z., Zhu, J., Ji, J., Li, F., Lu, X., 2002. Two origins of illite at the Dexing porphyry Cu deposit, East China: Implications for ore-forming fluid constraint on illite crystallinity. Clays and Clay Minerals 50, 381–

387. https://doi.org/10.1346/000986002760833756

Juárez-Arriaga, E., Lawton, T.F., Ocampo-Díaz, Y.Z.E., Stockli, D.F., Solari, L., 2019. Sediment provenance, sediment-dispersal systems, and major arc-magmatic events recorded in the Mexican foreland basin, North-Central and Northeastern Mexico. International Geology Review 61, 2118–2142. https://doi.org/10.1080/00206814.2019.1581848

Kadir, S., Kart, F., 2009. The occurrence and origin of the söğüt kaolinite deposits in the paleozoic saricakaya granite-granodiorite complexes and overlying neogene sediments (Bilecik, Northwestern Turkey). Clays and Clay Minerals 57, 311–329. https://doi.org/10.1346/CCMN.2009.0570304

Keller, W.D., 1961. Hydrothermal Kaolinization (Endellitization) of Volcanic Glassy Rock. Clays and Clay Minerals 10, 333–343. https://doi.org/10.1346/ccmn.1961.0100129

Keller, W.D., Hanson, R.F., 1969. Hydrothermal argillation of volcanic pipes in limestone in Mexico. Clays and Clay Minerals 17. https://doi.org/10.1346/CCMN.1969.0170103

Keller, W.D., Hanson, R.F., 1968. Hydrothermal alteration of a rhyolite flow breccia near San Luis Potosi, Mexico, to refractory kaolin. Clays and Clay Minerals 16, 223–229. https://doi.org/10.1346/ccmn.1968.0160304

Keller, W.D., Hanson, R.F., Huang, W.H., Cervantes, A., 1971. Sequential active alteration of rhyolitic volcanic rock to endellite and a precursor phase of it at a spring in Michoacan, Mexico. Clays and Clay Minerals 19. https://doi.org/10.1346/ccmn.1971.0190209

Kubler, B., 1968. Évaluation quantitative du métamorphisme par la cristallinité de l'illite, état des progrès realisés ces dernières années. Centre de Recherches de Pau (Societé Nationale des Petôoles d'Aquitaine) 2, 385–397.

Kubler, B., 1967. La cristallinité de l'illite et les zones tout á fair supérieures du métamorphisme, in: Etages Tectoniques, Colloque de Neuchâtel 1966. pp. 105–121.

Kübler, B., Jaboyedoff, M., 2000. Illite crystallinity. Comptes Rendus de l'Academie de Sciences - Serie IIa:

Sciences de la Terre et des Planetes 331, 75–89. https://doi.org/10.1016/S1251-8050(00)01395-1

Labarthe Hernández, G., Jiménez López, L., Motilla Moreno, J., 1992. Jasperoide--guía posible en la exploración minera, Mesa Central, México. Revista mexicana de ciencias geológicas 10, 137–142.

Madondo, J., Canet, C., González-partida, E., Rodríguez-díaz, A.A., Núñez-useche, F., Alfonso, P., Rajabi, A., Pi, T., Blignaut, L., Vafeas, N., 2020. Geochemical constraints on the genesis of the ' Montaña de Manganeso ' vein-type Mn deposit , Mexican Plateau. Ore Geology Reviews 125. https://doi.org/10.1016/j.oregeorev.2020.103680

Maza, S.N., Collo, G., Morata, D., Lizana, C., Camus, E., Taussi, M., Renzulli, A., Mattioli, M., Godoy, B., Alvear, B., Pizarro, M., Ramírez, C., Rivera, G., 2018. Clay mineral associations in the clay cap from the Cerro Pabellón blind geothermal system, Andean Cordillera, Northern Chile. Clay Minerals 53, 117–141. https://doi.org/10.1180/clm.2018.9

McKeown, N.K., Bishop, J.L., Cuadros, J., Hillier, S., Amador, E., Makarewicz, H.D., Parente, M., Silver, E.A., 2011. Interpretation of reflectance spectra of clay mineral-silica mixtures:Implications for Martian clay mineralogy at Mawrth Vallis. Clays and Clay Minerals 59, 400–415. https://doi.org/10.1346/CCMN.2011.0590404

Merriman, R.J., Frey, M., 2009. Patterns of Very Low-Grade Metamorphism in Metapelitic Rocks, Low-Grade Metamorphism. https://doi.org/10.1002/9781444313345.ch3

Moore, D.M., Reynolds, R.C., 1989. X-ray diffraction and the identification and analysis of clay minerals. Oxford University Press.

Moore, D.M., Reynolds, R.C. j., 1997. X-Ray Diffraction and the Identification and Analysis of Clay Minerals, second edition, Oxford University Press.

Nieto-Samaniego, Á.F., Alaniz-Álvarez, S.A., Camprubí, A., 2007. Mesa Central of México: Stratigraphy, structure, and Cenozoic tectonic evolution, in: Special Paper 422: Geology of México: Celebrating the Centenary of the Geological Society of México. Geological Society of America, pp. 41–70. https://doi.org/10.1130/2007.2422(02)

Nieto-Samaniego, Á.F., Macías-Romo, C., Alaniz-Álvarez, S.A., 1996. Nuevas edades isotópicas de la cubierta volcánica cenozoica de la parte meridional de la Mesa Central, México. Revista Mexicana de Ciencias Geologicas 13, 117–122.

Pandarinath, K., Torres-Alvarado, I.S., Pushparani, D.E., Verma, S.P., 2006. X-ray diffraction analysis of hydrothermal minerals from the Los Azufres Geothermal System, Mexico. International Geology Review 48, 174–190. https://doi.org/10.2747/0020-6814.48.2.174

Pirajno, F., 2009. Hydrothermal Processes and Wall Rock Alteration, in: Hydrothermal Processes and Mineral Systems. Springer Netherlands, Dordrecht, pp. 73–164. https://doi.org/10.1007/978-1-4020-8613-7_2

Reyes, A.G., 1990. Petrology of Philippine geothermal systems and the application of alteration mineralogy to their assessment. Journal of Volcanology and Geothermal Research 43, 279–309.

Severmann, S., Mills, R.A., Palmer, M.R., Fallick, A.E., 2004. The origin of clay minerals in active and relict hydrothermal deposits. Geochimica et Cosmochimica Acta 68, 73–88. https://doi.org/10.1016/S0016-7037(03)00235-7

Sillitoe, R.H., 2015. Epithermal paleosurfaces. Mineralium Deposita 50, 767–793. https://doi.org/10.1007/s00126-015-0614-z

Sillitoe, R.H., 1993. Epithermal Models: Genetic Types, Geometrical Controls and Shallow Features. Mineral Deposit Modeling: Geological Association of Canada 403–417.

Simmons, S.F., Arehart, G., Simpson, M.P., Mauk, J.L., 2000. Origin of massive calcite veins in the Golden Cross low-sulfidation, epithermal Au-Ag deposit, New Zealand. Economic Geology 95, 99–112. https://doi.org/10.2113/gsecongeo.95.1.99

Simmons, S.F., Browne, P.R.L., 2000. Hydrothermal minerals and precious metals in the Broadlands-Ohaaki geothermal system: Implications for understanding low-sulfidation epithermal environments. Economic Geology 95, 971–999. https://doi.org/10.2113/gsecongeo.95.5.971

Simmons, S.F., White, N.C., John, D.A., 2005. Geological characteristics of epithermal precious and base

metal deposits. Economic Geology 100th Anniversary.

Simpson, M.P., 2015. Reflectance spectrometry [SWIR] of alteration minerals surrounding the Favona epithermal vein. Waihi vein system, Hauraki Goldfield. AusIMM New Zealand Branch Annual Conference 2015 490–499.

Srodon, J., Morgan, D.J., Eslinger, E. V., Eberl, D.D., Karlinger, M.R., 1986. Chemistry of illite/smectite and end-member illite. Clays & Clay Minerals 34, 368–378. https://doi.org/10.1346/CCMN.1986.0340403

Thompson, A., Thompson, J., 1996. Atlas of Alteration: A field and petrographic guide to hydrothermal alteration minerals, Mineral Deposits Division, Geological Association of Canada.

Thompson, A.J.B., Hauff, P.L., Robitaille, A.J., 1999. Alteration Mapping in Exploration: Application of Short-Wave Infrared (SWIR) Spectroscopy. Society of Economic Geologists 15–27.

Thompson, J.F.H., Abidin, H.Z., Both, R.A., Martosuroyo, S., Rafferty, W.J., Thompson, A.J.B., 1994. Alteration and epithermal mineralization in the Masupa Ria volcanic center, Central Kalimantan, Indonesia. Journal of Geochemical Exploration 50, 429–456. https://doi.org/10.1016/0375-6742(94)90035-3

Tillick, D.A., Peacor, D.R., Mauk, J.L., 2001. Genesis of dioctahedral phyllosilicates during hydrothermal alteration of volcanic rocks: I. The golden cross epithermal ore deposit, New Zealand. Clays and Clay Minerals 49, 126–140. https://doi.org/10.1346/CCMN.2001.0490203

Trask, P.D., Cabo, J.R.J., 1948. Manganese Deposits of Mexico. Geologic Investigations in the American Republics, 1946; pp. 209-316.

Tristán-González, M., Aguillón-Robles, A., Barboza-Gudiño, J.R., Cruz-Márquez, J., García-Arreola, M.E., Bellon, H., Franzetti, M., Labarthe-Hernández, G., 2015. Caraterísticas geoquímicas y significado tectónico del complejo de diques y domos félsicos del Paleoceno-Eoceno de La Tesorera, Zacatecas, en la Mesa Central, México. Revista Mexicana de Ciencias Geologicas 32, 455–474.

Tristán-González, M., Aguirre-Díaz, G.J., Labarthe-Hernández, G., Torres-Hernández, J.R., Bellon, H., 2009.

Post-Laramide and pre-Basin and Range deformation and implications for Paleogene (55-25 Ma) volcanism in central Mexico: A geological basis for a volcano-tectonic stress model. Tectonophysics 471, 136–152. https://doi.org/10.1016/j.tecto.2008.12.021

Tristán-González, M., Labarthe-Hernández, G., Aguirre-Díaz, G.J., Aguillón-Robles, A., 2008. Tectono-volcanic control of fissure type vents for the 28 Ma Panalillo ignimbrite in the Villa de Reyes Graben, San Luis Potosí, México. IOP Conference Series: Earth and Environmental Science 3, 12026. https://doi.org/10.1088/1755-1307/3/1/012026

Tritlla, J., Camprubi, A., Morales-Ramírez, J.M., Iriondo, A., Corona-Esquivel, R., González-Partida, E., Levresse, G., Carrillo-Chávez, A., 2004. The Ixtacamaxtitlán kaolinite deposit and sinter (Puebla State, Mexico): A magmatic-hydrothermal system telescoped by a shallow paleoaquifer. Geofluids 4, 329–340. https://doi.org/10.1111/j.1468-8123.2004.00095.x

Vázquez, F., Torres, L.M., Garza, L.L., Martínez, A., López, W., 2009. Caracterización por XANES, análisis mineralógico y aplicación industrial de un depósito de caolín de México. Materiales de Construccion 59, 113–121. https://doi.org/10.3989/mc.2009.43507

Vázquez, M., Bauluz, B., Nieto, F., Morata, D., 2016. Illitization sequence controlled by temperature in volcanic geothermal systems: The Tinguiririca geothermal field, Andean Cordillera, Central Chile. Applied Clay Science 134, 221–234. https://doi.org/10.1016/j.clay.2016.04.011

Vázquez, M., Nieto, F., Morata, D., Droguet, B., Carrillo-Rosua, F.J., Morales, S., 2014. Evolution of clay mineral assemblages in the Tinguiririca geothermal field, Andean Cordillera of central Chile: An XRD and HRTEM-AEM study. Journal of Volcanology and Geothermal Research 282, 43–59. https://doi.org/10.1016/j.jvolgeores.2014.05.022

Wang, L., Percival, J.B., Hedenquist, J.W., Hattori, K., Qin, K., 2021. Alteration Mineralogy of the Zhengguang Epithermal Au-Zn Deposit, Northeast China: Interpretation of Shortwave Infrared Analyses During Mineral Exploration and Assessment. Economic Geology 116, 389–406. https://doi.org/10.5382/econgeo.4792

Wilson, I.F., Rocha, V.S., 1948. Manganese deposits of the Montaña de Manganeso mine, San Luis Potosí, Mexico.

Yan, Y., Tillick, D.A., Peacor, D.R., Simmons, S.F., 2001. Genesis of dioctahedral phyllosilicates during hydrothermal alteration of volcanic rocks: II. The Broadlands-Ohaaki hydrothermal system, New Zealand. Clays and Clay Minerals 49, 141–155. https://doi.org/10.1346/CCMN.2001.0490204

Yang, K., Browne, P.R.L., Huntington, J.F., Walshe, J.L., 2001. Characterising the hydrothermal alteration of the Broadlands-Ohaaki geothermal system, New Zealand, using short-wave infrared spectroscopy. Journal of Volcanology and Geothermal Research 106, 53–65. https://doi.org/10.1016/S0377-0273(00)00264-X

Yang, K., Huntington, J.F., Gemmell, J.B., Scott, K.M., 2011. Variations in composition and abundance of white mica in the hydrothermal alteration system at Hellyer, Tasmania, as revealed by infrared reflectance spectroscopy. Journal of Geochemical Exploration 108, 143–156. https://doi.org/10.1016/j.gexplo.2011.01.001

Yang, K., Lian, C., Huntington, J.F., Peng, Q., Wang, Q., 2005. Infrared spectral reflectance characterization of the hydrothermal alteration at the Tuwu Cu-Au deposit, Xinjiang, China. Mineralium Deposita 40, 324–336. https://doi.org/10.1007/s00126-005-0479-7

Yildiz, A., Başaran, C., 2015. Sediment-hosted kaolin deposit from çakmaktepe (Uşak, Turkey): Its mineralogy, geochemistry, and genesis. Clays and Clay Minerals 63, 235–261. https://doi.org/10.1346/CCMN.2015.0630401

Zamora-Vega, O., Richards, J.P., Spell, T., Dufrane, S.A., Williamson, J., 2018. Multiple mineralization events in the Zacatecas Ag-Pb-Zn-Cu-Au district, and their relationship to the tectonomagmatic evolution of the Mesa Central, Mexico. Ore Geology Reviews 102, 519–561. https://doi.org/10.1016/j.oregeorev.2018.09.010

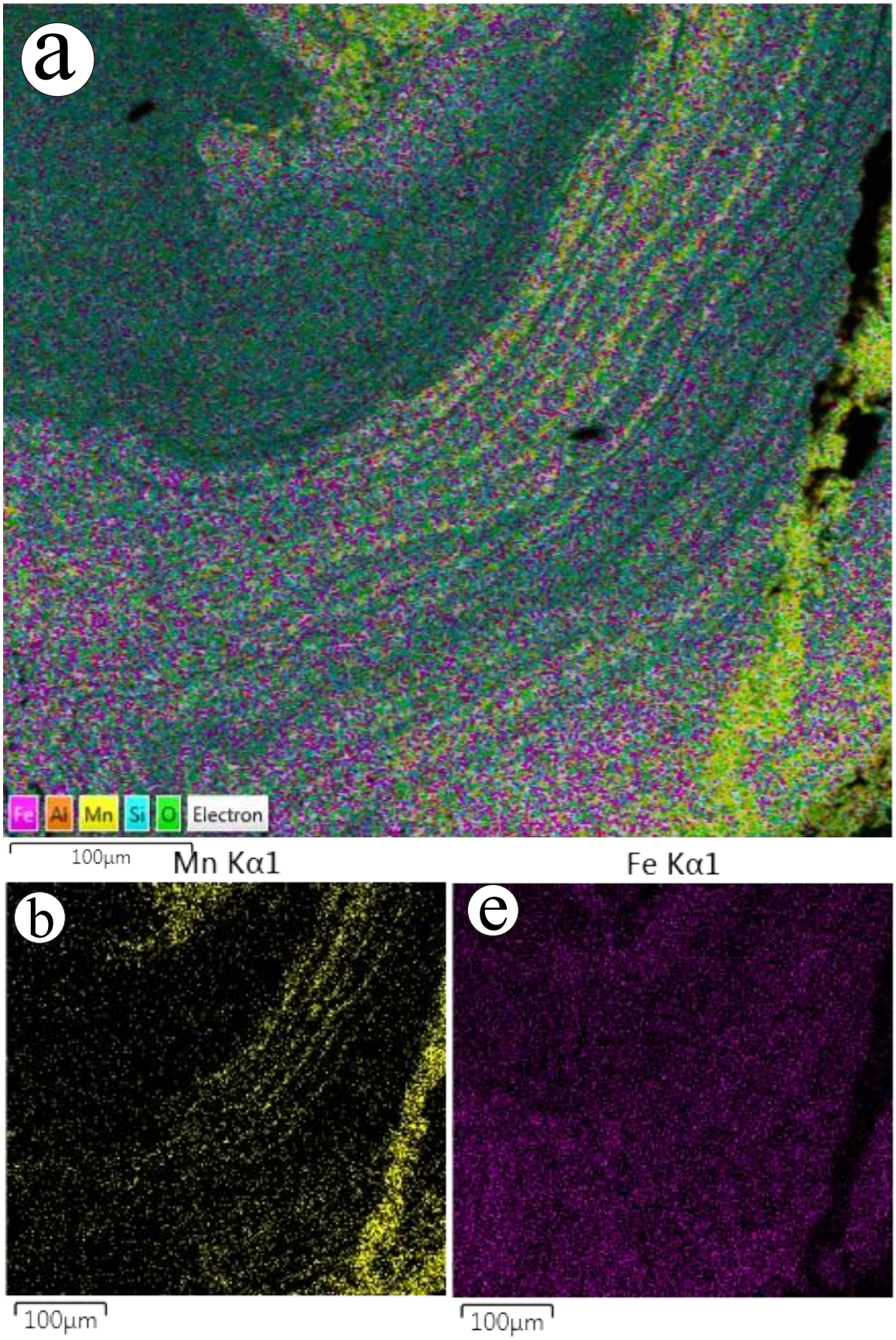
a
Fe
Al
Mn
Si
O
Electron
100µm
Mn Kα1
b
100µm
Fe Kα1
e
100µm

Geochemistry 81 (2021) 125789

Contents lists available at ScienceDirect

Geochemistry

journal homepage: www.elsevier.com/locate/chemer

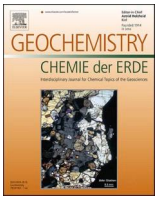

Geochemical evidence for a multi-source origin of manganese in the Montaña de Manganeso deposit, central Mexico

Joseph Madondo [a,*], Carles Canet [b,c], Eduardo González-Partida [d], Fernando Núñez-Useche [e], Augusto A. Rodríguez-Díaz [c], Abdorrahman Rajabi [f], Vanessa Colás [e], Lauren Blignaut [g], Nicholas Andrew Vafeas [h]

[a] Posgrado en Ciencias de la Tierra, Universidad Nacional Autónoma de México, Ciudad Universitaria, 04510 CdMx, Mexico
[b] Centro de Ciencias de la Atmósfera, Universidad Nacional Autónoma de México, Ciudad Universitaria, 04510 CdMx, Mexico
[c] Instituto de Geofísica, Universidad Nacional Autónoma de México, Ciudad Universitaria, 04510 CdMx, Mexico
[d] Centro de Geociencias, Universidad Nacional Autónoma de México, Juriquilla, 76230 Querétaro, Mexico
[e] Instituto de Geología, Universidad Nacional Autónoma de México, Ciudad Universitaria, 04510 CdMx, Mexico
[f] School of Geology, College of Science, University of Tehran, Tehran, Iran
[g] Department of Geology, University of Johannesburg, Corner Kingsway Avenue & University Road, Auckland Park, South Africa
[h] Irish Centre for Research in Applied Geosciences, O'Brien Centre for Science (East), University College Dublin, Belfield, Dublin 4, Ireland

ARTICLE INFO

Handling Editor: Astrid Holzheid

Keywords:
Mn oxides
Vein deposits
REE geochemistry
Hydrothermal origin
San Luis Potosí
Mexico

ABSTRACT

The Montaña de Manganeso is a manganese vein-type deposit spatially associated with back-arc basin remnants of the Guerrero tectonostratigraphic terrane. The study of major- and trace-element geochemical characteristics of the deposit provides insight into the controls on ore-forming processes within the area. The deposit is characterized by low Co, Cu and Ni abundances, and high Ba (>10,000 ppm) contents and Mn/Fe ratios (<500), typical of hydrothermal Mn deposits. In addition, the low ∑REE abundances (18.7 to 103 ppm), negative Ce anomalies (0.2 to 0.6), and positive Y (1.00 to 2.34) and Eu anomalies (0.6 to 4.4) also suggest a hydrothermal source for the deposit. Discrimination plots involving ∑REE and Zr vs. (Cu + Ni + Co) and Ce/Ce* vs. Nd and Y/Ho further indicate a hydrothermal source in an oxidizing depositional environment. The Mn-Fe-(Ni + Cu + Co), MnO_2-MgO-Fe_2O_3, (Cu/Zn)/Fe_2O_3 vs. (Zn/Ni)/MnO_2 and Na/Mg diagrams display intermediate signatures between marine and terrestrial environments. This suggest that the Montaña de Manganeso deposit is the result of two metallogenic stages: (I) the earliest stage, which involved the formation of Mn oxides by hydrothermal/diagenetic processes in the Arperos back-arc basin during the Cretaceous; and (II) the latest stage took place subsequent to accretion the Guerrero tectonostratigraphic terrane onto the continent and involved the remobilization of the Cretaceous submarine Mn oxides (and associated trace elements) and subsequent redeposition by Tertiary continental hydrothermal activity.

1. Introduction

With a global shift toward environmentally friendly energy production, manganese (Mn) oxides have generated an increased interest from the scientific community due to their low-cost applicability in technologies, such as rechargeable batteries, supercapacitors, catalysts, and lithium-manganese-oxide cathode batteries (Post, 1999; Barbato and Gautier, 2001; Tompsett and Islam, 2013; Birkner and Navrotsky, 2017; Fan et al., 2018). Nevertheless, the extraction of Mn oxides requires a complete and multidisciplinary understanding of the genesis of the deposits that contain them.

Mn oxides occur in a variety of modern and ancient geological settings throughout the geological epochs (Roy, 1997). Their accumulation is primarily a function of the redox potential and pH within the surrounding depositional environment through a combination of hydrothermal, hydrogenetic and/or diagenetic processes (Nicholson, 1992; Roy, 1992; Hein et al., 1997; Del Rio-Salas et al., 2013; Sinisi et al., 2018). Globally, the largest Mn deposits are the sedimentary-diagenetic type such as the Chiatura (Georgia) and Nikopol (Ukraine) deposits (Hein and Bolton, 1994; Kuleshov, 2017; Sasmaz et al., 2020, 2021). The

* Corresponding author.
E-mail address: joseph.madondo85@gmail.com (J. Madondo).

https://doi.org/10.1016/j.chemer.2021.125789
Received 3 March 2021; Received in revised form 5 June 2021; Accepted 6 June 2021
Available online 11 June 2021

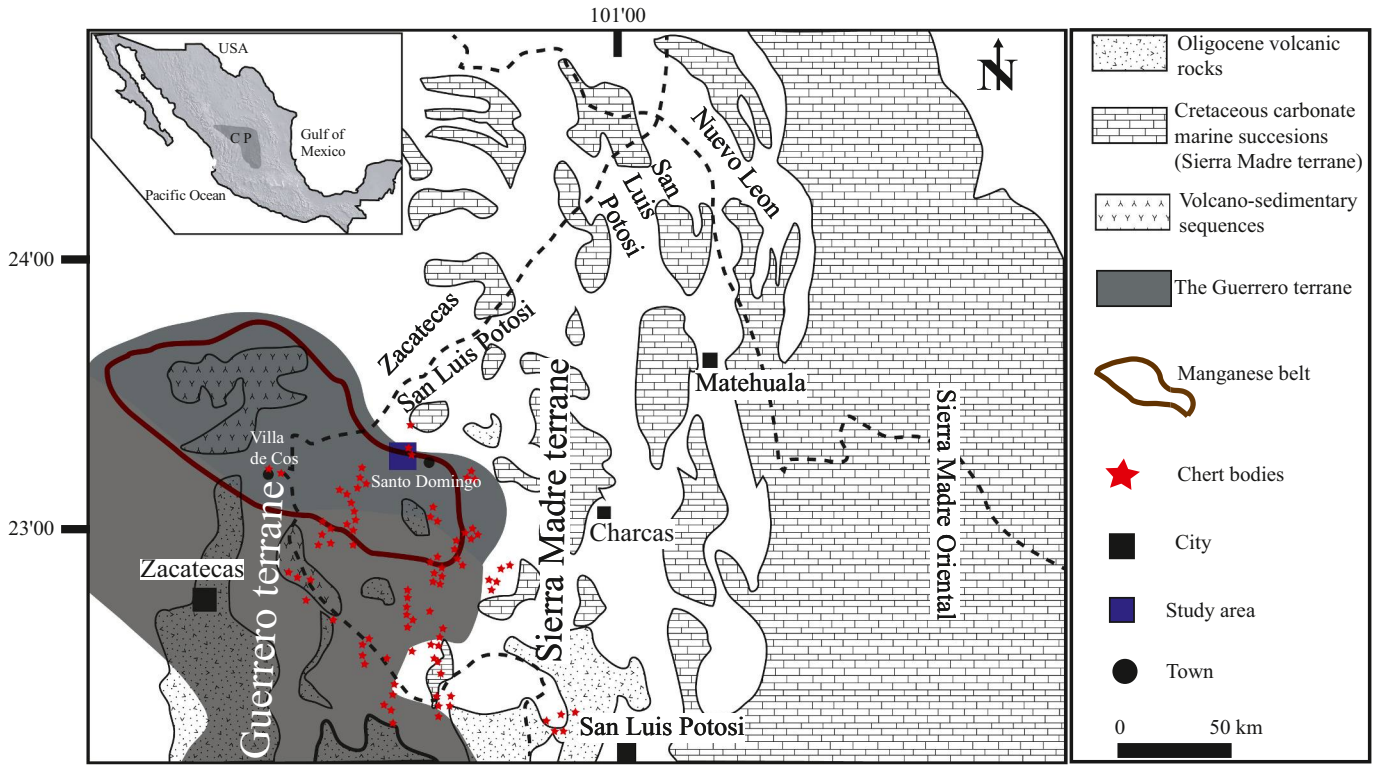

Fig. 1. A simplified geologic map of central-northern Mexico showing the location of the study area (modified after Hoppe et al., 2002). The boundary between the Guerrero and Sierra Madre terranes is adapted from Gomez and Gongora (2001). Insert: map of Mexico showing the location of the Central Plateau (C·P).

most widespread — though economically less significant — are hydrothermal deposits. They occur mainly as strata-bound layers and epithermal veins formed in diverse tectonic settings (Roy, 1997).

Mn deposits are documented throughout Mexico (Trask and Cabo, 1948; Wilson and Rocha, 1948). The giant Upper Jurassic sediment-hosted deposits of the Molango district in Hidalgo (east-central Mexico) are considered as the largest and most important Mn deposits in North America (Okita et al., 1988; Okita and Shanks, 1992). Epigenetic hydrothermal Mn deposits, however, are widely scattered in various mining districts throughout Mexico, with at least 335 deposits and occurrences reported in 20 states (Trask and Cabo, 1948). Well-known Mn hydrothermal deposits are those of Talamantes district (Chihuahua, northwestern Mexico), San Francisco district (Jalisco, central Mexico) and the Boleo region (Baja California Sur, northwest Mexico) (Wilson and Rocha, 1948; Zantop, 1978, 1981; Rodríguez-Díaz et al., 2005, 2010; Del Rio-Salas et al., 2008, 2013; Conly et al., 2011). While some early attempts were made to characterize and study the genesis of these deposits (Zantop, 1978, 1981,), it is only during the past two decades that sustained research has been published (Corona-Esquivel et al., 2000; Del Rio-Salas et al., 2008, 2013; Gómez-Caballero et al., 2010; Rodríguez-Díaz et al., 2010, 2019; Conly et al., 2011).

The Montaña de Manganeso Mn deposit (San Luis Potosí, central Mexico) was the major producer of Mn ore in Mexico during the 1940s (Wilson and Rocha, 1948). The occurrence of Mn oxides at the Montaña de Manganeso is well documented in reports of the Mexican Geological Survey (COREMI, 1980, 2001). The mineralogy of the Montaña de Manganeso deposit was first investigated by Wilson and Rocha (1948), who identified the Mn ore as primarily comprising pyrolusite with subordinated manganite and braunite. Alexandri (1977) further identified cryptomelane, nsutite, bementite and Mn diopside. More recently, Madondo et al. (2020) documented the occurrence of todorokite, birnessite and the hollandite group minerals. The genetic models proposed for the Montaña de Manganeso deposit have ranged from purely hot spring type deposits to multistage sedimentary-exhalative/hydrothermal type deposits (Alfaro and Alexandri, 1976; Alexandri, 1977; Tristán-González and Torres Hernández, 2000; COREMI, 2001; Olvera-Rosas et al., 2013; Madondo et al., 2020). A two-stage genesis for the Montaña de Manganeso deposit was first proposed by Alfaro and Alexandri (1976) who suggested that the Montaña de Manganeso deposit formed by remobilization of pre-existing ores. The idea was later retaken by COREMI (2001) who noticed pre-existing Mn-bearing chert fragments within the host rocks and interpreting them as evidence of a primary, seafloor volcano-sedimentary origin. Tristán-González and Torres Hernández (2000) also observed at Providencia (ca. 30 km SW of Montaña de Manganeso deposit) that the Mn mineralization and the host rocks shared common deformation features which could only be attributed to the Laramide orogenesis. Olvera-Rosas et al. (2013), concluded that primary manganese in the El Burrito and Manganita deposits at Villa de Cos (ca. about 60 km W of Montaña de Manganeso deposit) — also within the Mn belt — was probably deposited during the rift stage in a back-arc basin; a later hydrothermal stage, was suggested for the fault and fracture-controlled Mn mineralization of the deposits.

These models are mainly based on the geological setting of the deposit, with little mineralogical or geochemical data considered. However, as Mn oxides have a strong adsorption capacity and high uptake of certain cations from the surrounding fluid into their crystal structure (Bau et al., 1996; Sinisi et al., 2012), they acquire the geochemical signatures of the mineralizing fluids (Conly et al., 2011; Papavassiliou et al., 2017). Hence, Mn oxide mineralogy and trace element composition can be used to determine the depositional environment and conditions of formation of the deposit (Nicholson, 1992; Roy, 1992; Conly et al., 2011; Sasmaz et al., 2014, 2020). In this study, this approach is applied to provide new insights into the geochemical signature of the Montaña de Manganeso deposit with the aim of refining the current genetic model through the interpretation of multiple geochemical proxies. The proposed model contributes to the understanding of the processes involved in the genesis of this type of deposits, which is also key to better planning the extraction and use of Mn oxides.

Fig. 2. (A) Panoramic view of an outcrop of the Montaña de Manganeso deposit, seen from the SW and showing silicified Fe—Mn oxides ± quartz ± barite. Hydrothermal alteration is conspicuous. (B) Silicified Mn-oxides overlying the volcaniclastic sandstone horizon. (C) Steep stockwork of hematitic faults and breccia zones that represent the feeder zone for the upwelling hydrothermal fluids. (D) Silicified Mn oxide vein cuts through oxidized and hydrothermally altered volcaniclastic sediments of the host rocks. (E) Stratabound Mn oxides.

2. Geological setting

2.1. Regional framework

The Montaña de Manganeso deposit is located in the northern part of the Mexican Central Plateau physiographic province, within the poorly defined boundary between the Sierra Madre and Guerrero tectonostratigraphic terranes (Fig. 1) (Centeno-García and Silva-Romo, 1997). The evolution of the Mesozoic Basin of Central Mexico, included in the Sierra Madre terrane, was controlled by rifting and extensional tectonics related to the breakup of Pangea and subsequent opening of the Gulf of Mexico (Centeno-Garcia et al., 1993; Centeno-García and Silva-Romo, 1997; Martini and Ortega-Gutiérrez, 2018). This resulted in an Upper Triassic to Upper Cretaceous sedimentary succession (Carrillo-Bravo, 1982; Juárez-Arriaga et al., 2019) overlying a Triassic basement composed of low-grade metamorphic marine rocks (Barboza-Gudiño et al., 1998). In detail, this succession consists of Upper Triassic submarine fan turbidites (La Ballena Formation), Lower to Middle Jurassic volcanic and volcaniclastic deposits (Nazas Formation) (Centeno-García and Silva-Romo, 1997; Barboza-Gudiño et al., 1999, 2008; Centeno-García et al., 2008), and Upper Jurassic to Late Cretaceous clastic and shallow to deep marine carbonates (Zuloaga, La Caja, Taraises, Tamaulipas, Cuesta del Cura, Indidura and Caracol formations) (Carrillo-Bravo, 1982). On the other hand, the Guerrero tectonostratigraphic terrane, which is a product of subduction-related tectonics and terrane accretion along the paleo-Pacific margin (Centeno-Garcia et al., 1993; Centeno-García and Silva-Romo, 1997; Martini et al., 2011; Martini and Ortega-Gutiérrez, 2018), in this region is characterized by isolated remnants of back-arc origin (De Cserna, 1976; Centeno-García and Silva-Romo, 1997). The back-arc basin remnants comprise metamorphosed pelites, sandstone, conglomerate, pelagic limestone and basaltic pillow lavas exposed in the region of Fresnillo, eastern Zacatecas (De Cserna, 1976; Centeno-García and Silva-Romo, 1997).

Both the Sierra Madre and Guerrero tectonostratigraphic terranes were strongly deformed during the Laramide orogeny (Late Cretaceous) (Tristán-González et al., 2009b), forming a fold-and-thrust belt that covers most of central and western Mexico (Fitz-Diaz et al., 2014, 2018). The accretion of the Guerrero terrane arcs over the continent during the Laramide orogeny defined a suture zone at the boundary between the Guerrero and Sierra Madre terranes (Freydier et al., 2000; Centeno-García et al., 2003, 2008; Martini et al., 2013) that is estimated at approximately 100 km width in the study area (Sabanero-Sosa et al., 1999). Regional thrusts faults were also developed during the accretion. The post-Laramide extensional tectonics of the southern Basin and Range produced normal faults and reactivated the Laramide thrust faults creating NW-SE and NE-SW horst-and-graben structures (COREMI, 2001; Aguillón-Robles et al., 2009; Tristán-González et al., 2009b). The faults and structures provided the conduits for the ascent of magmas during the Eocene-Oligocene volcanism phase of the Sierra Madre Occidental, resulting in what have been termed the “graben calderas” (Aguirre-Díaz et al., 2008).

Volcanic rocks within the study region are poorly exposed due to the Cenozoic sedimentary cover (COREMI, 2001; Tristán-González et al., 2009b). However, volcanism is well documented further south in the Central Plateau and several authors have studied its evolution (McDowell et al., 1997; Aranda-Gómez and Mcdowell, 1998; Aranda-Gómez et al., 2007; Tristán-González et al., 2008, 2009a, 2012; Aguillón-Robles et al., 2009, 2014; Rodríguez-Ríos et al., 2013;). Subduction-related basaltic and andesitic volcanism occurred until 42 Ma, followed by a bimodal succession of high-silica rhyolites and alkaline basalts of intra-plate affinity between 42 and 31 Ma (Aguillón-Robles et al., 2014). During extensional, intra-plate tectonic activity, from 31 Ma to present-day, fissural alkaline basalts and andesites were formed (Aguillón-Robles et al., 2014).

2.2. Manganese deposits of the Central Plateau

In the Zacatecas and San Luis Potosi region Mn deposits are widely

distributed within the suture zone between the Guerrero and Sierra Madre terranes (Sabanero-Sosa et al., 1999). This region also hosts several volcanogenic (Pb—Zn—Cu) and epithermal (Au—Ag and base metal) deposits. VMS deposits were formed earlier in a back-arc setting, during the Cretaceous, while few others were formed on the epicontinental marine basins of eastern Mexico (Miranda-Gasca, 2000; Mortensen et al., 2008; Camprubí et al., 2017). The epithermal deposits were formed later, along major NW and NE-trending faults and related to Oligocene-Miocene magmatism (Camprubi et al., 2003; Nieto-Samaniego et al., 2007).

The Mn deposits of Zacatecas and San Luis Potosí are spatially scattered, but always occur near the Guerrero terrane back-arc basin remnants. Regarding the mineralization, these deposits display rather uniform characteristics such as: (*a*) fault-controlled mineralization; (*b*) discontinuous stratabound ore bodies and veins; (*c*) association with cherts and (*d*) development of pervasive hydrothermal alteration (COREMI, 2001; Sánchez-Rojas, 2013).

Mn mineralization at Montaña de Manganeso deposit is fault-controlled, developing as thick (5 to 30 m) irregular veins that are predominantly confined to NE-trending faults within strongly folded and fractured volcanic and volcaniclastic rocks (Trask and Cabo, 1948; Alexandri, 1977). On the exposed part of the deposit the host rocks are deformed and altered sandstones and shales with a significant volcanic glass component (Trask and Cabo, 1948). In underground exposures the host rocks comprise of altered sandstones, andesites and basaltic fragments. Mineralization also frequently occurs as fracture-filling veinlets and within cavities in breccias. The cross-cutting nature of the Mn veins is well-defined, exhibiting sharp contacts with the surrounding host rock (Fig. 2a). High rock porosity, favorable lithology, faults and fissures (Fig. 2b) enabled hydrothermal fluids to infiltrate and form prominent veins and occasionally strata-bound mineralization (Madondo et al., 2020). The deposit is affected by a pervasive hydrothermal alteration (Fig. 2c) and is strongly silicified such that the ore is frequently hard and brittle (Fig. A1 supplementary data).

Localized supergene alteration has resulted in the decomposition of the primary ore phases, rendering the ore soft and powdery with abundant reprecipitated colloform, pisolitic-like and globular oxy-hydroxides (Fig. A2 supplementary data).

In some underground exposures, however, the host rock is different from the succession exposed on the surface and comprise highly altered sandstones, andesites, basalts and Mn-bearing fragments (Fig. A3 supplementary data). Strata-bound Mn oxides are common (Fig. 2d) and radiolarites have been reported in some locations (COREMI, 2001). Both host rock and Mn-mineralization are highly deformed.

3. Methodology

44 rock samples were collected from surface outcrops and underground mine works at the Montaña de Manganeso deposit. Bulk mineralogy of a subset of 11 samples of the Mn mineralization unaffected by supergene processes was determined by X-ray diffraction (XRD) using an Empyrean diffractometer equipped with Ni filter, a Cu tube of fine focus and a PIXcel^{3d} detector available at the Instituto de Geología, Universidad Nacional Autónoma de México (Mexico). Measurements were performed in the 2θ angular range from 5° to 70°, with a step scan of 0.003° (2θ) and an integration time of 40 s per step. Rock samples were previously crushed and milled to 200 mesh and homogenized. Data was interpreted using HighScore Plus v4 software (PANalytical). Conventional search and match techniques for the analysis of the diffraction patterns were employed for qualitative and semi-quantitative analysis.

The following minerals were identified from the Montaña de Manganeso deposit by comparison with the Inorganic Crystal Structure Database (ICSD): pyrolusite (ICSD 980056006, ICSD 980073716, ICSD 980000393), cryptomelane (ICSD 980059159), todorokite (ICSD 980202727, birnessite (ICSD 980240249) ICSD 980054113)and the hollandite group minerals hollandite (ICSD 980027240, ICSD 980062096, ICSD 980172913) and romanechite (ICSD 980064973) hereafter referred by the group name hollandite.

Scanning electron microscopy (SEM) was used for Mn oxide textural characterization. This study was carried out on six polished thin sections previously examined by reflected light microscopy. Backscatter electron (BSE) microscopy and energy dispersive spectrometry (EDS) were conducted on all polished thin sections after they were coated with a thin layer of carbon (12 nm-thick) to improve electron dispersion. SEM-EDS analyses were carried out using a Tescan Vega 3 system equipped with an Oxford X-Max 50 mm^2 detector. Elemental X-ray mapping was performed simultaneously by employing four WDS spectrometers. Analyses were undertaken at an accelerating voltage of 20 kV, a beam intensity of 15 nA and a working distance of 15 mm. Interpretation was conducted using Oxford Aztec software V. 2.2 at the Central Analytical Facility of the Faculty of Science, at the University of Johannesburg.

Wavelength Dispersive X-ray Spectroscopy (WDS) analyses were performed on the same thin sections using a JEOL JXA-8900R EMPA instrument available at the Laboratorio Universitario de Petrología of the Instituto de Geofísica, Universidad Nacional Autónoma de México (México), in order to obtain quantitative microanalysis data. An accelerating voltage of 20 kV, a beam current of 20 nA, and a spot size of 1 μm were used for all analyses. A counting time of 40 s was used for all elements except for K and Na, where a counting time of 10 s was used. Plagioclase (CaKα), biotite (KKα), diopside (NaKα), rhodonite (FeKα), kaersutite (SiKα), almandine (MgKα), kaersutite (AlKα), sphalerite (ZnKα), galena (PbMα), barite (BaLα), bustamite (MnKα) and cuprite (CuKα) were used as standards for the analysis of the Mn oxides. The detection limits for all elements were 0.01 wt%. A rhodonite test sample was used to calibrate the equipment to assure maximum accuracy and precision.

Whole rock major and trace elements, as well as Rare Earth Elements (REE) of the 11 samples previously analyzed by DRX, were analyzed by Inductively Coupled Plasma–Mass spectrometry (ICP-MS) and Inductively Coupled Plasma Optical Emission Spectroscopy (ICP-OES; Ultra-trace 2 method) using a Perkin Elmer Sciex ELAN 9000 at Activation Laboratories (ActLabs) (Ancaster, Ontario, Canada). A correlation matrix was prepared using the software Statistica V. 13. The coefficient correlations are significant at $P < 0.05$ for $r > 0.25$. Binary and ternary discrimination diagrams were processed in GCDkit package for R V. 3.6.0.

The Ce and Eu anomalies (Ce/Ce* and Eu/Eu*) were calculated using the following the equations of Taylor and McLennan (1985):

$$\mathrm{Ce/Ce*} = (\mathrm{Ce})\mathrm{CN}/\sqrt{((\mathrm{La})\mathrm{CN}*(Pr)\mathrm{CN}\ )}$$

$$\mathrm{Eu/Eu*} = (\mathrm{Eu})\mathrm{CN}/\sqrt{((\mathrm{Sm})\mathrm{CN}*(\mathrm{Gd})\mathrm{CN}\ )}$$

In these expressions, Eu and Ce are the actual concentrations of these elements, and Eu* and Ce* are the predicted concentrations based on interpolation of neighboring REE. The subscript "CN" indicates chondrite-normalized values (Boynton, 1984). The Ce anomalies of PAAS-normalized abundances were calculated using the formula of Bau et al. (2014):

$$\mathrm{Ce/Ce*} = (\mathrm{Ce})\mathrm{PAAS}/((0.5\mathrm{La})\mathrm{PAAS} + (0.5Pr)\mathrm{PAAS}\ )$$

The heavy-REE (HREE), middle-REE (MREE) and light-REE (LREE) are defined as the elements from La to Nd, Sm to Tb and Dy to Lu, respectively.

4. Results

4.1. X-ray diffraction

According to XRD results, pyrolusite, cryptomelane, hollandite, todorokite and birnessite are the major Mn phases. Pyrolusite,

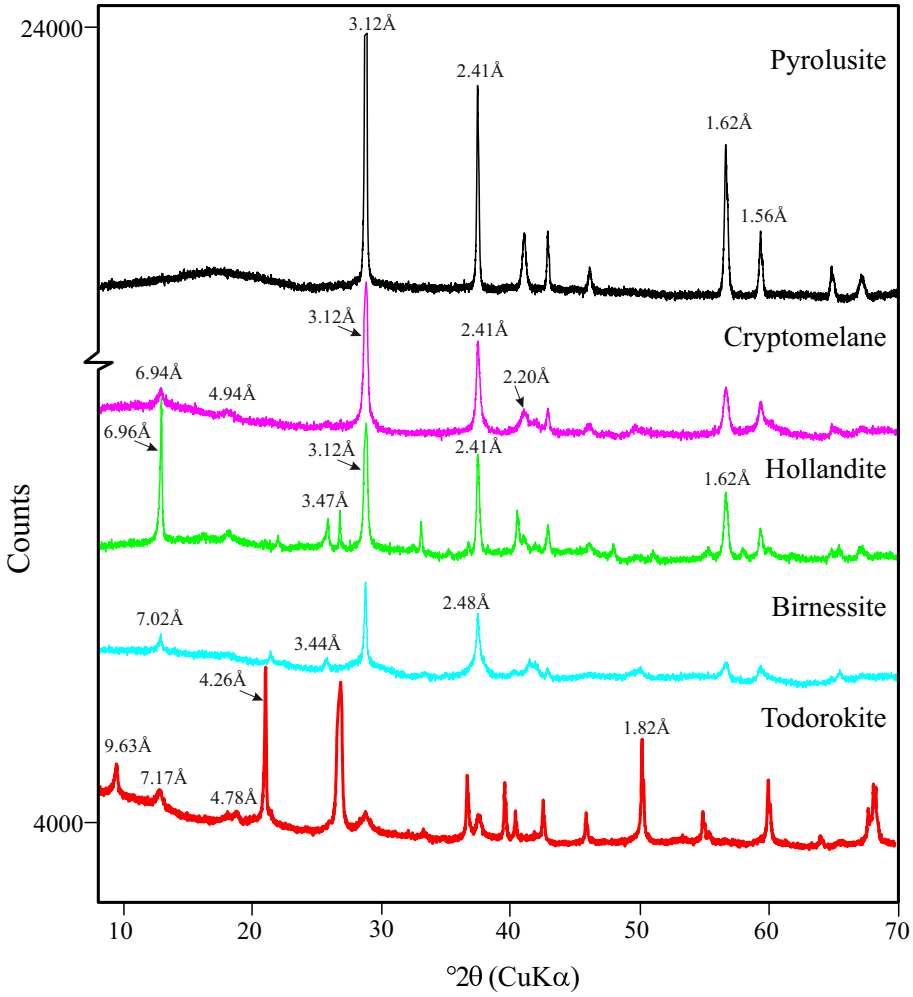

Fig. 3. Representative X-ray diffraction patterns of Mn oxides from the Montaña de Manganeso deposit with representative peak positions of cryptomelane, hollandite, pyrolusite, todorokite, romanechite and birnessite. Cryptomelane and pyrolusite patterns are displaced vertically for clarity.

cryptomelane and hollandite produced sharp XRD peaks of high resolution and intensity indicating high crystallinity, whereas birnessite and todorokite produced broad peaks of low intensity, indicating poor crystallinity and possibly structural disorder (Fig. 3). Despite the low crystallinity of birnessite and todorokite, they were identified by their diagnostic peaks. Todorokite has diagnostic peaks at 9.63 Å (9.62 Å Dolenec, 2003), 7.17 Å (7.09 Å; Post et al., 2003; 7.13 Å; Dolenec, 2003) and 4.78 Å (4.76 Å; Post and Bish, 1988; 4.8 Å; Roy et al., 1990), corresponding to 9.17, 12.33 and 18.53 2θ angle position; and birnessite has diagnostic peaks positioned at 2θ of 12.59 (7.02 Å), 25.84 (3.44 Å) and 36.18 (2.48 Å) (c.f 7.02, 3.50, 2.46 Å Lanson et al., 2002; 7.1, 3.5 and 2.4 Å Hein et al., 1997).

4.2. Scanning electron microscopy

Mn oxides from Montaña de Manganeso are fine-grained and exhibit banded, replacement and colloform textures (Figs. 4–8). Several point and line scan EDS analyses were performed across mineral aggregates whose composition are shown in the accompanying spectra (Figs. 4, 6, 7 and 8).

Hollandite frequently occur as light-colored colloform bands alternating with dark-colored chalcedony bands (Fig. 4a). The line scan analysis across the bands reveals that Fe exhibits a negative correlation with Ba and Mn (Fig. 4b, c), but displays a positive correlation with Si (Fig. 4d), due to the occurrence of Ba as a major cation in the hollandite group minerals and co-precipitation of Si and Fe as chert, respectively.

Pyrolusite principally occurs as colloform, interlayered bands with chalcedony (Fig. 5). Acquired SEM-BSE imagery of a concretion rich in pyrolusite show that the bands have variable brightness depending on the relative abundance of Mn and Si (Fig. 5a and b). Elemental distribution maps of Mn, Si, Ba and Fe (Fig. 5c–f) in the colloform bands show that the brighter bands are associated with a higher Mn content (Fig. 5c), and the darker bands with higher Si content. Fe and Ba are more uniformly distributed in the bands (Fig. 5e and f).

Cryptomelane also occurs as concentric colloform bands that intimately alternate, at micrometric level, with hollandite (Fig. 6). Alternating bands of hollandite and cryptomelane, with high and low Ba^{2+}/K^{+} ratios, respectively, can be differentiated by their brightness under BSE imaging, with bands rich in microcrystalline hollandite distinctly brighter and those bearing cryptomelane noticeably darker. Variability in brightness, however, is also related to changes in K + Ba concentrations, as shown in the line-scan profile of these cations (Fig. 6c). Cryptomelane is also observed to be intermixed with subordinate amounts of hollandite and possibly coronadite (Fig. 7a and b), expressed as variable minor amounts of Pb and Ba in the accompanying line scan (Fig. 7c).

Todorokite is predominantly fibrous (Fig. 8a) and exhibits high porosity, commonly filled with quartz (Fig. 8b). Pyrolusite occurs as late crystals within fractures in the todorokite (Fig. 8a).

4.3. Mineral chemistry (microprobe data)

Representative microprobe data for the Montaña de Manganeso Mn

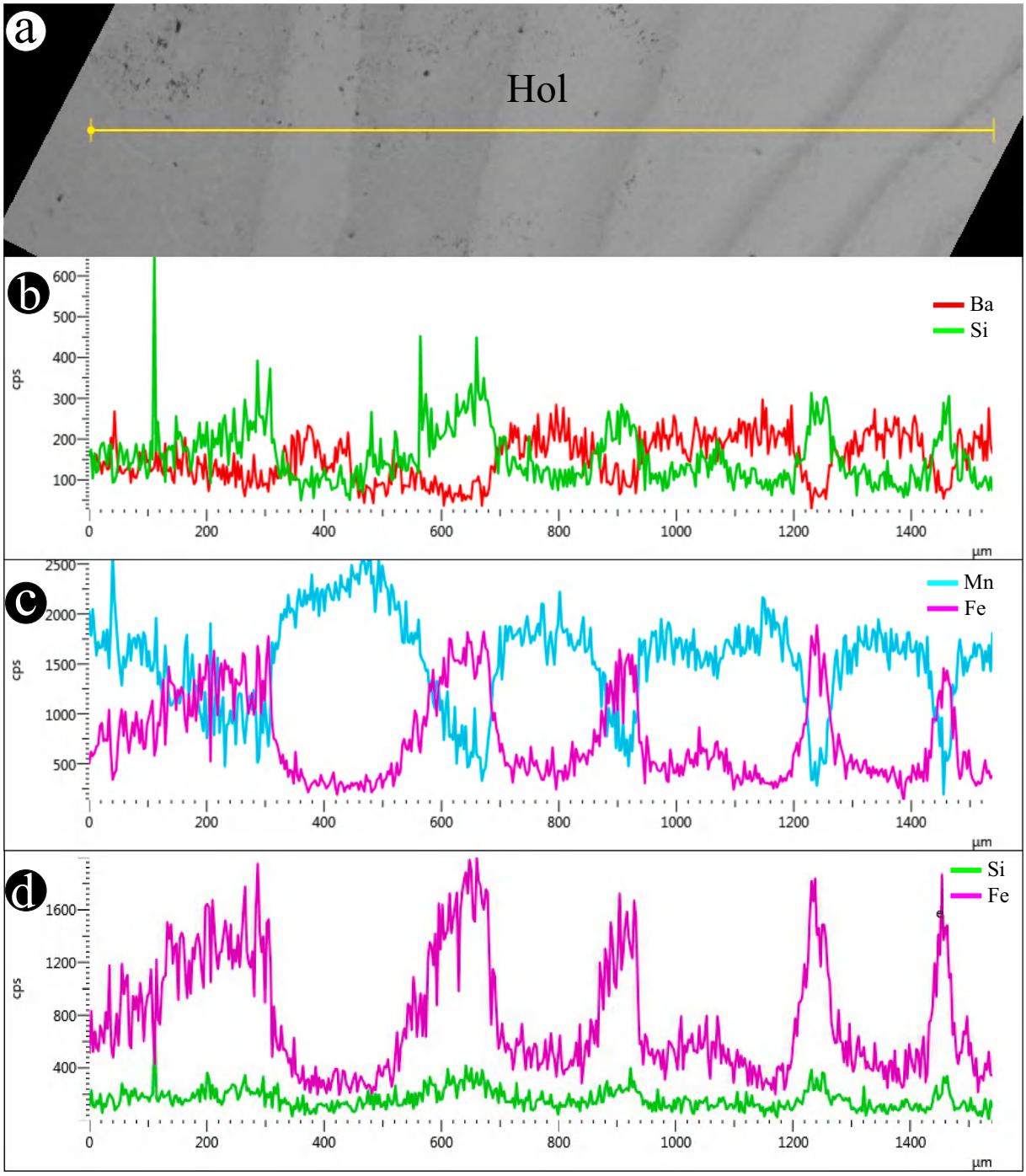

Fig. 4. (A and B) Hollandite-romanechite mixture with Fe—Si rich dark bands. (C) Ba—Si line scan revealing the negative correlation between the two. (D) Line scan showing positive correlation between Fe and Si.

ores is provided in Table A1. The fine-grained and intimately intermixed mode of occurrence of the ore minerals hindered the precise determination of quantitative mineral chemistry for the individual minerals identified by XRD. Therefore, microprobe results in most cases represent mixed chemical compositions rather than the chemistry of individual minerals.

Correlation data on some major and minor and trace element contents from the microprobe data are presented in Table 1. Significant positive correlations exist between CaO and SrO ($r = 0.75$) and between Na_2O and SrO ($r = 0.60$) (Table 1). Srontiomelane was not detected by XRD in any of the samples and no significant correlation exists between SrO and BaO ($r = 0.40$), suggesting that Sr is replacing Ca in Ca-bearing Mn oxides such as todorokite and birnessite. A negative correlation exists between MnO and BaO ($r = -0.73$). The negative correlation is surprising, given that Ba is generally incorporated into the crystal lattice of hollandite and romanechite, but in different structural sites than Mn. A negative correlation between MnO and FeO ($r = -0.57$) is consistent with Fe and Mn fractionation commonly observed in hydrothermal systems. The correlations between Mn and Cu and between Ni and Co are not significant ($-0.01 < r < 0.35$), hence these elements can be regarded as behaving independently from each other.

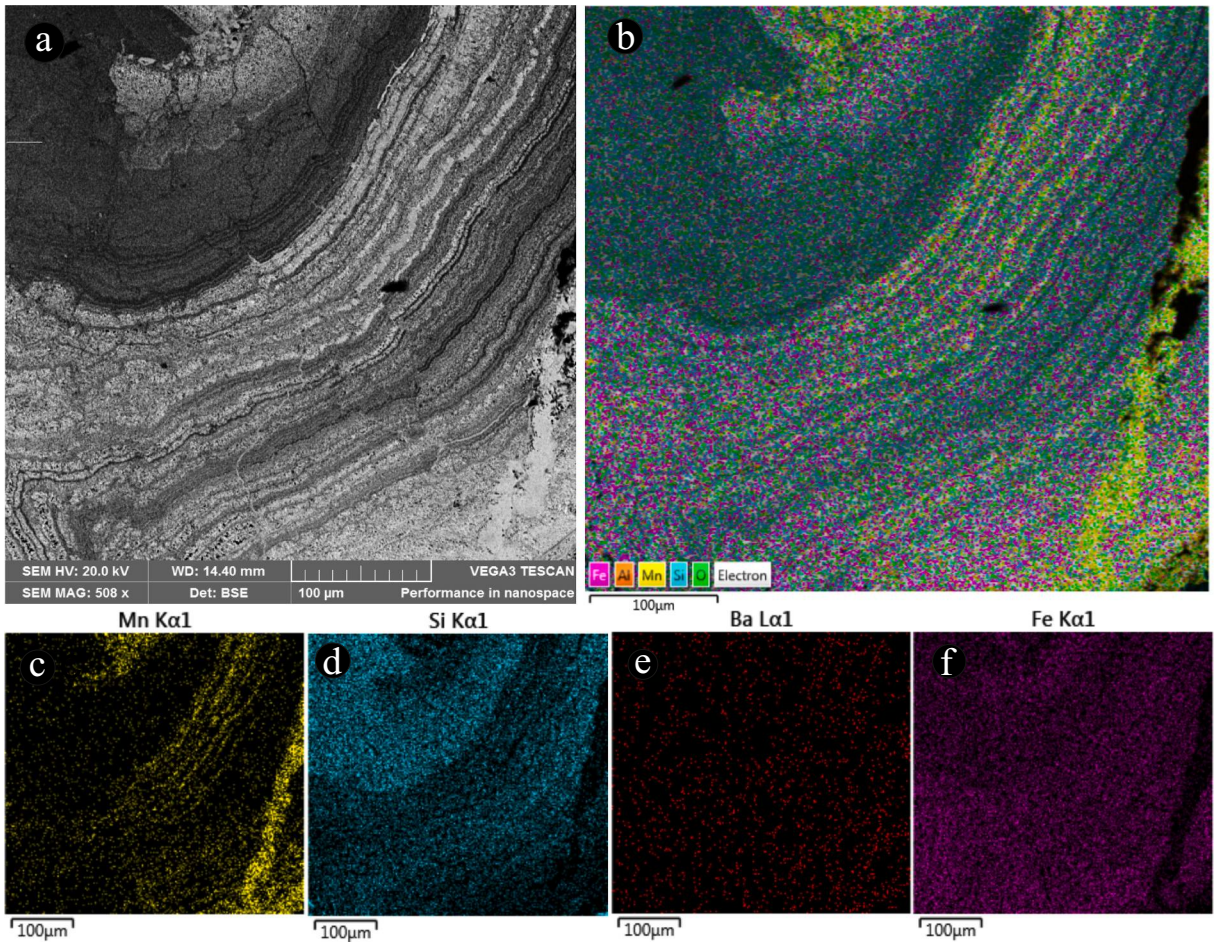

Fig. 5. (A) BSE image showing the colloform banding of pyrolusite. (B) Combined element map showing the distribution of Fe, Al, Mn, Si and O. (C–F) Elemental maps showing the distribution of Mn, Si, Ba and Fe in the colloform bands of pyrolusite.

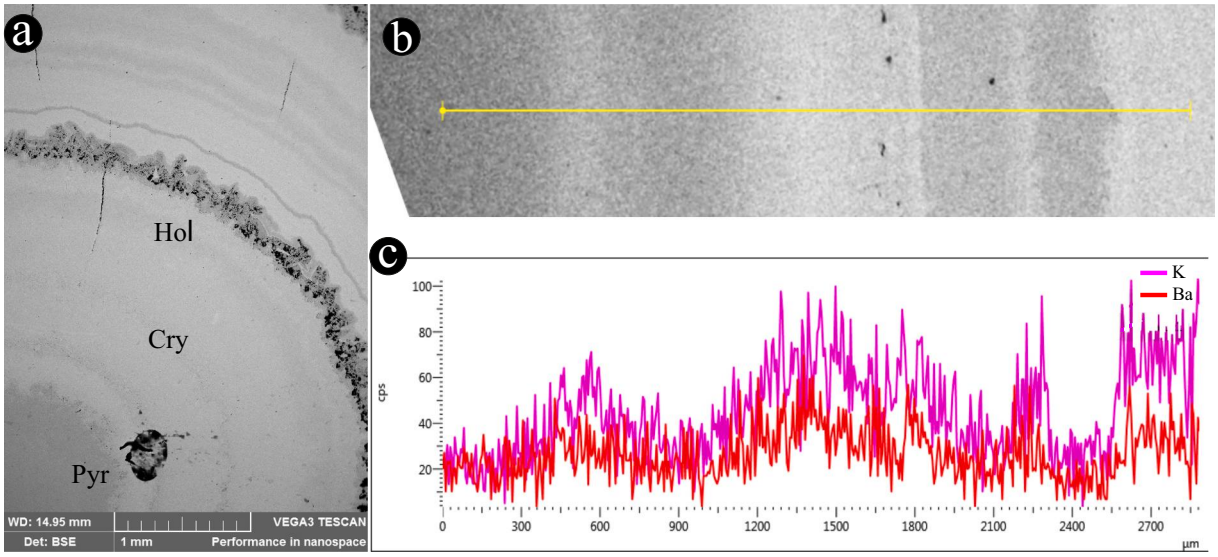

Fig. 6. (A) Cryptomelane-hollandite banding. (B) Point scan, and (C) line scans of the bands that reveal a positive correlation between K^{+} and Ba^{2+}.

4.4. *Whole rock geochemistry*

The whole rock (trace element) chemical composition of 11 representative samples of Mn ores from the Montaña de Manganeso deposit is shown in Table 2. Trace element contents of samples from Montaña de Manganeso deposit are highly variable, exhibiting similar Co (17 ppm), but higher Ba (<10 wt%), Sr (1300 ppm), As (183 ppm), V (137 ppm), Cr (117 ppm), Mo (88 ppm), Ni (68 ppm), Zn (151 ppm), and Cu (63 ppm)

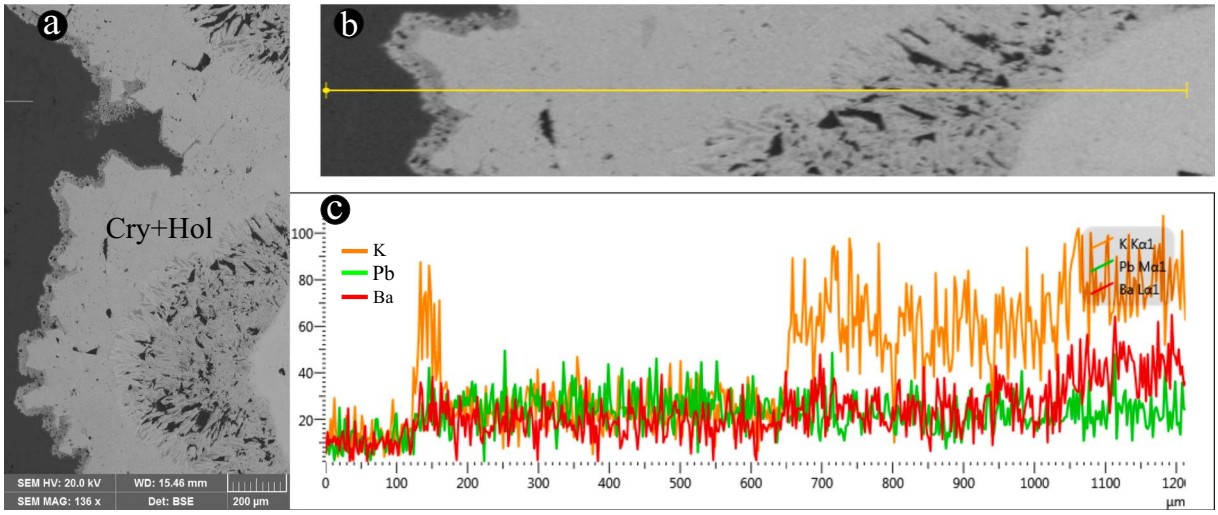

Fig. 7. (A) Hollandite–cryptomelane intermixed assemblage. (B) and (C) Line scan analysis of K, Pb and Ba.

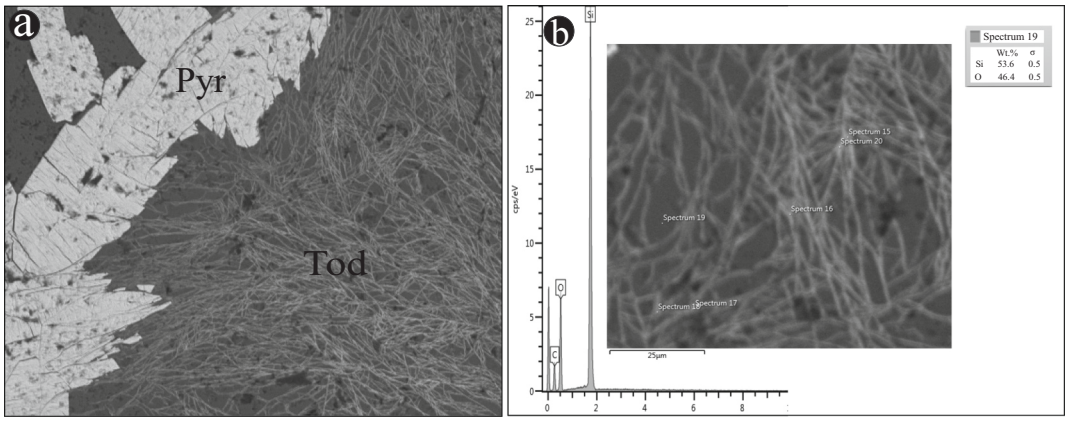

Fig. 8. (A) Fibrous todorokite with late prismatic pyrolusite crystals. (B) Point scans indicate presence of SiO_2 within todorokite pores.

Table 1
Correlation between the major element oxides of samples from Montaña de Manganeso deposit.

Variable	K_2O	Na_2O	CuO	Al_2O_3	MgO	CaO	SrO	MnO	PbO	FeO	BaO	ZnO	NiO	CoO
K_2O	1.00													
Na_2O	0.48	1.00												
CuO	0.02	−0.05	1.00											
Al_2O_3	−0.22	−0.11	−0.14	1.00										
MgO	−0.09	0.07	−0.05	−0.10	1.00									
CaO	0.05	0.40	−0.13	−0.18	0.34	1.00								
SrO	0.37	0.60	−0.06	−0.24	0.13	0.75	1.00							
MnO	−0.21	−0.42	−0.01	0.13	−0.38	−0.66	−0.56	1.00						
PbO	−0.11	−0.25	0.22	−0.10	−0.01	−0.28	−0.23	0.32	1.00					
FeO	−0.14	0.11	−0.13	0.05	0.24	0.39	0.15	−0.57	−0.14	1.00				
BaO	−0.01	0.35	0.00	−0.11	0.14	0.46	0.40	−0.73	−0.31	0.22	1.00			
ZnO	0.14	0.21	0.12	0.27	−0.15	−0.01	0.09	−0.11	−0.16	0.04	0.05	1.00		
NiO	−0.12	0.07	0.12	−0.03	0.21	0.34	0.25	−0.35	−0.09	0.31	0.28	0.00	1.00	
CoO	0.06	0.14	−0.03	0.15	−0.03	0.12	0.04	−0.06	−0.14	0.06	0.06	0.03	0.05	1.00

contents than the upper continental crust (Taylor and McLennan, 1995). Co/Zn ratios vary from 0.04 to 0.31, whereas Co/Ni ratios mostly range from 0.10 to 0.60, with one sample showing a value of 1.12. Total REE (ΣREE) contents are low, ranging from 19 to 103 ppm. Samples are enriched in LREEs compared with MREEs (La_{CN}/Sm_{CN} ratio from 1.54 to 16.98) and HREEs (La_{CN}/Yb_{CN} from 2.83 to 19.75). There is no significant enrichment of MREEs over HREEs (Gd_{CN}/Yb_{CN} from 0.88 to 1.20). Ce anomalies are negative, ranging from 0.2 to 0.6, whereas Y/Ho ratios range from 27.4 to 63.7 and Eu anomalies are variable, ranging from 0.6 to 4.4.

5. Discussion

The processes responsible for Mn mineralization at the Montaña de Manganeso deposit are determined through a comprehensive evaluation of multiple mineral and geochemical proxies. Geodynamic and

Table 2
Whole-rock chemical composition (trace elements) of selected samples of the Montaña de Manganeso deposit.

Sample	Li (ppm)	Cd (ppm)	B (ppm)	P (ppm)	S (ppm)	V (ppm)	Cr (ppm)	Ti (ppm)	Co (ppm)	Ni (ppm)	Pb (ppm)	Zn (ppm)	Th (ppm)	U (ppm)	Ag (ppm)	Au (ppb)	Co/Zn	Co/Ni
MM-102A	1.5	0.18	22	0.068	0.019	79	270	<0.01	9.9	75.3	11.6	130	<0.01	4.7	0.02	21.1	0.08	0.13
MM-T3B	6.7	0.13	37	0.104	0.008	69	2	<0.01	13.1	55.4	8.9	248	<0.01	3.6	0.05	2.1	0.05	0.24
MM-103	13.1	0.1	58	0.129	0.007	73	103	<0.01	10	119	2.8	191	<0.01	2.7	0.03	29.5	0.05	0.08
MM-25D (2)	1.4	0.17	27	0.012	0.014	308	20	<0.01	10.2	34.8	3.2	75.1	<0.01	1.8	0.16	8.5	0.14	0.29
MM-25D (1)	10.5	0.17	30	0.12	0.002	144	60	<0.01	14.9	66	0.2	125	<0.01	7.7	0.02	8.7	0.12	0.23
MM-106C	12.6	0.08	25	0.126	0.002	127	41	<0.01	18.5	70.8	1.1	132	<0.01	7.6	0.02	10.5	0.14	0.26
MM-6	7.3	1.16	19	0.026	0.007	85	76	<0.01	57.7	96.1	7.9	187	<0.01	4.5	0.05	4.4	0.31	0.60
MM-T3	33.6	<0.01	22	0.019	0.009	56	<1	<0.01	8.6	86.2	4.4	182	<0.01	4.9	0.02	<0.5	0.05	0.10
MM-105(2)	2.2	<0.01	14	0.111	0.008	94	141	<0.01	6.7	63	8.6	163	<0.01	3.7	<0.02	7.1	0.04	0.11
MM-208B	9.5	<0.01	15	0.058	0.016	57	256	<0.01	29.8	26.7	2.2	151	<0.01	4.7	0.02	2.8	0.20	1.12
MM-25C	5.4	<0.01	33	0.023	0.009	413	202	0.02	9.7	51.7	22	74.2	0.5	2.7	0.02	9.3	0.13	0.19

Sample	Cu (ppm)	Be (ppm)	Ga (ppm)	Ge (ppm)	As (ppm)	Se (ppm)	Rb (ppm)	Sr (ppm)	Te (ppm)	Zr (ppm)	Mo (ppm)	Tl (ppm)	W (ppm)	Cs (ppm)	Bi (ppm)	Sn (ppm)	Sb (ppm)	Hg (ppb)
MM-102A	51.1	4	<0.02	3.9	120	1.5	0.6	1340	0.02	3	129	3.46	1.1	0.18	0.04	0.4	3.31	650
MM-T3B	125	2.1	<0.02	9.1	149	3.6	1.5	1070	<0.02	2	32.1	0.18	1.6	0.18	0.02	1.04	3.29	360
MM-103	55.2	1.3	2.68	11.4	122	0.8	2.8	888	0.07	2.8	58.6	0.08	0.7	0.86	0.02	0.27	7.13	500
MM-25D (2)	30.7	0.6	<0.02	10	47.2	<0.1	6.3	2430	<0.02	2.9	34.9	0.27	0.2	0.06	0.02	0.23	2.02	250
MM-25D (1)	27.7	1.8	<0.02	40	383	1.3	2.3	429	0.11	2.3	184	0.07	0.8	0.17	<0.02	0.21	9.51	360
MM-106C	32.4	1.8	17.3	46.8	441	1.3	2.1	410	0.11	2.4	186	0.04	4	0.17	0.02	0.27	20	420
MM-6	66.4	2	22.7	3.9	198	0.4	3.1	>5000	<0.02	2.2	112	6.81	0.1	0.4	<0.02	0.19	0.95	300
MM-T3	122	3.3	<0.02	7.3	156	0.3	5	2500	0.06	0.7	40.7	0.97	0.4	0.79	0.02	0.49	2.05	40
MM-105 (2)	52.3	2.5	1.28	6.1	106	2.6	0.9	1160	0.04	2.5	131	1.44	0.1	0.04	<0.02	0.2	3.8	190
MM-208B	41.5	2.2	23.1	8.6	72.4	1.1	5.3	2550	0.04	1.4	27.9	0.19	0.9	0.3	0.03	0.43	6.56	580
MM-25C	84.4	1.5	2.69	1.1	220	<0.1	3.2	227	0.02	14.4	27.6	0.67	3.4	0.57	0.11	0.42	7.84	340

Sample	Sc (ppm)	Pr (ppm)	Gd (ppm)	Dy (ppm)	Ho (ppm)	Er (ppm)	Tm (ppm)	Nb (ppm)	La (ppm)	Ce (ppm)	Nd (ppm)	Sm (ppm)	Eu (ppm)	Tb (ppm)	Yb (ppm)	Lu (ppm)	Y (ppm)	Y/Ho	Y/Ho PAAS	Eu_{anom}	Ce_{anom}
MM-102A	0.5	1.1	1.6	1.9	0.4	1.2	0.2	<0.1	5.6	5.4	4.82	1.1	0.3	0.2	1.3	0.2	13.5	33.8	1.24	0.7	0.5
MM-T3B	0.4	1.3	1.3	1.2	0.3	0.9	0.2	<0.1	7.4	3.1	5.3	1.1	0.4	0.2	1.1	0.2	10.3	34.3	1.26	1.0	0.2
MM-103	0.6	1.3	1.1	1	0.2	0.6	<0.1	<0.1	7.9	6.6	5.05	0.9	0.4	0.1	0.4	<0.1	6.2	31.0	1.14	1.2	0.5
MM-25D (2)	0.7	0.7	0.5	0.7	0.1	0.4	<0.1	<0.1	4.2	1.6	3.06	0.5	0.2	<0.1	0.3	<0.1	6.37	63.7	2.34	1.2	0.2
MM-25D (1)	0.3	0.4	0.6	0.7	0.2	0.4	<0.1	<0.1	2.5	1.1	1.58	0.3	0.5	<0.1	0.5	0.1	9.58	47.9	1.76	3.6	0.3
MM-106C	0.2	0.4	0.4	0.5	0.2	0.4	<0.1	<0.1	4.4	1.5	1.69	0.3	0.5	<0.1	0.6	0.2	8.07	40.4	1.48	4.4	0.3
MM-6	1.6	3.3	6.5	5.3	1	2.4	0.3	<0.1	10.8	13.7	16.6	4.4	1.4	0.9	1.5	0.2	33.9	33.9	1.24	0.8	0.6
MM-T3	<0.1	0.9	0.9	1	0.2	0.3	<0.1	<0.1	4.2	3.2	4.27	1	0.2	0.1	0.3	<0.1	5.47	27.4	1.00	0.6	0.4
MM-105 (2)	1	0.9	1.6	1.7	0.4	1.2	0.2	<0.1	3.4	1.9	4.52	1.1	0.5	0.2	1.2	0.2	12.3	30.8	1.13	1.2	0.3
MM-208B	0.3	0.6	0.8	1	0.2	0.6	0.1	<0.1	5.4	2.2	3.27	0.2	0.3	0.1	0.7	0.1	8.42	42.1	1.55	2.3	0.3
MM-25C	2.2	2.6	2.7	2.2	0.4	0.9	0.1	<0.1	10.6	12.0	11.1	2	0.6	0.4	0.8	0.1	12.3	30.8	1.13	0.8	0.6

Detection limits for REE are: 0.1 for Pr, Eu, Tb, Gd, Sm, Dy, Ho, Er, Nb,Tm, Yb and Lu; 0.01 for Ce, 0.02 for Nd, 0.5 for La. Concentrations are in ppm.

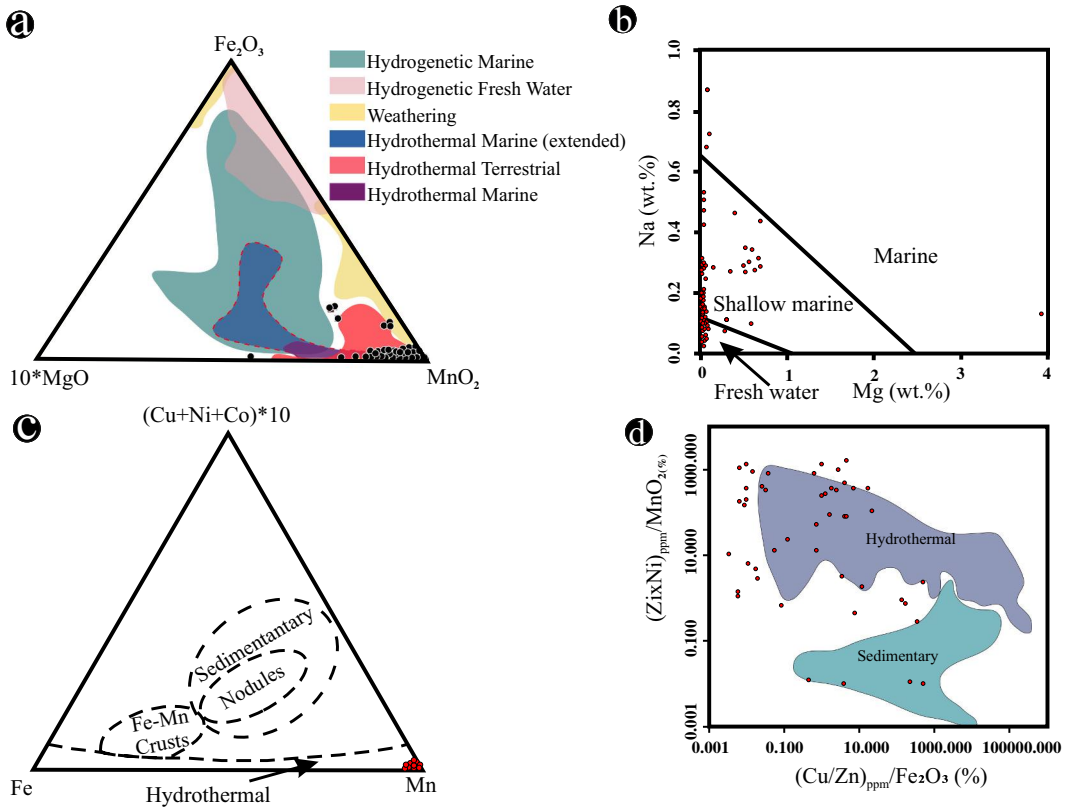

Fig. 9. Discrimination diagrams for Mn oxides of the Montaña de Manganeso deposit. (A) Mn-Fe-(Ni + Cu + Co) ternary diagram showing fields for marine hydrogenetic and hydrothermal Mn oxides (fields after Bonatti et al., 1972; Toth, 1980). (B) MnO_2-MgO-Fe_2O_3 ternary diagram showing fields of hydrothermal (terrestrial and marine), hydrogenetic (marine and fresh water) and supergene deposits (fields after Conly et al., 2011). (C) $(Cu/Zn)_{ppm}/Fe_2O_{3(\%)}$ vs. $(Zn/Ni)_{ppm}/MnO_{2(wt\%)}$ discriminating diagram showing fields for sedimentary and hydrothermal Mn oxides deposits (fields after Albuquerque et al., 2017 and references therein). (D) Na (wt%) vs. Mg (wt%) discriminating diagram for Mn deposits from different environmental settings.

paleogeographic considerations are taken into account to understand the deposit typology and to formulate a genetic model that provides a better insight into processes involved in the mineralization.

5.1. Mineralogy

Manganese oxides are deposited in a variety of environments (hydrothermal hotsprings, supergene marine, and supergene weathering environments) (Nicholson, 1992; Roy, 1992). Although Mn oxide mineralogy is not a diagnostic tool for identifying conditions of formation, the occurrence of poorly crystalline todorokite and birnessite (Fig. 3) at the Montaña de Manganeso deposit is reminiscent of Mn oxides that formed on the ocean floor by hydrogenetic processes and/or hydrothermal venting (Burns and Burns, 1978, 1979; Hein et al., 1997; Canet et al., 2008; Nakagawa et al., 2009; Brusnitsyn et al., 2017; Fan et al., 2018). Todorokite and birnessite have however been reported in some continental hydrothermal manganese deposits (e.g., Ostwald, 1982, 1988; Nicholson, 1992; Crespo and Lunar, 1997; Gutzmer and Beukes, 2000; Miura and Hariya, 2007). Cryptomelane and hollandite have been previously shown to form from alteration of birnessite and todorokite, respectively, under oxidizing conditions (Chen, 2006; Birkner and Navrotsky, 2017; Fan et al., 2018). This assemblage can also be indicative of low-temperature hydrothermal conditions (e.g. Roy, 1997; Post, 1999).

The colloform and crustiform textures of the hollandite–cryptomelane assemblage reflect deposition under varying physico-chemical regimes. Specifically, the occurrence of alternating millimetric to sub-millimetric Fe—Mn—Si banding (Figs. 4 and 5), as observed in some samples (Figs. 4 and 5), can be attributed to short lived changes in fluid composition and pH (e.g., Hein et al., 2008a).

5.2. Geochemistry

Manganese oxides have a strong adsorption capacity and high uptake into their crystal structure of certain cations, such that they acquire the geochemical signatures of the mineralizing fluid (Bau et al., 1996; Conly et al., 2011; Sinisi et al., 2012; Papavassiliou et al., 2017). Thus, geochemical data can be used to distinguish Mn deposits of different origins. In particular, the distribution of major and trace elements has been proven to be a valuable tool for this task (e.g., Bonatti et al., 1972; Toth, 1980; Choi and Hariya, 1992; Nicholson, 1992; Conly et al., 2011; Bau et al., 2014).

5.2.1. Major and trace elements

Several authors have proposed diverse sources to explain major and trace element enrichment in Fe—Mn deposits (Nicholson, 1992; Hein et al., 1997, 2000, 2008a). Proposed sources include the leaching of igneous rocks, sulfide mineralization, biogenic sediments, hydrothermal venting and the addition of metals from seawater (Hein et al., 1990, 1996, 2008b; Pelleter et al., 2017).

The major element composition of Fe—Mn deposits is commonly used to determine the origin of the mineralizing fluid (Dasgupta et al., 1999). Hydrothermal manganese deposits, for example are typically characterized by relatively high fractionation of Fe and Mn, resulting in very high or very low Mn/Fe ratios (0.001–4000) that depend on fluid temperature and redox conditions (Toth, 1980; Choi and Hariya, 1992; Hein et al., 1994, 1996, 1997; Burgath and Von Stackelberg, 1995). On the other hand, hydrogenetic deposits have Mn/Fe ratios approximately equal to 1 (Glasby et al., 1997, 2000; Oksuz, 2011). The Mn/Fe ratio is thus commonly used to discriminate between manganese deposits. In this study, the analyzed Mn oxides from Montaña de Manganeso deposit

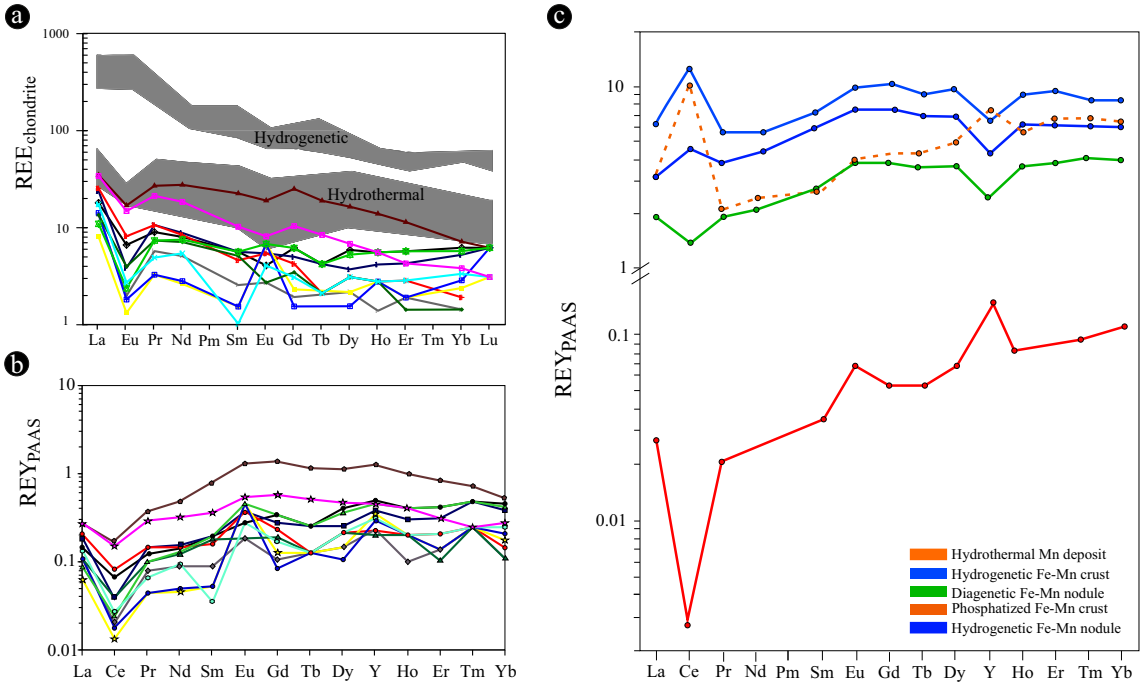

Fig. 10. REE patterns of samples from the Montaña de Manganeso deposit. (A) Chondrite-normalized REE (REECN) distribution patterns. (B) PAAS-normalized REE patterns. (C) Characteristic REE patterns of different types of Mn deposits.

have Mn/Fe ratios of up to 500 (Table A2), which are similar to the ones found in mid-oceanic ridge and subduction-related hydrothermal deposits (Roy, 1997), and are therefore consistent with a hydrothermal origin.

The MnO_2–MgO–Fe_2O_3 composition is also widely used to differentiate between different types of Mn deposits (e.g Conly et al., 2011). As shown in Fig. 9a, most samples of the Montaña de Manganeso deposit clustered within the hydrothermal terrestrial and hydrothermal marine fields. Additionally, the depositional environment where Mn oxides formed can be evaluated by considering their CaO–MgO–Na_2O–K_2O composition, with freshwater and marine chemical precipitates displaying markedly different Na and Mg contents (Nicholson, 1992; Dasgupta et al., 1999). In the Na—Mg discrimination diagram (Fig. 9b), the bulk of the Montaña de Manganeso samples fall within the shallow marine environment, with a few samples in the freshwater field.

The elemental association of some trace elements, particularly As—Ba—Cu—Li—Mo—Pb—Sb—Sr—V—Zn, is diagnostic of a hydrothermal signature in terrestrial and submarine systems. High Zn, Mo, Cd, Ni and Cr contents, relative to upper continental crust (Taylor and McLennan, 1985), might therefore be considered consistent with the hydrothermal origin for the Montaña de Manganeso deposit. This is reinforced by high Ba content (49.7 to >10,000 ppm) of the Montaña de Manganeso samples, which is comparable to the values found in modern submarine hydrothermal deposits (e.g., Oksuz, 2011).

Whole rock Pb, Zn, Cu concentrations in Montaña de Manganeso samples range from 0.2 to 22 ppm, 74.2 to 248 ppm and 27.2 to 125 ppm, respectively. While higher than the average crust (Taylor and McLennan, 1985), these values are relatively low in comparison with some hydrothermal Mn deposits (Hein et al., 1996, 2008; Pelleter et al., 2017). This, together with the lack of correlation between MnO and the base metal oxides (Table 1), and the absence of Pb- and Zn-bearing Mn oxides (e.g., chalcophanite and coronadite), suggests either the absence of base metals in the hydrothermal fluid or a complete precipitation of these metals at depth, with only Mn and Fe remaining in solution (Crespo and Lunar, 1997; Hein et al., 2008a, 2008b; Pelleter et al., 2017).

Co concentrations as well as Co/Zn and Co/Ni ratios have been used to determine the depositional environment and origin of Mn deposits (Bonatti et al., 1972; Choi and Hariya, 1992; Toth, 1980). As Co is generally enriched in hydrogenous deposits relative to hydrothermal deposits, elevated Co contents are believed to indicate a marine environment (Del Rio-Salas et al., 2008; Conly et al., 2011), whereas Ni and Zn can be of hydrothermal origin (Crerar et al., 1982; Hein et al., 1994, 1996, 1997; Pelleter et al., 2017). In Mn oxides from the Montaña de Manganeso deposit, Co ranges from 2.8 to 43.5 ppm (average 24.18 ppm) (Table 2); these low values rule out a significant hydrogenetic (i.e., seawater-derived) contribution during mineralization.

Average Co/Zn ratios of ca. 0.15 are believed to be indicative of hydrothermal deposits, and a ratio of 2.5 indicates hydrogenetic-type deposits (Toth, 1980). The Co/Zn ratio for the Montaña de Manganeso deposit samples (average 0.12 ppm) is close to 0.15 (Table 2), in agreement with the hydrothermal origin. Co/Ni ratios <1 are believed to indicate a sedimentary source, while Co/Ni > 1 represents a deep marine environment (Toth, 1980; Fernández and Moro, 1998; Maghfouri et al., 2017). The Co/Ni ratio of the Montaña de Manganeso deposit is <1 (average 0.3), indicating a sedimentary or marine signature for the deposit. In the Mn-Fe-(Co + Ni + Cu) ternary diagram, all samples from Montaña de Manganeso deposit plotted within the hydrothermal field (Fig. 9c). The Cu/Zn/Fe_2O_3-(Zn/Ni)/MnO_2 discriminating diagram shows a scattering of the samples, although most concentrate within or close to the hydrothermal field (Fig. 9d). The scattering of the samples is due to contributions from sources other than hydrothermal activity for Co, Ni and Zn.

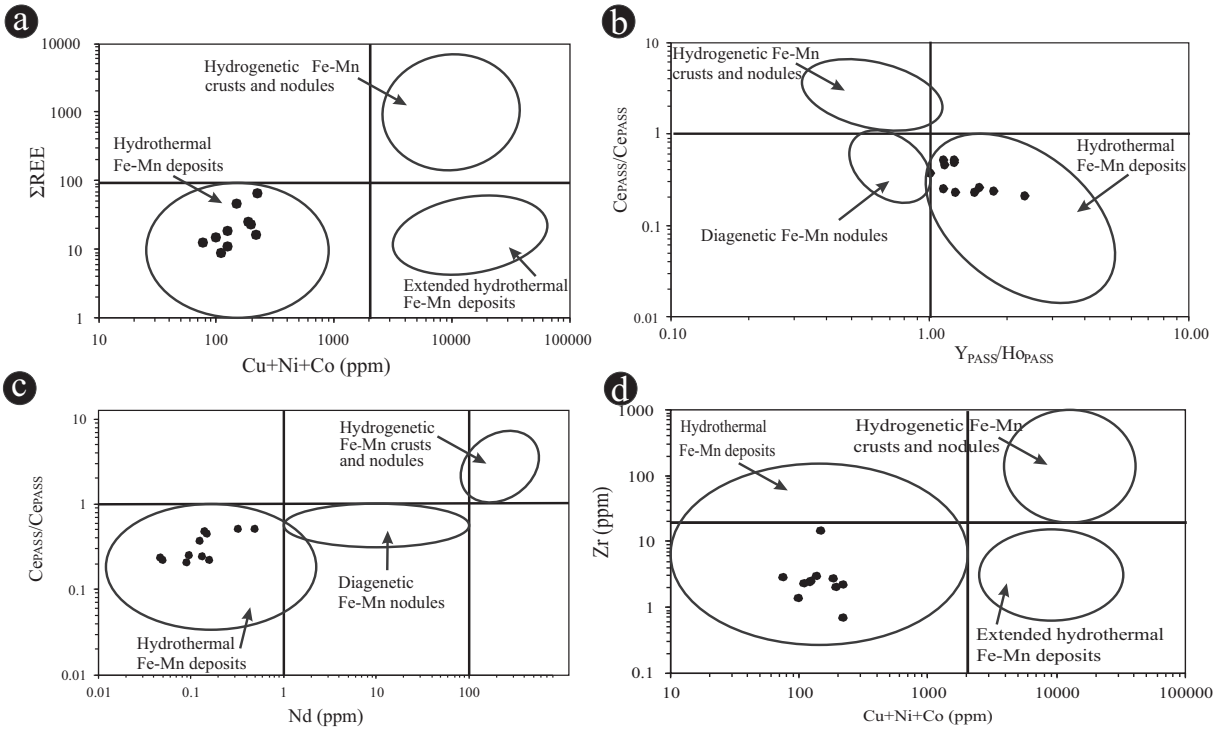

Fig. 11. REE based discrimination diagrams for Mn deposits (fields after Bau et al., 2014). (A) ∑REE vs (Cu + Ni + Co) diagram. (B) Ce/Ce* vs Y/Ho diagram. (C) Ce/Ce* vs Nd diagram. (D) Zr vs Cu + Ni + Co diagram.

5.2.2. Rare earth elements

Chondrite-normalized REE patterns of samples from Montaña de Manganeso deposit are marked by (a) an enrichment in the LREEs relative to the HREEs, (b) pronounced negative Ce anomalies, and (c) variable but mostly positive Eu anomalies (Fig. 10a). LREE enrichment is reflected in the La_{CN}/Sm_{CN} ratios (1.54- to 16.98) showing $LREE_{CN}$ enrichment over $MREE_{CN}$. This pattern is typical of submarine hydrothermal fluids and is thought to be caused by the exchange of REEs during dissolution of plagioclase (Michard and Albarède, 1986; Choi and Hariya, 1992; Lottermoser, 1992; Klinkhammer et al., 1994; Bau et al., 1998; Dubinin, 2004).

The bowed convex shape of the PAAS-normalized REE patterns of Montaña de Manganeso samples (Fig. 10b) is similar to that of continental geothermal systems and hot springs (Bau et al., 1998; Sanada et al., 2006; Wang et al., 2013). The well-defined negative Ce anomalies and positive Y anomalies are characteristic of hydrothermal deposits (Bau et al., 2014) (Fig. 10c).

The total REE content of the Montaña de Manganeso samples is low (ΣREE = 19–103 ppm), similar to that of many hydrothermal Mn deposits (ΣREE = 15–149 ppm, Bau et al., 2014; 13–126 ppm, Josso et al., 2017). These values contrast with those reported for hydrogenetic deposits (ΣREE = 1228–2282 ppm) and diagenetic deposits (ΣREE = 110–489 ppm) (Bau et al., 2014). This is consistent with the fact that samples from the Montaña de Manganeso deposit plot within the hydrothermal fields in all the REE-based discrimination diagrams (Fig. 11).

A comparison, however, of the REE values with the typical submarine hydrothermal field values shows that the Montaña de Manganeso samples are mostly depleted in REE relative to the submarine hydrothermal deposits (Fig. 10a). The low ∑REE of the Montaña de Manganeso samples could be a reflection of boiling, which is believed to have occurred at Montaña de Manganeso deposit (Madondo et al., 2020). Boiling in hydrothermal fluids decrease the REE concentrations, particularly in sub-areal hydrothermal systems as changes in fluid pH and temperature that occur during boiling affect the solubility of REE mineral phases in the hydrothermal fluid (Zierenberg et al., 2018; Fowler et al., 2019).

Hydrothermal Mn deposits are generally characterized by negative Ce anomalies (Crerar et al., 1982; Usui and Someya, 1997), whereas positive Ce anomalies in Fe—Mn deposits are regarded as typical of hydrogenetic precipitation (Choi and Hariya, 1992; Canet et al., 2008; Josso et al., 2017). Well-developed negative Ce anomalies of samples from Montaña de Manganeso deposit (from 0.2 to 0.6, Table 2) therefore indicate a hydrothermal origin. Fractionation of Ce from other REE probably occurred prior to Mn oxide precipitation (Wright et al., 1987; Öztürk and Hein, 1997; Sinisi et al., 2012; Öksüz and Okuyucu, 2014; Maghfouri et al., 2017).

Y has a trivalent state in hydrothermal fluids, and it has a similar geochemical behavior to REE, especially Ho because of identical valences and very similar ionic radii. However, Y is less effectively removed from fluids by metal particles than any of the trivalent REE (Bau et al., 1996; Nozaki et al., 1997), and this can result in the fractionation between Y and Ho (Bao et al., 2008). During the precipitation of Fe and Mn from the hydrothermal fluid, Fe oxyhydroxides precipitate first due to their lower solubility. They acquire low Y/Ho ratios due to the conservative behavior of Y during near vent mixing and preferential adsorption of Ho relative to Y on Fe particles (Bau et al., 1996, 1998, 2014; Nozaki et al., 1997; Bau and Dulski, 1999; Alexander et al., 2008). This causes a strong increase of the Y/Ho ratio of the residual hydrothermal fluid which is now Mn-enriched (Bau and Dulski, 1999). Similarly, upon precipitation of Mn oxides, Ho will be scavenged preferentially leading to a further increase in the Y/Ho ratio of the residual hydrothermal fluid. This implies, at least theoretically, a progressive increase in Y/Ho ratios as Fe—Mn oxyhydroxides are precipitated.

Y/Ho ratios of the Montaña de Manganeso samples varies from 27.4 to 63.7 (Table 2), ranging from near chondritic or crustal ratios (Y/Ho = 28: Bau, 1996; Bau and Dulski, 1999) to marine or submarine hydrothermal vent fluid ratios (Y/Ho = 51–160, Douville et al., 1999). The

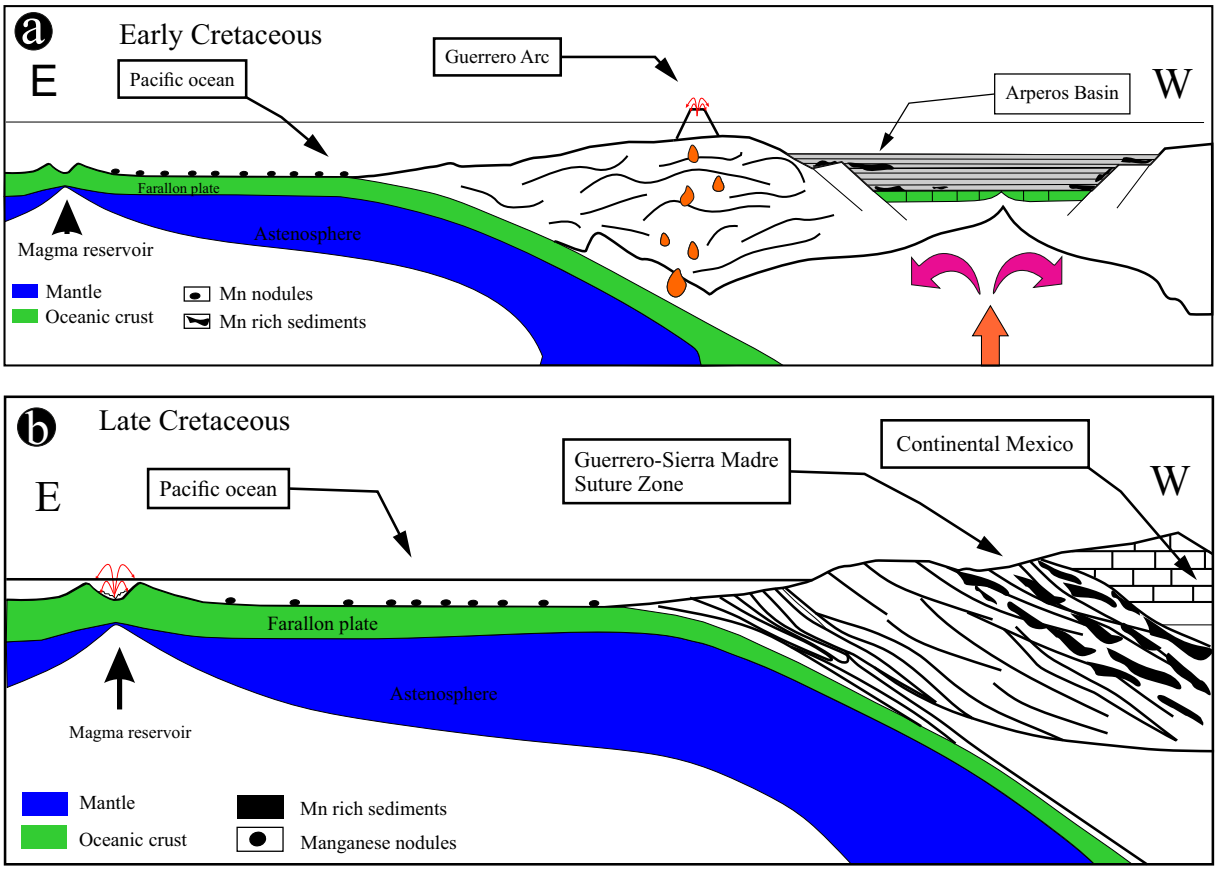

Fig. 12. Manganese enrichment at the Guerrero–Sierra Madre terranes boundary. Model adapted and modified after Nakagawa et al. (2011). (A) before accretion, (B) after accretion.

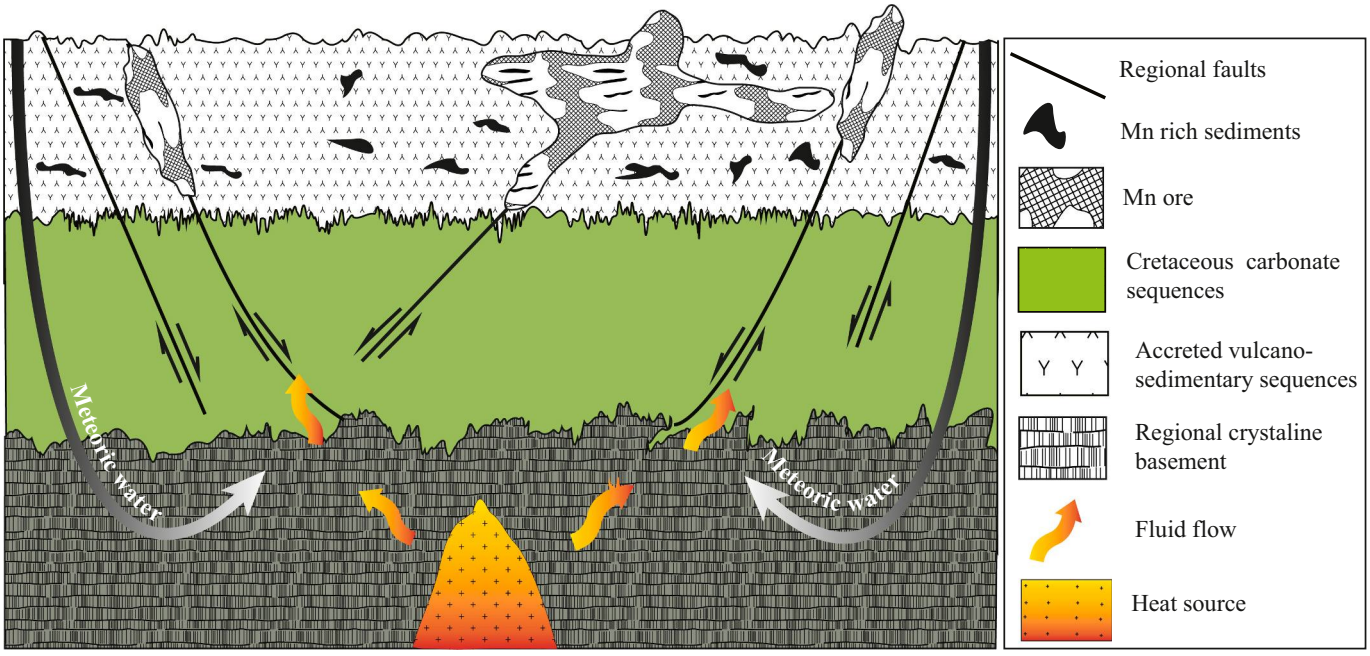

Fig. 13. Schematic diagram illustrating the proposed genetic model for the Montaña de Manganeso manganese deposit. Small undulating arrows show flow of magmatic-hydrothermal fluids and metals. Long convex arrows show meteoric water input into fractures and faults resulting in fluid mixing and the deposition of Mn oxides.

chondritic values were most likely inherited from leached basalt fragments (Y/Ho = 28: Bau, 1996; Bau et al., 1996) within the host rocks, while higher Y/Ho ratios (>44) indicate either a seawater component (Hein et al., 2000) or possibly a progressive enrichment in Y due to preferential adsorption of Ho by early stage Fe and Mn oxyhydroxides. The Y anomalies of the Montaña de Manganeso samples are positive, varying from 1.00 to 2.34 (Table 2). These values are within the range of hydrothermal Mn deposits (Y_{PASS}/Ho_{PASS} = 1.1–2.4; Bau et al., 2014).

5.3. Genetic considerations

The Montaña de Manganeso deposit displays some characteristics of submarine hydrothermal Mn deposits. Firstly, from a geological setting perspective, the association of the Montaña de Manganeso with rocks of the Guerrero terrane is indicative of a primary deposition of Mn within a back-arc basin (Roy, 1997).

Secondly, the samples from the Montaña de Manganeso deposits display super chondritic Y/Ho ratios that exceed 44 (indicative of seawater origin), positive Y anomalies (i.e., $Y_{PAAS}/Ho_{PAAS} > 1$) that trend toward the field of hydrogenetic/diagenetic deposits (Fig. 11a–d), and samples that plot in the marine hydrothermal field (Fig. 9a–d). Thirdly, the samples from Montaña de Manganeso deposit display well-developed negative Ce anomalies. The negative Ce anomalies of hydrothermal deposits are thought to be acquired from seawater (Lottermoser, 1992) and are typical of submarine hydrothermal deposits (Bau et al., 2014).

It is problematic, however, to explain a seawater geochemical signature in Montaña de Manganeso deposit. The geodynamic and paleogeographic evolution of the region shows that the region emerged during the Late Cretaceous Laramide orogenesis, acquiring its present continental configuration during the Basin and Range extension event (Nieto-Samaniego et al., 2007). The volcaniclastic upper units of the Mesozoic Basin of Central México, of Late Cretaceous age, are believed to mark the beginning of continental deposition in the Central Plateau. The age of the Montaña de Manganeso deposit was constrained to no later than the Eocene (<40 Ma; Madondo et al., 2020), which is more recent than the age of the last marine sedimentary deposition, and thus, indicates a continental origin of the deposit.

In order to conciliate these contrasting evidences, a new model for the Montaña de Manganeso deposit is proposed whereby the existence of both continental and submarine hydrothermal geochemical signatures can be explained by different sources of manganese to the mineralizing fluid through multistage mineralizing events or processes: the Montaña de Manganeso deposit basically formed in a two-stage process during distinct periods of the geodynamic evolution of the region. During stage 1, Mn-rich sediments, likely made up of birnessite and todorokite, would have been formed in the back-arc Arperos basin by seafloor hydrothermal processes (Fig. 12a, b). During the Late Cretaceous Laramide orogenesis, the Mn-rich sediments would have been accreted onto the continent. In the region, stage 1 mineralization is represented by the "sedimentary-exhalative" Mn deposits and mineralizations in Zacatecas and San Luis Potosi states, particularly in the localities of Villa de Cos (La Abundancia and La Manganita deposits), Villa de Ramos (Providencia), Illescas, La Bufita, and Mn-bearing chert fragments often found within Upper Cretaceous marine sediments (Tristán-González and Torres Hernández, 2000; COREMI, 2001; Olvera-Rosas et al., 2013; SGM, 2018). At Montaña de Manganeso deposit, stratabound Mn oxides observable in some exposures (Fig. 2e) likely represent the back-arc basin mineralization. Ore bodies are not fault-controlled and are affected by deformation events ascribed to the Late Cretaceous Laramide orogeny (Fig. A3).

Previous studies have demonstrated that silicification at Montaña de Manganeso deposit is a hydrothermal alteration product of the continental Tertiary silicic volcanism (Madondo et al., 2020). The silicified Mn oxide veins at Montaña de Manganeso can be explained as a product of hydrothermal remobilization and leaching of the stratabound Mn mineralization (Fig. 13). Subsequent to leaching and remobilization, the Mn-enriched hydrothermal fluids then penetrated fissures and permeable horizons forming veins and smaller irregular bodies. This two-stage hydrothermal genesis of the Montaña de Manganeso deposit explains the existence of both marine and continental geochemical signatures.

6. Conclusions

The Mn mineralization at Montaña de Manganeso deposit occurs mainly as fractured veins within folded and hydrothermally altered host rocks and, to a lesser extent, in the form of deformed stratabound bodies. The Mn deposits exhibit a rather simple mineral paragenesis consisting of Mn oxides such as birnessite, todorokite, pyrolusite and the cryptomelane-hollandite series. Ratios among major (Fe, Mn, Si, Al) and minor (Co, Ni, Cu, Zn) elements are consistent with the hydrothermal nature of the Montaña de Manganeso deposit. REE in ores of Montaña de Manganeso deposit display pronounced negative Ce anomalies, positive Y anomalies ($Y_{PAAS}/Ho_{PAAS} > 1$) and low $\sum$REE, also characteristic of hydrothermal deposits.

The tectonic setting, geodynamic and paleogeographic evolution of the study region, as well as the geochemical signature of the Montaña de Manganeso samples are consistent with a two-stage hydrothermal genesis of the deposit, as follows: a) Mn oxides, likely birnessite and todorokite were initially precipitated in Arperos back-arc basin by hydrothermal processes in Cretaceous times; and b) after their accretion to the Guerrero composite terrane, these oxides were later remobilized, altered to the cryptomelane-hollandite series and redeposited by continental hydrothermal fluids during the post Laramide Eocene-Oligocene tectonic and volcanic events. These later events obliterated the primary marine textural characteristics.

Supplementary data to this article can be found online at https://doi.org/10.1016/j.chemer.2021.125789.

CRediT authorship contribution statement

Joseph Madondo: Conceptualization, Formal analysis, Data curation, Investigation, Writing – original draft, Visualization. **Carles Canet:** Conceptualization, Data curation, Formal analysis, Methodology. **Eduardo González-Partida:** Funding acquisition, Investigation, Methodology, Writing – review & editing. **Fernando Núñez-Useche:** Investigation, Writing – review & editing. **Augusto A. Rodríguez-Díaz:** Supervision, Investigation, Writing – review & editing. **Abdorrahman Rajabi:** Methodology, Writing – review & editing. **Vanessa Colás:** Resources, Writing – review & editing. **Lauren Blignaut:** Resources, Writing – review & editing. **Nicholas Andrew Vafeas:** Resources, Writing – review & editing.

Declaration of competing interest

The authors declare that they have no known competing financial interests or personal relationships that could have appeared to influence the work reported in this paper.

Acknowledgments

This work was supported by the PAPIIT (DGAPA, UNAM) project IG100116 and CONACYT-Ciencia Básica (A1-S-14574). Dr. Teresa Pi Puig is thanked for carrying out XRD analyses. Carlos Linares López is thanked for the assistance in WDS analyses. Juan Tomás Vázquez Ramírez is thanked for thin section preparation. Prof. Nicolas Johannes Beukes is greatly thanked for access to the Central Analytical Facility of the University of Johannesburg where SEM imagery was carried out. Cesar Aguilar is greatly thanked for revising the first draft of this manuscript. We would also like to thank the Huajicori S.A de C.V company for providing access to mine.

Table A1
Microprobe data of all samples from Montaña de Manganeso deposit.

#	SiO_2	K_2O	Na_2O	CuO	Al_2O_3	MgO	CaO	SrO	MnO_2	PbO	FeO	BaO	ZnO	NiO	CoO	Total
1	0.41	0.04	0.15	0.02	1.21	0.00	0.49	0.07	96.5	0.00	0.44	0.14	0.00	0.03	0.03	99.5
2	1.98	1.00	0.18	0.02	0.09	6.49	0.46	0.15	79.4	0.03	0.17	0.61	0.00	0.00	0.00	90.6
3	0.17	1.11	0.14	0.00	0.19	0.08	0.30	0.21	95.7	0.02	0.23	0.47	0.00	0.00	0.01	98.6
4	0.25	1.15	0.10	0.01	0.18	0.20	0.34	0.23	97.3	0.00	0.19	0.59	0.00	0.01	0.00	100.2
5	0.07	4.30	0.73	0.00	0.17	1.36	0.20	1.35	85.1	0.00	0.17	2.16	0.00	0.04	0.00	95.7
6	0.66	0.03	0.11	0.00	0.36	0.05	0.13	0.00	98.9	0.09	0.21	0.05	0.00	0.00	0.00	100.4
7	0.30	0.08	0.06	0.00	0.21	2.66	0.21	0.04	95.7	0.04	0.19	0.07	0.02	0.03	0.01	99.6
8	0.93	0.63	0.16	0.00	0.12	2.00	0.49	0.16	93.9	0.00	0.20	0.48	0.00	0.01	0.00	99.1
9	0.30	0.59	0.11	0.03	0.40	0.46	0.26	0.08	96.6	0.00	0.18	0.49	0.07	0.02	0.01	99.6
10	0.14	5.53	0.72	0.00	0.44	0.55	0.29	0.78	90.1	0.00	0.21	0.93	0.00	0.00	0.03	99.7
11	0.07	5.20	0.80	0.02	0.48	0.36	0.31	1.19	91.3	0.00	0.16	0.93	0.02	0.00	0.02	100.4
12	0.25	1.32	0.68	0.00	0.22	0.05	0.30	0.64	88.9	0.00	0.31	4.03	0.03	0.00	0.03	96.8
13	0.33	1.12	0.71	0.00	2.59	0.03	0.28	0.56	88.5	0.00	0.63	4.14	0.11	0.00	0.02	99.0
14	0.48	1.21	0.64	0.05	0.15	0.033	0.31	0.56	88.7	0.04	0.33	4.38	0.05	0.04	0.02	100.0
15	0.10	1.52	0.42	0.00	0.08	0.01	0.26	0.63	87.3	0.02	0.10	8.80	0.00	0.01	0.00	96.7
16	0.08	1.33	0.34	0.01	0.07	0.08	0.35	0.99	84.9	0.00	0.01	9.45	0.00	0.00	0.00	97.6
17	0.11	1.20	0.38	0.02	0.11	0.01	0.30	0.60	86.2	0.00	0.11	10.00	0.02	0.01	0.02	99.1
18	0.09	1.22	0.35	0.02	0.11	0.03	0.29	0.71	85.9	0.00	0.07	10.18	0.02	0.04	0.00	99.1
19	0.82	0.03	0.08	0.00	0.29	0.11	0.44	0.04	96.9	0.00	0.09	0.27	0.05	0.03	0.00	99.2
20	0.90	0.05	0.15	0.00	0.22	0.06	0.51	0.02	96.6	0.00	0.09	0.27	0.00	0.02	0.03	98.9
21	0.13	1.12	0.33	0.02	0.10	0.01	0.29	0.74	84.7	0.00	0.21	10.27	0.08	0.00	0.00	98.0
22	0.14	1.17	0.57	0.00	0.09	0.04	0.29	0.72	84.8	0.00	0.14	10.28	0.00	0.00	0.00	98.2
23	1.07	0.03	0.06	0.00	0.15	0.07	0.40	0.02	97.8	0.01	0.25	0.28	0.00	0.00	0.00	100.1
24	0.96	0.05	0.06	0.00	0.18	0.07	0.46	0.03	97.4	0.02	0.22	0.27	0.00	0.02	0.01	99.8
25	0.82	0.06	0.07	0.00	0.73	0.03	0.36	0.02	97.3	0.03	0.18	0.17	0.01	0.01	0.01	99.8
26	0.73	0.05	0.06	0.00	0.76	0.05	0.33	0.05	98.2	0.03	0.23	0.21	0.00	0.01	0.00	100.7
27	0.78	0.05	0.02	0.00	0.34	0.03	0.33	0.02	96.8	0.00	0.19	0.17	0.03	0.00	0.00	98.8
28	0.95	0.05	0.07	0.01	0.22	0.04	0.37	0.06	96.8	0.03	0.12	0.24	0.00	0.00	0.02	99.0
29	0.12	1.52	0.62	0.00	0.14	0.66	0.84	2.12	79.5	0.00	0.25	5.51	0.04	0.03	0.00	91.4
30	0.21	1.09	0.41	0.00	0.19	0.92	1.05	2.52	78.3	0.00	0.68	6.64	0.05	0.03	0.00	92.1
31	0.20	0.90	0.39	0.01	0.17	0.84	0.93	2.13	75.9	0.00	0.75	7.84	0.06	0.03	0.02	90.2
32	0.25	0.93	0.47	0.03	0.21	0.88	0.94	2.27	75.3	0.00	1.18	7.53	0.02	0.03	0.01	90.1
33	0.24	0.97	0.60	0.00	0.19	1.14	1.09	2.05	76.1	0.00	1.80	6.78	0.02	0.00	0.02	91.0
34	0.20	0.97	0.46	0.00	0.25	1.01	1.00	2.35	76.7	0.00	1.09	6.41	0.00	0.02	0.02	90.5
35	0.73	0.98	0.40	0.01	0.34	0.38	0.61	1.41	76.2	0.00	9.33	3.30	0.00	0.02	0.01	93.8
36	1.18	0.61	0.32	0.00	0.45	1.42	0.81	0.77	65.6	0.00	15.16	6.83	0.04	0.05	0.01	93.3
37	1.12	0.62	0.41	0.00	0.41	1.57	0.80	0.67	66.3	0.00	14.55	6.74	0.00	0.02	0.02	93.2
38	0.94	0.67	0.45	0.00	0.38	1.53	0.81	0.73	68.6	0.00	11.82	7.05	0.05	0.02	0.00	93.1
39	0.27	0.73	0.43	0.00	0.18	1.12	0.50	0.21	76.2	0.00	0.81	10.06	0.00	0.03	0.01	90.6
40	0.28	0.79	0.37	0.01	0.29	1.06	0.59	0.31	75.9	0.00	0.33	9.94	0.00	0.01	0.02	89.9
41	0.24	0.72	0.39	0.00	0.28	1.13	0.56	0.28	75.1	0.00	0.83	9.89	0.02	0.01	0.00	89.5
42	0.30	0.72	0.37	0.00	0.71	0.84	0.55	0.21	75.0	0.00	0.50	10.86	0.01	0.02	0.02	90.1
43	0.21	3.06	0.98	0.00	0.06	0.15	0.49	0.94	85.6	0.00	0.35	1.05	0.05	0.02	0.00	92.3
44	0.23	3.05	1.18	0.02	0.15	0.11	0.42	0.88	86.2	0.00	0.37	0.88	0.07	0.00	0.01	93.6
45	0.82	2.78	0.92	0.01	0.08	0.10	0.42	0.76	84.9	0.01	0.41	2.01	0.04	0.01	0.00	93.3
46	1.20	0.09	0.20	0.00	0.30	0.08	0.41	0.14	90.6	0.00	1.97	0.82	0.05	0.01	0.01	95.9
47	1.30	0.17	0.11	0.00	1.78	0.13	0.23	0.00	89.2	0.00	1.47	1.28	0.02	0.03	0.00	95.7
48	0.56	2.42	0.31	0.03	0.12	0.09	0.55	0.86	82.6	0.00	0.52	3.41	0.04	0.01	0.02	91.5
49	0.42	0.08	0.00	0.00	0.41	0.00	0.08	0.00	90.2	0.00	1.16	0.10	0.01	0.00	0.00	92.5
50	1.52	3.09	0.28	0.00	0.25	0.02	0.35	0.66	81.1	0.00	2.71	2.86	0.06	0.03	0.01	93.4
51	0.08	3.43	0.14	0.02	0.59	0.01	0.11	0.07	83.3	0.00	0.13	5.51	0.09	0.00	0.01	93.5
52	3.00	1.14	0.18	0.04	0.37	0.03	0.16	0.02	84.2	0.00	0.71	4.99	0.05	0.03	0.02	94.4
53	0.06	1.90	0.32	0.00	0.00	0.04	0.33	0.11	83.6	0.00	0.16	4.43	0.02	0.00	0.01	91.0
54	0.30	1.78	0.40	0.00	0.09	0.04	0.27	0.46	83.5	0.00	0.41	4.90	0.01	0.00	0.00	92.2
55	0.01	0.42	0.03	0.13	0.00	0.02	0.09	0.01	90.1	0.04	0.23	0.59	0.01	0.03	0.00	91.7
56	0.00	0.08	0.00	0.01	0.00	0.05	0.04	0.00	91.6	0.06	0.70	0.17	0.03	0.03	0.01	92.8
57	0.18	2.63	0.37	0.02	0.07	0.59	0.71	1.19	81.4	0.00	0.47	3.29	0.01	0.02	0.00	91.0
58	2.56	2.49	0.39	0.02	0.32	0.23	0.59	0.71	84.0	0.00	0.14	1.45	0.06	0.00	0.01	93.0
59	0.25	0.43	0.18	0.02	0.25	0.07	0.26	0.10	90.9	0.03	0.23	0.56	0.04	0.00	0.01	93.3
60	0.19	2.63	0.49	0.03	0.06	0.05	0.58	1.23	86.5	0.02	0.29	0.89	0.01	0.00	0.00	93.0
61	1.19	1.14	0.16	0.06	0.49	0.80	0.54	0.27	75.9	0.00	0.20	8.61	0.02	0.00	0.00	89.4
62	1.03	1.10	0.06	0.01	0.76	0.78	0.53	0.21	76.8	0.00	0.17	8.57	0.00	0.05	0.01	90.1
63	0.17	3.67	0.28	0.01	0.24	0.01	0.40	0.69	88.1	0.01	0.12	0.67	0.00	0.00	0.00	94.4
64	0.14	3.30	0.22	0.03	0.17	0.03	0.35	0.50	86.8	0.02	0.15	1.48	0.00	0.00	0.01	93.2
65	0.19	3.53	0.22	0.00	0.26	0.05	0.49	0.90	86.8	0.00	0.18	0.93	0.01	0.00	0.02	93.6
66	0.14	0.61	0.05	0.02	0.22	0.01	0.12	0.03	91.8	0.00	0.23	0.17	0.04	0.00	0.00	93.4
67	0.27	0.45	0.00	0.02	0.58	0.04	0.09	0.00	92.2	0.09	0.19	0.18	0.02	0.00	0.01	94.1
68	0.14	0.26	0.04	0.01	0.24	0.00	0.13	0.00	93.3	0.00	0.20	0.04	0.00	0.00	0.00	94.4
69	0.66	0.40	0.04	0.01	0.27	0.01	0.16	0.05	91.7	0.00	0.17	0.20	0.00	0.00	0.01	93.5
70	0.55	0.55	0.04	0.00	0.20	0.00	0.07	0.00	92.0	0.00	0.15	0.13	0.00	0.01	0.01	93.7
71	0.70	0.04	0.02	0.00	0.57	0.03	0.01	0.00	92.8	0.00	0.17	0.03	0.00	0.01	0.02	94.4
72	0.10	0.18	0.02	0.01	1.11	0.00	0.08	0.00	92.9	0.02	0.12	0.14	0.04	0.00	0.01	94.3
73	0.07	0.36	0.06	0.02	0.89	0.00	0.07	0.00	92.8	0.00	0.23	0.09	0.07	0.00	0.01	94.5

(*continued on next page*)

Table A1 (*continued*)

#	SiO_2	K_2O	Na_2O	CuO	Al_2O_3	MgO	CaO	SrO	MnO_2	PbO	FeO	BaO	ZnO	NiO	CoO	Total
74	0.40	0.13	0.00	0.00	0.78	0.02	0.10	0.00	92.3	0.00	0.17	0.09	0.01	0.00	0.00	94.0
75	0.13	3.58	0.22	0.00	0.27	0.03	0.33	0.49	85.8	0.00	0.15	1.93	0.07	0.00	0.01	93.0
76	0.14	3.48	0.22	0.01	0.12	0.05	0.41	0.68	84.8	0.04	0.13	2.73	0.01	0.01	0.00	92.8
77	0.16	3.85	0.20	0.01	0.11	0.06	0.41	0.87	84.6	0.01	0.13	2.04	0.02	0.02	0.01	92.5
78	0.16	4.16	0.16	0.00	0.28	0.06	0.24	0.27	87.3	0.00	0.15	1.83	0.06	0.00	0.01	94.7
79	0.14	3.57	0.25	0.00	0.08	0.02	0.38	0.75	86.3	0.05	0.16	2.44	0.00	0.00	0.00	94.1
80	0.20	3.46	0.24	0.00	0.54	0.01	0.30	0.42	86.7	0.00	0.12	1.27	0.01	0.00	0.01	93.3
81	0.15	3.62	0.28	0.03	0.13	0.06	0.42	0.82	85.3	0.04	0.12	2.24	0.07	0.01	0.00	93.3
82	0.12	3.44	0.19	0.00	0.09	0.06	0.42	0.87	84.6	0.01	0.13	3.04	0.02	0.03	0.00	93.0
83	0.20	0.19	0.02	0.01	0.74	0.03	0.12	0.00	94.4	0.00	0.15	0.11	0.04	0.00	0.00	96.0

Table A2
Whole-rock chemical composition (major elements) of 3 samples of the Montaña de Manganeso deposit.

Sample	SiO_2	K_2O	Na_2O	Al_2O_3	MgO	CaO	SrO	MnO	FeO	BaO	Mn/Fe	SiO_2/Al_2O_3
MM-102A	1.074	0.643	0.334	0.579	0.799	0.684	1.124	57.289	13.620	4.360	4.2	1.856
MM-25D(2)	2.898	1.521	0.238	0.230	1.115	0.569	0.327	75.589	0.166	0.536	500	12.586
MM-T3	5.431	0.818	0.273	0.403	0.166	0.737	0.276	62.497	10.137	0.628	6.2	13.461
Avg	3.134	0.991	0.281	0.404	0.693	0.663	0.575	65.125	7.974	1.508	7.5	9.301

References

Aguillón-Robles, A., Tristán-González, M., Aguirre-Díaz, G.J., Bellon, H., 2009. Syn-extensional intra-plate trachydacite-rhyolitic dome volcanism of the Mesa Central, southern Sierra Madre Occidental volcanic province, Mexico. J. Volcanol. Geotherm. Res. 187, 33–52. https://doi.org/10.1016/j.jvolgeores.2009.08.021.

Aguillón-Robles, A., Tristán-González, M., Aguirre-Díaz, G., López-Doncel, R.A., Bellon, H., Martínez-Esparza, G., 2014. Eocene to Quaternary mafic-intermediate volcanism in San Luis Potosí, central Mexico: the transition from Farallon plate subduction to intra-plate continental magmatism. J. Volcanol. Geotherm. Res. 276, 152–172. https://doi.org/10.1016/j.jvolgeores.2014.02.019.

Aguirre-Díaz, G.J., Labarthe-Hernández, G., Tristán-González, M., Nieto-Obregón, J., Gutiérrez-Palomares, I., 2008. The ignimbrite flare-up and graben calderas of the Sierra Madre Occidental, Mexico. In: Developments in Volcanology. Elsevier, pp. 143–180. https://doi.org/10.1016/S1871-644X(07)00004-6.

Albuquerque, M.F. dos S., Horbe, A.M.C., Botelho, N.F., 2017. Genesis of manganese deposits in southwestern Amazonia: mineralogy, geochemistry and paleoenvironment. Ore Geol. Rev. 89, 270–289. https://doi.org/10.1016/j.oregeorev.2017.06.012.

Alexander, B.W., Bau, M., Andersson, P., Dulski, P., 2008. Continentally-derived solutes in shallow Archean seawater: rare earth element and Nd isotope evidence in iron formation from the 2.9 Ga Pongola Supergroup, South Africa. Geochim. Cosmochim. Acta 72, 378–394. https://doi.org/10.1016/j.gca.2007.10.028.

Alexandri, R.R., 1977. Estudio Geológico del Yacimiento Montaña de Manganeso. Bsc Thesis.

Alfaro, C.M., Alexandri, R.R., 1976. Estudio Geológico del Yacimiento Montaña de Manganeso. Technical File CRM 240132 (Unpublished).

Aranda-Gómez, J.J., Mcdowell, F.W., 1998. Paleogene extension in the southern basin and range province of Mexico: syndepositional tilting of Eocene red beds and Oligocene volcanic rocks in the Guanajuato mining district. Int. Geol. Rev. 40, 116–134. https://doi.org/10.1080/00206819809465201.

Aranda-Gómez, J.J., Molina-Garza, R., McDowell, F.W., Vassallo-Morales, L.F., Ortega-Rivera, M.A., Solorio-Munguía, J.G., Aguillón-Robles, A., 2007. The relationships between volcanism and extension in the Mesa Central: the case of Pinos, Zacatecas, Mexico. Rev. Mex. Cien. Geol. 24, 216–233.

Bao, S.X., Zhou, H.Y., Peng, X.T., Ji, F.W., Yao, H.Q., 2008. Geochemistry of REE and yttrium in hydrothermal fluids from the Endeavour segment, Juan de Fuca Ridge. Geochem. J. 42, 359–370. https://doi.org/10.2343/geochemj.42.359.

Barbato, S., Gautier, J.L., 2001. Hollandite cathodes for lithium ion batteries. 2. Thermodynamic and kinetics studies of lithium insertion into $BaMMn_7O_{16}$ (M = Mg, Mn, Fe, Ni). Electrochim. Acta 46, 2767–2776. https://doi.org/10.1016/S0013-4686(01)00506-0.

Barboza-Gudiño, J.R., Tristán-González, M., Torres-Hernández, J.R., 1998. The late Triassic-early Jurassic active continental margin of western North America in northeastern Mexico. Geofis. Int. 37, 283–292.

Barboza-Gudiño, J.R., Tristán-González, M., Torres-Hernández, J.R., 1999. Tectonic setting of pre-Oxfordian units from central and northeastern Mexico: a review. In: Special Paper 340: Mesozoic Sedimentary and Tectonic History of North-Central Mexico. Geological Society of America, pp. 197–210. https://doi.org/10.1130/0-8137-2340-x.197.

Barboza-Gudiño, J.R., Orozco-Esquivel, M.T., Gómez-Anguiano, M., Zavala-Monsiváis, A., 2008. The Early Mesozoic volcanic arc of western North America in northeastern Mexico. J. S. Am. Earth Sci. 25, 49–63. https://doi.org/10.1016/j.jsames.2007.08.003.

Bau, M., 1996. Controls on the fractionation of isovalent trace elements in magmatic and aqueous systems: evidence from Y/Ho, Zr/Hf, and lanthanide tetrad effect. Contrib. Mineral. Petrol. 123, 323–333. https://doi.org/10.1007/s004100050159.

Bau, M., Dulski, P., 1999. Comparing yttrium and rare earths in hydrothermal fluids from the Mid-Atlantic Ridge: implications for Y and REE behaviour during near-vent mixing and for the Y/Ho ratio of Proterozoic seawater. Chem. Geol. 155, 77–90. https://doi.org/10.1016/S0009-2541(98)00142-9.

Bau, M., Koschinsky, A., Dulski, P., Hein, J.R., 1996. Comparison of the partitioning behaviours of yttrium, rare earth elements, and titanium between hydrogenetic marine ferromanganese crusts and seawater. Geochim. Cosmochim. Acta 60, 1709–1725. https://doi.org/10.1016/0016-7037(96)00063-4.

Bau, M., Usui, A., Pracejus, B., Mita, N., Kanai, Y., Irber, W., Dulski, P., 1998. Geochemistry of low-temperature water–rock interaction: evidence from natural waters, andesite, and iron-oxyhydroxide precipitates at Nishiki-numa iron-spring, Hokkaido, Japan. Chem. Geol. 151, 293–307. https://doi.org/10.1016/S0009-2541(98)00086-2.

Bau, M., Schmidt, K., Koschinsky, A., Hein, J., Kuhn, T., Usui, A., 2014. Discriminating between different genetic types of marine ferro-manganese crusts and nodules based on rare earth elements and yttrium. Chem. Geol. 381, 1–9. https://doi.org/10.1016/j.chemgeo.2014.05.004.

Birkner, N., Navrotsky, A., 2017. Thermodynamics of manganese oxides: sodium, potassium, and calcium birnessite and cryptomelane. Proc. Natl. Acad. Sci. U. S. A. 114, E1046–E1053. https://doi.org/10.1073/pnas.1620427114.

Bonatti, E., Fisher, D.E., Joensuu, O., Rydell, H.S., Beyth, M., 1972. Iron-manganese-barium deposit from the northern Afar Rift (Ethiopia). Econ. Geol. 67, 717–730. https://doi.org/10.2113/gsecongeo.67.6.717.

Boynton, W.V., 1984. Cosmochemistry of the rare earth elements: meteorite studies. Dev. Geochem. 2, 63–114. https://doi.org/10.1016/B978-0-444-42148-7.50008-3.

Brusnitsyn, A.I., Kuleshov, V.N., Perova, E.N., Zaitsev, A.N., 2017. Ferromanganese carbonate metasediments of the Sob area, Polar Urals: bedding conditions, composition, and genesis. Lithol. Miner. Resour. 52, 192–213. https://doi.org/10.1134/s0024490217030026.

Burgath, K., Von Stackelberg, U., 1995. Sulfide-impregnated volcanics and ferromanganese incrustations from the Southern Lau Basin (Southwest Pacific). Mar. Georesour. Geotechnol. 13, 263–308. https://doi.org/10.1080/10641199509388288.

Burns, R.G., Burns, V.M., 1979. Manganese oxides, in: Burns, R.G. (Ed.), Marine Minerals. De Gruyter, Berlin, Boston, pp. 1–46. doi:https://doi.org/10.1515/9781501508646-005; https://doi.org/10.1016/0012-821X(78)90020-1.

Burns, V.M., Burns, R.G., 1978. Authigenic todorokite and phillipsite inside deep sea manganese nodules. Am. Mineral. 63, 827–831.

Camprubi, A., Ferrari, L., Cosca, M.A., Cardellach, E., Canals, A., Canals, À., 2003. Ages of epithermal deposits in Mexico. Regional significance and links with the evolution of tertiary volcanism. Econ. Geol. 98, 1029–1037. https://doi.org/10.2113/gsecongeo.98.5.1029.

Camprubí, A., González-Partida, E., Torró, L., Alfonso, P., Canet, C., Miranda-Gasca, M. A., Martini, M., González-Sánchez, F., 2017. Mesozoic volcanogenic massive sulfide

(VMS) deposits in Mexico. Ore Geol. Rev. 81, 1066–1083. https://doi.org/10.1016/j.oregeorev.2015.07.027.
Canet, C., Prol-Ledesma, R.M., Bandy, W.L., Schaaf, P., Linares, C., Camprubí, A., Tauler, E., Mortera-Gutiérrez, C., 2008. Mineralogical and geochemical constraints on the origin of ferromanganese crusts from the Rivera Plate (western margin of Mexico). Mar. Geol. 251, 47–59. https://doi.org/10.1016/j.margeo.2008.01.012.
Carrillo-Bravo, J., 1982. Exploración Petrolera de la Cuenca Mesozoica del Centro de México. Bol. Asoc. Mex. Geól. Petrol. 34, 21–46.
Centeno-García, E., Silva-Romo, G., 1997. Petrogenesis and tectonic evolution of Central Mexico during Triassic-Jurassic time. Rev. Mex. Cien. Geol. 14, 244–260.
Centeno-Garcia, E., Ruis, J., Coney, P.J., Patchett, P.J., Ortega- Gutierrez, F., 1993. Guerrero terrane of Mexico: its role in the southern Cordillera from new geochemical data. Geology 21, 419–422. https://doi.org/10.1130/0091-7613(1993)021.
Centeno-García, E., Corona-Chávez, P., Talavera-Mendoza, O., Iriondo, A., 2003. Geologic and tectonic evolution of the western Guerrero terrane—a transect from Puerto Vallarta to Zihuatanejo, Mexico. In: Geologic Transects across Cordilleran Mexico: Guidebook for the Field Trips of the 99th Geological Society of America Cordilleran Section Annual Meeting. Geological Society of America.
Centeno-García, E., Guerrero-Suastegui, M., Talavera-Mendoza, O., 2008. The Guerrero composite terrane of western Mexico: collision and subsequent rifting in a supra-subduction zone. In: Special Paper 436: Formation and Applications of the Sedimentary Record in Arc Collision Zones. Geological Society of America, pp. 279–308. https://doi.org/10.1130/2008.2436(13).
Chen, C.C., 2006. Transformation of synthetic birnessite to cryptomelane: an electron microscopic study. Clay Clay Miner. 34, 565–571. https://doi.org/10.1346/ccmn.1986.0340510.
Choi, J.H., Hariya, Y., 1992. Geochemistry and depositional environment of Mn oxide deposits in the Tokoro Belt, northeastern Hokkaido, Japan. Econ. Geol. 87, 1265–1274. https://doi.org/10.2113/gsecongeo.87.5.1265.
Conly, A.G., Scott, S.D., Bellon, H., 2011. Metalliferous manganese oxide mineralization associated with the Boléo Cu-Co-Zn district, Mexico. Econ. Geol. 106, 1173–1196. https://doi.org/10.2113/econgeo.106.7.1173.
Consejo de Recursos Minerales (COREMI), 1980. Estudios geofísicos de orientación efectuados en el area de Montaña de Manganeso, S.L.P: Proyecto Manganeso Convenio México-España. In: Pachuca, Hgo. Consejo de Recursos Minerales (Coremi), 2001. Informe final de la carta geológico-minera Villa de Santo Domingo F14-A-31. Pachuca, Hgo.
Consejo de Recursos Minerales (COREMI), 2001. Informe final de la carta geológico-minera Villa de Santo Domingo F14-A-31. Pachuca, Hgo, Hgo.
Corona-Esquivel, R., Ortega-Gutiérrez, F., Reyes-Salas, M., Lozano-Santacruz, R., Miranda-Gasca, M.A., 2000. Mineralogical study of the La Hueca Cretaceous iron-manganese deposit, Michoacán, southwestern Mexico. Rev. Mex. Cien. Geol. 17, 143–152.
Crerar, D.A., Namson, J., Chyi, M.S., Williams, L., Feigenson, M.D., 1982. Manganiferous cherts of the Franciscan assemblage; I, general geology, ancient and modern analogues, and implications for hydrothermal convection at oceanic spreading centers. Econ. Geol. 77, 519–540. https://doi.org/10.2113/gsecongeo.77.3.519.
Crespo, A., Lunar, R., 1997. Terrestrial hot-spring Co-rich Mn mineralization in the Pliocene-Quaternary Calatrava Region (central Spain). Geol. Soc. Spec. Publ. 119, 253–264. https://doi.org/10.1144/GSL.SP.1997.119.01.16.
Dasgupta, H.C., Sambasiva Rao, V.V., Krishna, C., 1999. Chemical environments of deposition of ancient iron- and manganese-rich sediments and cherts. Sediment. Geol. 125, 83–98. https://doi.org/10.1016/S0037-0738(98)00148-1.
De Cserna, Z., 1976. Geology of the Fresnillo area, Zacatecas, Mexico. Bull. Geol. Soc. Am. 87, 1191–1199. https://doi.org/10.1130/0016-7606(1976)87.
Del Rio-Salas, R., Ruiz, J., Ochoa-Landín, L., Noriega, O., Barra, F., Meza-Figueroa, D., Paz-Moreno, F., 2008. Geology, geochemistry and Re-Os systematics of manganese deposits from the Santa Rosalía Basin and adjacent areas in Baja California Sur, México. Miner. Depos. 43, 467–482. https://doi.org/10.1007/s00126-008-0177-3.
Del Rio-Salas, R., Ochoa-Landín, L., Eastoe, C.J., Ruiz, J., Meza-Figueroa, D., Valencia-Moreno, M., Zúñiga-Hernández, H., Zúñiga-Hernández, L., Moreno-Rodríguez, V., Mendívil-Quijada, H., 2013. Genesis of manganese oxide mineralization in the Boleo region and Concepción peninsula, Baja California Sur: constraints from Pb-Sr isotopes and REE geochemistry. Rev. Mex. Cien. Geol. 30, 482–499.
Dolenec, T., 2003. Todorokite — a 10 Å manganate from the Jabuka Pit (Central Adriatic). Mater. Geoenviron. 50, 453–466.
Douville, E., Bienvenu, P., Charlou, J.L., Donval, J.P., Fouquet, Y., Appriou, P., Gamo, T., 1999. Yttrium and rare earth elements in fluids from various deep-sea hydrothermal systems. Geochim. Cosmochim. Acta 63, 627–643. https://doi.org/10.1016/S0016-7037(99)00024-1.
Dubinin, A.V., 2004. Geochemistry of rare earth elements in the ocean. Lithol. Miner. Resour. 39, 289–307. https://doi.org/10.1023/B:LIMI.0000033816.14825.a2.
Fan, C., Xu, L., Zhao, W., 2018. Transformation of birnessite into hollandite under the influence of silver cations in aqueous medium. J. Solid State Chem. 268, 136–148. https://doi.org/10.1016/j.jssc.2018.08.039.
Fernández, A., Moro, M.C., 1998. Origin and depositional environment of Ordovician stratiform iron mineralization from Zamora (NW Iberian Peninsula). Miner. Depos. 33, 606–619. https://doi.org/10.1007/s001260050176.
Fitz-Diaz, E., Hudleston, P., Tolson, G., Van Der Pluijm, B., 2014. Progressive, episodic deformation in the Mexican Fold-Thrust Belt (central Mexico): evidence from isotopic dating of folds and faults. Int. Geol. Rev. 56, 734–755. https://doi.org/10.1080/00206814.2014.896228.
Fitz-Diaz, E., Lawton, T.F., Juárez-Arriaga, E., Chávez-Cabello, G., 2018. The Cretaceous-Paleogene Mexican orogen: structure, basin development, magmatism and tectonics. Earth Sci. Rev. 183, 56–84. https://doi.org/10.1016/j.earscirev.2017.03.002.
Fowler, A.P.G., Zierenberg, R.A., Reed, M.H., Palandri, J., Óskarsson, F., Gunnarsson, I., 2019. Rare earth element systematics in boiled fluids from basalt-hosted geothermal systems. Geochim. Cosmochim. Acta 244, 129–154. https://doi.org/10.1016/j.gca.2018.10.001.
Freydier, C., Lapierre, H., Ruiz, J., Tardy, M., Martinez-R, J., Coulon, C., 2000. The Early Cretaceous Arperos basin: an oceanic domain dividing the Guerrero arc from nuclear Mexico evidenced by the geochemistry of the lavas and sediments. J. S. Am. Earth Sci. 13, 325–336. https://doi.org/10.1016/S0895-9811(00)00027-4.
Glasby, G.P., Stüben, D., Jeschke, G., Stoffers, P., Garbe-Schönberg, C.D., 1997. A model for the formation of hydrothermal manganese crusts from the Pitcairn Island hotspot. Geochim. Cosmochim. Acta 61, 4583–4597. https://doi.org/10.1016/s0016-7037(97)00262-7.
Glasby, G.P., Iizasa, K., Yuasa, M., Usui, A., 2000. Submarine hydrothermal mineralization on the Izu–Bonin arc, south of Japan: an overview. Mar. Georesour. Geotechnol. 18, 141–176. https://doi.org/10.1080/10641190009353785.
Gómez-Caballero, A.J., Villaseñor-Cabral, M., Santiago-Jacinto, P., Ponce-Abad, F., 2010. Hypogene Ba-rich todorokite and associated nanometric native silver in the San Miguel Tenango mining area, Zacatlán, Puebla, Mexico. Can. Mineral. 48, 1237–1253. https://doi.org/10.3749/canmin.48.5.1237.
Gutzmer, J., Beukes, N.J., 2000. Asbestiform manjiroite and todorokite from the Kalahari manganese field, South Africa. S. Afr. J. Geol. 103, 163–174. https://doi.org/10.2113/1030163.
Hein, J.R., Bolton, B., 1994. Formation of the Chiatura and Nikopol manganese carbonate ores, Georgia and Ukraine. In: Abstracts, Fermor Lecture Meeting, The Geological Society of London, 26–27 September 1994, London, UK (12p).
Hein, J.R., Schulz, M.S., Kang, J.K., 1990. Insular and submarine ferromanganese mineralization of the Tonga-Lau region. Mar. Min. 9, 305–354.
Hein, J.R., Hsueh-Wen, Y., Gunn, S.H., Gibbs, A.E., Chung-ho, W., 1994. Composition and origin of hydrothermal ironstones from central Pacific seamounts. Geochim. Cosmochim. Acta 58, 179–189. https://doi.org/10.1016/0016-7037(94)90455-3.
Hein, J.R., Gibbs, A.E., Clague, D.A., Torresan, M., 1996. Hydrothermal mineralization along submarine rift zones, Hawaii. Mar. Georesour. Geotechnol. 14, 177–203. https://doi.org/10.1080/10641199609388310.
Hein, J.R., Koschinsky, A., Halbach, P., Manheim, F.T., Bau, M., Kang, J.-K., Lubick, N., 1997. Iron and manganese oxide mineralization in the Pacific. In: Nicholson, K., Hein, J.R., Bfihn, B., Dasgupta, S. (Eds.), Manganese Mineralization: Geochemistry and Mineralogy of Terrestrial and Marine Deposits, Geological Society Special Publication, pp. 123–138. https://doi.org/10.1144/GSL.SP.1997.119.01.09.
Hein, J.R., Stamatakis, M.G., Dowling, J.S., 2000. Trace metal-rich Quaternary hydrothermal manganese oxide and barite deposit, Milos Island, Greece. Trans. Inst. Min. Metall. Sect B Appl Earth Sci. 109 https://doi.org/10.1179/aes.2000.109.2.67.
Hein, J.R., Clague, D.A., Koski, R.A., Embley, R.W., Dunham, R.E., 2008a. Metalliferous sediment and a silica-hematite deposit within the Blanco fracture zone, Northeast Pacific. Mar. Georesour. Geotechnol. 26, 317–339. https://doi.org/10.1080/10641190802430986.
Hein, J.R., Schulz, M.S., Dunham, R.E., Stern, R.J., Bloomer, S.H., 2008b. Diffuse flow hydrothermal manganese mineralization along the active Mariana and southern Izu-Bonin arc system, western Pacific. J. Geophys. Res. Solid Earth 113, B08S14. https://doi.org/10.1029/2007JB005432.
Hoppe, M., Barboza-Gudiño, J.R., Schulz, H.M., 2002. Late Triassic submarine fan deposits in northwestern San Luis Potosí, Mexico — lithology, facies and diagenesis. Neu. Jahrb. Geol. Palaontol. Monatsh. 12, 705–724.
Josso, P., Pelleter, E., Pourret, O., Fouquet, Y., Etoubleau, J., Cheron, S., Bollinger, C., 2017. A new discrimination scheme for oceanic ferromanganese deposits using high field strength and rare earth elements. Ore Geol. Rev. 87, 3–15. https://doi.org/10.1016/j.oregeorev.2016.09.003.
Juárez-Arriaga, E., Lawton, T.F., Ocampo-Díaz, Y.Z.E., Stockli, D.F., Solari, L., 2019. Sediment provenance, sediment-dispersal systems, and major arc-magmatic events recorded in the Mexican foreland basin, North-Central and Northeastern Mexico. Int. Geol. Rev. 61, 2118–2142. https://doi.org/10.1080/00206814.2019.1581848.
Klinkhammer, G., Elderfield, H., Edmond, J., Mitra, A., 1994. Geochemical implications of rare earth element patterns in hydrothermal fluids from mid-ocean ridges. Geochim. Cosmochim. Acta 58, 5105–5113. https://doi.org/10.1016/0016-7037(94)90297-6.
Kuleshov, V., 2017. Isotope Geochemistry. The Origin and Formation of Manganese Rocks and Ores. Elsevier Amsterdam, Netherlands, 427p.
Lanson, B., Drits, V.A., Gaillot, A., Silvester, E., Manceau, A., Lanson, B., Drits, V.A., Gaillot, A., Silvester, E., Plançon, A., 2002. Structure of heavy metal sorbed birnessite. Part 1: results from X-ray diffraction. Am. Mineral. 87, 1631–1645.
Lottermoser, B.G., 1992. Rare earth elements and hydrothermal ore formation processes. Ore Geol. Rev. 7, 25–41. https://doi.org/10.1016/0169-1368(92)90017-F.
Madondo, J., Canet, C., González-Partida, E., Rodríguez-Díaz, A.A., Núñez-Useche, F., Alfonso, P., Rajabi, A., Pi, T., Blignaut, L., Vafeas, N., 2020. Geochemical constraints on the genesis of the 'Montaña de Manganeso' vein-type Mn deposit, Mexican Plateau. Ore Geol. Rev. 125 https://doi.org/10.1016/j.oregeorev.2020.103680.
Maghfouri, S., Rastad, E., Mousivand, F., Choulet, F., Ye, L., 2017. Geological and geochemical constraints on the Cheshmeh-Frezi volcanogenic stratiform manganese deposit, southwest Sabzevar basin, Iran. Ore Geol. Rev. 89, 96–113. https://doi.org/10.1016/j.oregeorev.2017.06.015.
Martini, M., Ortega-Gutiérrez, F., 2018. Tectono-stratigraphic evolution of eastern Mexico during the break-up of Pangea: a review. Earth Sci. Rev. 183, 38–55. https://doi.org/10.1016/j.earscirev.2016.06.013.
Martini, M., Mori, L., Solari, L., Centeno-García, E., 2011. Sandstone provenance of the Arperos Basin (Sierra de Guanajuato, Central Mexico): Late Jurassic–Early Cretaceous back-arc spreading as the foundation of the Guerrero Terrane. J. Geol. 119, 597–617. https://doi.org/10.1086/661989.

Martini, M., Solari, L., Camprubí, A., 2013. Kinematics of the Guerrero terrane accretion in the Sierra de Guanajuato, central Mexico: new insights for the structural evolution of arc-continent collisional zones. Int. Geol. Rev. 55, 574–589. https://doi.org/10.1080/00206814.2012.729361.

McDowell, F.W., Roldán-Quintana, J., Amaya-Martínez, R., 1997. Interrelationship of sedimentary and volcanic deposits associated with Tertiary extension in Sonora, Mexico. Bull. Geol. Soc. Am. 109, 1349–1360. https://doi.org/10.1130/0016-7606(1997)109.

Michard, A., Albarède, F., 1986. The REE content of some hydrothermal fluids. Chem. Geol. 55, 51–60. https://doi.org/10.1016/0009-2541(86)90127-0.

Miranda-Gasca, M.A., 2000. The metallic ore-deposits of the Guerrero Terrane, western Mexico: an overview. J. S. Am. Earth Sci. 13, 403–413. https://doi.org/10.1016/S0895-9811(00)00032-8.

Miura, H., Hariya, Y., 2007. Recent manganese oxide deposits in Hokkaido, Japan. Geol. Soc. Lond. Spec. Publ. 119, 281–299. https://doi.org/10.1144/gsl.sp.1997.119.01.18.

Mortensen, J.K., Hall, B.V., Bissig, T., Friedman, R.M., Danielson, T., Oliver, J., Rhys, D. A., Ross, K.V., Gabites, J.E., 2008. Age and paleotectonic setting of volcanogenic massive sulfide deposits in the Guerrero Terrane of Central Mexico: constraints from U–Pb age and Pb isotope studies. Econ. Geol. 103, 117–140. https://doi.org/10.2113/gsecongeo.103.1.117.

Nakagawa, M., Santosh, M., Maruyama, S., 2009. Distribution and mineral assemblages of bedded manganese deposits in Shikoku, Southwest Japan: implications for accretion tectonics. Gondwana Res. 16, 609–621. https://doi.org/10.1016/j.gr.2009.05.003.

Nakagawa, M., Santosh, M., Maruyama, S., 2011. Manganese formations in the accretionary belts of Japan: implications for subduction-accretion process in an active convergent margin. J. Asian Earth Sci. 42, 208–222. https://doi.org/10.1016/j.jseaes.2011.04.005.

Nicholson, K., 1992. Contrasting mineralogical-geochemical signatures of manganese oxides: guides to metallogenesis. Econ. Geol. 87, 1253–1264. https://doi.org/10.2113/gsecongeo.87.5.1253.

Nieto-Samaniego, Á.F., Alaniz-Álvarez, S.A., Camprubí, A., 2007. Mesa Central of México: stratigraphy, structure, and Cenozoic tectonic evolution. In: Special Paper 422: Geology of México: Celebrating the Centenary of the Geological Society of México. Geological Society of America, pp. 41–70. https://doi.org/10.1130/2007.2422(02).

Nozaki, Y., Zhang, J., Amakawa, H., 1997. The fractionation between Y and Ho in the marine environment. Earth Planet. Sci. Lett. 148, 329–340. https://doi.org/10.1016/S0012-821X(97)00034-4.

Okita, P.M., Shanks, W.C., 1992. Origin of stratiform sediment hosted manganese carbonate ore deposites: examples from Molango, Mexico, and TaoJiang, China. Chem. Geol. 99, 139–164.

Okita, P.M., Maynard, J.B., Spiker, E.C., Force, E.R., 1988. Isotopic evidence for organic matter oxidation by manganese reduction in the formation of stratiform manganese carbonate ore. Geochim. Cosmochim. Acta 52, 2679–2685. https://doi.org/10.1016/0016-7037(88)90036-1.

Oksuz, N., 2011. Geochemical characteristics of the Eymir (Sorgun-Yozgat) manganese deposit, Turkey. J. Rare Earths 29, 287–296. https://doi.org/10.1016/S1002-0721(10)60446-2.

Öksüz, N., Okuyucu, N., 2014. Mineralogy, geochemistry, and origin of Buyukmahal manganese mineralization in the Artova ophiolitic complex, Yozgat, Turkey. J. Chem. 2014, 1–11. https://doi.org/10.1155/2014/837972.

Olvera-Rosas, L.E., Aguilar de Lira, Á., Avitud, A., 2013. Manganeso y procesos volcánicos de rift post arco. In: AIMMGM, XXX Convención Internacional de Minería. Acapulco, pp. 2011–2018.

Ostwald, J., 1982. Some observations on todorokites from marine and terrestrial environments. Mineral. Mag. 46, 253–256. https://doi.org/10.1180/minmag.1982.046.339.12.

Ostwald, J., 1988. Mineralogy of the Groote Eylandt manganese oxides: a review. Ore Geol. Rev. 4, 3–45. https://doi.org/10.1016/0169-1368(88)90003-0.

Öztürk, H., Hein, J.R., 1997. Mineralogy and stable isotopes of black shale-hosted manganese ores, Southwestern Taurides, Turkey. Econ. Geol. 92, 733–744. https://doi.org/10.2113/gsecongeo.92.6.733.

Papavassiliou, K., Voudouris, P., Kanellopoulos, C., Glasby, G., Alfieris, D., Mitsis, I., 2017. New geochemical and mineralogical constraints on the genesis of the Vani hydrothermal manganese deposit at NW Milos island, Greece: comparison with the Aspro Gialoudi deposit and implications for the formation of the Milos manganese mineralization. Ore Geol. Rev. 80, 594–611. https://doi.org/10.1016/j.oregeorev.2016.07.023.

Pelleter, E., Fouquet, Y., Etoubleau, J., Cheron, S., Labanieh, S., Josso, P., Bollinger, C., Langlade, J., 2017. Ni-Cu-Co-rich hydrothermal manganese mineralization in the Wallis and Futuna back-arc environment (SW Pacific). Ore Geol. Rev. 87, 126–146. https://doi.org/10.1016/j.oregeorev.2016.09.014.

Post, J.E., 1999. Manganese oxide minerals: crystal structures and economic and environmental significance. In: Proceedings of the National Academy of Sciences, pp. 3447–3454. https://doi.org/10.1073/pnas.96.7.3447.

Post, J.E., Bish, D.L., 1988. Rietveld refinement of the coronadite structure. Am. Mineral. 74, 913–917.

Post, J.E., Heaney, P.J., Hanson, J., 2003. Synchrotron X-ray diffraction study of the structure and dehydration behavior of todorokite. Am. Mineral. 88, 142–150. https://doi.org/10.2138/am-2003-0117.

Rodríguez-Díaz, A., Villaseñor-Cabral, G., Canet, C., Prol-Ledesma, R.M., Camprubí, A., 2005. Clasificación de los yacimientos de manganeso y ejemplos de depósitos mexicanos e internacionales. Bol. Miner. 16, 33–43 doi:0186-470X.

Rodríguez-Díaz, A.A., Blanco-Florido, D., Canet, C., Gervilla-Linares, F., González-Partida, E., Prol-Ledesma, R.M., Morales-Ruano, S., García-Vallès, M., 2010. Metallogeny of the Santa Rosa manganese deposit, Baja California Sur, Mexico. Bol. Soc. Geol. Mex. 62, 141–159.

Rodríguez-Díaz, A.A., Canet, C., Villanueva-Estrada, R.E., Chacón, E., Gervilla, F., Velasco-Tapia, F., Cruz-Gámez, E.M., González-Partida, E., Casas-García, R., Linares-López, C., Pérez-Zárate, D., 2019. Recent Mn-Ag deposits in coastal hydrothermal springs in the Baja California Peninsula, Mexico. Mineral. Deposita 54, 849–866. https://doi.org/10.1007/s00126-018-0846-9.

Rodríguez-Ríos, R., Tristán-González, M., Aguillón-Robles, A., 2013. Estructura y geoquímica de un grupo de domos dacíticos del norponiente del campo volcánico de san luis potosí, méxico. Bol. Soc. Geol. Mex. 65, 109–122. https://doi.org/10.18268/bsgm2013v65n1a9.

Roy, S., 1992. Environments and processes of manganese deposition. Econ. Geol. 87, 1218–1236. https://doi.org/10.2113/gsecongeo.87.5.1218.

Roy, S., 1997. Genetic diversity of manganese deposition in the terrestrial geological record. Geol. Soc. Spec. Publ. 119, 5–27. https://doi.org/10.1144/GSL.SP.1997.119.01.02.

Roy, S., Bandopadhyay, P.C., Perseil, E.A., Fukuoka, M., 1990. Late diagenetic changes in manganese ores of the Upper Proterozoic Penganga Group, India. Ore Geol. Rev. 5, 341–357. https://doi.org/10.1016/0169-1368(90)90038-O.

Sabanero-Sosa, H.M., Salinas-Prieto, J.C., González-Arroyo, A., Ocejo-Paredes, T., 1999. Caracterización tectonica e implicaciones metalogeneticas de la faja de plata. Geomimet 230, 16–36.

Sanada, T., Takamatsu, N., Yoshiike, Y., 2006. Geochemical interpretation of long-term variations in rare earth element concentrations in acidic hot spring waters from the Tamagawa geothermal area, Japan. Geothermics 35, 141–155. https://doi.org/10.1016/J.GEOTHERMICS.2006.02.004.

Sánchez-Rojas, L.E., 2013. Jasperoides en el límite de los terrenos Guerrero y Sierra Madre Oriental. In: AIMMGM, XXX Convención Internacional de Minería. Acapulco, pp. 312–319.

Sasmaz, A., Turkyılmaz, B., Ozturk, N., Yavuz, F., Kumral, M., 2014. Geology and geochemistry of Middle Eocene Maden complex ferromanganese deposits from the Elazıg-Malatyă region, eastern Turkey. Ore Geol. Rev. 56, 352–372.

Sasmaz, A., Zagnitko, V.M., Sasmaz, B., 2020. Major, trace and rare earth element (REE) geochemistry of the Oligocene stratiform manganese oxide-hydroxide deposits in the Nikopol, Ukraine. Ore Geol. Rev. 126, 103772.

Sasmaz, A., Sasmaz, B., Hein, J.R., 2021. Geochemical approach to the genesis of the Oligocene-stratiform manganese-oxide deposit, Chiatura (Georgia). Ore Geol. Rev. 128, 103910.

Servicio Geologico Mexicano (SGM), 2018. Monografía Geológica Minera del Estado de Zacatecas. Pachuca, Hgo.

Sinisi, R., Mameli, P., Mongelli, G., Oggiano, G., 2012. Different Mn-ores in a continental arc setting: geochemical and mineralogical evidences from Tertiary deposits of Sardinia (Italy). Ore Geol. Rev. 47, 110–125. https://doi.org/10.1016/j.oregeorev.2012.03.006.

Sinisi, R., Mongelli, G., Perri, F., Rizzo, G., 2018. The braunite ($3Mn_2O_3{\cdot}MnSiO_3$)-rich mineralization in the metasedimentary succession from southern Apennines (Italy): genesis constraints. Ore Geol. Rev. 94, 1–11. https://doi.org/10.1016/j.oregeorev.2018.01.014.

Taylor, S.R., McLennan, S.M., 1985. The Continental Crust: Its Composition and Evolution. An Examination of the Geochemical Record Preserved in Sedimentary Rocks. Blackwell, Oxford, 312p.

Taylor, S.R., McLennan, S.M., 1995. The geochemical evolution of the continental crust. Rev. Geophys. https://doi.org/10.1029/95RG00262.

Tompsett, D.A., Islam, M.S., 2013. Electrochemistry of hollandite α-MnO_2: Li-ion and Na-ion insertion and Li_2O incorporation. Chem. Mater. 25, 2515–2526. https://doi.org/10.1021/cm400864n.

Toth, J.R., 1980. Deposition of submarine crusts rich in manganese and iron. Geol. Soc. Am. Bull. 91, 44–54. https://doi.org/10.1130/0016-7606(1980)91.

Trask, P.D., Cabo, J.R., 1948. Manganese deposits of Mexico. Geol. Investig. Am. Repub. 1946, 209–316.

Tristán-González, M., Torres Hernández, J.R., 2000. Informe de la carta geologico-minera y geoquímica. Carta Hernández F13-B49. Pachuca, Hgo.

Tristán-González, M., Labarthe-Hernández, G., Aguirre-Díaz, G.J., Aguillón-Robles, A., 2008. Tectono-volcanic control of fissure type vents for the 28 Ma Panalillo ignimbrite in the Villa de Reyes Graben, San Luis Potosí, México. IOP Conf. Ser. Earth Environ. Sci. 3, 12026. https://doi.org/10.1088/1755-1307/3/1/012026.

Tristán-González, M., Aguillón-Robles, A., Barboza-Gudiño, J.R., Torres-Hernández, J.R., Bellon, H., López-Donce, R., Rodríguez-Ríos, R., Labarthe-Hernández, G., 2009a. Geocronología y distribución espacial del vulcanismo en el Campo Volcánico de San Luis Potosí. Bol. Soc. Geol. Mex. 61, 287–303. https://doi.org/10.18268/BSGM2009v61n3a1.

Tristán-González, M., Aguirre-Díaz, G.J., Labarthe-Hernández, G., Torres-Hernández, J. R., Bellon, H., 2009b. Post-Laramide and pre-Basin and Range deformation and implications for Paleogene (55–25 Ma) volcanism in central Mexico: a geological basis for a volcano-tectonic stress model. Tectonophysics 471, 136–152. https://doi.org/10.1016/j.tecto.2008.12.021.

Tristán-González, M., Torres Hernández, J.R., Labarthe Hernández, G., Aguillón Robles, A., Yza Guzmán, R., 2012. Control estructural para el emplazamiento de vetas y domos félsicos en el distrito minero de Zacatecas, México. Bol. Soc. Geol. Mex. 64, 353–367. https://doi.org/10.18268/BSGM2012v64n3a7.

Usui, A., Someya, M., 1997. Distribution and composition of marine hydrogenetic and hydrothermal manganese deposits in the northwest Pacific. Geol. Soc. Lond., Spec. Publ. 119, 177–198. https://doi.org/10.1144/gsl.sp.1997.119.01.12.

Wang, X.Y., Zeng, Z.G., Chen, S., Yin, X.B., Chen, C.T.A., 2013. Rare earth elements in hydrothermal fluids from Kueishantao, off northeastern Taiwan: indicators of shallow-water, sub-seafloor hydrothermal processes. Chin. Sci. Bull. 58, 4012–4020. https://doi.org/10.1007/s11434-013-5849-4.

Wilson, I.F., Rocha, V.S., 1948. Manganese deposits of the Montaña de Manganeso mine, San Luis Potosí, Mexico. In: Trask, P.D., Cabo, J.R. (Eds.), 1948. Manganese Deposits of Mexico, U.S Geological Survey Bulletin, 954-F, pp. 267–271.

Wright, J., Schrader, H., Holser, W.T., 1987. Paleoredox variations in ancient oceans recorded by rare earth elements in fossil apatite. Geochim. Cosmochim. Acta 51, 631–644. https://doi.org/10.1016/0016-7037(87)90075-5.

Zantop, H., 1978. Geologic setting and genesis of iron oxides and manganese oxides in the San Francisco manganese deposit, Jalisco, Mexico. Econ. Geol. 73, 1137–1149. https://doi.org/10.2113/gsecongeo.73.6.1137.

Zantop, H., 1981. Trace elements in volcanogenic manganese oxides: the San Francisco manganese deposit, Jalisco, Mexico. Econ. Geol. 76, 545–555. https://doi.org/10.2113/gsecongeo.76.3.545.

Zierenberg, R., Fowler, A., Reed, M., Palanderi, J., 2018. Maximizing REE recovery in geothermal systems. United States. https://www.osti.gov/servlets/purl/1501682 (accessed 13 January 2021) doi:10.2172/1501682.

CHAPTER 6

GENESIS OF THE MONTAÑA DE MANGANESO DEPOSIT

Ore Geology Reviews 125 (2020) 103680

Contents lists available at ScienceDirect

Ore Geology Reviews

journal homepage: www.elsevier.com/locate/oregeorev

Geochemical constraints on the genesis of the 'Montaña de Manganeso' vein-type Mn deposit, Mexican Plateau

Joseph Madondo[a], Carles Canet[b,c,*], Eduardo González-Partida[d], Augusto A. Rodríguez-Díaz[c], Fernando Núñez-Useche[e], Pura Alfonso[f], Abdorrahman Rajabi[g], Teresa Pi[e], Lauren Blignaut[h], Nicholas Vafeas[i]

[a] Posgrado en Ciencias de la Tierra, Universidad Nacional Autónoma de México, Ciudad Universitaria, 04510 CdMx, Mexico
[b] Centro de Ciencias de la Atmósfera, Universidad Nacional Autónoma de México, Ciudad Universitaria, 04510 CdMx, Mexico
[c] Instituto de Geofísica, Universidad Nacional Autónoma de México, Ciudad Universitaria, 04510 CdMx, Mexico
[d] Centro de Geociencias, Universidad Nacional Autónoma de México, Juriquilla, 76230 Querétaro, Mexico
[e] Instituto de Geología, Universidad Nacional Autónoma de México, Ciudad Universitaria, 04510 CdMx, Mexico
[f] Departament d'Enginyeria Minera, Industrial i TIC, Universitat Politècnica de Catalunya, Av. de les Bases de Manresa 61-73, 08242 Manresa, Spain
[g] School of Geology, College of Science, University of Tehran, Tehran, Iran
[h] Department of Geology, University of Johannesburg, Corner Kingsway Avenue & University Road, Aukland Park, South Africa
[i] Irish Centre for Research in Applied Geosciences, O'Brien Centre for Science (East), University College Dublin, Belfield, Dublin 4, Ireland

ARTICLE INFO

Keywords:
Stable isotopes
Geochronology
Fluid inclusions
Epithermal
Manganese oxides
San Luis Potosí

ABSTRACT

Manganese mineralization at Montaña de Manganeso, San Luis Potosí state, consists of oxide ores that form sharp contacts with volcanic host rocks. The orebodies are generally in the form of veins and irregular masses, and locally as mineralized breccias. Petrographic analyses indicate that the mineralization is multi-episodic, with colloform and crustiform textures predominating. The X-ray diffraction and electron microscopy show that manganese oxides (todorokite, birnessite, pyrolusite, romanechite and cryptomelane) are the main ore minerals, while iron oxides (goethite and hematite) are accessory. The most common gangue minerals are calcite and quartz with subordinate amounts of barite.

According to fluid inclusion microthermometry, the mineralization is associated with aqueous solutions of intermediate salinity (8–16 wt% NaCl equivalent) and temperatures between 101 and 140 °C. Stable isotope analysis of calcite ($\delta^{13}C_{PDB}$: −7.76 to −6.32‰; $\delta^{18}O_{PDB}$: −8.01 to −4.71‰) and barite ($\delta^{34}S$: 7.9–13.6‰) shows a contribution of magmatic volatiles to hydrothermal fluids dominated by meteoric water (calculated $\delta^{18}O_{fluid}$: 6.58–13.14‰, relative to SMOW). Argillic alteration is the most widespread hydrothermal alteration at Montaña de Manganeso and indicates fluid temperature below ~150 °C and near neutral pH. Much more local, advanced argillic alteration, revealed by the occurrence of kaolinite, is interpreted as a steam-heated overprint, which in turn suggests a boiling process that must have happened at greater depths. The Mn ores formed through a process of mixing of: (*a*) boiled-off hydrothermal fluids, with (*b*) cold, diluted meteoric water. Our results support a hot-spring deposit model, according to which Montaña de Manganeso corresponds to the shallowest portion of an epithermal system formed in a continental volcanic arc setting.

1. Introduction

Mexico has a substantial number of continental and shallow submarine hydrothermal manganese deposits. Most of them occur as veins hosted in Tertiary, silicic to intermediate volcanic rocks, locally developing stratabound to semi-concordant lenticular bodies (Hewett, 1964; Zantop, 1978; Laznicka, 1992; Roy, 1992; Roy, 1997; Rodríguez Díaz et al., 2010). The majority of these deposits would have formed in the shallow epithermal environment (Hewett, 1964; Hewett, 1968; Roy, 1997; Liakopoulos et al., 2001; Leal et al., 2008; Rodríguez Díaz et al., 2010; Conly et al., 2011). These deposits have not received as much attention as their sedimentary counterparts (*e.g.* Molango, central-eastern Mexico; Okita and Shanks, 1992; Kalahari deposits, South Africa; Gutzmer and Beukes, 1996; and Úrkút, Hungary; Polgari et al., 2012), because they are generally small and uneconomic. However, there is a renewed interest in them due to their genetic links with

* Corresponding author at: Centro de Ciencias de la Atmósfera, Universidad Nacional Autónoma de México, Ciudad Universitaria, 04510 CdMx, Mexico.
E-mail address: ccanet@atmosfera.unam.mx (C. Canet).

https://doi.org/10.1016/j.oregeorev.2020.103680
Received 10 November 2019; Received in revised form 24 June 2020; Accepted 7 July 2020
Available online 14 July 2020
0169-1368/

epithermal deposits and geothermal systems (Liakopoulos et al., 2001; Canet et al., 2005b).

Within the Central Plateau of Mexico, in the northwest of San Luis Potosí state and easternmost part of Zacatecas state, there is a NW-SE trending belt of manganese deposits (Gómez Torres and Góngora Flemate, 2001), whose genesis is poorly understood. The manganese deposits in this belt are associated with 'jasperoids' (rocks formed by silicification of pre-existing rocks) and have no evident spatial relationship with volcanic structures. The orebodies are hosted by Upper Cretaceous rocks that belong to (*a*) the accreted volcano-sedimentary Guerrero terrane, or (*b*) the volcaniclastic Caracol Formation (COREMI, 2001). The Montaña de Manganeso manganese deposit, in the northeast of San Luis Potosí state, is the largest among numerous manganese vein deposits within the Central Plateau and the only one that has been significantly exploited.

Previous research on Montaña de Manganeso addressed particular aspects of the geology, mineralogy and structure of this deposit, with a few studies having been published (Rocha and Wilson, 1946; Trask and Cabo, 1948; Wilson and Rocha, 1948). Geophysical exploration was carried out during the 1980's as part of a Mexico-Spain project on manganese (COREMI, 1980). These previous works set the geologic framework of the deposit (COREMI, 2001). However, the tectonic setting, the age of the deposit, the genesis and nature of the ore-forming fluids, the deposition mechanism(s), and the mineral paragenesis were not well understood or even addressed.

In this study we describe in detail the mineralogical and geochemical characteristics of the Montaña de Manganeso vein-type manganese deposit. These characteristics of the manganese mineralization are interpreted to constrain its genesis. We focus on the ore paragenesis and hydrothermal alteration, as well as C, O and S stable isotope systematics to determine the source of the ore-forming fluids and processes experienced by them. We also study fluid inclusions to estimate physicochemical conditions of the mineralizing fluids and deposition mechanism(s); U-Pb geochronology helps constrain the age of the deposit. It is hoped the findings of this study can be applied for exploration of the vein-type manganese deposits that are widespread in the Central Plateau and similar deposits worldwide.

2. Geological setting

2.1. Regional framework

The study area is situated in the Central Plateau physiographic province (Fig. 1), an elevated plateau (average altitude: ~2000 m a.s.l.) bounded to the north and east by the Sierra Madre Oriental, to the west by the Sierra Madre Occidental, and to the south by the E-W El Bajío fault (Nieto-Samaniego et al., 2005).

The oldest rocks in the Central Plateau are Upper Triassic–middle Jurassic turbidites (La Ballena and Nazas formations) that constitute the regional basement (Centeno-García and Silva-Romo, 1997; Barboza-Gudiño et al., 2010). Overlying them in the westernmost part of the Central Plateau are Jurassic volcano-sedimentary rocks belonging to the Guerrero terrane (Fig. 1) (Campa and Coney, 1983; Centeno-García and Silva-Romo, 1997; Centeno-Garcia et al., 2003). In the central and eastern Central Plateau, marine carbonate sequences (Zuloaga, La Caja, Taraises, Tamaulipas, Cuesta del Cura, Indidura and Caracol formations) were deposited on the Valles–San Luis Potosí platform, belonging to the Sierra Madre terrane (Fig. 1).

The Montaña de Manganeso mining district encompasses the border between the Sierra Madre terrane to the N and NE, and the Guerrero terrane to the W and SW (Fig. 2). The former is a continental margin produced by the breakup of Pangaea and the opening of the Gulf of Mexico, whereas the latter is an ocean floor and island arc volcano-sedimentary complex associated with the Cordilleran convergent margin (Centeno-Garcia et al., 1993; Silva-Romo et al., 2000). The concurrence of both terranes in the region is due to a process of

Fig. 1. A schematic representation of the geology of the Zacatecas San Luis Potosí region showing location of the Central Plateau and the study area (modified from Tristán-González et al., 2015). Insert: Map of Mexico showing the position of the Central Plateau.

accretion caused by the Laramide orogenesis (Centeno-Garcia et al., 2003; Centeno-García et al., 2008; Martini et al., 2012).

The Montaña de Manganeso deposit forms part of the NW-SE-trending Zacatecas San Luis Potosí manganese belt. The study region can be understood as the result of the compression effects caused by the accretion of the Guerrero terrane over continental Mexico (Centeno-García et al., 2003; Centeno-García et al., 2008; Martini et al., 2012; Centeno-García, 2017). The accretion deformed the Mesozoic rocks and created a suture zone close to 100 km in width (Sabanero-Sosa et al., 1999). Post-Laramidic extension events produced mostly NW-SE-trending normal faults related to the Basin and Range system, which were superimposed over the thrust faults created by the accretion. Some of these thrust faults were reactivated. These fault types control mineralization within the Zacatecas San Luis Potosí manganese belt (COREMI, 2001; Aguirre-Díaz et al., 2007). The extension also created NW-SE horst-and-graben structures, which favored the deposition of Quaternary gravel and sand that cover the older formations throughout much of the area (COREMI, 2001; González-Villalvaso and López-Soto, 2009; Tristán-González et al., 2009a).

In the Zacatecas San Luis Potosí region volcanism is represented mainly by rhyolitic-rhyodacitic lava flows that are product of Eocene-Oligocene volcanism (Nieto-Samaniego et al., 1996; Aguillón-Robles et al., 2014). During the Eocene-Oligocene period, significant bimodal andesitic-rhyolitic volcanic events occurred in the Central Plateau associated with ignimbritic silicic volcanism of the Sierra Madre Occidental. This volcanism occurred mostly as multiple discrete episodes of small rhyolitic volcanic fissures mostly controlled by major NW–SE trending fault systems of the region (Aguirre-Díaz et al., 2008; Tristán-González et al., 2008; Tristán-González et al., 2009b; Aguillón-Robles et al., 2014). The emplacement of rhyolitic and andesitic rocks during the Eocene-Oligocene magmatic events within the Central Plateau is well documented. The oldest igneous rocks are andesitic lavas dated at approximately 44 Ma (K–Ar: ~44 Ma; Labarthe-Hernández et al., 1982; Tristán-González et al., 2008) and felsic ignimbrites (K–Ar: 46.8–42.3 Ma; Ponce and Clark, 1988). However, peak volcanism occurred between 32 and 21 Ma associated with the ignimbritic flare-up event (Nieto-Samaniego et al., 1996; Aguillón-Robles et al., 2014).

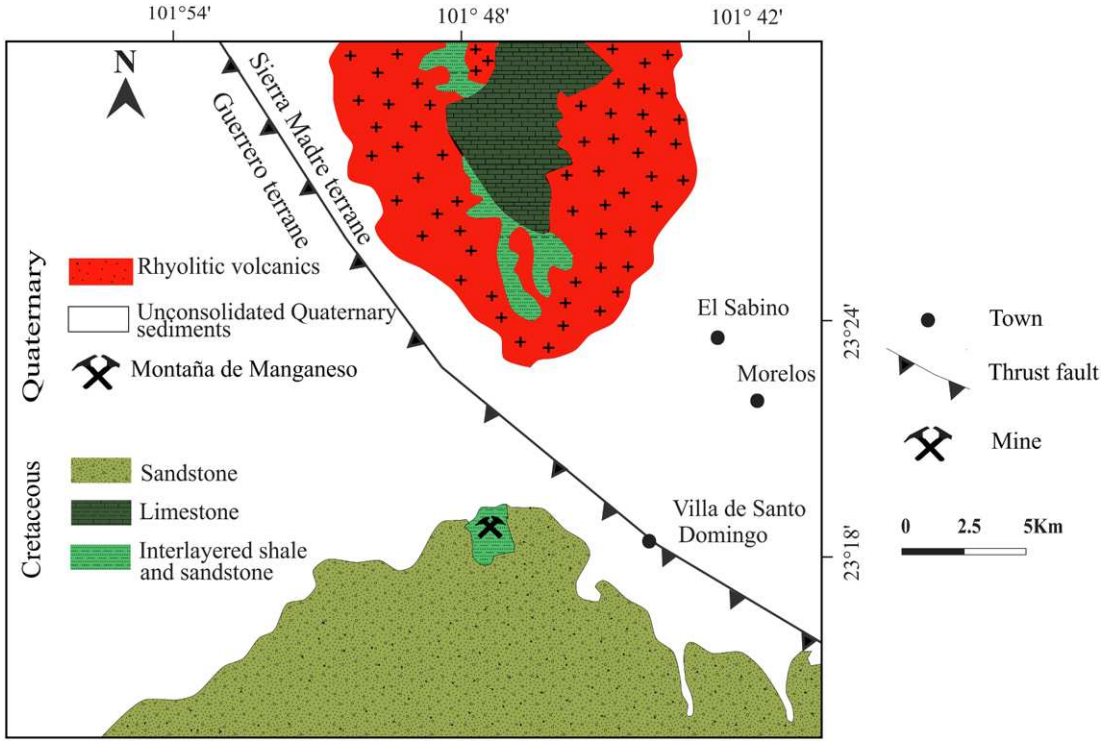

Fig. 2. Generalized geologic map of the study area.

2.2. Geology of Montaña de Manganeso

Mineral deposits found in the Central Plateau, particularly those of precious and base metals, are associated with major fault systems such as those of San Luis–Tepehuanes, Taxco–San Miguel de Allende and El Bajío, which controlled the emplacement of volcanic rocks as well as of mineralizing fluids (Damon et al., 1981; Clark et al., 1982; Nieto-Samaniego et al., 2005; Camprubí, 2009; Jiménez-Franco et al., 2020). According to Sabanero-Sosa et al. (1999), the emplacement of manganese deposits (and possibly of most Au-Ag and base metal deposits) in the Central Plateau is controlled by the thrust and normal faults of the Sierra Madre–Guerrero suture zone, which would explain the NW-SE arrangement of the deposits of the Zacatecas San Luis Potosí manganese belt (Gómez Torres and Góngora Flemate, 2001).

The deposits of the Zacatecas San Luis Potosí manganese belt show different styles of epigenetic mineralization, occurring as mantos, veins and chimneys, and are in all cases spatially related to jasperoids (Trask and Cabo, 1948). Jasperoids form by silicic replacement of preexisting rocks -presumably limestone- (Grenne and Slack, 2003; Kostov, 1977). They develop layers that range from a few centimeters to several meters in thickness and show variations in thickness along strike. The jasperoids related to manganese deposits and occurrences are in most cases hosted within the Upper Cretaceous Indidura and Caracol formations, with only a few reported in the volcano-sedimentary rocks of the Guerrero terrane (COREMI, 2001). Jasperoids are resistant to weathering and hence commonly form hilly outcrops.

The Montaña de Manganeso mine is one of the oldest manganese mines in Mexico, with production known to have occurred more or less continuously since the World War I. Total reserves and production are not available; however, a historical peak production of about 100 000 tons of ore were produced in 1939, making this mine the largest producer of manganese ore of that time in Mexico (Alexandri, 1976). The mine is operated by the Huajicari, S.A. de C.V company and current production is about 4000 metric tons per day (Servicio Geológico Mexican, 2011).

The Montaña de Manganeso deposit crops out on a small hill that protrudes about 30 m above the surrounding terrain. It is approximately 300 m long and 100 m wide. Due to the irregular distribution of the manganese mineralization, mine works are diverse and include stopes, adits and galleries. Manganese ores occur mainly as fault-controlled irregular veins, between 5 and 30 m thick (Fig. 3A and B), confined for the most part to NE-trending faults (Trask and Cabo, 1948; Alexandri, 1976). The manganese mineralization is spatially associated with jasperoids. Although there is no evidence of magmatic activity on the surface, Paleogene magmatism has been invoked as a presumed deep heat source driving the hydrothermal process that produced both jasperoids and manganese mineralization (Labarthe-Hernández et al., 1992; Sánchez-Rojas, 2013).

At Montaña de Manganeso, jasperoids are hosted by the volcaniclastic sedimentary rocks of the Caracol Formation and occur as gray and red massive (instead of layered) bodies, whose continuity along strike rarely exceeds a few meters (Fig. 4A and B); jasperoids and manganese ores are closely associated, generally presenting mutual cutting relationships and gradational contacts (Fig. 4A).

The origin and depositional environment of the host rocks at Montaña de Manganeso are still unresolved. According to the boundaries of the Guerrero terrane as established by Campa and Coney (1983), Sedlock et al. (1993) and Centeno-García and Silva-Romo (1997), Montaña de Manganeso occurs within the continental Sierra Madre terrane. The structural control on Montaña de Manganeso is believed to be evidence that the deposit formed in the post-collision extensional environment at the end of the Laramide orogeny and the beginning of the Basin and Range province (Sabanero-Sosa et al., 1999; COREMI, 2001). However, more recent studies suggest that Montaña de Manganeso belongs to the oceanic Guerrero terrane (Gómez Torres and Góngora Flemate, 2001; Sabanero-Sosa et al., 1999; Consejo de Recursos Minerales (COREMI), 2001).

3. Sampling and analytical methods

Rock samples (n = 44) representative of host rocks, altered host rocks and of manganese ore samples were collected from surface

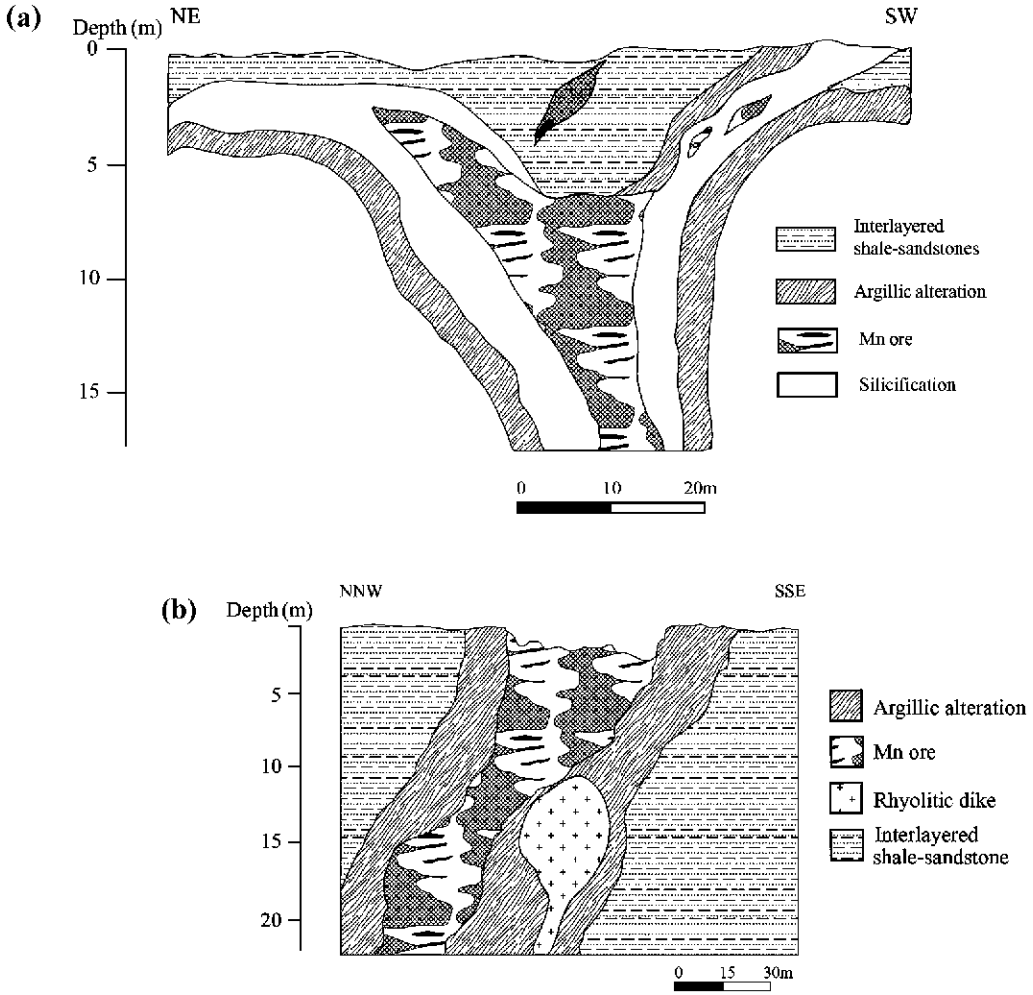

Fig. 3. Structure of the mineralized zones of the Montaña de Manganeso deposit. (A) Cross section of one of the veins from the surface outcrops, and (B) from underground workings with an associated dated andesitic dike.

outcrops and underground mine works. Quartz crystals were specifically collected for fluid inclusion (FI) studies. Rocks with conspicuous alteration were sampled every 0.5 m from the mineralization.

A total of 21 polished thin sections were prepared at the Centro de Geociencias of the Universidad Nacional Autónoma de México (UNAM). Of these, 14 were prepared as doubly polished sections for FI analyses (300 μm thick), whilst seven were prepared as thin polished sections (30 μm thick) for petrography and electron microprobe analysis. Petrographic observations were done on the polished thin sections under both reflected and transmitted light, using a Carl Zeiss microscope model Axiolab coupled with Axiovision software for photomicrography at the Instituto de Geofísica, UNAM.

Nineteen samples were analyzed by short-wave infrared (SWIR) reflectance spectroscopy using a portable LabSpec Pro Spectrophotometer (Analytical Spectral Devices, Inc.) at the Instituto de Geofísica, UNAM. Measurements were done in the SWIR (1300–2500 nm) wavelength region. Samples were spectrally measured in the laboratory, without any treatment prior to spectra collection. Identification of SWIR active minerals was done manually by comparing the wavelength position of the absorption features and the general shape of the spectra (without hull subtraction) with spectral libraries and tables (USGS Spectroscopy Lab of Clark et al., 2007).

Bulk mineralogy of three samples of altered host rock and 16 of Mn mineralization was determined by X-ray diffraction (XRD) using an EMPYREAN diffractometer equipped with Ni filter, a Cu tube of fine focus and a PIXcel^{3d} detector, at the Instituto de Geología, UNAM. Measurements were performed in the 2θ angular range from 5° to 70°, in step scanning with a step scan of 0.003° (2θ) and an integration time of 40 s per step. Rock samples were previously crushed, quartered, pulverized to 200 mesh and homogenized. For clay mineralogy identification, three oriented aggregates of samples (that were selected based on SWIR spectra) were subjected to chemical (glycolation) and thermal (heat) treatment (*cf.* Środoń, 2013). Preparation of clay samples followed the methods of Brindley and Brown (1980) and Moore and Reynolds (1989), whilst the identification followed the procedures described by Środoń (2013) and Środoń (2006). The manganese mineralogy was identified using the reference intensity ratios values listed in the PDF-4 database included into the X'Pert HighScore Plus software (PANalytical). Mn oxides were identified based on their XRD patterns (Post, 1999).

Scanning electron microscopy (SEM) was used as a technique complementary to light microscopy for mineral and textural characterization. This study was carried out on six polished sections, which were previously examined by reflected light microscopy. The chemistry of certain minerals was determined semi-quantitatively by energy dispersive spectrometry (EDS). Images were obtained using backscattered electrons (BSE). The analyses were carried out on a JEOL SEM system equipped with EDS available at the Instituto de Geofísica, UNAM. Complementary images were also taken using a Vega 3 Tescan system equipped with an Oxford X-Max 50 mm^2 energy dispersive spectrometer (EDS) using an Oxford Aztec software V. 2.2 at the Central Analytical Facility of the Faculty of Science of the University of

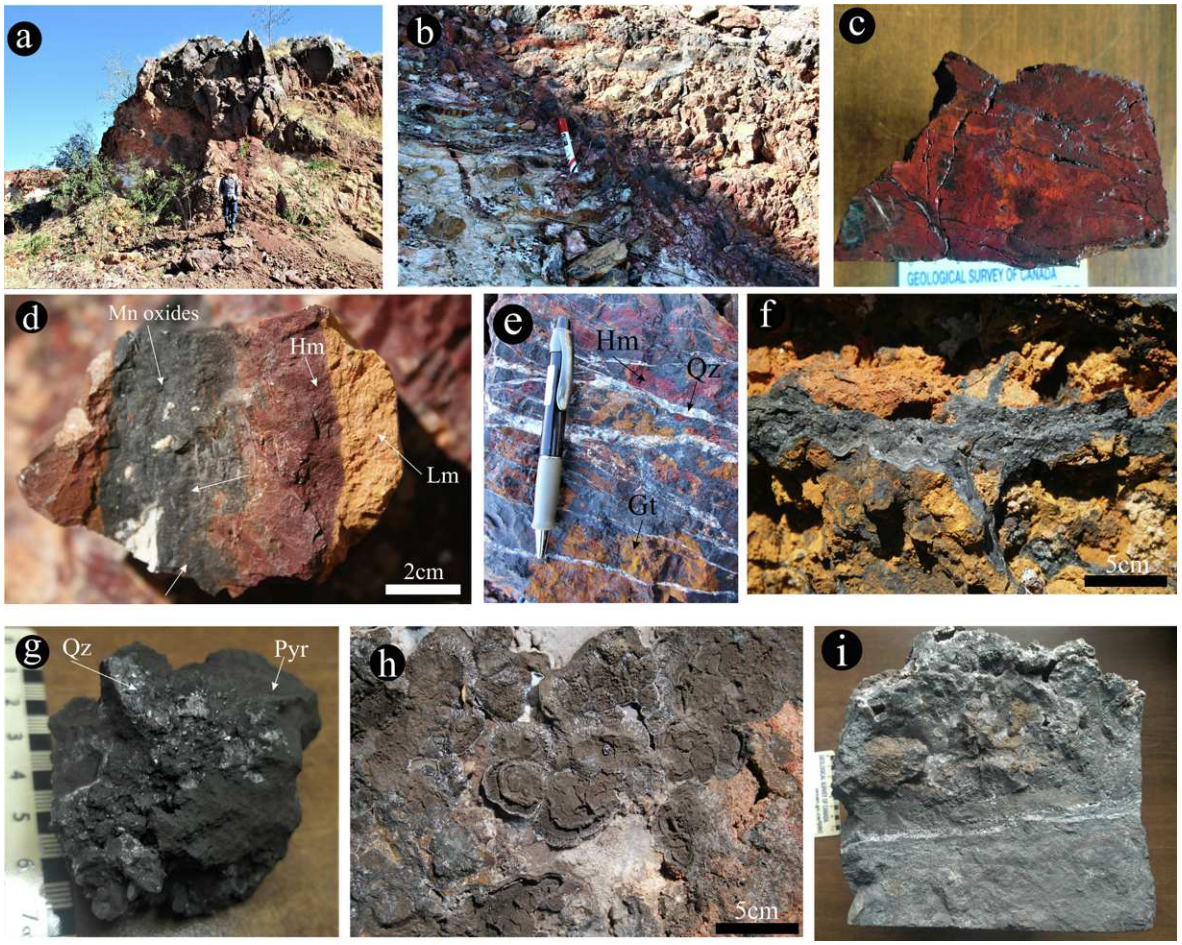

Fig. 4. Mineralization styles and ore textures at Montaña de Manganeso. (A) Massive black jasperoids closely associated with manganese ore cut across the host rock. (B) Locally, the host rocks are completely leached and whitened. The intensity of alteration is higher near the orebodies. C) Hematitic jasperoids showing the typical deep red color (D) A complete separation of Mn and Fe in the jasperoids is commonly observed (E) Some jasperoids are more diverse, with comparable quantities of hematite, Mn oxides and goethite. Late sterile millimetric veins of up to 4 mm crosscut the jasperoids. (F and H) Supergene birnessite and pyrolusite have formed on recent sediments. (G) Quartz on soft friable pyrolusite product of supergene alteration of massive black ore. (I) Massive black jasperoid. The amount of manganese decreases upwards whilst chalcedony increases.

Johannesburg. Wavelength Dispersive X-ray Spectroscopy (WDS) analyses were performed at UNAM to obtain quantitative microanalysis (microprobe data) of selected minerals. Quantitative WDS analyses of Mn oxides were carried out using an accelerating voltage of 20 kV, a beam current of 20nA, a spot size of 1 μm, and a counting time of 10 s for K and Na and 40 s for all other elements. Plagioclase (CaKα), biotite (KKα), diopside (NaKα), rhodonite (FeKα), kaersutite (SiKα), almandine (MgKα), kaersutite (AlKα), sphalerite (ZnKα), galena (PbMα), barite (BaLα), bustamite (MnKα) and cuprite (CuKα) were used as standards for the analysis of the Mn oxides. The detection limits for all elements is 0.04 wt%. The equipment was calibrated frequently with a rhodonite test sample to assure maximum accuracy and precision.

Fluid inclusion (FI) microthermometry was carried out on a Linkam THMSG 600 thermal plate (freezing/heating stage) and a coupled image analysis system to record phase changes at the Centro de Geociencias, UNAM. Liquid nitrogen and a thermal resistor were used for cooling and heating, respectively. The heating-freezing stage is mounted on a binocular Olympus BH 60 infrared microscope with a maximum magnification of 500×. The FI were cooled to −100 °C and phase transition temperatures were measured upon heating. The FI were heated up to a temperature of approximately 150 °C to get the homogenization temperature (T_h). The heating rate was maintained at about 5 °C per minute during the initial stages of each heating run and reduced to 0.1 °C per minute when the phase transitions were approached. Following the observations and recommendations by Bodnar et al. (1985) and Sander and Black (1988), we analyzed only FI hosted by minerals lacking evidence of recrystallization. Given that only a few and isolated primary inclusions were available, individual FI -instead of FI assemblages- were measured. Finally, melting of ice temperatures (T_m) and T_h were recorded. The reproducibility of the measurements was ± 0.2 °C below 0 °C (T_m) and ± 2 °C for T_h. Salinity was calculated from microthermometric data using the Bodnar (1993) equations and assuming a H_2O-NaCl system (Bodnar, 1983). Trapping pressure and fluid density of FI were estimated using the program HOKIEFLINCS_H_2O-NaCl (Steele-MacInnis et al., 2012).

Isotopic compositions are expressed in δ notation (in deviation ‰), where

$$\delta = [(R_{Sample}/R_{Standard}) - 1] \times 1000$$

and R_{Sample} and $R_{Standard}$ are the ratios $^{34}S/^{32}S$, $^{18}O/^{16}O$ and $^{13}C/^{12}C$ in sample and standard, respectively. Sulfur isotope data are reported relative to the Vienna Canyon del Diablo Troilite (V-CTD) standard, carbon isotope data are reported relative to the Vienna-Pee Dee Belemnite (V-PDB) standard, and oxygen isotope data are reported relative to the V-PDB and the Vienna Standard Mean Ocean Water (V-SMOW) standards. Stable isotope analyses were performed on six calcite samples ($\delta^{13}C$ and $\delta^{18}O$) and seven barite samples ($\delta^{34}S$). This study started with mechanical separation of the minerals by a dental drill and by the handpicking of chips. A minimum of 50 mg of calcite per sample was separated and pulverized with an agate mortar and

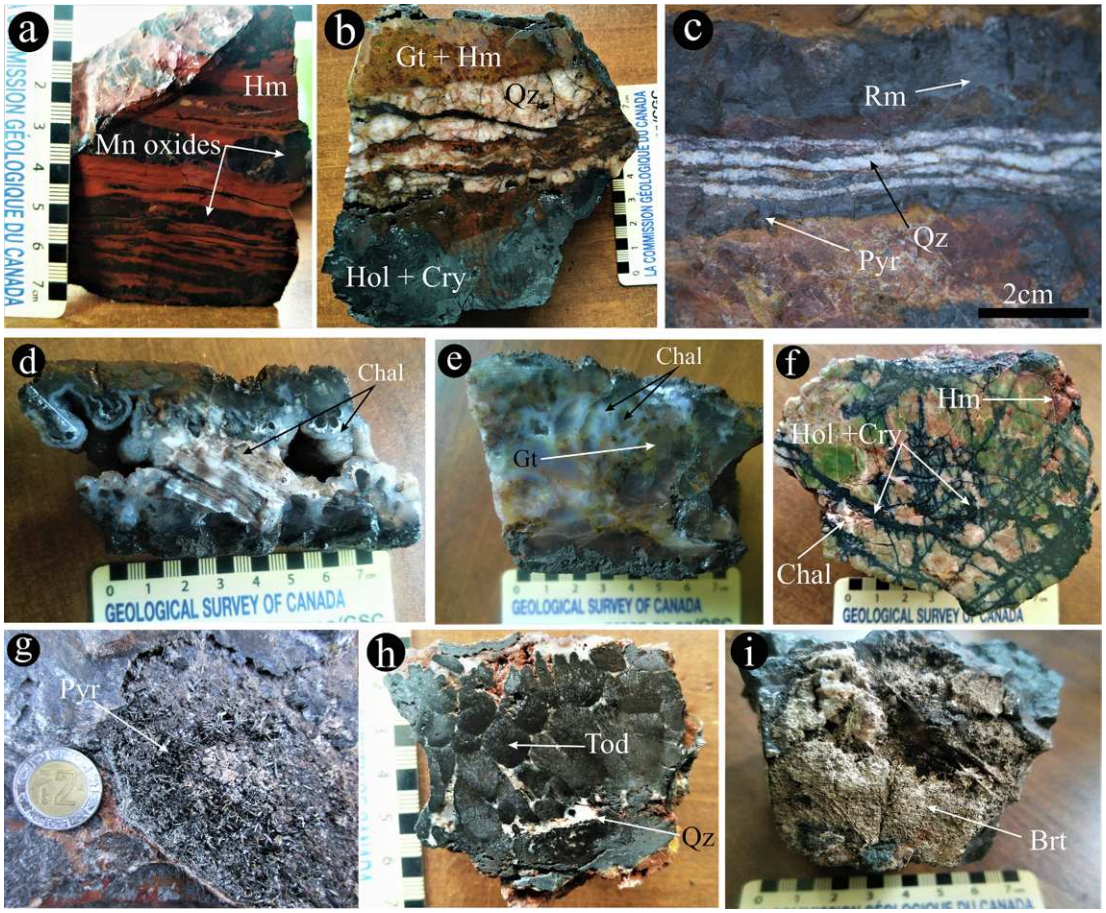

Fig. 5. Textural features of the manganese ore and gangue minerals in hand specimens. (A) Laminae of Fe and Mn oxyhydroxides. (B) Coarse crystalline quartz cuts across a brown jasper and is itself cut by hollandite and cryptomelane. (C) Crustiform-like, open-space filling of fractures by crystalline quartz is common at Montaña de Manganeso deposit. (D) botryoidal chalcedony commonly fills vugs. (E) Translucent chalcedony is commonly associated with goethite forming brown jasperoids, whilst white chalcedony is commonly associated with hematite forming the more abundant hematitic jasperoids. (F) Brecciated jasperoid with hollandite, cryptomelane and hematite filling fractures (G) Acicular pyrolusite crystals. (H) Fibrous todorokite with late quartz filling interstices. (I) Barite forming well-formed crystals on black jasperoid. Key: Pyr = pyrolusite, Cry = cryptomelane, Tod = todorokite, Hol = hollandite, Rm = romanechite Qz = quartz, Chal = chalcedony, Brt = barite, Hm = hematite Gt = goethite.

pestle. The extraction of CO_2 from carbonates for isotope analysis followed standard techniques of McCrea (1950); this gas was extracted by reacting calcite with phosphoric acid at a temperature of 25 °C and analyzed with a Thermo FinniganMAT 253 mass spectrometer coupled with Gas Bench II at the Laboratorio Nacional de Geoquímica y Mineralogía of the Instituto de Geología, UNAM. For sulfur isotopes, pure barite samples were analyzed by mass spectrometry using an Ea-Delta Plus XP Thermofisher. These analyses were carried out at the facilities of the Centres Científics i Tecnològics of the Universitat de Barcelona. The analytical precision was within ± 0.1‰ at 1σ.

To constrain the maximum age of the deposit, zircons from a dike weakly altered by the mineralizing hydrothermal fluid were dated using the U–Pb method. A rock sample was crushed and milled using conventional techniques at the Centro de Geociencias, UNAM. Zircons for U–Pb geochronology were separated using conventional magnetic and heavy liquid methods and were subsequently handpicked under a binocular microscope. The procedure included the crushing of samples in a jaw crusher and grinding in an agate bowl, followed by sieving of the < 250 μm fraction. Non-magnetic minerals were separated using a Frantz separator. Twenty-eight zircon grains were separated (#EGP-815 in Table 6) and mounted in epoxy and photographed prior to the analysis. Zircon U–Pb isotopic dating was performed using a Thermo iCapQc ICPMS coupled to a Resonetics, Resolution M050 excimer laser workstation at the Centro de Geociencias, UNAM. Analyzed spots were 23 μm and Helium was used as a carrier gas. The NIST-SRM 610 glass and the Pleišovice reference zircon (ca. 337 Ma; Sláma et al., 2008) were used in combination to correct for instrumental drift and downhole fractionation and to recalculate elemental concentrations using the inhouse software U-Pb.age (Solari and Tanner, 2011). The inhouse *U–Pb.age* software was used for processing the data and age calculation and concordia diagrams were prepared using Isoplot *3.75* (Ludwig, 2012). $^{207}Pb/^{206}Pb$ ratios, ages and errors are calculated according to Petrus and Kamber (2012). Uncertainties for individual analyses of the zircon grains are quoted at the 1σ level, and the errors on weighted mean ages are quoted at 95% confidence level. Common Pb correction was applied using the method of Andersen (2002).

4. Results

4.1. Geology of the ore deposit

Manganese mineralization occurs as irregular bodies or veins of 5–30 m wide, along NE-trending fissures. Most of these bodies remain open to depth as only easily accessible parts of the bodies near surface have been exploited. The mineralization occurs within an area about 100 m wide and at least 300 m long. Fig. 3 shows a schematic representation of two of the largest veins at Montaña de Manganeso, one from the open pit (Fig. 3A) and another from underground workings (Fig. 3B). The veins mostly form sharp contacts with the host rocks (sandstone and shale of the Caracol Formation; Fig. 4A), although at

times gradational contacts can be observed where the mineralization is underlain by shale beds. A complete separation of Mn and Fe is commonly observed (Fig. 4D). The main vein at Montaña de Manganeso is about 10 m wide and a vertical extent of about 5 m is exposed. It has an elongated flared shape and its lower part is brecciated. The ore is silicified, grading outward to a black jasperoid. A few meters from the mineralized vein, the wall rocks (sandstone and shale of the Caracol Formation) are completely whitened and partially leached denoting acidic fluids (Fig. 4B). The XRD and SWIR analyses (Figs. A1 and A2, supplementary data) show that the mineralogy of altered samples is mostly composed of montmorillonite, kaolinite, mixed-layered illite/smectite and minor illite. These patches of advanced argillic alteration could be an overprint, probably a steam-heated acid alteration over the original argillic alteration assemblage (Thompson and Thompson, 1996).

Silicification is the most prevalent alteration type at Montaña de Manganeso, spectacularly represented by massive bodies of red and black jasperoids. Some jasperoid bodies have a thickness of more than 20 m and extend over the whole mineralized zone. The jasperoids display various macroscopic textures, from massive to laminated to brecciated. Textures with evidence of sealing and fracturing are also observed (Figs. 5B, C and 6I). The massive hematitic (red) jasperoids are the most common and have aphanitic textures (Fig. 4C), although the black jasperoids (Fig. 4I) are the ones associated with the manganese ores (Fig. 4G). Some jasperoids have late-stage, irregular thin veins, of up to 4 mm, made up of quartz, calcite and Mn oxides presenting mutually cross-cutting relationships, which suggest they are coeval and cogenetic (Fig. 4E and 5F), whilst others present alternating hematite-rich and hematite-poor laminae (Fig. 4D and 5A). Brecciation is also common in some jasperoids (Fig. 5F). Besides massive and breccia textures, some manganese ores and associated jasperoids also occur in botryoidal (Fig. 5D), acicular (Fig. 5G) and fibrous (Fig. 5H) textures.

4.2. Ore mineralogy and mineral chemistry

The XRD analyses identified pyrolusite, todorokite, romanechite, birnessite, hollandite and cryptomelane as the major Mn minerals. Pyrolusite mainly occurs as a fine-grained mass (Fig. 6C) that occasionally presents desiccation cracks (Figs. A3G, supplementary data). Pyrolusite also forms masses of euhedral, spindle-shaped and bladed crystals, up to a few mm in length (Fig. 6B). Todorokite is predominantly fibrous (Fig. 6A and B), whilst birnessite is mainly fine grained (Fig. 6A and F). Cryptomelane, hollandite and romanechite occur mainly as colloform bands (Fig. 6D and A3I). Hollandite occasionally forms spindle-shaped crystals (Fig. 6C), replacing either pyrolusite (Fig. 6C) or cryptomelane (Fig. 6E). Silica polymorphs form the predominant gangue minerals followed by calcite and barite. Silica is mostly found in the jasperoids in the form of cryptocrystalline quartz and chalcedony (Fig. 5D and E). Crystalline quartz is mostly associated with manganese ores and generally presents mutually cross-cutting relationship with Mn oxides (Figs. 4E and 6I). Of great interest, however, is the coarse crystalline quartz that forms crustiform banding with manganese ore, as it suggests coprecipitation of quartz and manganese ore (Fig. 5C and 6I). Barite and calcite fill open spaces within Mn oxides and are commonly cut by them (Fig. 6G and H).

Microprobe data for the Montaña de Manganeso manganese ores is provided in Table A1 (supplementary data). The fine-grained and intimately intermixed mode of occurrence of the ore minerals hindered precise determination of quantitative mineral chemistry of the individual minerals detected by XRD and SEM. Some microprobe results therefore might represent mixed analyses. Characterized minerals (and mineral mixtures) are: (*a*) todorokite-rich mixture (with subordinate hollandite-romanechite), (*b*) hollandite-romanechite isomorphous series, (*c*) cryptomelane (with traces of hollandite-romanechite), and (*d*) near pure pyrolusite.

A todorokite-rich mineral mixture was analyzed, with K_2O concentrations (< 1.9 wt%) higher than the reported ideal compositions of todorokite (Gutzmer and Beukes, 2000). The BaO concentrations (< 5.0 wt%) are also higher than those typical of pure todorokite, indicating the presence hollandite-romanechite (Table A1). Hollandite–romanechite is rich in BaO (< 10.9 wt%) and MnO (< 72.5 wt%). Cryptomelane shows high concentrations of K_2O (< 4.2 wt%) and remarkably high concentrations of BaO (< 3.0 wt%) (*cf.* Miura et al., 1987); this barium enrichment may be an indication of cryptomelane–romanechite–hollandite intermediates. Pyrolusite has the simplest composition, being almost pure MnO_2 (96.5–98.9 wt%).

4.3. Paragenesis

Based on field observations, cross-cutting relationships and microscopic textures, a three-stage paragenetic sequence is determined, namely: (*a*) initial hydrothermal stage -stage 1-, (*b*) a main hydrothermal stage -stage 2-, and (*c*) a supergene alteration stage -stage 3- (Fig. 7). Stage 1 is characterized by the precipitation of pyrolusite, todorokite and birnessite, with minor silica (chalcedony and cryptocrystalline quartz) (Fig. 6 A and B), whereas during stage 2 much of the silica precipitated, leading to the formation of massive jasperoids, accompanied by hollandite-romanechite and cryptomelane (Fig. 6C, D and E). In Fig. 6B and C, hollandite from stage 2 is replacing pyrolusite and todorokite from stage 1. Stage 2 seems to be multi-episodic. The explosive nature of the hydrothermal system of this stage is revealed by the occurrence of breccias (Figs. 4E and 5F). Quartz co-precipitated with Mn minerals, filling voids and interstices between Mn oxide crystals (Fig. 5C and H). Barite (Figs. 5I and 6G) and some calcite (Fig. 6H) also precipitated during this stage, probably related to the formation of Ba-rich (romanechite-hollandite) and Ca-rich Mn oxides (todorokite). Both barite and calcite are commonly seen crosscut by Mn oxides.

The supergene alteration stage 3 is indicated by the formation of pisolitic-like and colloform Mn oxides on recent sediments (Fig. 4F and H). In hand specimens they commonly form a soft and powdery layer over hard massive ores (Fig. 4G). Birnessite and pyrolusite are the main Mn oxides of the supergene stage (Fig. 6F). Birnessite probably formed through the oxidation and dehydration of todorokite (Roy, 1981).

5. Stable isotopes

Table 1 shows the stable isotope composition of calcite from Montaña de Manganeso. The $\delta^{13}C_{VPDB}$ data show a narrow variation range, between −7.8 and −6.3‰, with an average of −7.0‰. The $\delta^{18}O_{VPDB}$ ranges between −8.0 and −4.7‰, with an average of −7.0‰. The isotopic composition for the hydrothermal fluid in equilibrium with calcite ($\delta^{18}O_{fluid}$) (for the temperature range of 101–140 °C, according to FI calculations), was obtained using the fractionation equation of O'Neil et al. (1969), and varies between 6.6 and 13.1‰ (relative to VSMOW). A comparison of the $\delta^{13}C_{VPDB}$ values of the Montaña de Manganeso with other hydrothermal manganese deposits reported in literature in shown in Table 2.

Sulfur isotope composition of barite from Montaña de Manganeso is shown in Table 3. The $\delta^{34}S$ values range from 7.9 to 10.3‰, except one value of 13.6‰. Table 4 shows a comparison of the $\delta^{34}S$ values of the Montaña de Manganeso deposit with other manganese and barium deposits of hydrothermal origin.

6. Fluid inclusions (FI)

In this study, primary and secondary FI were recognized using the criteria of Roedder (1984) and Bodnar et al. (1985). Only primary FI were used for microthermometric analysis. A summary of FI microthermometric data is provided in Table 5. Based on the phases present at room temperature and phase transitions observed during heating and

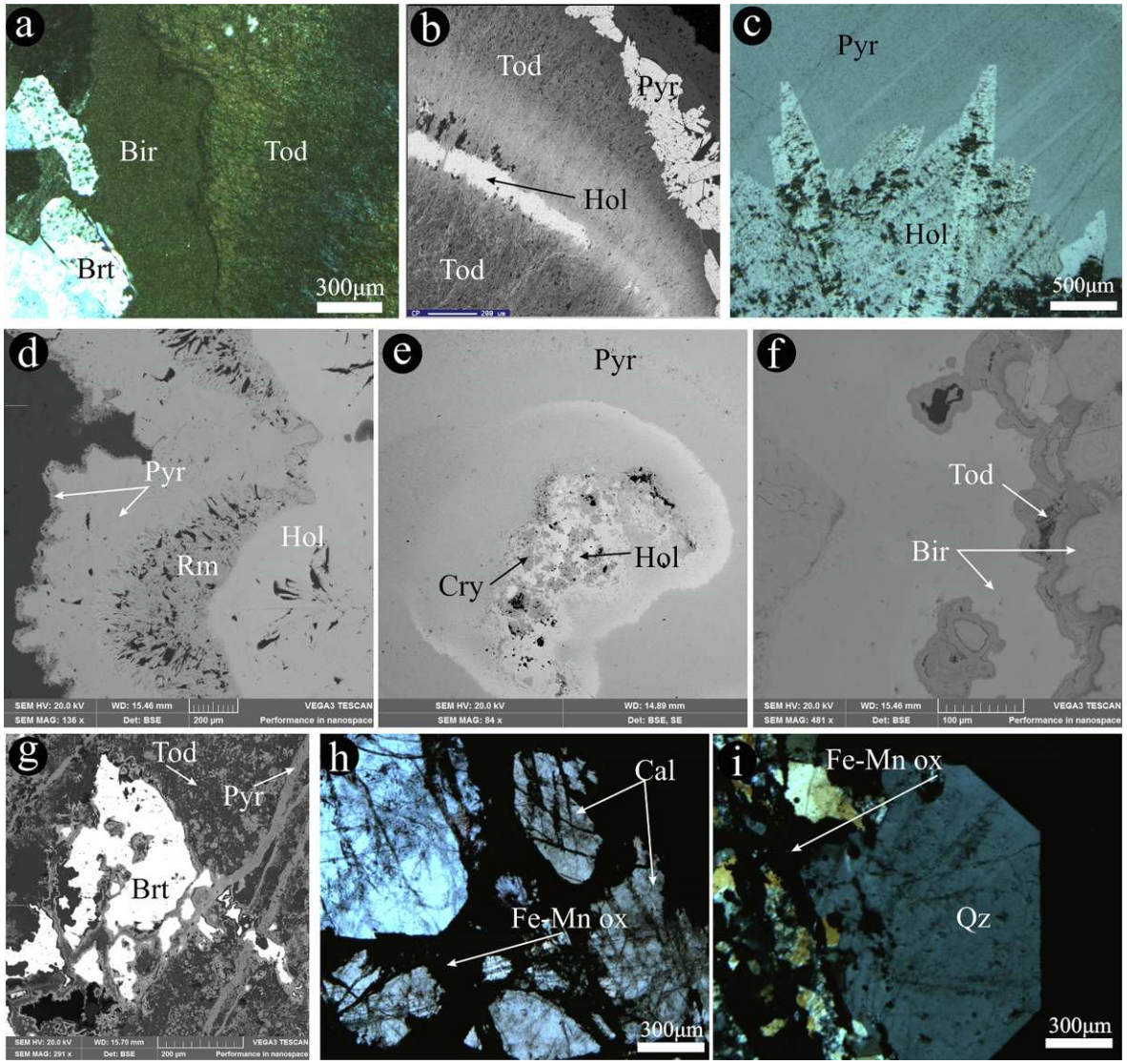

Fig. 6. Manganese minerals identified by SEM EDS/WDS. (A) Fine-grained birnessite with fibrous todorokite from stage 1. Bright large crystals of barite from stage 2. (B) Todorokite is replaced by second stage hollandite and pyrolusite. (C) Large crystals of hollandite replace fine-grained pyrolusite from stage 1. (D) Colloform concentric bands of romanechite and hollandite with a rim of pyrolusite (E) A nodule-like structure with cryptomelane and hollandite in the inner core and pyrolusite on the edge. The cryptomelane-hollandite core is being altered to pyrolusite. (F) Fine-grained birnessite of supergene origin. (G) Co-existing barite and pyrolusite and todorokite. Pyrolusite crystals can be clearly observed cutting barite within a matrix of todorokite. This clearly indicates formation of barite after todorokite, but before pyrolusite. (H) Calcite is crosscut by unidentified Fe-Mn oxides. (I) A coarse crystalline quartz crystal fractured by a veinlet of Fe-Mn oxides. Key: Pyr = pyrolusite, Cry = cryptomelane, Tod = todorokite, Hol = hollandite, Qz = quartz, Fe-Mn ox = Fe and Mn oxyhydroxides, Chal = chalcedony, Brt = barite, Rm = romanechite, Cal = calcite, Bir = birnessite.

cooling, two types of FI were identified in quartz from stage 2: (*a*) liquid (L-type), and (*b*) liquid-rich two-phase (L + V-type) inclusions (Fig. 8A and B). The majority of FI belong to the second type and range in size from 5 to 30 µm. They contain a liquid phase and a vapor bubble without daughter crystals. Isolated and clustered FI both occur in the crystals. The L-type FI are mostly colorless and ovoid. These FI were very small, generally < 5 µm, and were not measured.Fig. 9.

The L + V-type FI are larger and mostly elongated or ovoid and have liquid–vapor ratios of ~90–95% (Fig. 8A). Due to the high liquid–vapor ratios, they homogenized to the liquid phase during microthermometric studies. No vapor-rich, three phase or multiphase inclusions were observed, and thus necking as a post entrapment process was ruled out. In this study, the eutectic temperature (T_e), necessary to estimate the composition of the dissolved salts in the aqueous fluid was not measured because the size of most of the inclusions and the poor transparency of quartz crystals did not allow precise measurements. None of these samples showed evidence of heterogeneous trapping of fluids.

Clathrates were not observed during freezing experiments, indicating that CO_2 contents were below 3.7 wt% (Hedenquist and Henley, 1985). Phase transitions measured were melting of the last crystal of ice and total homogenization of the inclusion. T_m ranges from −12.0 to −5.1 °C (mean: −8.2 °C), and the corresponding salinity from 8.0 to 16.0 wt% NaCl equivalent, with an average of 12.2%. T_h (for L + V-type) varies from 101 to 140 °C (mean: 117 °C). Trapping pressure of the FI ranges from 1.0 to 3.4 bar with an average of 1.7 bar, consistent with a near-surface environment. Fluid densities range from 0.995 to 1.059 g/cm^3, with an average of 1.029 g/cm^3.

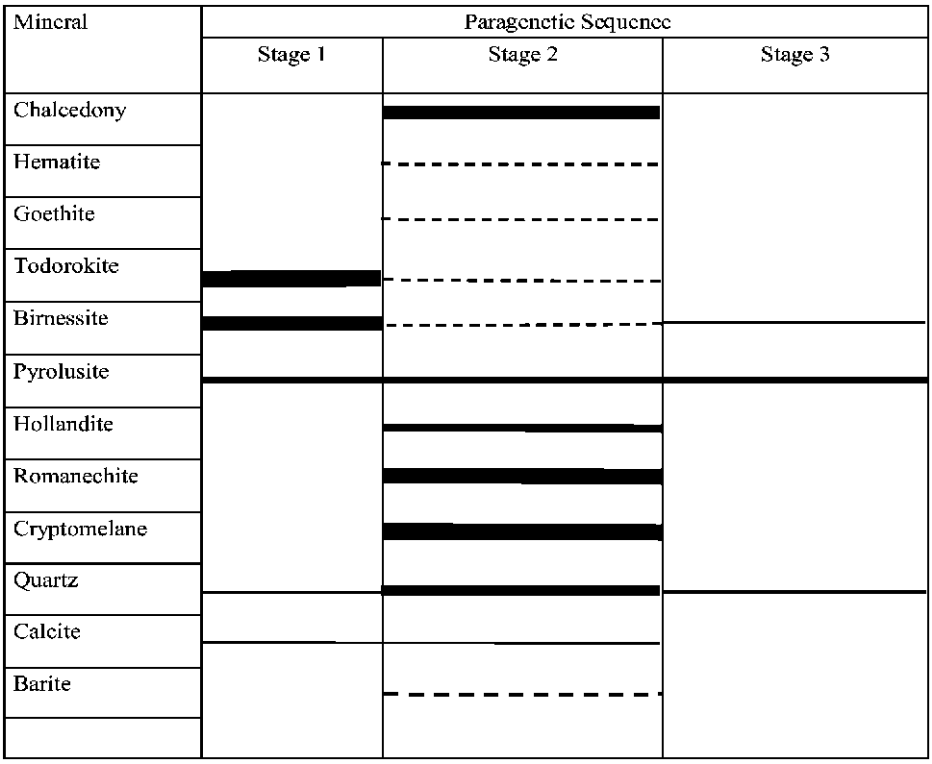

Fig. 7. Mineral paragenesis at the Montaña de Manganeso deposit. The thickness of each line indicates the abundance of the mineral. Solid lines indicate major minerals and dashed lines indicate accessory minerals in each stage.

Table 1
Summary of Carbon and Oxygen isotopic analyses of six calcite samples from Montaña de Manganeso. The isotope data are presented as conventional per mil values. The min–max values of homogenization temperatures of fluid inclusions were used to calculate the oxygen isotope values of the hydrothermal water in equilibrium with calcite ($\delta^{18}O_{fluid}$), calculated using the fractionation equation of O'Neil et al., (1969).

# Sample	$\delta^{13}C_{PDB}$ (‰)	$\delta^{18}O_{PDB}$ (‰)	$\delta^{18}O_{VSMOW}$ (‰)	$\delta^{18}O_{fluid}$ (‰) Min-Max
1 MM-T1(A)	−7.41	−5.17	25.58	9.51–12.67
2 MM-5	−7.05	−6.03	24.69	8.63–11.79
3 MM-25D	−6.50	−8.01	22.65	6.58–9.74
4 MM-27(A)	−7.76	−4.71	26.05	9.99–13.14
5 MM-100E	−6.32	−5.84	24.89	8.82–11.98
6 MM-202	−7.24	−4.79	25.97	9.91–13.06

Table 2
Comparison of the $\delta^{13}C_{VPDB}$ values of the Montaña de Manganeso with other hydrothermal Mn deposits reported in literature.

Deposit	$\delta^{13}C_{VPDB}$	
Atasu Mn deposits (Kazakhstan)	−10 to −4	Kuleshov (2017)
Toyoha deposits, Hokkaido (Japan)	−9 to −5	Nitta and Inoue (2011)
Luis Lopez deposits (Mexico)	−7.7–1.2	Casey (2011)
Santa Eulalia deposits (Mexico)	−10.1 to −1.6	Casey (2011)
Montaña de Manganeso deposit	−7.8 to −6.3	*This study*

7. Geochronology

Intrusive rocks in the vicinity of Montaña de Manganeso deposit are scarce. As a result, a single andesitic dike spatially associated with the mineralization was dated (Fig. 3b). The andesitic dike cuts across the

Table 3
Sulfur isotope ratios of seven barite samples of Montaña de Manganeso. The sulfur isotope data are presented as conventional per mil (‰) values.

# Sample	$\delta^{34}S$ (‰)
1 MM-100A-1	9.3
2 MM-100A-2	9.1
3 MM-100D-1	8.2
4 MM-100D-2	7.9
5 MM-100D-3	10.3
6 MM-100D-4	8.7
7 MM-106C	13.6

Table 4
Comparison of the $\delta^{34}S$ values of the Montaña de Manganeso with other related deposits.

Deposit	Type	$\delta^{34}S_{CDT}$
Vani, Milos (Greece)	Shallow water hydrothermal Mn deposits	21.3[a]
Pampean Ranges (Argentina)	Epithermal Mn deposits	4.9–7.7[b]
Bijgan deposits (Iran)	Submarine hydrothermal barite	9.5–15.3[c]
Juan de Fuca Ridge	Submarine hydrothermal barite	10.1[d]
El Tule	Celestine-barite hydrothermal deposit	6.4–13.2[e]
Montaña de Manganeso	Hydrothermal Mn deposit	7.9–13.6[f]

[a] Hein et al. (2000). Average of two values
[b] Leal (2002).
[c] Ehya (2012).
[d] Goodfellow and Blaise (1988).
[e] Kesler (1977).
[f] This study.

Table 5
Summary of the microthermometric data of all the fluid inclusions from Montaña de Manganeso.

	Sample	Mineral	#	Th (°C)	Tm-ice (°C)	Salinity (wt%NaCleq)	Depth (m)	Pressure (bar)	Bulk Density (g/cm3)
1	MN#1	Quartz	17	106–111	−8.8 to −8.2	12.6	18	1.2–1.4	1.037–1.041
2	MN#2	Quartz	18	119–124	−9.8 to −9.0	13.7	43	1.8–2.1	1.035–1.041
3	MN#3	Quartz	19	125–130	−8.6 to −8.6	12.4	53	2.1–2.5	1.024–1.027
4	MN#4	Quartz	16	121–128	−8.5 to −7.7	11.9	53	1.9–2.3	1.023–1.026
5	MN#5	Quartz	14	105–107	−7.0 to −7.0	10.5	13	1.1–1.2	1.027–1.028
6	MN#6	Quartz	9	101–105	−6.3 to −6.3	9.6	9	1.0–1.1	1.022–1.025
7	MN#7	Quartz	31	114–126	−8.5 to −7.8	12.3	43	1.5–2.2	1.026–1.030
8	MN#8	Quartz	25	106–114	−7.6 to −6.7	11.2	28	1.2–1.5	1.025–1.030
9	MN#9	Quartz	30	108–120	−10.8 to −8.1	14.8	34	1.2–1.8	1.036–1.053
10	MN#10	Quartz	10	130–132	−10.9 to −10.9	14.9	51	2.4–2.6	1.040–1.042
11	MN#11	Quartz	7	106–111	−5.0 to −5.0	8.0	16	1.2–1.4	1.006–1.010
12	MN#12	Quartz	22	105–115	−7.4 to −6.5	11.0	28	1.1–1.6	1.022–1.028
13	MN#14	Quartz	20	117–129	−12.0 to −11.5	11.7	34	1.6–2.3	1.050–1.059
14	MN#15	Quartz	17	120–140	−7.0 to −7.0	16.0	51	1.9–3.4	0.995–1.017

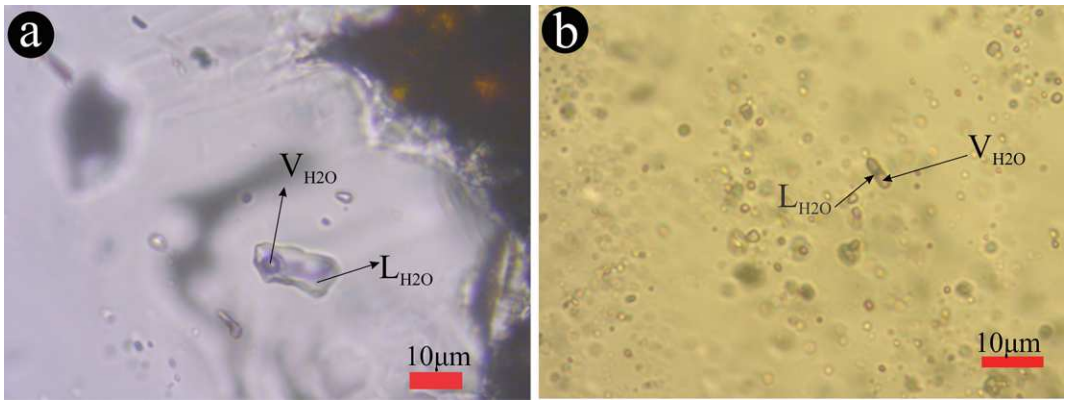

Fig. 8. Photomicrographs of typical fluid inclusions measured (at room temperature) from the Montaña de Manganeso deposit. (A) Isolated, relatively large elongated fluid inclusions (L + V-type) interpreted as primary. (B) A large number of inclusions are ovoid, but present similar liquid–vapor ratios (90–95%) as the elongated ones. Few irregularly shaped inclusions are also present. None of the inclusions present daughter crystals or show evidence of clathrates during measurement.

host rocks, but not the manganese ores. It shows weak alteration at surface, the result of the action of mineralizing hydrothermal fluids. Therefore, the U-Pb age of the dike sets the maximum age of the deposit. Zircons from the andesite dike are transparent, colorless, have columnar habit and display oscillatory zoning (Fig. 10), consistent with a magmatic origin (Möller et al., 2003).

The U and Th contents in the analyzed zircons range from 140 to 2340 ppm and from 67 to 1671 ppm, respectively, with Th/U ratios from 0.32 to 0.97. Thirteen spots yield concordant $^{206}Pb/^{238}U$ ages, from 39.1 to 42.2 Ma, with a weighted mean age of 40.65 ± 0.42 Ma

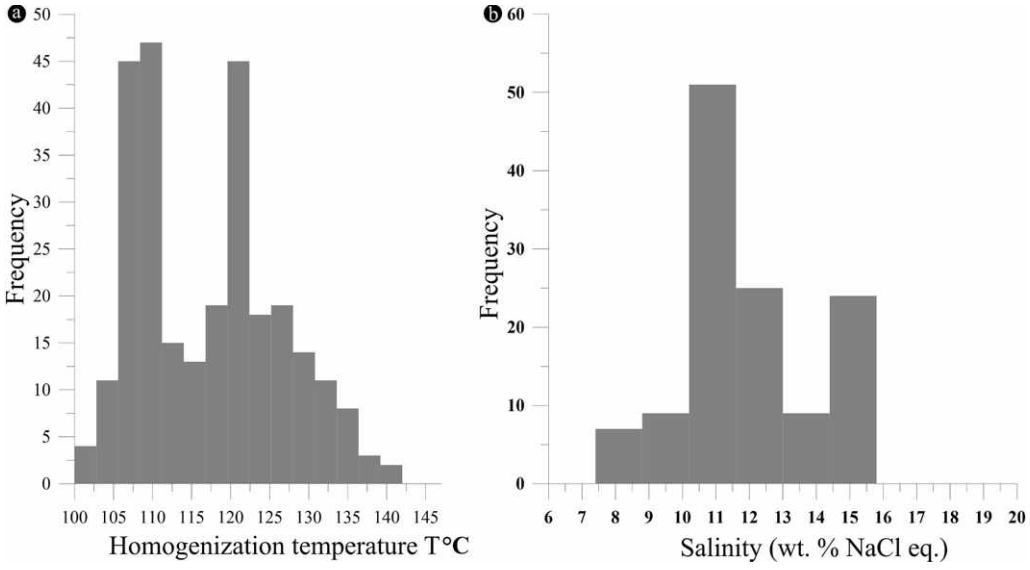

Fig. 9. Histograms of homogenization temperatures and salinities of fluid inclusions from Montaña de Manganeso.

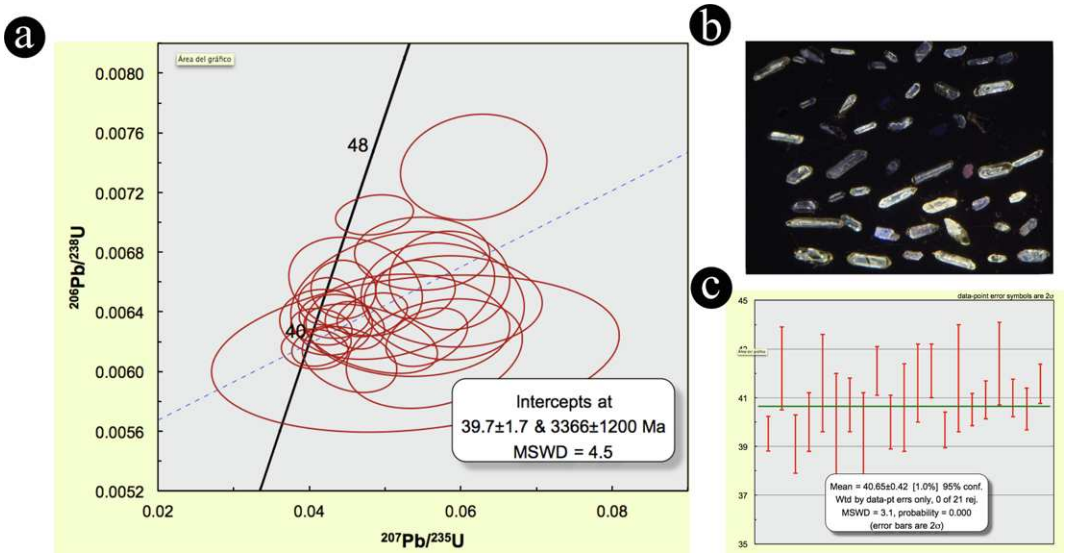

Fig. 10. U-Pb dating results. (A) Zircon U–Pb concordia diagrams, (B) Analyzed zircon grains and (C) Weighted mean model ages for the Montaña de Manganeso deposit.

(MSWD = 3.1; n = 13). This is interpreted as the crystallization age of the dike. The analytical results are in Table 6.

8. Discussion

The nature and evolution of the mineralizing fluids in the Montaña de Manganeso deposit are approached from a comprehensive evaluation of the stable isotopes and FI data in terms of the paragenetic stages. Geological and geochronological data are then integrated to formulate a genetic model of the deposit.

8.1. Ore-forming fluids

Fluid inclusion analyses of quartz from stage 2 indicate ore forming fluids of rather low temperature (101–140 °C) and intermediate salinity (8–16 wt% NaCl equivalent). It is reasonable to assume that similar fluids were also responsible for mineral precipitation of stage 1. Stage 3 minerals are likely to have been precipitated by mixing with meteoric, descending waters.

Temperature decrease and to a lesser extent pressure and pH changes in the hydrothermal system probably caused precipitation of cryptocrystalline quartz and chalcedony, which together with Mn and Fe oxides formed the jasperoids. Barite could have formed as a result of Eh rise (*e.g.* Leal et al., 2008). A variation in the physicochemical conditions caused the paragenetic change from a birnessite-todorokite assemblage (stage 1) to a cryptomelane-hollandite-romanechite assemblage (stage 2). A possible mechanism of this evolution could be that proposed by Glasby et al. (2005) for the Vani deposit, Greece. According to these authors, boiling at depth produces the precipitation of sulfides; therefore, the ascending fluids became depleted in elements such as Ba, Pb and Zn and enriched in Na, K and Mg, and thus the shallow deposits consist of todorokite and birnessite. During a second episode, the hydrothermal fluid becomes enriched in Ba, Pb and Zn as a result of the dissolution of barite and sulfides, and re-mineralizes the original Mn oxide assemblage to a cryptomelane-hollandite-romanechite one. Pyrolusite seems to have been deposited during the whole life of the hydrothermal system, including stage 3 (supergene origin), together with birnessite that probably formed from the collapse of todorokite (Roy, 1981).

The $\delta^{13}C$ of calcite (−7.8 to −6.3‰) suggests a magmatic C origin (range: −7 to −5‰; Hoefs, 1980; Hoefs, 2009), with values considerably higher than those of sedimentary organic matter (~−25‰; Hoefs, 1980) and lower than those of marine carbonate (~0‰; Hoefs, 2015). The $\delta^{13}C_{VPDB}$ values in calcite from Montaña de Manganeso are similar to those reported in other hydrothermal manganese deposits (Table 2). The Montaña de Manganeso values are closer to those of the Toyoha hot-spring type deposits of Hokkaido, Japan, where C has a primarily magmatic origin (Nitta and Inoue, 2011). However, even if C has a primarily magmatic origin, it is likely that the isotopic composition of the fluid has been influenced by the host rocks during ascent of the hydrothermal fluid. The $\delta^{18}O_{fluid}$ values calculated from calcite compositions are in the range 6.6–13.1‰, slightly higher than those of magmatic fluids (range: 6–10‰; Hoefs, 2009). A plausible explanation for these values is that fluids interacted with both volcanic and sedimentary members of the Caracol Formation. An ^{18}O enrichment of the fluid due to adiabatic boiling (Albinson et al. 2001) can also be evoked.

The $\delta^{34}S$ values of barite from Montaña de Manganeso (average 9.5‰) are far below those of Tertiary sulfate seawater (20–22‰; Bottrell and Newton, 2006) and higher than magmatic sulfur (0‰; Shanks, 2001 and references therein), but similar to those reported for sulfates in other magmatic-hydrothermal systems (range: 8–15‰; Rye, 2005). Table 4 shows a comparison of the $\delta^{34}S$ values of Montaña de Manganeso with other regional and global Mn and Ba deposits of hydrothermal origin. The El Tule celestine-barite deposit, NE Mexico, is a low-temperature hydrothermal vein-type deposit, with $\delta^{34}S$ values from 6.4 to 13.2‰ (Kesler, 1977). Similar low $\delta^{34}S$ values are also reported globally from other hydrothermal manganese and barium deposits (Table 4).

These values could be explained by disproportionation of magmatic SO_2 during phase separation —boiling— (10–17‰; Shanks, 2013) and/or mixing of steam heated sulfate from oxidation of H_2S with magmatic sulfate (Rye, 2005). This implies boiling at depth, in agreement with what is suggested by ore and alteration paragenesis and by calcite and oxygen isotopes.

In the T_h–salinity diagram (Fig. 11A), salinity decreases with decreasing temperature, suggesting that a hotter, high-salinity fluid mixed with a cooler, low-salinity fluid (Wilkinson, 2001). As supported by the C and S isotope systematics, the high temperature and high salinity fluid may have been of magmatic origin, whereas the low temperature and low salinity fluid was likely meteoric. Thus, fluid mixing is most likely the responsible mechanism for manganese precipitation at Montaña de Manganeso.

Although there is no evidence of boiling at the manganese mineralization (shallow) level of the hydrothermal system, the Montaña de

Table 6
Zircon U–Pb isotope data for the Montaña de Manganeso dyke.

							CORRECTED RATIOS[2]			
	U (ppm)[1]	Th (ppm)[1]	Th/U	$^{207}Pb/^{206}Pb$	± 2σ abs	$^{207}Pb/^{235}U$	± 2 σ abs	$^{206}Pb/^{238}U$	± 2 σ abs	$^{208}Pb/^{232}Th$
Zircon-003	2049	1211	0.59	0.0481	0.0041	0.0407	0.0036	0.0062	0.0001	0.0019
Zircon-005	324	142.4	0.44	0.0533	0.0077	0.0461	0.0072	0.0066	0.0003	0.0023
Zircon-006	948	916	0.97	0.0528	0.0068	0.0453	0.0051	0.0061	0.0002	0.0019
Zircon-007	842	719	0.85	0.0579	0.0079	0.0481	0.0072	0.0062	0.0002	0.0021
Zircon-008	243.1	165.7	0.68	0.0650	0.0110	0.0576	0.0088	0.0065	0.0003	0.0021
Zircon-009	205.4	76.4	0.37	0.0670	0.0190	0.0540	0.0220	0.0061	0.0004	0.0023
Zircon-011	570	285.8	0.50	0.0479	0.0062	0.0422	0.0050	0.0063	0.0002	0.0021
Zircon-013	257	139	0.54	0.0690	0.0100	0.0565	0.0095	0.0061	0.0003	0.0027
Zircon-014	243	186.9	0.77	0.0612	0.0081	0.0617	0.0079	0.0074	0.0003	0.0027
Zircon-016	1391	925	0.66	0.0499	0.0043	0.0486	0.0042	0.0071	0.0001	0.0023
Zircon-017	1180	519	0.44	0.0498	0.0043	0.0445	0.0035	0.0066	0.0002	0.0021
Zircon-018	1161	590	0.51	0.0659	0.0050	0.0555	0.0044	0.0062	0.0002	0.0024
Zircon-019	187.8	109.1	0.58	0.0660	0.0130	0.0530	0.0110	0.0063	0.0003	0.0026
Zircon-020	280.6	201.4	0.72	0.0650	0.0100	0.0590	0.0096	0.0065	0.0003	0.0024
Zircon-021	1551	1390	0.90	0.0617	0.0048	0.0540	0.0043	0.0066	0.0002	0.0023
Zircon-022	1977	1002	0.51	0.0499	0.0036	0.0416	0.0032	0.0062	0.0001	0.0022
Zircon-023	167.8	68	0.41	0.0530	0.0130	0.0510	0.0110	0.0065	0.0004	0.0030
Zircon-024	2340	1671	0.71	0.0501	0.0039	0.0416	0.0033	0.0063	0.0001	0.0020
Zircon-025	1777	1034	0.58	0.0503	0.0046	0.0433	0.0038	0.0064	0.0001	0.0022
Zircon-027	343	171.9	0.50	0.0699	0.0084	0.0585	0.0065	0.0066	0.0003	0.0027
Zircon-028	1492	752	0.50	0.0538	0.0045	0.0483	0.0038	0.0064	0.0001	0.0021
Zircon-029	1604	854	0.53	0.0538	0.0042	0.0460	0.0032	0.0063	0.0001	0.0019
Zircon-030	444.5	144.2	0.32	0.0586	0.0084	0.0549	0.0073	0.0068	0.0002	0.0028
Zircon-034	1273	514.6	0.40	0.0467	0.0039	0.0423	0.0031	0.0065	0.0001	0.0022

			CORRECTED AGES (Ma)								
	± 2 σ abs	Rho	$^{206}Pb/^{238}U$	± 2 σ	$^{207}Pb/^{235}U$	± 2 σ	$^{207}Pb/^{206}Pb$	± 2 σ	Best age (Ma)	± 2 σ	Disc %
Zircon-003	0.0001	−0.07	39.5	0.7	40.5	3.5	259.0	79.0	39.5	0.7	2.42
Zircon-005	0.0003	−0.22	42.2	1.7	45.6	6.9	720.0	120.0	42.2	1.7	7.46
Zircon-006	0.0002	−0.29	39.1	1.2	44.9	4.9	470.0	150.0	39.1	1.2	12.92
Zircon-007	0.0002	−0.43	40.0	1.2	47.7	6.8	560.0	180.0	40.0	1.2	16.14
Zircon-008	0.0003	−0.09	41.6	2.0	56.5	8.4	1050.0	130.0	41.6	2.0	26.37
Zircon-009	0.0009	0.23	39.3	2.7	53.0	20.0	1110.0	290.0	39.3	2.7	25.85
Zircon-011	0.0002	−0.06	40.7	1.1	41.9	4.8	390.0	130.0	40.7	1.1	2.86
Zircon-013	0.0003	0.27	39.3	1.9	55.5	8.9	1230.0	180.0	39.3	1.9	29.19
Zircon-014	0.0002	0.12	47.3	1.9	60.5	7.5	720.0	120.0	47.3	1.9	21.82
Zircon-016	0.0002	0.19	45.3	0.7	48.1	4.1	345.0	81.0	45.3	0.7	5.78
Zircon-017	0.0002	−0.03	42.1	1.0	44.1	3.4	382.0	83.0	42.1	1.0	4.54
Zircon-018	0.0002	0.35	40.0	1.1	54.8	4.2	842.0	82.0	40.0	1.1	27.01
Zircon-019	0.0003	−0.04	40.6	1.8	52.0	10.0	1030.0	170.0	40.6	1.8	21.92
Zircon-020	0.0003	−0.03	41.6	1.6	57.9	9.1	960.0	150.0	41.6	1.6	28.15
Zircon-021	0.0002	0.06	42.1	1.1	53.3	4.1	650.0	100.0	42.1	1.1	21.01
Zircon-022	0.0001	0.26	39.7	0.7	41.3	3.1	388.0	74.0	39.7	0.7	3.92
Zircon-023	0.0005	0.29	41.8	2.2	50.0	10.0	770.0	160.0	41.8	2.2	16.40
Zircon-024	0.0001	−0.19	40.5	0.7	41.3	3.2	335.0	83.0	40.5	0.7	1.91
Zircon-025	0.0001	0.01	40.9	0.8	44.3	3.7	410.0	110.0	40.9	0.8	7.65
Zircon-027	0.0003	−0.01	42.4	1.7	57.5	6.0	1060.0	120.0	42.4	1.7	26.26
Zircon-028	0.0002	0.32	41.0	0.8	47.9	3.7	380.0	100.0	41.0	0.8	14.43
Zircon-029	0.0001	−0.20	40.5	0.9	45.7	3.1	431.0	79.0	40.5	0.9	11.29
Zircon-030	0.0004	0.00	43.6	1.3	54.1	6.9	760.0	120.0	43.6	1.3	19.41
Zircon-034	0.0002	0.04	41.6	0.8	42.1	3.0	324.0	75.0	41.6	0.8	1.26

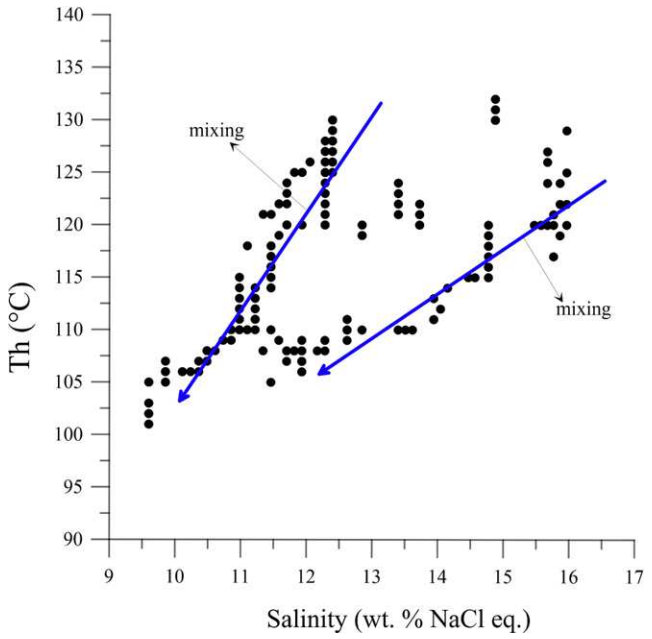

Fig. 11. Fluid inclusion characteristics of the Montaña de Manganeso deposit. (A) The deposition mechanism for the manganese oxides is likely fluid mixing (dilution) (Wilkinson, 2001).

Manganeso deposit exhibits textures with evidence of fracturing and sealing (Figs. 5B, C and 6K), a common occurrence in deposits where boiling occurred. These textures together with the overprinted kaolinization suggest that vein opening and sealing was episodic, and that boiling probably took place at depth, so that boiled off brines rose through the faults. Close to the paleosurface, these boiled off brines mixed with meteoric waters and deposited Mn oxides. Such a mechanism is known to occur during the collapse of hydrothermal systems when ascending fluids mixing with meteoric waters cause precipitation of the remaining metals in solution (Cooke and Simmons, 2000).

Existence of a Eh gradient and differences in solubility likely fractionated Mn from Fe as the fluid ascended to the surface. The fractionation is reflected in the spatially detached Fe-rich jasperoids and Mn-rich veins. Iron oxides precipitate at relatively low Eh values compared with Mn oxides (Hem, 1963). The high solubility of Mn means it can stay longer in solution, long after other metals have precipitated. Unlike Fe, Mn does not form sulfide minerals in hydrothermal systems. Thus, sulfide formation separates Mn and Fe in a shallow crustal hydrothermal system. This could partly explain the absence of base metal and Fe sulfides at Montaña de Manganeso, and suggests that sulfide mineralization may be expected at depth.

8.2. Metallogeny and deposit model

Manganese mineralization in the Central Plateau has a regional character and probably had its inception in hydrothermal activity associated with the regional Eocene-Oligocene magmatism of the Central Plateau. During the Eocene-Oligocene period, significant bimodal andesitic-rhyolitic volcanic events occurred in the Central Plateau associated with ignimbritic silicic volcanism of the Sierra Madre Occidental. Volcanism in the Zacatecas San Luis Potosí belt occurred mostly as multiple discrete episodes of small rhyolitic volcanic fissures mostly controlled by major NW–SE trending fault systems (Aguirre-Díaz et al., 2008; Tristán-González et al., 2008; Tristán-González et al., 2009b; Aguillón-Robles et al., 2014). This volcanism, occurring within the Basin and Range grabens, could have provided the heat for the hydrothermal systems that formed the manganese deposits. The Eocene-Oligocene magmatism is already known to be associated with epithermal polymetallic deposits (*e.g.* Guanajuato and Fresnillo; Camprubí and Albinson, 2007; Camprubí and Albinson, 2006; Camprubí et al., 2009).

The occurrence of manganese mineralization as fault-controlled veins, breccias and irregular bodies suggests an epigenetic origin for the Montaña de Manganeso deposit, which must have originated from hydrothermal fluids upwelling along faults. The control of the deposit by NE- and NW-trending faults suggests that the deposit is related to the post-Laramidic extensional tectonics associated with the formation of the Basin and Range province (Aranda-Gómez and Mcdowell, 1998; Alaniz-Álvarez and Nieto-Samaniego, 2007; Aranda-Gómez et al., 2007; Nieto-Samaniego et al., 2007).

The Eocene age of the andesitic dike, as determined by U-Pb isotopic analyses, is not necessarily the age of mineralization, which may have occurred shortly after dike emplacement or may be significantly later. The dike emplacement certainly occurred before the hydrothermal alteration associated with mineralization, which affected it and hence this age should be best considered as the limiting maximum age for the deposit. The genesis of the manganese deposits of the Zacatecas

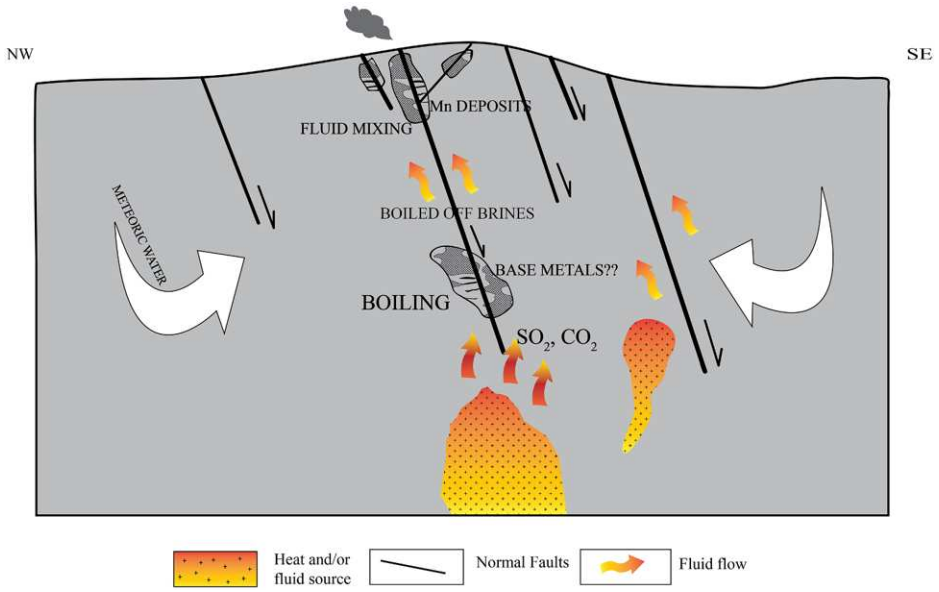

Fig. 12. Schematic diagram illustrating the possible genetic model for the manganese deposit of Montaña de Manganeso. Small undulating arrows show flow of magmatic-hydrothermal fluids and metals from an igneous source. Long convex arrows indicate meteoric water input into fractures and faults resulting in fluid mixing and the deposition of Mn oxides.

San Luis Potosí belt is related to the extension that occurred after the collision of the Guerrero and Sierra Madre terranes. Eocene-Oligocene magmatic events resulted in rhyolitic-andesitic intrusions, and the related hydrothermal fluids ascended along faults and fissure zones of surrounding country rocks. This led to phase separation and likely deposition of base metals at depth. Boiled off brines now enriched in manganese continued ascending to the surface where they interacted with the host rocks, mixed with oxygenated meteoric waters and cooled depositing abundant silica, tetravalent Mn oxides, scarce barite and calcite (Fig. 12). Our model proposes that the Eocene-Oligocene volcanic episode had a relatively distal influence on the formation of Montaña de Manganeso, analogous to the continental "hot-spring type" deposits (Crespo and Lunar, 1997; Canet et al., 2005a; Miura and Hariya, 2007; Del Rio-Salas et al., 2013; Rodríguez-Díaz et al., 2019). This mechanism of formation of Montaña de Manganeso is similar to that proposed for the manganese deposits of the SW USA (Hewett, 1964) and the Ilfeld deposits in Germany (Nicholson et al., 1997).

9. Conclusions

Montaña de Manganeso, hosted by Cretaceous volcaniclastic sedimentary rocks, is a fault-controlled, vein-type hydrothermal manganese deposit.

The ore deposit formed through two main hydrothermal stages and a minor supergene stage. Fluid inclusion microthermometry, coupled with C, O and S isotope systematics, indicate that aqueous fluids of low temperature (101–140 °C) and intermediate salinity (8.0–16.0 wt% NaCl equivalent) were derived from magmatic sources and evolved through fluid/rock interaction and mixing with descending meteoric waters.

The age of the deposit is constrained to no later than Eocene, according to zircon U-Pb geochronology. This age coincides with the ignimbrite flare-up event in the Central Plateau.

Tectonic setting and geological characteristics are compatible with a hot-spring deposit model, according to which Montaña de Manganeso corresponds to the shallowest portion of an epithermal system formed in a continental volcanic arc setting. Consequently, base and precious metals could be expected at depth where boiling probably occurred.

Declaration of Competing Interest

The authors declare that they have no known competing financial interests or personal relationships that could have appeared to influence the work reported in this paper.

Acknowledgments

This work was supported by the PAPIIT (DGAPA, UNAM) project IG100116 and forms part of J.M's PhD dissertation. Carlos Linares López is thanked for the assistance in WDS analyses. Edith Cienfuegos Alvarado and Francisco Javier Otero Trujano are thanked for the carbon and oxygen isotopic analyses. Colleagues Andrea Hernandez Cervantes, Irvin González Romo and Urenia Navarro are thanked for their help during fieldwork and preparation of graphics. Prof. Nicolas Johannes Beukes is greatly thanked for access to the Central Analytical Facility of the University of Johannesburg were SEM imagery was carried out. We would also like to thank the three anonymous reviewers whose comments greatly improved the manuscript.

Appendix A. Supplementary data

Supplementary data to this article can be found online at https://doi.org/10.1016/j.oregeorev.2020.103680.

References

Aguillón-Robles, A., Tristán-González, M., De Jesús Aguirre-Díaz, G., López-Doncel, R.A., Bellon, H., Martínez-Esparza, G., 2014. Eocene to Quaternary mafic-intermediate volcanism in San Luis Potosí, central Mexico: the transition from Farallon plate subduction to intra-plate continental magmatism. J. Volcanol. Geoth. Res. 276, 152–172. https://doi.org/10.1016/j.jvolgeores.2014.02.019.

Aguirre-Díaz, G.J., Obregon, J.N., Tristán González, M., González-Partida, E., 2007. Hydrothermal precious-metal deposits related to graben-calderas of the Sierra Madre Occidental. In: Eos, Transactions, American Geophysical Union, 88(23). Joint Assembly Supplement, abstract T23A-05.

Aguirre-Díaz, G.J., Labarthe-Hernández, G., Tristán-González, M., Nieto-Obregón, J., Gutiérrez-Palomares, I., 2008. The ignimbrite flare-up and graben calderas of the Sierra Madre Occidental, Mexico. In: Developments in Volcanology. Elsevier, pp. 143–180. https://doi.org/10.1016/S1871-644X(07)00004-6.

Alaniz-Álvarez, S.A., Nieto-Samaniego, Á.F., 2007. The Taxco–San Miguel de Allende fault system and the Trans-Mexican Volcanic Belt: two tectonic boundaries in central México active during the Cenozoic. In: Special Paper 422: Geology of México: Celebrating the Centenary of the Geological Society of México. Geological Society of America, pp. 301–316. https://doi.org/10.1130/2007.2422(10).

Albinson, T., Norman, D.I., Cole, D., Chomiak, B., 2001. Controls on formation of low-sulfidation epithermal deposits in Mexico: constraints from fluid inclusion and stable isotope data. In: Albinson, T., Nelson, C.E. (Eds.), New Mines and Discoveries in Mexico and Central America. Society of Economic Geologists. https://doi.org/10.5382/SP.08.01.

Alexandri, R.R., 1976. Estudio Geológico del Yacimiento Montaña de Manganeso. Universidad Autónoma de San Luis Potosí.

Andersen, T., 2002. Correction of common lead in U-Pb analyses that do not report 204Pb. Chem. Geol. 192, 59–79.

Aranda-Gómez, J.J., Mcdowell, F.W., 1998. Paleogene extension in the southern basin and range province of Mexico: syndepositional tilting of eocene red beds and oligocene volcanic rocks in the Guanajuato Mining District. Int. Geol. Rev. 40, 116–134. https://doi.org/10.1080/00206819809465201.

Aranda-Gómez, J.J., Molina-Garza, R., McDowell, F.W., Vassallo-Morales, L.F., Ortega-Rivera, M.A., Solorio-Munguía, J.G., Aguillón-Robles, A., 2007. The relationships between volcanism and extension in the Mesa Central: the case of Pinos, Zacatecas, Mexico. Rev. Mex. Cienc. Geol. 24, 216–233.

Barboza-Gudiño, J.R., Zavala-Monsiváis, A., Venegas-Rodríguez, G., Barajas-Nigoche, L.D., 2010. Late Triassic stratigraphy and facies from northeastern Mexico: tectonic setting and provenance. Geosphere 6, 621–640. https://doi.org/10.1130/GES00545.1.

Bodnar, R.J., 1983. A method of calculating fluid inclusion volumes based on vapor bubble diameters and P-V-T-X properties of inclusion fluids. Econ. Geol. 78, 535–542. https://doi.org/10.2113/gsecongeo.78.3.535.

Bodnar, R.J., 1993. Revised equation and table for determining the freezing point depression of H2O-Nacl solutions. Geochim. Cosmochim. Acta 57, 683–684. https://doi.org/10.1016/0016-7037(93)90378-A.

Bodnar, R.J., Burnham, C.W., Sterner, S.M., 1985. Synthetic fluid inclusions in natural quartz. III. Determination of phase equilibrium properties in the system H2O-NaCl to 1000°C and 1500 bars. Geochim. Cosmochim. Acta 49, 1861–1873. https://doi.org/10.1016/0016-7037(85)90081-X.

Bottrell, S.H., Newton, R.J., 2006. Reconstruction of changes in global sulfur cycling from marine sulfate isotopes. Earth Sci. Rev. 75 (1–4), 59–83.

Brindley, G.W., Brown, G., 1980. Crystal Structures of Clay Minerals and their X-Ray Identification. Mineralogical Society of Great Britain and Ireland, Colchester and London. https://dx.doi.org/10.1180/mono-5.

Campa, M.F., Coney, P.J., 1983. Tectono-stratigraphic terranes and mineral resource distributions in Mexico. Can. J. Earth Sci. 20, 1040–1051. https://doi.org/10.1139/e83-094.

Camprubí, A., 2009. Major metallogenic provinces and epochs of Mexico. Soc. Geol. Appl. Min. Deposits News 1, 7–20.

Camprubí, A., Albinson, T., 2006. Depósitos epitermales en México: actualización de su conocimiento y reclasificación empírica. Bol. Soc. Geol. Mex. 58, 27–81.

Camprubí, A., Albinson, T., 2007. Epithermal deposits in México—update of current knowledge, and an empirical reclassification. In: Special Paper 422: Geology of México: Celebrating the Centenary of the Geological Society of México, pp. 377–415. https://doi.org/10.1130/2007.2422(14).

Camprubí, A., González-Partida, E., Saldívar, D., Alfonso, P., Canet, C., 2009. Fluid inclusion and S isotope study in the San Carlos epithermal vein of the Fresnillo district, Zacatecas, Mexico. J. Geochem. Explor. 101, 19. https://doi.org/10.1016/j.gexplo.2008.11.042.

Canet, C., Prol-Ledesma, R.M., Proenza, J.A., Rubio-Ramos, M.A., Forrest, M.J., Torres-Vera, M.A., Rodríguez-Díaz, A.A., 2005a. Mn-Ba-Hg mineralization at shallow submarine hydrothermal vents in Bahía Concepción, Baja California Sur, Mexico. Chem. Geol. 224, 96–112. https://doi.org/10.1016/j.chemgeo.2005.07.023.

Canet, C., Prol-Ledesma, R.M., Torres-Alvarado, I., Gilg, H.A., Villanueva, R.E., Cruz, R.-L.-S., 2005b. Silica-carbonate stromatolites related to coastal hydrothermal venting in Bahía Concepción, Baja California Sur, Mexico. Sed. Geol. 174, 97–113. https://doi.org/10.1016/j.sedgeo.2004.12.001.

Casey, H., 2011. Geochemistry of Manganese Oxides And Age Of Mineralization At The Santa Eulalia Mining District, Mexico. MSc - Thesis.

Centeno-García, E., 2017. Mesozoic tectono-magmatic evolution of Mexico: an overview. Ore Geol. Rev. 81, 1035–1052. https://doi.org/10.1016/j.oregeorev.2016.10.010.

Centeno-García, E., Corona-Chávez, P., Talavera-Mendoza, O., Iriondo, A., 2003. Geologic and tectonic evolution of the western Guerrero terrane—a transect from Puerto

Vallarta to Zihuatanejo, Mexico. Geologic Transects across Cordilleran Mexico: Guidebook for the Field Trips of the 99th Geological Society of America Cordilleran Section Annual Meeting. Geological Society of America.
Centeno-García, E., Olvera-Carranza, K., Corona-Esquivel, R., Camprubi, A., Tritlla, J., Sanchez-Martinez, S., 2003. Depositional environment and paleogeographic distribution of the Jurassic-Cretaceous arc in the western and northern Guerrero terrane, Mexico. In: Geological Society of America, Cordilleran Section, 99th Annual Meeting.
Centeno-García, E., Guerrero-Suastegui, M., Talavera-Mendoza, O., 2008. The Guerrero Composite terrane of western Mexico: collision and subsequent rifting in a supra-subduction zone. In: Special Paper 436: Formation and Applications of the Sedimentary Record in Arc Collision Zones. Geological Society of America, pp. 279–308. https://doi.org/10.1130/2008.2436(13).
Centeno-García, E., Ruis, J., Coney, P.J., Patchett, P.J., Ortega- Gutierrez, F., 1993. Guerrero terrane of Mexico: its role in the southern Cordillera from new geochemical data. Geology 21, 419–422. https://doi.org/10.1130/0091-7613(1993)021<0419:GTOMIR>2.3.CO;2.
Centeno-García, E., Silva-Romo, G., 1997. Petrogenesis and tectonic evolution of Central Mexico during Triassic-Jurassic time. Rev. Mex. Cienc. Geol. 14, 244–260.
Clark, R.N., Swayze, G.A., Wise, R.A., Livo, K.E., Hoefen, T.M., Kokaly, R.F., Sutley, S.J., 2007. USGS Digital Spectral Library splib06a [WWW Document]. USGS Digital Data Series. URL < http://speclab.cr.usgs.gov > (accessed 8.4.19).
Clark, K.F., Foster, C.T., Damon, P.E., 1982. Cenozoic mineral deposits and subduction-related magmatic arcs in Mexico. Geol. Soc. Am. Bull. 93, 533. https://doi.org/10.1130/0016-7606(1982)93<533:CMDASM>2.0.CO;2.
Conly, A.G., Scott, S.D., Bellon, H., 2011. Metalliferous manganese oxide mineralization associated with the Boléo Cu-Co-Zn district, Mexico. Econ. Geol. 106, 1173–1196. https://doi.org/10.2113/econgeo.106.7.1173.
Consejo de Recursos Minerales (COREMI), 1980. Estudios geofisicos de orientación efectuados en el area de Montaña de Manganeso, S.L.P: Proyecto Manganeso Convenio Mexico-España. Pachuca, Hgo.
Consejo de Recursos Minerales (COREMI), 2001. Informe final de la carta geologico-minera Villa de Santo Domingo F14-A-31. Pachuca, Hgo.
Cooke, D.R., Simmons, S.F., 2000. Characteristics and genesis of epithermal gold deposits. Rev. Econ. Geol. 13, 221–244.
Crespo, A., Lunar, R., 1997. Terrestrial hot-spring Co-rich Mn mineralization in the Pliocene-Quaternary Calatrava Region (central Spain). Geol. Soc., Lond., Spec. Publ. 119, 253–264. https://doi.org/10.1144/gsl.sp.1997.119.01.16.
Damon, P., Shafiqullah, M., Clark, K., 1981. Evolución de los arcos magmáticos en México y su relación con la metalogénesis. Rev. Mexi. Cienc. Geol. 5, 223–238.
Del Rio-Salas, R., Ochoa-Landín, L., Eastoe, C.J., Ruiz, J., Meza-Figueroa, D., Valencia-Moreno, M., Zúñiga-Hernández, H., Zúñiga-Hernández, L., Moreno-Rodríguez, V., Mendívil-Quijada, H., 2013. Genesis of manganese oxide mineralization in the boleo region and concepción peninsula, baja california sur: Constraints from Pb-Sr isotopes and REE geochemistry. Rev. Mexi. Cienc. Geol. 30, 482–499.
Ehya, F., 2012. Rare earth element and stable isotope (O, S) geochemistry of barite from the Bijgan deposit, Markazi Province, Iran. Mineral. Petrol. 104, 81–93. https://doi.org/10.1007/s00710-011-0172-8.
Glasby, G.P.P., Papavassiliou, C.T.T., Mitsis, J., Valsami-Jones, E., Liakopoulos, A., Renner, R.M.M., 2005. The Vani manganese deposit, Milos island, Greece: a fossil stratabound Mn – Ba – Pb – Zn – As – Sb – W-rich hydrothermal deposit. In: Developments in Volcanology. Elsevier, pp. 255–291. https://doi.org/10.1016/S1871-644X(05)80045-2.
González-Villalvaso, L., López-Soto, R., 2009. Geología del yacimiento Madero, Zacatecas, México. In: Clark, K.F., Salas-Pizá, G., Cubillas-Estrada, R. (Eds.), Geología Económica de México. Servicio Geológico Mexicano — asociación de Ingenieros de Minas, Metalurgistas y Geólogos de México, pp. 902–909.
Gómez Torres, S.A., Góngora Flemate, D., 2001. Geología y mineralización del terreno Guerrero en el Altiplano. Geomimet 28–38.
Goodfellow, W.D., Blaise, B., 1988. Sulfide formation and hydrothermal alteration of hemipelagic sediment in Middle Valley, Northern Juan de Fuca Ridge. Can. Mineral. 26 (3), 675–696.
Grenne, T., Slack, J.F., 2003. Bedded jaspers of the Ordovician Løkken ophiolite, Norway: seafloor deposition and diagenetic maturation of hydrothermal plume-derived silica-iron gels. Miner. Deposita 38, 625–639. https://doi.org/10.1007/s00126-003-0346-3.
Gutzmer, J., Beukes, N.J., 1996. Mineral paragenesis of the Kalahari manganese field, South Africa. Ore Geol. Rev. https://doi.org/10.1016/S0169-1368(96)00011-X.
Gutzmer, J., Beukes, N.J., 2000. Asbestiform manjiroite and todorokite from the Kalahari manganese field, South Africa. South Afr. J. Geol. 103, 163–174. https://doi.org/10.2113/1030163.
Hedenquist, J.W., Henley, R.W., 1985. Hydrothermal eruptions in the Waiotapu geothermal system, New Zealand; their origin, associated breccias, and relation to precious metal mineralization. Econ. Geol. 80, 1640–1668. https://doi.org/10.2113/gsecongeo.80.6.1640.
Hein, J.R., Stamatakis, M.G., Dowling, J.S., 2000. Trace metal-rich Quaternary hydrothermal manganese oxide and barite deposit, Milos island, Greece. In: Fifth Biennial Meeting of SGA and Tenth Quadrennial Symposium of IAGOD, pp. 67–75.
Hem, J.D., 1963. Chemical equilibria affecting the behavior of manganese in natural water. International Association of Scientific Hydrology. Bulletin 8, 30–37. https://doi.org/10.1080/02626666309493334.
Hewett, D.F., 1964. Veins of hypogene manganese oxide minerals in the southwestern United States. Econ. Geol. 59, 1429–1472. https://doi.org/10.2113/gsecongeo.59.8.1429.
Hewett, D.F., 1968. Silver in Veins of Hypogene Manganese Oxides. Geol. Surv. Circ. 553, 9.
Hoefs, J., 1980. Stable Isotope Geochemistry, second ed., Minerals and Rocks. Springer Berlin Heidelberg, Berlin, Heidelberg. https://dx.doi.org/10.1007/978-3-662-02290-0.
Hoefs, J., 2009. Stable Isotope Geochemistry, 6th ed. Springer Berlin Heidelberg, Verlag Berlin Heidelberg. https://dx.doi.org/10.1086/628108.
Hoefs, J., 2015. Stable Isotope Geochemistry, seventh ed. Springer International Publishing, Cham. https://doi.org/10.1007/978-3-319-19716-6.
Jiménez-Franco, A., Canet, C., Alfonso, P., González-Partida, E., Rajabi, A., Escalante, E., 2020. The Velardeña Zn–(Pb–Cu) skarn-epithermal deposits, northern Mexico: new data of mineral assemblages, geochemistry and fluid inclusions. Bol. Soc. Geol. Mex. 72 (3).
Kesler, S.E., 1977. Geochemistry of manto fluorite deposits, northern Coahuila, Mexico. Econ. Geol. 72, 204–218. https://doi.org/10.2113/gsecongeo.72.2.204.
Kostov, R.I., 2010. Review of the mineralogical systematics of jasper and related rocks. Geol. Min. Resour. 13, 8–12.
Kuleshov, V.N., 2017. Manganese carbonates in modern sediments. In: Maynard, J.B., Kuleshov, V.N. (Eds.), Isotope Geochemistry: The Origin and Formation of Manganese Rocks and Ores. Elsevier, pp. 5–62. https://doi.org/10.1016/B978-0-12-803165-0.00002-1.
Labarthe-Hernández, G., Jimenez-Lopez, L.S., Motilla-Moreno, J.L., 1992. Jasperoide Guia Posible En La Exploracion Minera Mesa Central, Mexico. Revista 10, 137–142.
Labarthe-Hernández, G., Tristán-González, M., Aranda-Gómez, J.J., 1982. Revisión estratigráfica del Cenozoico de la parte central del Estado de San Luis Potosí. Folleto Téc. 85.
Laznicka, P., 1992. Manganese deposits in the global lithogenetic system: quantitative approach. Ore Geol. Rev. 7, 279–356. https://doi.org/10.1016/0169-1368(92)90013-B.
Leal, P.R., 2002. inclusiones fluidas e isotopos estables en la ganga de los yacimientos de manganeso del norte de la provincia de Córdoba. Rev. Asoc. Geol. Argentina 57, 251–259.
Leal, P.R., Correa, M.J., Ametrano, S.J., Etcheverry, R.O., De Brodtkorb, M.K., 2008. The manganese deposits of the Pampean Ranges, Argentina. Can. Mineral. 46, 1215–1233. https://doi.org/10.3749/canmin.46.5.1215.
Liakopoulos, A., Glasby, G.P., Papavassiliou, C.T., Boulegue, J., 2001. Nature and origin of the Vani manganese deposit, Milos, Greece: an overview. Ore Geol. Rev. 18, 181–209. https://doi.org/10.1016/S0169-1368(01)00029-4.
Ludwig, K.R., 2012. User's Manual for Isoplot 3.75, a Geochronological Toolkit for Microsoft Excel. Berkeley Geochronology Center Special Publication, pp. 1–72.
Martini, M., Fitz, E., Solari, L., Camprubi, A., Hudleston, P.J., Lawton, T.F., Tolson, G., Centeno-García, E., 2012. The Late Cretaceous fold-thrust belt in the Peña de Bernal–Tamazunchale area and its possible relationship to the accretion of the Guerrero terrane. In: The Southern Cordillera and Beyond. Geological Society of America, pp. 19–38. https://doi.org/10.1130/2012.0025(02).
McCrea, J.M., 1950. On the isotopic chemistry of carbonates and a paleotemperature scale. J. Chem. Phys. 18, 849–857. https://doi.org/10.1063/1.1747785.
Miura, H., Banerjee, H., Hariya, Y., Dasgupta, S., Roy, S., 1987. Hollandite and cryptomelane in the manganese oxide deposits of the Sausar Group, India. Mineral. J. 13, 424–433. https://doi.org/10.2465/minerj.13.424.
Miura, H., Hariya, Y., 2007. Recent manganese oxide deposits in Hokkaido, Japan. Geol. Soc., Lond., Spec. Publ. 119, 281–299. https://doi.org/10.1144/gsl.sp.1997.119.01.18.
Möller, A., O'Brien, P.J., Kennedy, A., Kröner, A., 2003. The use and abuse of Th-U ratios in the interpretation of zircon. In: EGS-AGU-EUG Joint Assembly, pp. 12113.
Moore, D.M., Reynolds, R.C., 1989. X-ray Diffraction and the Identification and Analysis of Clay Minerals. Oxford University Press.
Nicholson, K., Hein, J.R., Fihn, B., Dasgupta, S., 1997. Manganese mineralization: geochemistry and mineralogy of terrestrial and marine deposits. Geol. Soc. Spec. Pub. 16, 123–138.
Nieto-Samaniego, Á.F., Alaniz-Álvarez, S.A., Camprubí, A., 2007. Mesa Central of México: stratigraphy, structure, and Cenozoic tectonic evolution. In: Special Paper 422: Geology of México: Celebrating the Centenary of the Geological Society of México, https://doi.org/10.1130/2007.2422(02).
Nieto-Samaniego, Á.F., Alaniz-Álvarez, S.A., Camprubí í Cano, A., 2005. La Mesa Central de México: estratigrafía, estructura y evolución tectónica cenozoica. Bol. Soc. Geol. Mex. 57, 285–318. https://doi.org/10.18268/bsgm2005v57n3a3.
Nieto-Samaniego, Á.F., Macías-Romo, C., Alaniz-Álvarez, S.A., 1996. Nuevas edades isotópicas de la cubierta volcánica cenozoica de la parte meridional de la Mesa Central, México. Rev. Mex. Cienc. Geol. 13, 117–122.
Nitta, M., Inoue, A., 2011. Carbon and oxygen isotope compositions of calcite and rhodochrosite from geothermal exploratory drills TH-4 and TH-6 near the Toyoha Deposit, Hokkaido, Japan. Resour. Geol. 61, 159–173. https://doi.org/10.1111/j.1751-3928.2011.00156.x.
O'Neil, J.R., Clayton, R.N., Mayeda, T.K., 1969. Oxygen isotope fractionation in divalent metal carbonates. J. Chem. Phys. 51, 5547–5558. https://doi.org/10.1063/1.1671982.
Okita, P.M., Shanks, W.C., 1992. Origin of stratiform sediment hosted manganese carbonate ore deposites: examples from Molango, Mexico, and TaoJiang, China. Chem. Geol. 99, 139–164.
Petrus, J.A., Kamber, B.S., 2012. VizualAge: a novel approach to laser ablation ICP-MS U-Pb geochronology data reduction. Geostand. Geoanal. Res. 36, 247–270. https://doi.org/10.1111/j.1751-908X.2012.00158.x.
Polgari, M., Hein, J.R., Toth, A.L., Pal-Molnár, E., Vigh, T., Biró, L., Fintor, K., 2012. Microbial action formed Jurassic Mn-carbonate ore deposit in only a few hundred years (Úrkút, Hungary). Geology 40, 903–906. https://doi.org/10.1130/G33304.1.
Ponce, B.F., Clark, K.F., 1988. The Zacatecas mining district: a tertiary caldera complex associated with precious and base metal mineralization. Econ. Geol. 83, 1668–1682. https://doi.org/10.2113/gsecongeo.83.8.1668.

Post, J.E., 1999. Manganese oxide minerals: crystal structures and economic and environmental significance. In: Proceedings of the National Academy of Sciences, pp. 3447–3454. https://doi.org/10.1073/pnas.96.7.3447.
Rocha, V.S., Wilson, I.F., 1946. Depositos de Manganeso denominados Montaña de Manganeso en el Estado de San Luis Potosi.
Rodríguez Díaz, A.A., Blanco Florido, D., Canet, C., Gervilla Linares, F., Eduardo, E., Prol Ledesma, R.M., Morales Ruano, S., García Vallè, M., 2010. Metalogenia del depósito de manganeso Santa Rosa, Baja California Sur, México. Bol. Soc. Geol. Mex. 62, 141–159. https://doi.org/10.18268/BSGM2010v62n1a8.
Rodríguez-Díaz, A.A., Canet, C., Villanueva-Estrada, R.E., Chacón, E., Gervilla, F., Velasco-Tapia, F., Cruz-Gámez, E.M., González-Partida, E., Casas-García, R., Linares-López, C., Pérez-Zárate, D., 2019. Recent Mn-Ag deposits in coastal hydrothermal springs in the Baja California Peninsula, Mexico. Miner. Deposita 54, 849–866. https://doi.org/10.1007/s00126-018-0846-9.
Roedder, E., 1984. Fluid inclusions. De Gruyter, Berlin, Boston. https://dx.doi.org/10.1515/9781501508271.
Roy, S., 1981. Manganese Deposits. Academic Press.
Roy, S., 1992. Environments and processes of manganese deposition. Econ. Geol. 87, 1218–1236. https://doi.org/10.2113/gsecongeo.87.5.1218.
Roy, S., 1997. Genetic diversity of manganese deposition in the terrestrial geological record. Geol. Soc., Lond., Spec. Publ. 119, 5–27. https://doi.org/10.1144/gsl.sp.1997.119.01.02.
Rye, R.O., 2005. A review of the stable-isotope geochemistry of sulfate minerals in selected igneous environments and related hydrothermal systems. Chem. Geol. 215, 5–36. https://doi.org/10.1016/j.chemgeo.2004.06.034.
Sabanero-Sosa, H.M., Salinas-Prieto, J.C., González-Arroyo, A., Ocejo-Paredes, T., 1999. Caracterización tectonica e implicaciones metalogeneticas de la faja de plata. Geomimet 230, 16–36.
Sánchez-Rojas, L., 2013. Jasperoides en el límite de los terrenos Guerrero y Sierra Madre Oriental. In: AIMMGM, XXX Convención Internacional de Minería. Acapulco, pp. 312–319.
Sander, M.V., Black, J.E., 1988. Crystallization and recrystallization of growth-zoned vein quartz crystals from epithermal systems: implications for fluid inclusion studies. Econ. Geol. 83, 1052–1060. https://doi.org/10.2113/gsecongeo.83.5.1052.
Sedlock, R.L., Ortega-Gutiérrez, F., Speed, R.C., Ortega-Gutiérrez, F., Speed, R.C., 1993. Tectonostratigraphic Terranes and Tectonic Evolution of Mexico, pp. 153.
Servicio Geológico Mexicano (SGM), 2011. Panorama minero del estado de San Luis Potosí. Servicio Geológico Mexicano, 64.
Shanks, W.C., 2001. Stable Isotopes in Seafloor Hydrothermal Systems: vent fluids, hydrothermal deposits, hydrothermal alteration, and microbial processes. Rev. Mineral. Geochem. 43, 469–525. https://doi.org/10.2138/gsrmg.43.1.469.
Shanks, W.C., 2013. Stable Isotope Geochemistry of Mineral Deposits. In: Holland, H.D., Turekian, K.K. (Eds.), Treatise on Geochemistry, Second edition. Elsevier.
Silva-Romo, G., Arellano-Gil, J., Mendoza-Rosales, C., Nieto-Obregón, J., 2000. A submarine fan in the Mesa Central, Mexico. J. S. Am. Earth Sci. 13, 429–442. https://doi.org/10.1016/S0895-9811(00)00034-1.
Sláma, J., Košler, J., Condon, D., Crowley, J., Gerdes, A., Hanchar, J., Horstwood, M., Morris, G., Nasdala, L., Norberg, N., Schaltegger, U., Schoene, B., Tubrett, M., Whitehouse, M., 2008. A new natural reference material for U-Pb and Hf isotopic microanalysis. Chem. Geol. 249, 1–35.
Solari, L.A., Tanner, M., 2011. UPb.age, a fast data reduction script for LA-ICP-MS U-Pb geochronology. Rev. Mex. Cienc. Geol. 28, 83–91.
Środoń, J., 2006. Identification and quantitative analysis of clay minerals. Dev. Clay Sci. 1, 765–787. https://doi.org/10.1016/S1572-4352(05)01028-7.
Środoń, J., 2013. Identification and quantitative analysis of clay minerals. In: Developments in Clay Science. Elsevier, pp. 25–49. https://doi.org/10.1016/B978-0-08-098259-5.00004-4.
Steele-MacInnis, M., Lecumberri-Sanchez, P., Bodnar, R.J., 2012. HokieFlincs_H2O-NaCl: a Microsoft Excel spreadsheet for interpreting microthermometric data from fluid inclusions based on the PVTX properties of H 2O-NaCl. Comput. Geosci. 49, 334–337. https://doi.org/10.1016/j.cageo.2012.01.022.
Thompson, A., Thompson, J., 1996. Atlas of Alteration: A field and petrographic guide to hydrothermal alteration minerals. Mineral Deposits Division, Geological Association of Canada.
Trask, P.D., Cabo, J.R., 1948. Manganese deposits of Mexico. In: Geologic Investigations in the American Republics, 1946, pp. 209–316. https://doi.org/10.3133/b954F.
Tristán-González, M., Aguillón-Robles, A., Barboza-Gudiño, J.R., Cruz-Márquez, J., García-Arreola, M.E., Bellon, H., Franzetti, M., Labarthe-Hernández, G., 2015. Caraterísticas geoquímicas y significado tectónico del complejo de diques y domos félsicos del Paleoceno-Eoceno de La Tesorera, Zacatecas, en la Mesa Central, México. Rev. Mex. Cienc. Geol. 32, 455–474.
Tristán-González, M., Aguillón-Robles, A., Barboza-Gudiño, J.R., Torres-Hernández, J.R., Bellon, H., López-Donce, R., Rodríguez-Ríos, R., Labarthe-Hernández, G., 2009a. Geocronología y distribución espacial del vulcanismo en el Campo Volcánico de San Luis Potosí. Bol. Soc. Geol. Mex. 61, 287–303. https://doi.org/10.18268/BSGM2009v61n3a1.
Tristán-González, M., Aguirre-Díaz, G.J., Labarthe-Hernández, G., Torres-Hernández, J.R., Bellon, H., 2009b. Post-Laramide and pre-Basin and Range deformation and implications for Paleogene (55–25 Ma) volcanism in central Mexico: a geological basis for a volcano-tectonic stress model. Tectonophysics 471, 136–152. https://doi.org/10.1016/j.tecto.2008.12.021.
Tristán-González, M., Labarthe-Hernández, G., Aguirre-Díaz, G.J., Aguillón-Robles, A., 2008. Tectono-volcanic control of fissure type vents for the 28 Ma Panalillo ignimbrite in the Villa de Reyes Graben, San Luis Potosí, México. In: IOP Conference Series: Earth and Environmental Science, https://doi.org/10.1088/1755-1307/3/1/012026.
Wilkinson, J., 2001. Fluid inclusions in hydrothermal ore deposits. Lithos 55, 229–272. https://doi.org/10.1016/S0024-4937(00)00047-5.
Wilson, I.F., Rocha, V.S., 1948. Manganese deposits of the Montaña de Manganeso mine, San Luis Potosí, Mexico.
Zantop, H., 1978. Setting and genesis of iron oxides and manganese oxides in the San Francisco Manganese Deposit, Jalisco, Mexico. Econ. Geol. 73, 1137–1149.

CHAPTER 7

GENERAL DISCUSSION AND CONCLUSIONS

This investigation has produced valuable information on the processes and causes of manganese mineralization in the Montaña de Manganeso deposit. The genetic process has been evaluated from three different angles (a) geodynamic evolution of the study region (b) timing of mineralization (c) nature of the mineralizing fluid. As a result, new data on the depositional environment, age of mineralization, mechanism of deposition as well as fluid temperature, salinity and pH were produced that allowed the refinement of the existing genetic model of the Montaña de Manganeso deposit. The research highlights, including key results and major findings, are summarized below. Refer to the papers in the corresponding chapters for a more detailed conclusion on the points addressed here.

7.1 Key results and their interpretation

Manganese mineralization at Montaña de Manganeso occurs mainly as irregular bodies or veins of 5–30 m wide, within folded and hydrothermally altered host rocks and, to a lesser extent, in the form of deformed stratabound bodies. The mineralization occurs within an area about 100 m wide and at least 300 m long, controlled by NW- SE trending faults (with subordinate NE-SW and E-W directions). The NW-SE trending direction fairly coincides with that of the regional San Luis-Tepehuanes-fault system, which controlled the distribution of several mineral deposits in the Central Plateau (Camprubí and Albinson, 2007; Nieto-Samaniego et al., 2007).

The Montaña de Manganeso deposit exhibit a rather simple mineral paragenesis consisting of Mn oxides such as birnessite, todorokite, pyrolusite and the cryptomelane-hollandite series as ore minerals and hematite and goethite as accessory minerals. Quartz (and its polymorphs tridymite and chalcedony), calcite and barite are the common gangue minerals. These minerals formed through two main hydrothermal stages and a minor supergene stage. Stage 1 is characterized by the precipitation of pyrolusite, todorokite and birnessite, with minor silica (chalcedony and cryptocrystalline quartz), whereas during stage 2 much of the silica

precipitated, leading to the formation of massive jasperoids, accompanied by hollandite-romanechite and cryptomelane. The supergene alteration stage 3 is indicated by the formation of pisolitic-like and colloform Mn oxides on recent sediments.

The nature of the ore forming fluids as determined by isotopic (C-O-S) and fluid inclusion systematics indicate that mineralizing fluids were low temperature (101–140 °C) aqueous fluids of intermediate salinity (8.0–16.0 wt% NaCl equivalent) derived from magmatic sources (average $\delta^{13}C$ = -7.0‰; average $\delta^{34}S$ = 8.9‰) that evolved through fluid/rock interaction and mixing with meteoric waters. Fluid/rock interaction produced an argillic type alteration, characterized by the presence of illite, illite-smectite, smectite and kaolinite. The physico-chemical conditions (temperature and pH) estimated from this clay assemblage indicate that alteration resulted from low temperature, near neutral pH fluids dominated by bicarbonate waters with a minor acid sulphate component.

Geochemically the Montana de Manganeso deposit displays a chemical signature of both continental and submarine hydrothermal Mn deposits (Table A1; supplementary data; chapter 5). Super chondritic Y/Ho ratios that exceed 44, positive Y anomalies (i.e., YPAAS/HoPAAS > 1) and well-developed negative Ce anomalies are characteristics acquired from seawater (Lottermoser, 1992) and are typical of submarine hydrothermal deposits (Bau et al., 2014). However, the Mn-Fe-(Ni + Cu + Co), MnO_2-MgO-Fe_2O_3, (Cu/Zn)/Fe_2O_3 vs. (Zn/Ni)/MnO_2 and Na/Mg discrimination diagrams (Fig. 9; Chapter 5) show intermediate signatures between marine and terrestrial environments. A continental origin is also supported by the age of the deposit. (<40 Ma), which is more recent than the age of the last marine sedimentary deposition, and thus, indicates a formation under continental, subaerial conditions.

Although not strictly a discriminatory factor among the various manganese genetic types, the mineralogy of the Montaña de Manganeso might also be a reflection of this dual character. The paragenetic sequence of the Montaña de Manganeso deposit (Fig.7; Chapter 6) indicate the formation of early stage poorly crystalline todorokite and birnessite (Fig. 3; Chapter 5). Although these minerals have been reported in some continental hydrothermal manganese deposits (e.g., Ostwald, 1982, 1988; Nicholson, 1992; Crespo and Lunar, 1997; Gutzmer and Beukes, 2000; Miura and Hariya, 2007), they are commonly formed on the ocean floor by hydrogenetic processes and/or hydrothermal venting (Burns and Burns, 1978,

1979; Hein et al., 1997; Canet et al., 2008; Nakagawa et al., 2009; Brusnitsyn et al., 2017; Fan et al., 2018). The paragenetically late minerals at Montaña de Manganeso – cryptomelane and hollandite – are common in land based deposits (hydrothermal and supergene) and have been previously shown to form from alteration of birnessite and todorokite, respectively, under oxidizing conditions (Chen, 2006; Birkner and Navrotsky, 2017; Fan et al., 2018).

7.2 The genetic model

Manganese mineralization in the Central Plateau has a regional character and probably had its origin in hydrothermal activity associated with the opening of the Arperos basin. The Montana de Manganeso deposit is located on a suture zone of the Guerrero and Sierra Madre tectonostratigraphic terranes (Centeno-García and Silva-Romo, 1997; Freydier et al., 2000; Centeno-García et al., 2003, 2008; Martini et al., 2013) whose evolution was controlled mainly by the subduction-related tectonics along the paleo-Pacific margin, leading to the opening and subsequent closure of the continental Arperos back arc basin (Figs. A4, A5; supplementary material, Chapter 5;) (Centeno-Garcia et al., 1993; Centeno-García and Silva-Romo, 1997; Martini et al., 2011; Ortega-Flores et al., 2015; Martini and Ortega-Gutierrez, 2018).

Back-arc settings are ideal for the formation of Mn deposits associated with submarine volcanism or hydrothermalism (Roy, 1981, 1992; Şaşmaz et al., 2014; Maghfouri et al., 2017). Well known manganese deposits formed by submarine volcanism close to spreading centers include the deposits of Waziristan, Pakistan (Shah and Moon, 2007); Apennine ophiolitic complex, Italy (Bonatti et al., 1976; Sinisi et al., 2018, 2012); the Semail nappe, Oman (Fleet and Robertson, 1980); the Franciscan assemblages, USA (Chyi et al., 1984; Crerar et al., 1982) and the Trodoos massif, Cyprus (Roy, 1992). Montaña de Manganeso, however, differed from the above cited examples in that manganese sourced from the opening Arperos basin did not lead to substantial or economic concentrations of manganese because the extension of the Arperos basin likely produced only an incipient oceanic crust (Lapierre *et al.*, 1992; Martini *et al.*, 2011, Fig. 1A) and therefore a full ophiolitic sequence, typical of the above mentioned examples, did not form. Still, it is hypothesized in this work that

manganese was emitted and preconcentrated in the basin sediments which later formed the host rocks of the Montaña de Manganeso deposit.

The preconcentrated manganese oxides (and associated trace elements) were then remobilized, leached, and altered during the second stage of deposit formation which occurred during the Eocene-Oligocene as a result of the Sierra Madre Occidental related silicic volcanism. Regional thrusts faults developed during the accretion of the Guerrero terrane and the normal faults that developed during the post-Laramide extensional tectonics of the southern Basin and Range provided the conduits for the ascent of felsic magmas (Aguillon-Robles et al., 2009; Tristan-Gonzalez et al., 2009). Mn-enriched hydrothermal fluids then penetrated fissures and permeable horizons forming veins and smaller irregular bodies. In this second stage Mn ores formed in the shallowest portion of an epithermal system through a process of mixing of: (*a*) boiled-off hydrothermal fluids, with (*b*) cold, diluted meteoric waters. The tectonic setting and geological characteristics during this second stage are compatible with a hot-spring deposit model, according to which the Montaña de Manganeso corresponds to the shallowest portion of an epithermal system formed in a continental volcanic arc setting.

Most of the original characteristics of the stratabound mineralization associated with emissions in the back arc basin were obliterated, first by the closure and subsequent accretion of the back arc basin sediments over the Sierra Madre terrane, and then by silicification caused by the Eocene-Oligocene volcanism. Nevertheless, the Montaña de Manganeso still retains a marine geochemical signature normally associated with deposits formed in a submarine hydrothermal setting.

7.2 Implications for Mn deposits in the Central Plateau

In the model proposed in this investigation, manganese was preconcentrated in the host rocks by the hydrothermal activity associated with the rifting and opening of the Arperos basin. This model has important genetic implications for several manganese deposits in central Mexico. A look at the areal extension of the Arperos basin (Fig. 1), suggest that this model can be applied to several of the manganese deposits in central Mexico (see distribution of Mn deposits in Fig. A6;). Indeed, it can be argued that most manganese deposits in Mexico

were formed from similar processes involving manganese enrichment from hydrothermal activity related either to the opening of the Gulf of Mexico (Molango Mn deposits), the opening of the Gulf of California (Bahia Concepcion deposits) or the opening of the Arperos basin (e.g Montaña de Manganeso deposits).

References

Aguillón-Robles, A., Tristán-González, M., Aguirre-Díaz, G.J., Bellon, H., 2009. Syn-extensional intra-plate trachydacite-rhyolitic dome volcanism of the Mesa Central, southern Sierra Madre Occidental volcanic province, Mexico. Journal of Volcanology and Geothermal Research 187, 33–52. https://doi.org/10.1016/j.jvolgeores.2009.08.021

Alaniz-Álvarez, S.A., Nieto-Samaniego, Á.F., 2007. The Taxco–San Miguel de Allende fault system and the Trans-Mexican Volcanic Belt: Two tectonic boundaries in central México active during the Cenozoic, in: Special Paper 422: Geology of México: Celebrating the Centenary of the Geological Society of México. Geological Society of America, pp. 301–316. https://doi.org/10.1130/2007.2422(10)

Aranda-Gómez, J.J., Mcdowell, F.W., 1998. Paleogene Extension in the Southern Basin and Range Province of Mexico: Syndepositional Tilting of Eocene Red Beds and Oligocene Volcanic Rocks in the Guanajuato Mining District. International Geology Review 40, 116–134. https://doi.org/10.1080/00206819809465201

Aranda-Gómez, J.J., Molina-Garza, R., McDowell, F.W., Vassallo-Morales, L.F., Ortega-Rivera, M.A., Solorio-Munguía, J.G., Aguillón-Robles, A., 2007. The relationships between volcanism and extension in the Mesa Central: The case of Pinos, Zacatecas, Mexico. Revista Mexicana de Ciencias Geologicas 24, 216–233.

Birkner, N., Navrotsky, A., 2017. Thermodynamics of manganese oxides: Sodium, potassium, and calcium birnessite and cryptomelane. Proceedings of the National Academy of Sciences of the United States of America 114, E1046–E1053. https://doi.org/10.1073/pnas.1620427114

Bonatti, E., Zerbi, M., Kay, R., Rydell, H., 1976. Metalliferous deposits from the Apennine ophiolites: Mesozoic equivalents of modern deposits from oceanic spreading centers. Bulletin of the Geological Society of America 87, 83–94. https://doi.org/10.1130/0016-7606(1976)87<83:MDFTAO>2.0.CO;2

Brusnitsyn, A.I., Kuleshov, V.N., Perova, E.N., Zaitsev, A.N., 2017. Ferromanganese carbonate metasediments of the Sob area, Polar Urals: Bedding conditions, composition, and genesis. Lithology and Mineral Resources 52, 192–213. https://doi.org/10.1134/s0024490217030026

Burns, R.G., Burns, V.M., 1979. MANGANESE OXIDES, in: Burns, R.G. (Ed.), Marine Minerals. De Gruyter, Berlin, Boston, pp. 1–46. https://doi.org/10.1515/9781501508646-005

Burns, V.M., Burns, R.. G., 1978. Authigenic todorokite and phillipsite inside deep sea manganese nodules. American Mineralogist 63, 827–831.

Canet, C., Prol-Ledesma, R.M., Bandy, W.L., Schaaf, P., Linares, C., Camprubí, A., Tauler, E., Mortera-Gutiérrez, C., 2008. Mineralogical and geochemical constraints on the origin of ferromanganese crusts from the Rivera Plate (western margin of Mexico). Marine Geology 251, 47–59. https://doi.org/10.1016/j.margeo.2008.01.012

Centeno-García, E., Corona-Chávez, P., Talavera-Mendoza, O., Iriondo, A., 2003. Geologic and tectonic evolution of the western Guerrero terrane—A transect from Puerto Vallarta to Zihuatanejo, Mexico, in: Geologic Transects across Cordilleran Mexico: Guidebook for the Field Trips of the 99th Geological Society of America Cordilleran Section Annual Meeting. Geological Society of America.

Centeno-García, E., Guerrero-Suastegui, M., Talavera-Mendoza, O., 2008. The Guerrero Composite Terrane of western Mexico: Collision and subsequent rifting in a supra-subduction zone. Geological Society of America. https://doi.org/10.1130/2008.2436(13)

Centeno-García, E., Ruíz, J., Coney, P.J., Patchett, P.J., Ortega-Gutiérrez, F., 1993. Guerrero terrane of Mexico: Its role in the Southern, Cordillera from new geochemical data. Geology 21, 419–422. https://doi.org/10.1130/0091-7613(1993)021<0419:GTOMIR>2.3.CO;2

Centeno-García, E., Silva-Romo, G., 1997. Petrogenesis and tectonic evolution of Central Mexico during Triassic-Jurassic time. Revista Mexicana de Ciencias Geologicas 14, 244–260.

Chen, C.-C., 2006. Transformation of Synthetic Birnessite to Cryptomelane: An Electron Microscopic Study. Clays and Clay Minerals 34, 565–571. https://doi.org/10.1346/ccmn.1986.0340510

Chyi, M.S., Crerar, D.A., Carlson, R.W., Stallard, R.F., 1984. Hydrothermal Mn-deposits of the Franciscan Assemblage, II. Isotope and trace element geochemistry, and implications for hydrothermal convection at spreading centers. Earth and Planetary Science Letters 71, 31–45. https://doi.org/10.1016/0012-821X(84)90050-5

Conly, A.G., Scott, S.D., Bellon, H., 2011. Metalliferous manganese oxide mineralization associated with the Boléo Cu-Co-Zn district, Mexico. Economic Geology 106, 1173–1196. https://doi.org/10.2113/econgeo.106.7.1173

Crerar, D.A., Namson, J., Chyi, M.S., Williams, L., Feigenson, M.D., 1982. Manganiferous cherts of the Franciscan assemblage; I, General geology, ancient and modern analogues, and implications for hydrothermal convection at oceanic spreading centers. Economic Geology 77, 519–540. https://doi.org/10.2113/gsecongeo.77.3.519

Crespo, A., Lunar, R., 1997. Terrestrial hot-spring Co-rich Mn mineralization in the Pliocene-Quaternary Calatrava Region (central Spain). Geological Society Special Publication 119, 253–264. https://doi.org/10.1144/GSL.SP.1997.119.01.16

Fan, C., Xu, L., Zhao, W., 2018. Transformation of birnessite into hollandite under the influence of silver cations in aqueous medium. Journal of Solid State Chemistry 268, 136–148. https://doi.org/10.1016/j.jssc.2018.08.039

Fleet, A.J., Robertson, A.H.F., 1980. Ocean- ridge metalliferous and pelagic sediments of the Semail Nappe, Oman. Journal, Geological Society 137. https://doi.org/10.1144/gsjgs.137.4.0403

Freydier, C., Lapierre, H., Ruiz, J., Tardy, M., Martinez-R, J., Coulon, C., 2000. The Early Cretaceous

Arperos basin: An oceanic domain dividing the Guerrero arc from nuclear Mexico evidenced by the geochemistry of the lavas and sediments. Journal of South American Earth Sciences 13, 325–336. https://doi.org/10.1016/S0895-9811(00)00027-4

Gutzmer, J., Beukes, N.J.N.J., 2000. Asbestiform manjiroite and todorokite from the Kalahari manganese field, South Africa. South African Journal of Geology 103, 163–174. https://doi.org/10.2113/1030163

Hein, J.R., Koschinsky, A., Halbach, P., Manheim, F.T., Bau, M., Kang, J.-K.K., Lubick, N., 1997. Iron and manganese oxide mineralization in the Pacific. Geological Society Special Publication 119, 123–138. https://doi.org/10.1144/GSL.SP.1997.119.01.09

Lapierre, H., Tardy, M., Coulon, C., Hernandez, E.O., Bourdier, J.-L., Reyes, J.M., Freydier, C., 1992. Caractérisation, genèse et évolution géodynamique du terrain de Guerrero (Mexique occidental). Canadian Journal of Earth Sciences 29, 2478–2489. https://doi.org/10.1139/e92-194

Maghfouri, S., Rastad, E., Mousivand, F., Choulet, F., Ye, L., 2017. Geological and geochemical constraints on the Cheshmeh-Frezi volcanogenic stratiform manganese deposit, southwest Sabzevar basin, Iran. Ore Geology Reviews 89, 96–113. https://doi.org/10.1016/j.oregeorev.2017.06.015

Martini, M., Mori, L., Solari, L., Centeno-García, E., 2011. Sandstone Provenance of the Arperos Basin (Sierra de Guanajuato, Central Mexico): Late Jurassic–Early Cretaceous Back-Arc Spreading as the Foundation of the Guerrero Terrane. The Journal of Geology 119, 597–617. https://doi.org/10.1086/661989

Martini, M., Ortega-Gutiérrez, F., 2018. Tectono-stratigraphic evolution of eastern Mexico during the break-up of Pangea: A review. Earth-Science Reviews 183, 38–55. https://doi.org/10.1016/j.earscirev.2016.06.013

Martini, M., Solari, L., Camprubí, A., 2013. Kinematics of the Guerrero terrane accretion in the Sierra de Guanajuato, central Mexico: New insights for the structural evolution of arc-continent collisional zones. International Geology Review 55, 574–589. https://doi.org/10.1080/00206814.2012.729361

Miura, H., Hariya, Y., 2007. Recent manganese oxide deposits in Hokkaido, Japan. Geological Society, London, Special Publications 119, 281–299. https://doi.org/10.1144/gsl.sp.1997.119.01.18

Nakagawa, M., Santosh, M., Maruyama, S., 2009. Distribution and mineral assemblages of bedded manganese deposits in Shikoku, Southwest Japan: Implications for accretion tectonics. Gondwana Research 16, 609–621. https://doi.org/10.1016/j.gr.2009.05.003

Nicholson, K., 1992. Contrasting mineralogical-geochemical signatures of manganese oxides: guides to metallogenesis. Economic Geology 87, 1253–1264. https://doi.org/10.2113/gsecongeo.87.5.1253

Nieto-Samaniego, Á.F., Alaniz-Álvarez, S.A., Camprubí, A., 2007. Mesa Central of México: Stratigraphy, structure, and Cenozoic tectonic evolution, in: Special Paper 422: Geology of México: Celebrating the Centenary of the Geological Society of México. Geological Society of America, pp. 41–70. https://doi.org/10.1130/2007.2422(02)

Ortega-Flores, B., Solari, L.A., De Jesús Escalona-Alcázar, F., 2016. The mesozoic successions of western sierra de zacatecas, central Mexico: Provenance and tectonic implications. Geological Magazine 153, 696–717. https://doi.org/10.1017/S0016756815000977

Ostwald, J., 1988. Mineralogy of the Groote Eylandt manganese oxides: A review. Ore Geology Reviews 4, 3–45. https://doi.org/10.1016/0169-1368(88)90003-0

Ostwald, J., 1982. Some observations on todorokites from marine and terrestrial environments. Mineralogical Magazine 46, 253–256. https://doi.org/10.1180/minmag.1982.046.339.12

Roy, S., 1992. Environments and processes of manganese deposition. Economic Geology 87, 1218–1236. https://doi.org/10.2113/gsecongeo.87.5.1218

Roy, S., 1981. Manganese deposits. Academic Press.

Şaşmaz, A., Türkyilmaz, B., Öztürk, N., Yavuz, F., Kumral, M., 2014. Geology and geochemistry of Middle Eocene Maden complex ferromanganese deposits from the Elaziğ-Malatya region, eastern Turkey. Ore Geology Reviews. https://doi.org/10.1016/j.oregeorev.2013.06.012

Sinisi, R., Mameli, P., Mongelli, G., Oggiano, G., 2012. Different Mn-ores in a continental arc setting: Geochemical and mineralogical evidences from Tertiary deposits of Sardinia (Italy). Ore Geology Reviews 47, 110–125. https://doi.org/10.1016/j.oregeorev.2012.03.006

Sinisi, R., Mongelli, G., Perri, F., Rizzo, G., 2018. The braunite (3Mn2O3·MnSiO3)-rich mineralization in the metasedimentary succession from southern Apennines (Italy): Genesis constraints. Ore Geology Reviews 94, 1–11. https://doi.org/10.1016/j.oregeorev.2018.01.014

Shah, M., Moon, C.J., 2007. Manganese and ferromanganese ores from different tectonic settings in the NW Himalayas, Pakistan. Journal of Asian Earth Sciences 29, 455–465. https://doi.org/10.1016/j.jseaes.2005.11.002

Tristán-González, M., Aguirre-Díaz, G.J., Labarthe-Hernández, G., Torres-Hernández, J.R., Bellon, H., 2009. Post-Laramide and pre-Basin and Range deformation and implications for Paleogene (55-25 Ma) volcanism in central Mexico: A geological basis for a volcano-tectonic stress model. Tectonophysics 471, 136–152. https://doi.org/10.1016/j.tecto.2008.12.021

Supplementary data (Chapter 4)

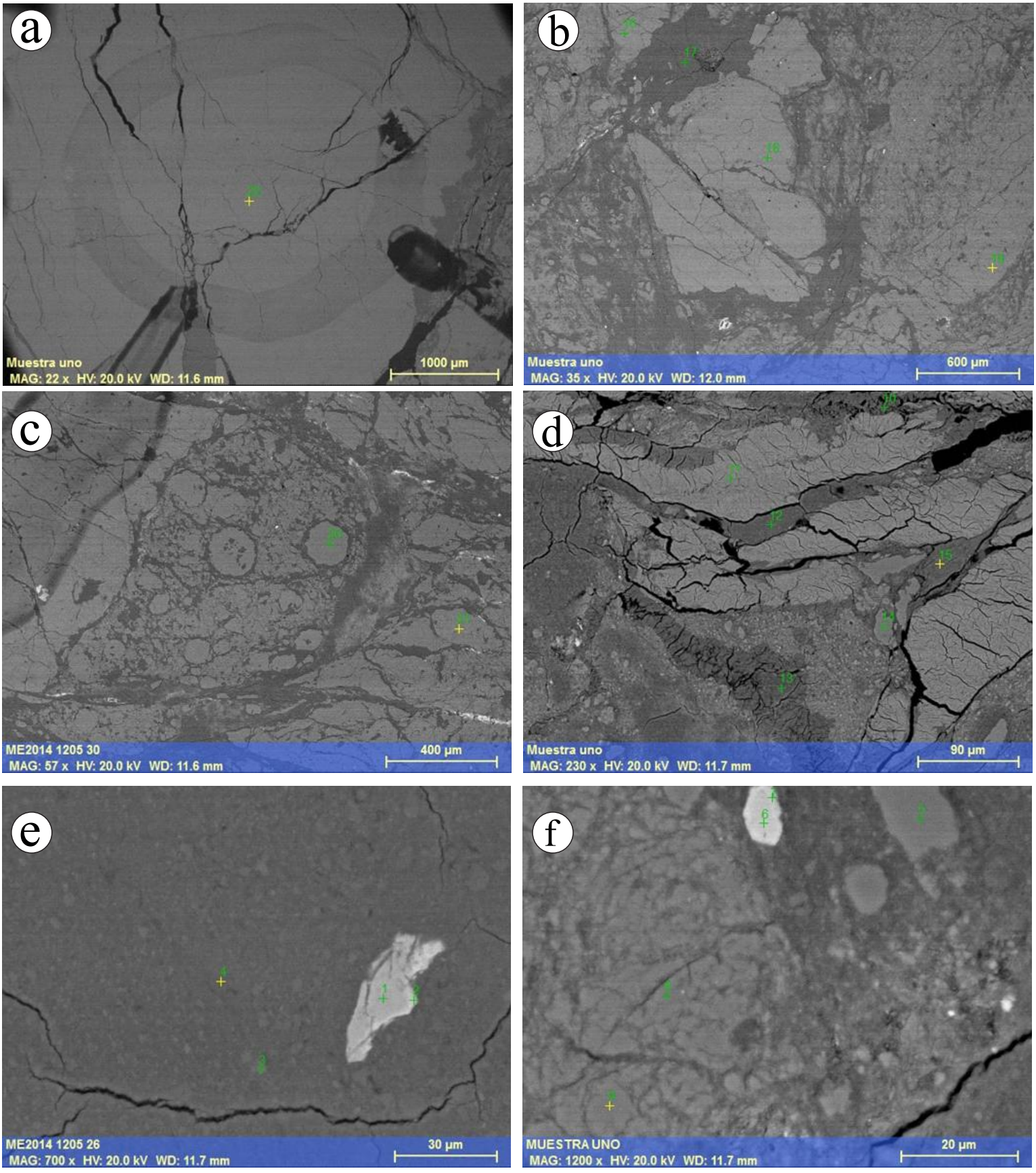

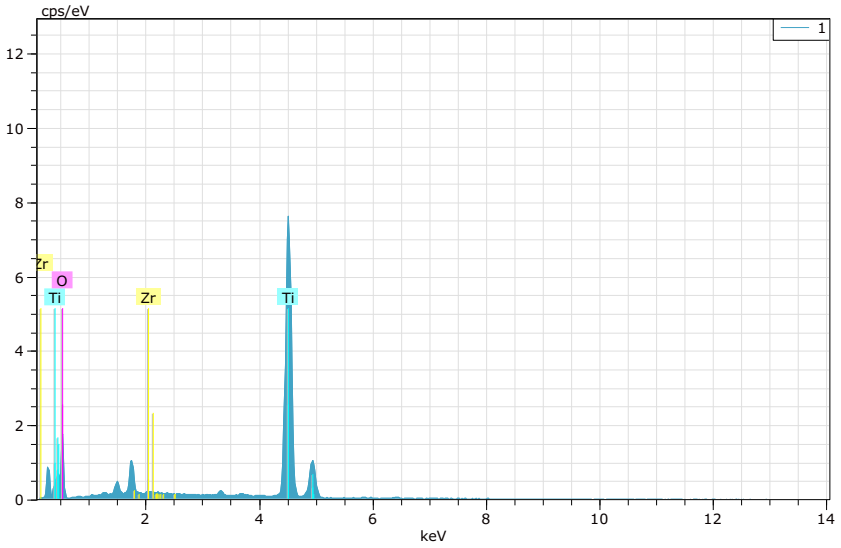

Spectrum: 1

El	AN	Series	unn. C [wt.%]	norm. C [wt.%]	Atom. C [at.%]	Compound	Comp. C [wt.%]	norm. Comp. C [wt.%]	Error (1 Sigma) [wt.%]
Ti	22	K-series	49.83	59.75	33.26	TiO2	99.67	83.14	1.45
O	8	K-series	33.37	40.01	66.67		0.00	0.00	6.01
Zr	40	L-series	0.20	0.24	0.07	ZrO2	0.33	0.27	0.05
		Total:	83.41	100.00	100.00				

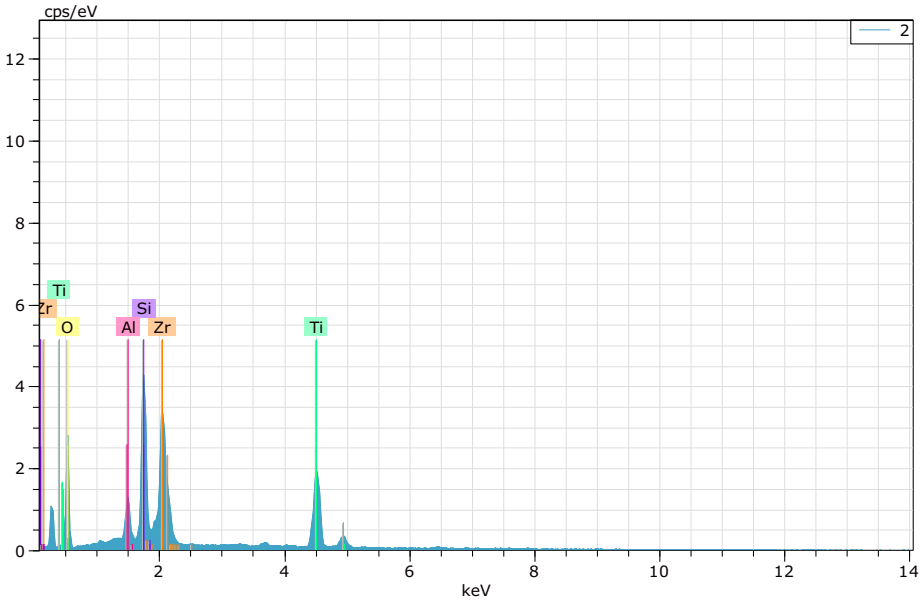

Spectrum: 2

El	AN	Series	unn. C [wt.%]	norm. C [wt.%]	Atom. C [at.%]	Compound	Comp. C [wt.%]	norm. Comp. C [wt.%]	Error (1 Sigma) [wt.%]
O	8	K-series	24.69	38.17	66.08		0.00	0.00	5.19
Zr	40	L-series	18.67	28.87	8.77	ZrO2	39.00	25.22	0.84
Ti	22	K-series	11.87	18.36	10.62	TiO2	30.63	19.81	0.47
Si	14	K-series	7.23	11.18	11.03	SiO2	23.93	15.47	0.38
Al	13	K-series	2.21	3.41	3.50	Al2O3	6.45	4.17	0.18
		Total:	64.68	100.00	100.00				

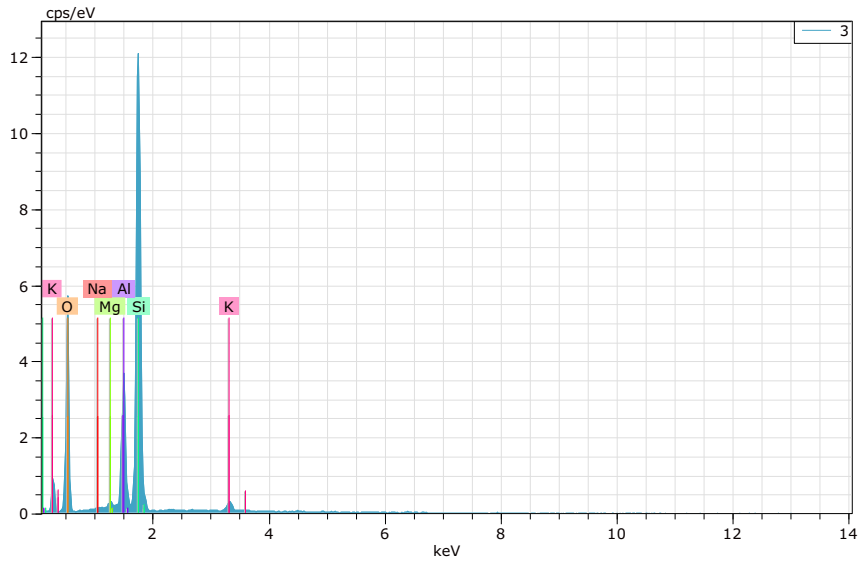

Spectrum: 3

El	AN	Series	unn. C [wt.%]	norm. C [wt.%]	Atom. C [at.%]	Compound	Comp. C [wt.%]	norm. Comp. C [wt.%]	Error (1 Sigma) [wt.%]
O	8	K-series	37.34	51.13	64.68		0.00	0.00	6.64
Si	14	K-series	26.18	35.85	25.83	SiO2	76.70	56.01	1.21
Al	13	K-series	7.84	10.74	8.06	Al2O3	20.29	14.82	0.47
K	19	K-series	1.09	1.49	0.77	K2O	1.79	1.31	0.11
Mg	12	K-series	0.37	0.51	0.42	MgO	0.84	0.61	0.08
Na	11	K-series	0.20	0.28	0.25	Na2O	0.38	0.28	0.07
		Total:	73.03	100.00	100.00				

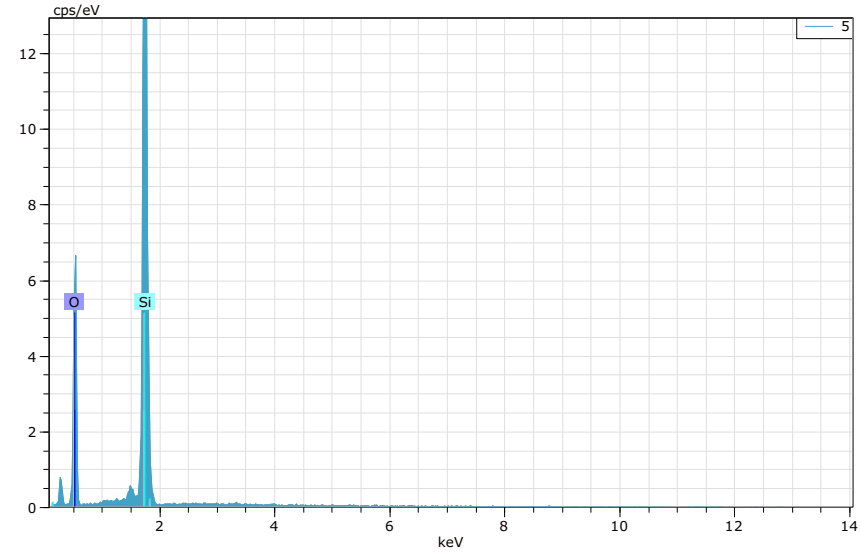

Spectrum: 5

El	AN	Series	unn. C [wt.%]	norm. C [wt.%]	Atom. C [at.%]	Compound	Comp. C [wt.%]	norm. Comp. C [wt.%]	Error (1 Sigma) [wt.%]
O	8	K-series	40.54	53.26	66.67		0.00	0.00	7.48
Si	14	K-series	35.58	46.74	33.33	SiO2	100.00	76.12	1.62
		Total:	76.12	100.00	100.00				

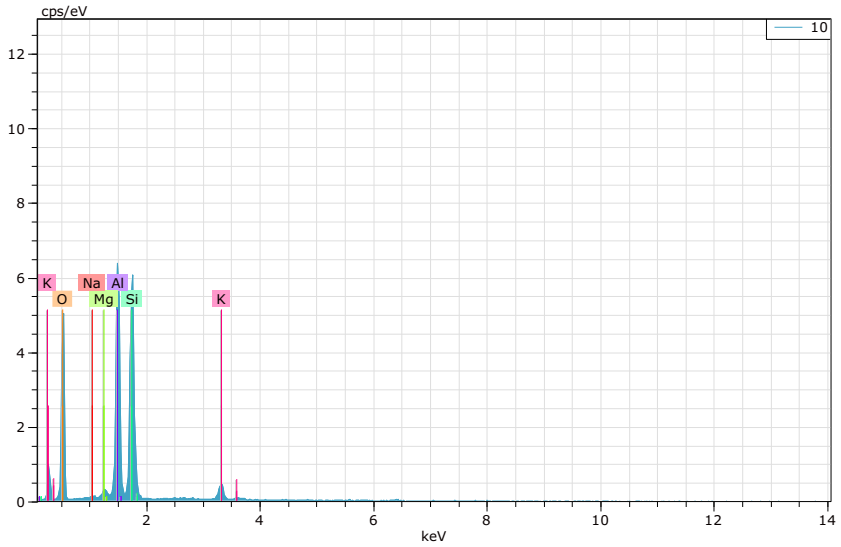

Spectrum: 10

El	AN	Series	unn. C [wt.%]	norm. C [wt.%]	Atom. C [at.%]	Compound	Comp. C [wt.%]	norm. Comp. C [wt.%]	Error (1 Sigma) [wt.%]
O	8	K-series	35.01	49.08	62.68		0.00	0.00	6.03
Si	14	K-series	17.15	24.04	17.49	SiO2	51.43	36.68	0.82
Al	13	K-series	16.40	22.99	17.41	Al2O3	43.45	30.99	0.88
K	19	K-series	1.92	2.69	1.40	K2O	3.24	2.31	0.14
Mg	12	K-series	0.63	0.89	0.74	MgO	1.47	1.05	0.10
Na	11	K-series	0.22	0.31	0.28	Na2O	0.42	0.30	0.07
		Total:	71.33	100.00	100.00				

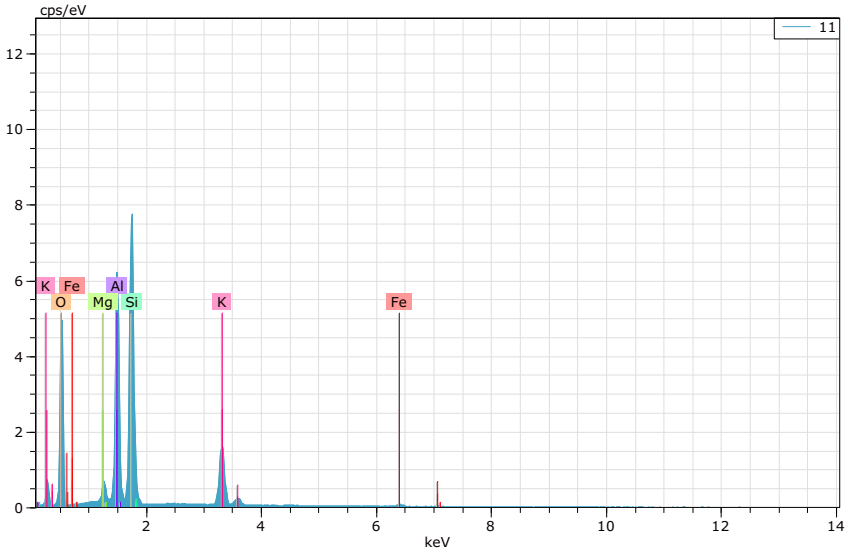

Spectrum: 11

El	AN	Series	unn. C [wt.%]	norm. C [wt.%]	Atom. C [at.%]	Compound	Comp. C [wt.%]	norm. Comp. C [wt.%]	Error (1 Sigma) [wt.%]
O	8	K-series	36.91	46.51	61.28		0.00	0.00	5.22
Si	14	K-series	18.91	23.83	17.89	SiO2	50.99	40.46	0.85
Al	13	K-series	14.25	17.95	14.03	Al2O3	33.92	26.92	0.73
K	19	K-series	6.88	8.66	4.67	K2O	10.44	8.28	0.26
Mg	12	K-series	1.59	2.01	1.74	MgO	3.33	2.64	0.13
Fe	26	K-series	0.82	1.03	0.39	FeO	1.33	1.05	0.08
		Total:	79.36	100.00	100.00				

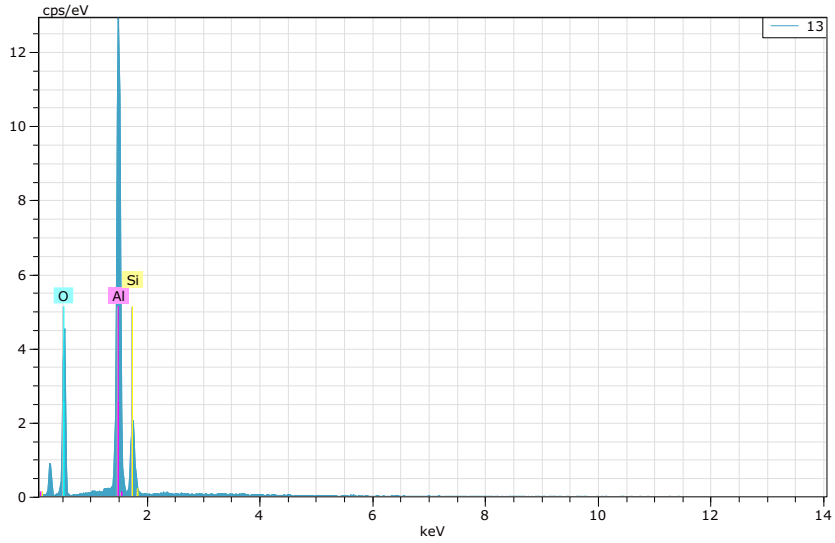

Spectrum: 13

El	AN	Series	unn. C [wt.%]	norm. C [wt.%]	Atom. C [at.%]	Compound	Comp. C [wt.%]	norm. Comp. C [wt.%]	Error (1 Sigma) [wt.%]
O	8	K-series	34.67	48.31	61.35		0.00	0.00	7.17
Al	13	K-series	30.42	42.39	31.92	Al2O3	80.09	57.48	1.60
Si	14	K-series	6.68	9.31	6.73	SiO2	19.91	14.29	0.43
		Total:	71.77	100.00	100.00				

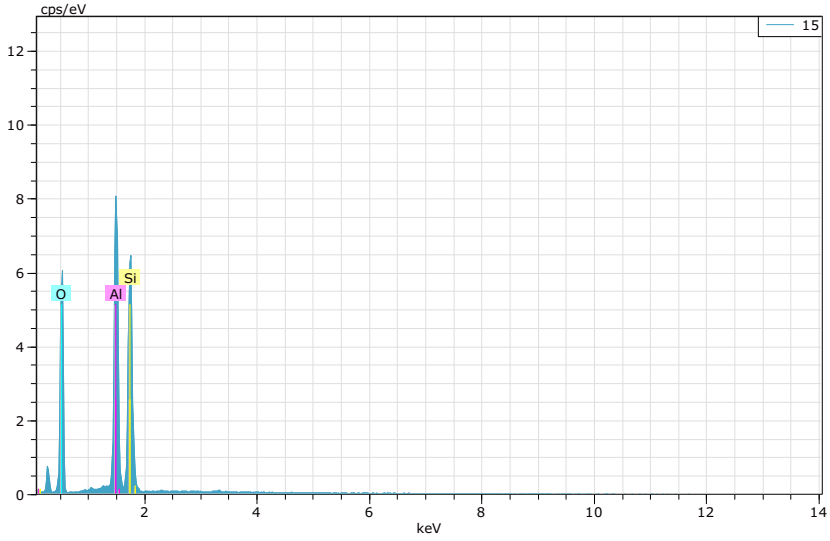

Spectrum: 15

El	AN	Series	unn. C [wt.%]	norm. C [wt.%]	Atom. C [at.%]	Compound	Comp. C [wt.%]	norm. Comp. C [wt.%]	Error (1 Sigma) [wt.%]
O	8	K-series	37.97	50.27	63.48		0.00	0.00	6.94
Al	13	K-series	19.29	25.55	19.13	Al2O3	48.27	36.46	1.05
Si	14	K-series	18.26	24.18	17.39	SiO2	51.73	39.07	0.91
		Total:	75.53	100.00	100.00				

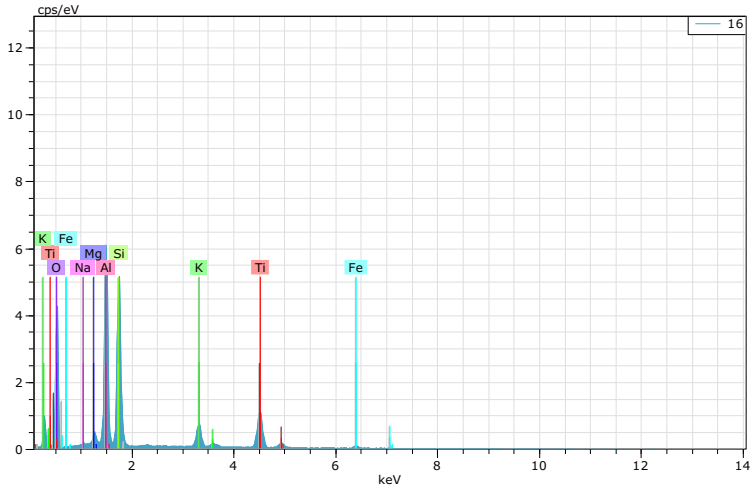

Spectrum: 16

El	AN	Series	unn. C [wt.%]	norm. C [wt.%]	Atom. C [at.%]	Compound	Comp. C [wt.%]	norm. Comp. C [wt.%]	Error (1 Sigma) [wt.%]
O	8	K-series	37.94	45.91	62.03		0.00	0.00	6.21
Al	13	K-series	16.60	20.09	16.10	Al2O3	37.97	31.37	0.87
Si	14	K-series	13.51	16.35	12.59	SiO2	34.99	28.91	0.65
Ti	22	K-series	8.75	10.59	4.78	TiO2	17.66	14.60	0.35
K	19	K-series	3.19	3.86	2.13	K2O	4.65	3.84	0.17
Mg	12	K-series	1.29	1.56	1.39	MgO	2.59	2.14	0.13
Fe	26	K-series	0.84	1.02	0.39	FeO	1.31	1.08	0.11
Na	11	K-series	0.51	0.62	0.59	Na2O	0.84	0.69	0.09
		Total:	82.64	100.00	100.00				

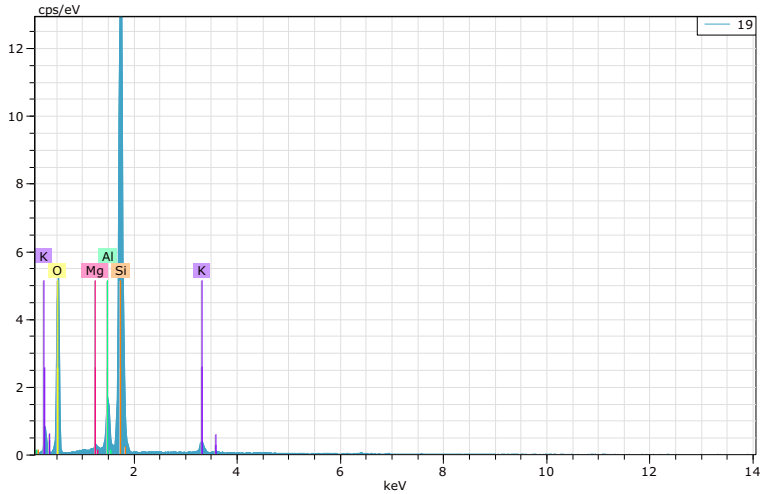

Spectrum: 19

El	AN	Series	unn. C [wt.%]	norm. C [wt.%]	Atom. C [at.%]	Compound	Comp. C [wt.%]	norm. Comp. C [wt.%]	Error (1 Sigma) [wt.%]
O	8	K-series	38.99	51.57	65.27		0.00	0.00	7.75
Si	14	K-series	30.58	40.45	29.17	SiO2	86.54	65.43	1.42
Al	13	K-series	3.88	5.13	3.85	Al2O3	9.69	7.32	0.29
K	19	K-series	1.58	2.09	1.08	K2O	2.52	1.90	0.15
Mg	12	K-series	0.57	0.76	0.63	MgO	1.26	0.95	0.11
		Total:	75.61	100.00	100.00				

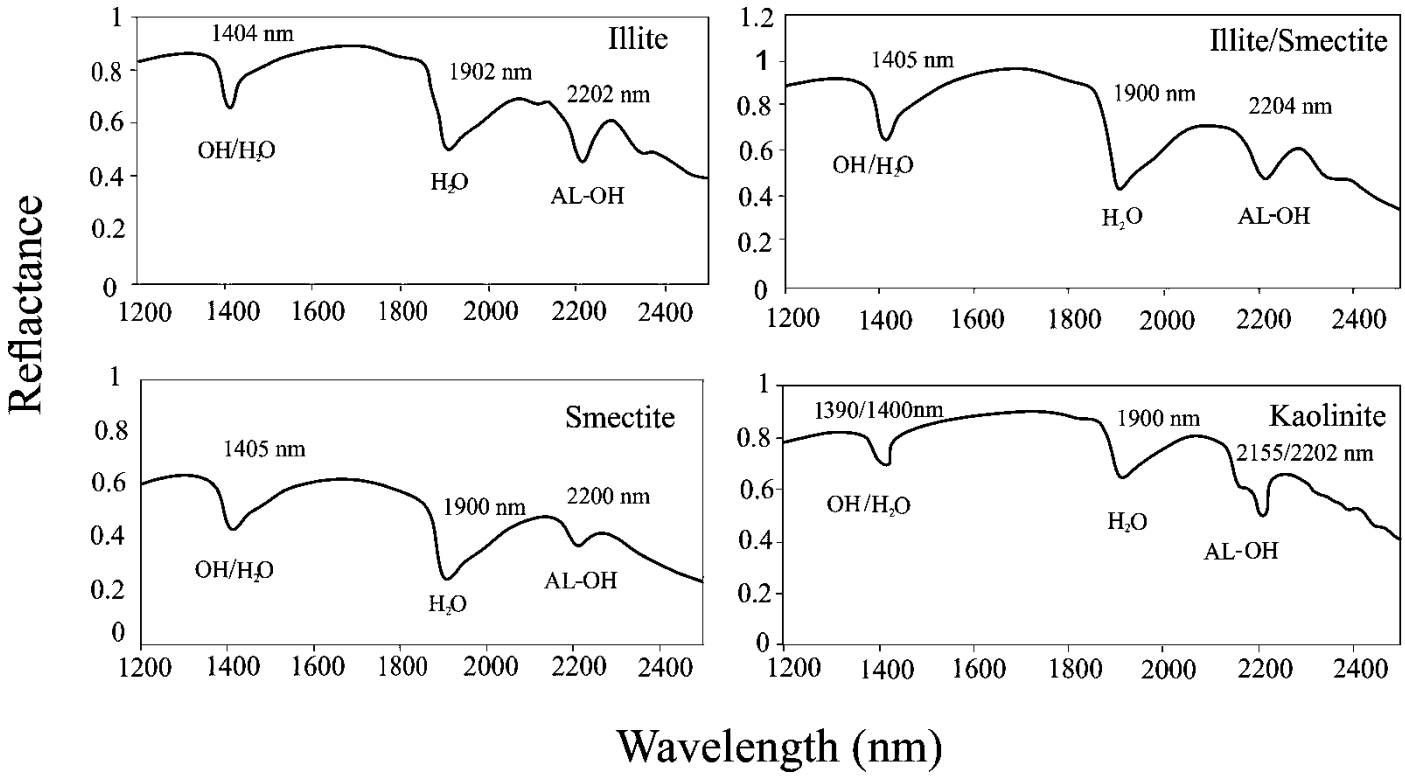

Fig. A3. Representative spectra of illite, illite-smectite, smectite and kaolinite from the Montaña de Manganeso samples

Supplementary material (Chapter 5)

Fig. A1. Characteristics of Mn ores from the Montaña de Manganeso deposit A) Ores frequently present sharp contacts with the host rocks. B) Crystalline quartz over soft and powdery ore. C) Mn ore is strongly silicified such that it is frequently hard and brittle D) Chalcedony formed within vugs in silicified Mn ore. E) Botryoidal chalcedony filling open spaces F) Mn oxides fill fractures within coarse crystalline quartz.

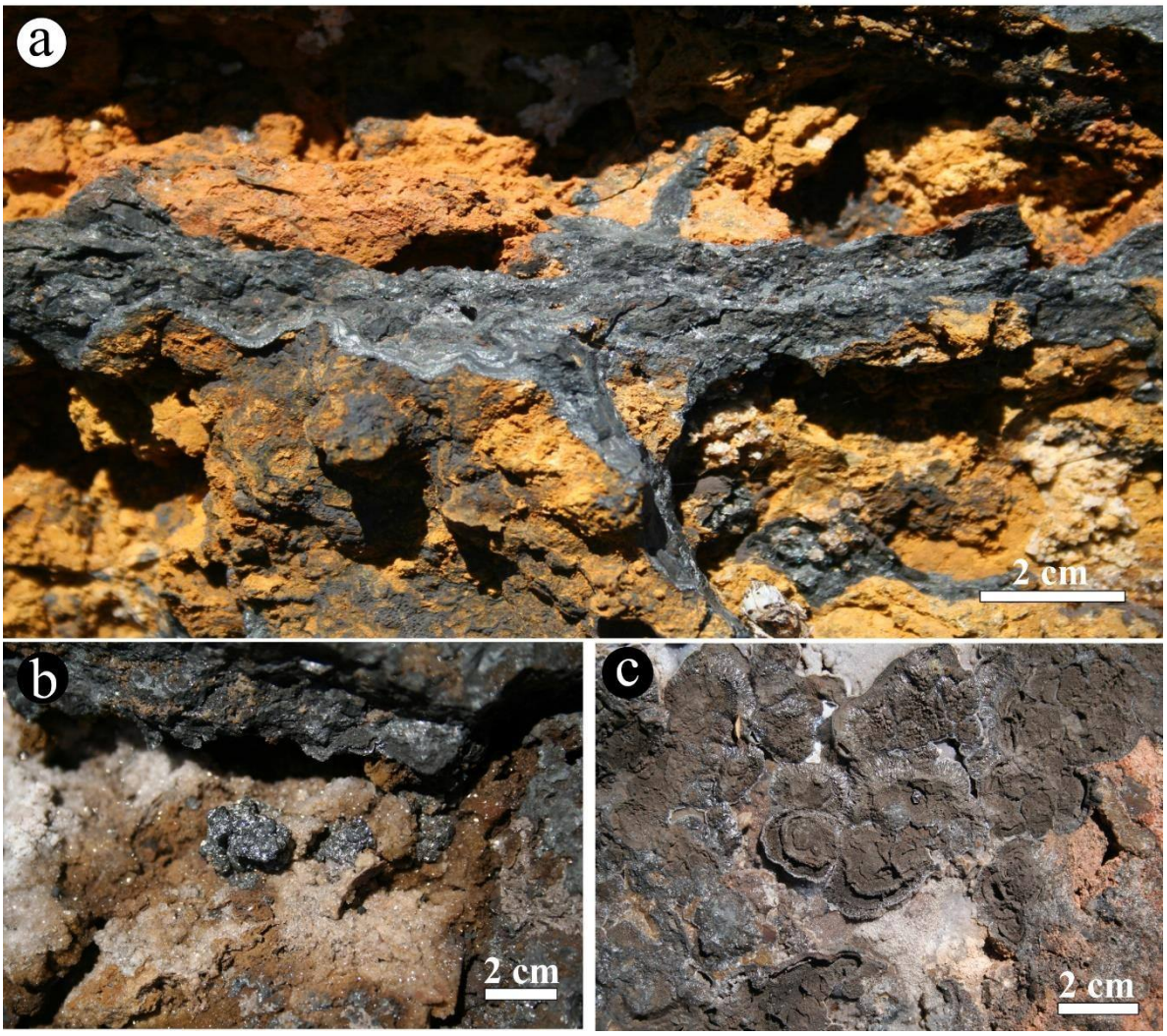

Fig. A2 Localized supergene alteration of Mn oxides. A) Colloform B) Globular C) pisolitic-like textures produced by supergene alteration.

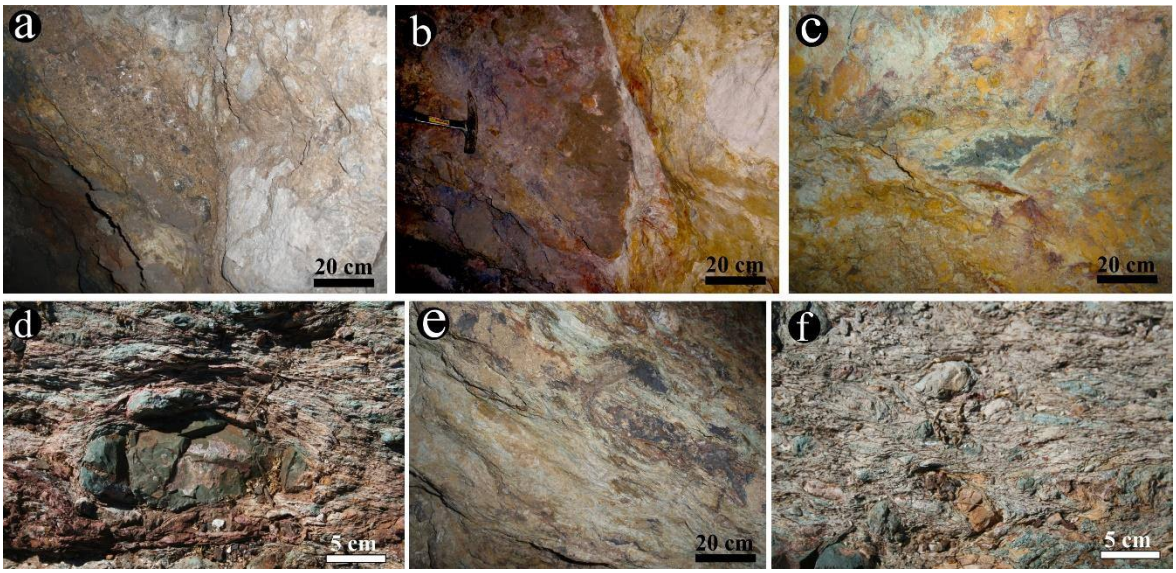

Fig. A3 Host rocks from underground exposures. (A) and (B) Mn-bearing fragments within host rocks. (C) Highly altered andesites. (D) Boudinage, product of Cretaceous deformation events. (E) Highly altered andesitic-basaltic rocks. (F) A mélange produced by the accretion of the Guerrero terrane over the Sierra Madre terrane

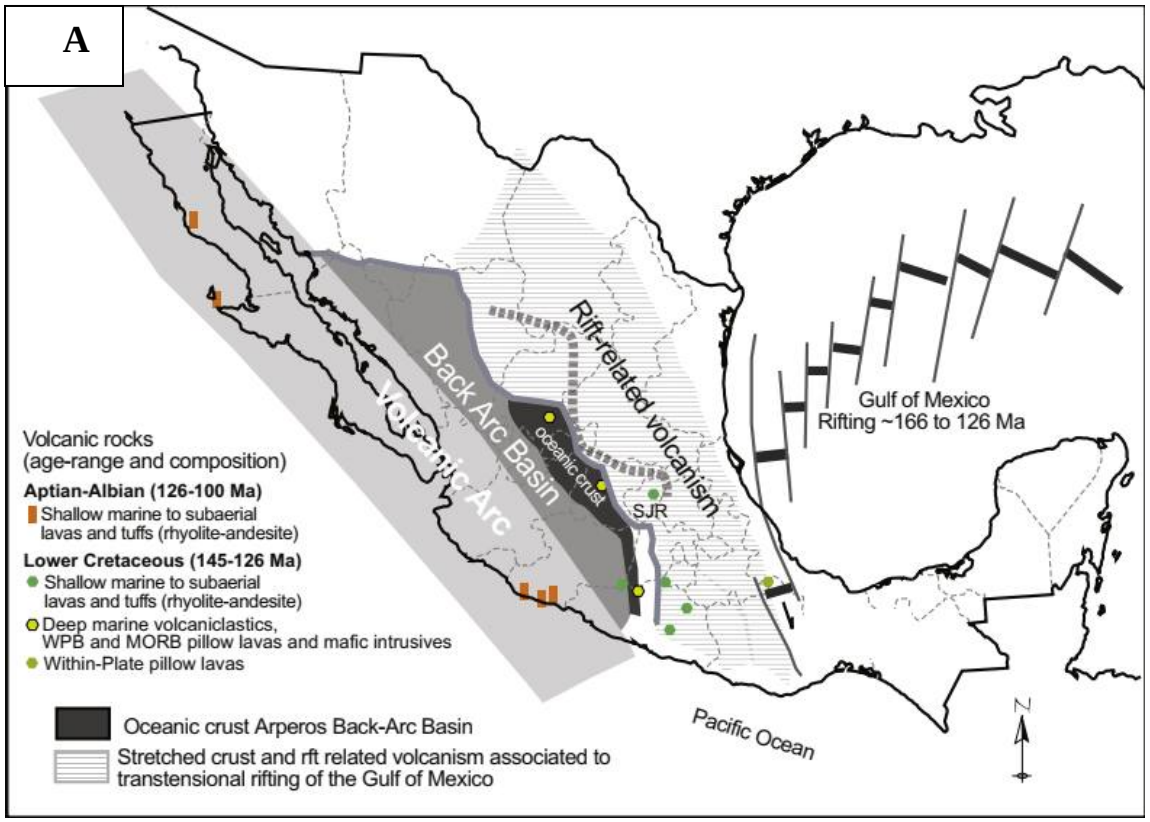

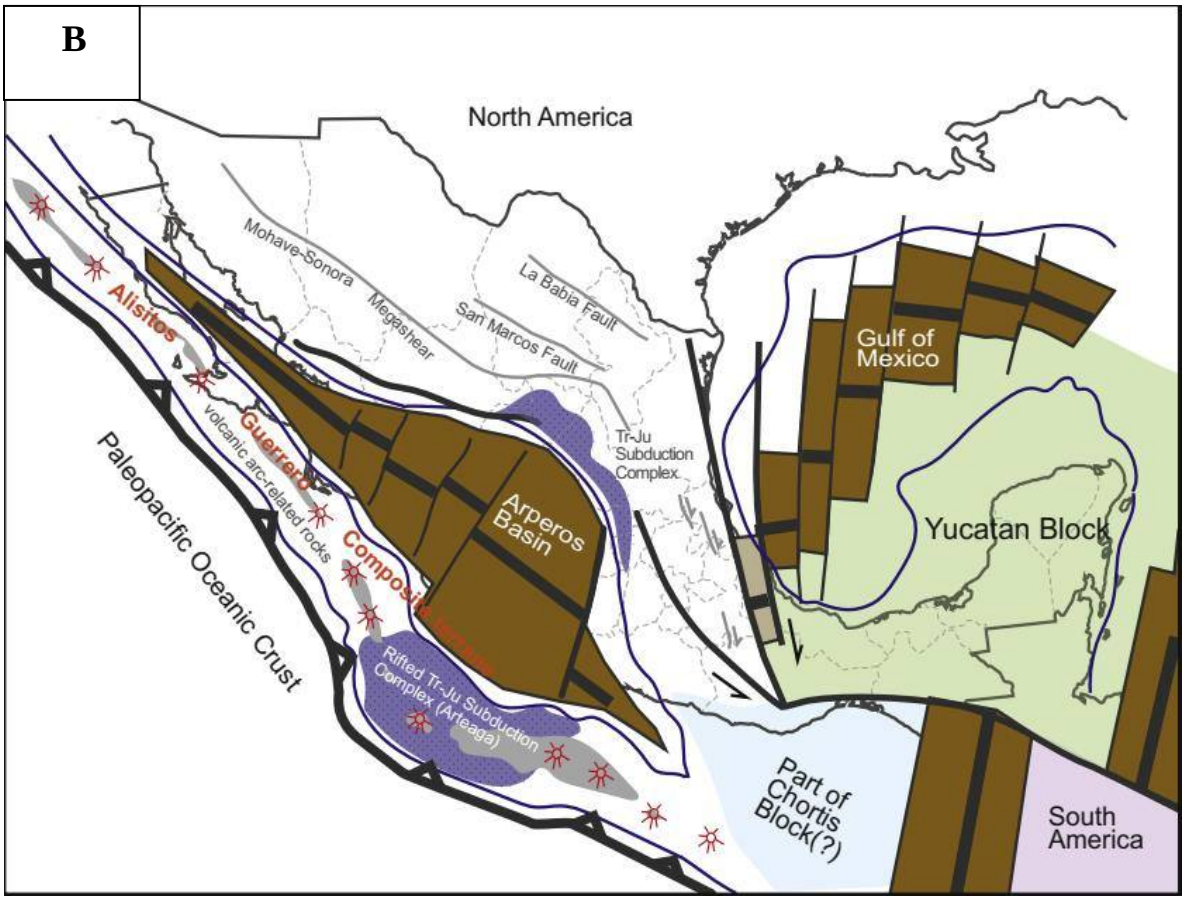

Fig. A4. Development of the Arperos basin (from Centeno-Garcia, 2017). The areal extension of the Arperos basin suggest that the model suggested in this work can be applied to several of the Mn deposits in central Mexico (see distribution of Mn deposits in Fig. A6 below).

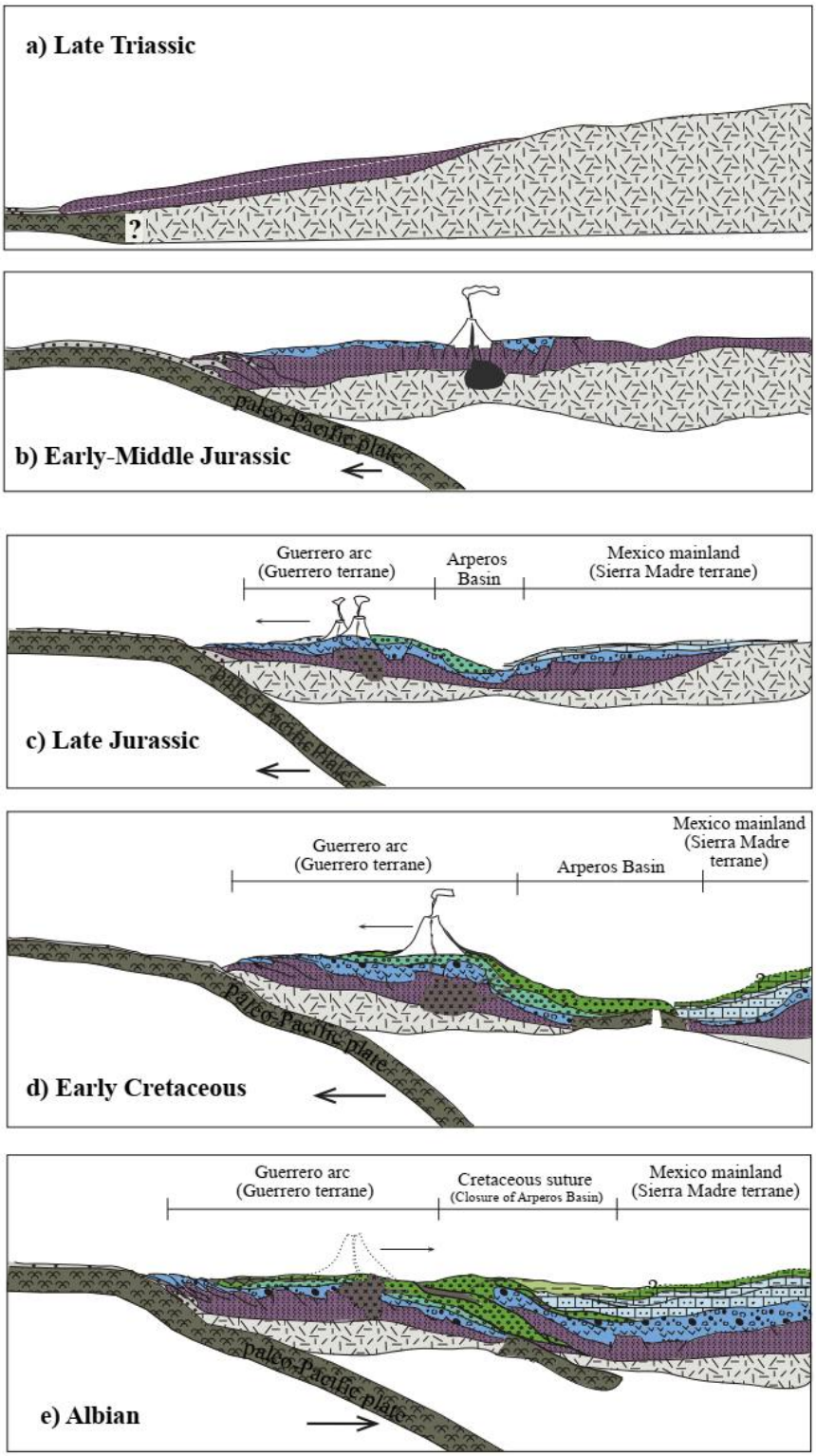

Fig. A5. Opening and closure of the Arperos basin (from Ortega-Flores et al., 2016)

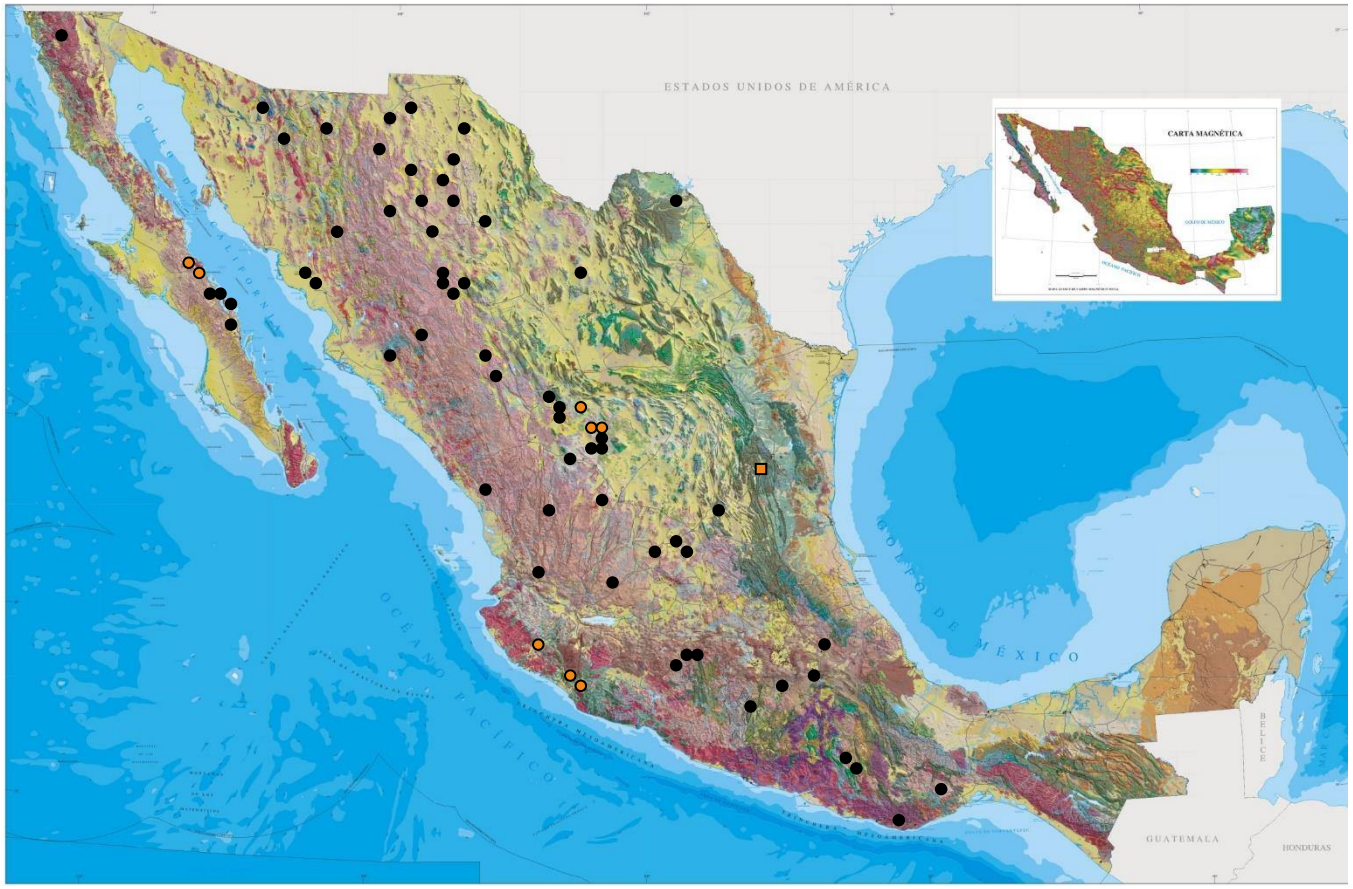

Fig. A6. Distribution of Mn deposits in Mexico (from Rodriguez-Diaz, 2018)

Table A1. Comparison of the geochemical signature of the Montaña de Manganeso deposit with typical submarine and continental hydrothermal deposits.

	Ophiolite hosted				Continental hydrothermal				
	Wasiristan complex (Pakistan)[a]	Apennine complex (Italy)[b]	Fransiscan assemblage (USA)[c]	Troodos Massif (Cyprus)[d]	Pampean Ranges (Argentina)[e] (Epithermal)	Southwest USA[f] (Epithermal)	Calatrava Region (Spain) [g] (Hot-spring)	Bahia Concepcion (Mexico) [h] (Shallow marine)	Montaña de Manganeso (This study)
SiO2 (wt%)	43.69	42.8	32.33	19.3	0.21	0.45	3.04	3.07	2.996
TiO2 (wt%)	0.32	0.1	0.12	0.2		0	0.17	0.01	na
Al2O3 (wt%)	0.73	6.6	2.29	4.1	0.14	0.32	2.05	0.28	0.342
Fe2O3 (wt%)	2.96	1.8	1.74	44.2	0.86	0.33	1.15	0.69	1.082
MnO (wt%)	45.88	31.3	44.18	9.1	84.99[#]	73.24[#]	72.98[#]	72.79[#]	70.725
MgO (wt%)	0.6	0.2	2.45	1.7	0.02	0.11	0.26	2.45	<0.402
CaO (wt%)	1.28	0.2	1.75	2.5	na	0.27	0.44	1.95	0.394
Na_2O (wt%)	0.29	1.8	0.57	na	0.14	0.23	0.18	1.13	0.286
K_2O (wt%)	0.22	4.9	0.17	0.8	1.43	1.26	3.32	0.75	1.448
P_2O_5 (wt%)	0.25	na	0.05	1.4	na	0.04	0.39	na	na
Ba (ppm)	415	2558	1 545	1071	1571	74000	<9.22*	26200	<10.861*
Sr (ppm)	na	712	524.5	1044	0	2320	1872	1110	1636
V (ppm)	144	4.5	222.2	1106	352.1	320	1381	205	136
Cr (ppm)	46	4.5	11.1	42	13	90	69	30	106
Co (ppm)	11	10	33.1	125	79.9	154	5229	27	17
Ni (ppm)	36	40	320.8	254	15.7	30	655	22	67
Cu (ppm)	72	13	133	846	1876.7	340	746	120	62.6
Zn (ppm)	64	120	345.7	361	221.9	4700	662	229	151
Pb (ppm)	49	38	na	265	1666	136000	9	29	6.6
Th (ppm)	2	21.9	<0.05	na	na	nd	2.7	0.9	<0.01
Rb (ppm)	2	170	nd	22	na	na	na	10	3
Y (ppm)	na	239	14.9	92	30	19	na	na	11.5
Nb (ppm)	na	10	na	na	29.8	42	na	na	<0.1
Zr (ppm)	na	311	0.43	183	11	5.8	na	na	3.3
Mo (ppm)	2	11	na	na	83.8	720	na	19	87.6
Sc (ppm)	2	1.6	0.11	na	<5	14.4	na	na	0.7
Fe/Mn	0.065	0.058	0.039	4.857	0.010	0.005	0.016	0.009	xxx
Co/Zn	0.172	0.083	0.096	0.346	0.360	0.033	7.899	0.118	0.12
Co/Ni	0.306	0.250	0.103	0.492	5.089	5.133	7.983	1.227	0.30

[a] (Shah and Moon, 2007)

[b] Data from volcanic hosted (VH3) Cala Fico deposit (Sinisi et al., 2012)

[c] Average ore values from Ladd-Buckeye district (Hein et al., 1987)

[d] Boyle (1990)

[e] Average values of different minerals (Table 2 and 3, Leal et al., 2008)

[f] Major elements from Hewett and Fleischer (1960), minor and trace elements from Hewett (1964, Table 2). Minor and trace element data converted to ppm from %.

[g] Average values of cryptomelane from Crespo and Lunar (1997); Pb and Th from Crespo et al., (1995).

[h] Major oxides from Bahia Concepcion are average values from Canet et al., (2005)(Table 3). Trace elements are from Rodriguez-Diaz et al., 2019

Supplementary material (Chapter 6)

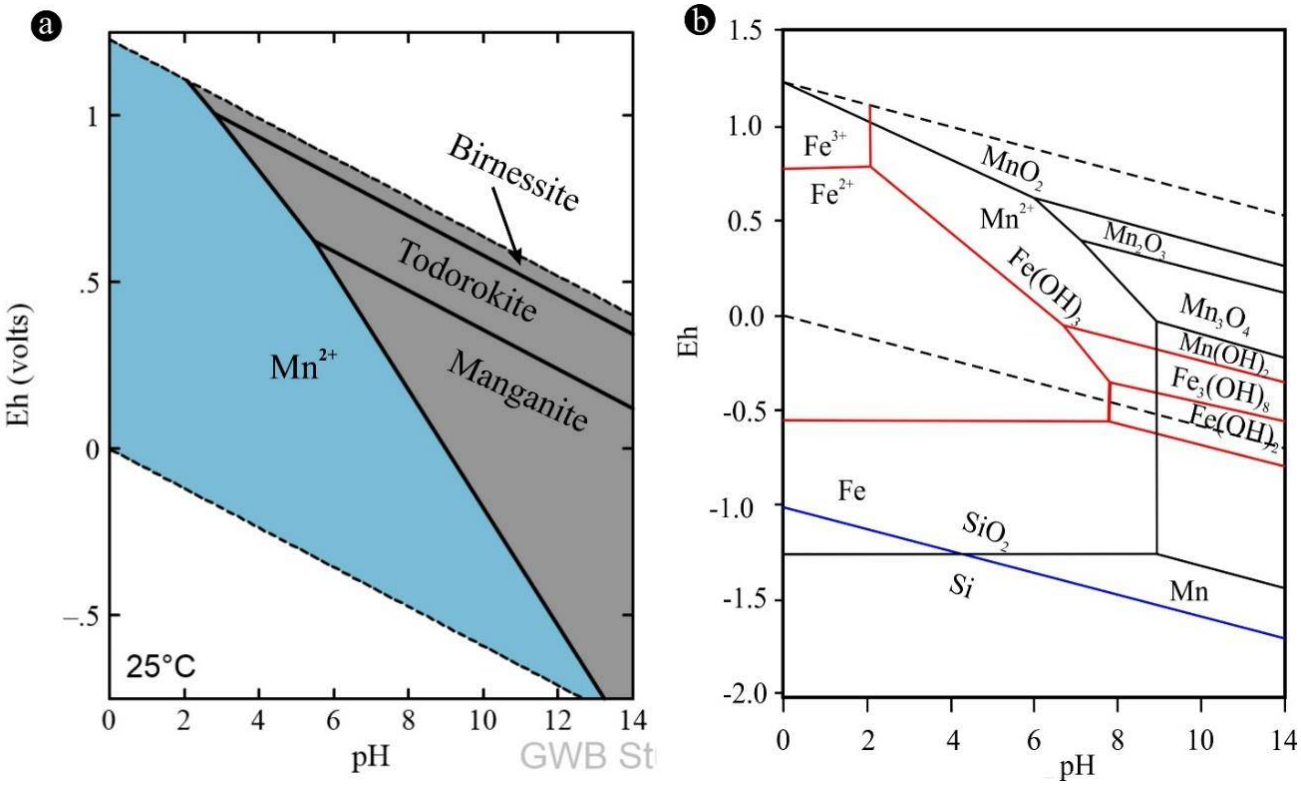

Fig. A1. Eh-Ph diagram showing stability regions of Mn, Fe and Si compounds. A) Eh-pH diagram for the Mn-H_2O system for seawater at 25°C calculated from Geochemist's Workbench database. Birnessite swapped for Mn^{2+}, Hausmanite, bixbyite and pyrolusite suppressed. Shaded areas represent soluble phases (blue) and insoluble phases (grey) b) Integrated Eh-pH diagram for the Si-Fe-Mn-H_2O system under hydrothermal conditions (300°C). Sloping dotted lines represent the stability boundaries of H_2-H_2O and H_2O-O_2. Blue, red and black solid lines represent the stability boundaries of Si, Fe and Mn, respectively. Diagram modified after (Yang et al., 2014).

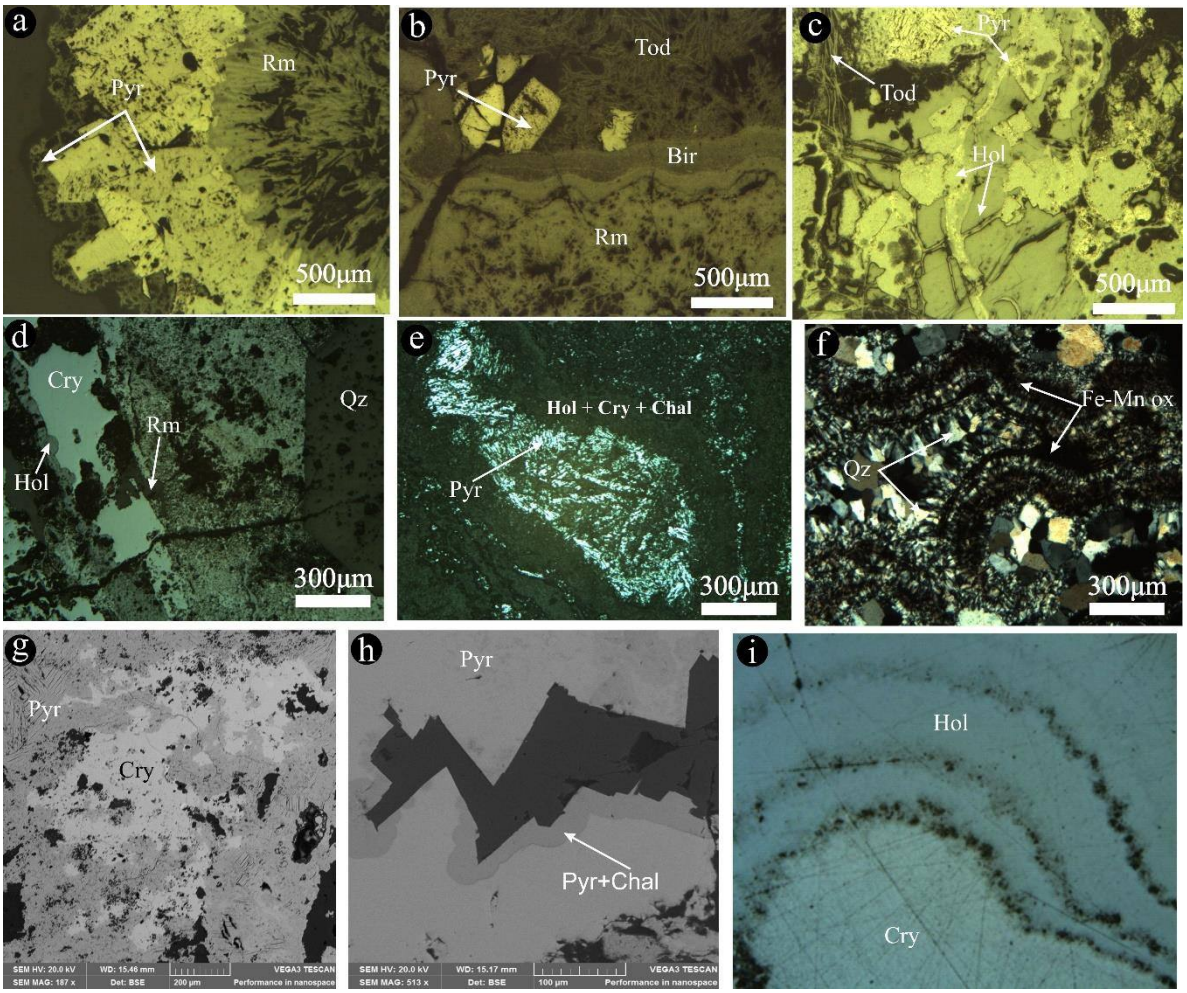

Fig. A2. Photomicrographs of different manganese oxides identified by petrography in the Montaña de Manganeso samples.